

---

INSTITUTE FOR REMOTE SENSING APPLICATIONS

# **FRACTALS IN GEOSCIENCE AND REMOTE SENSING**

Proceedings of a Joint JRC/EARSeL Expert Meeting  
Ispra, Italy 14-15 April 1994

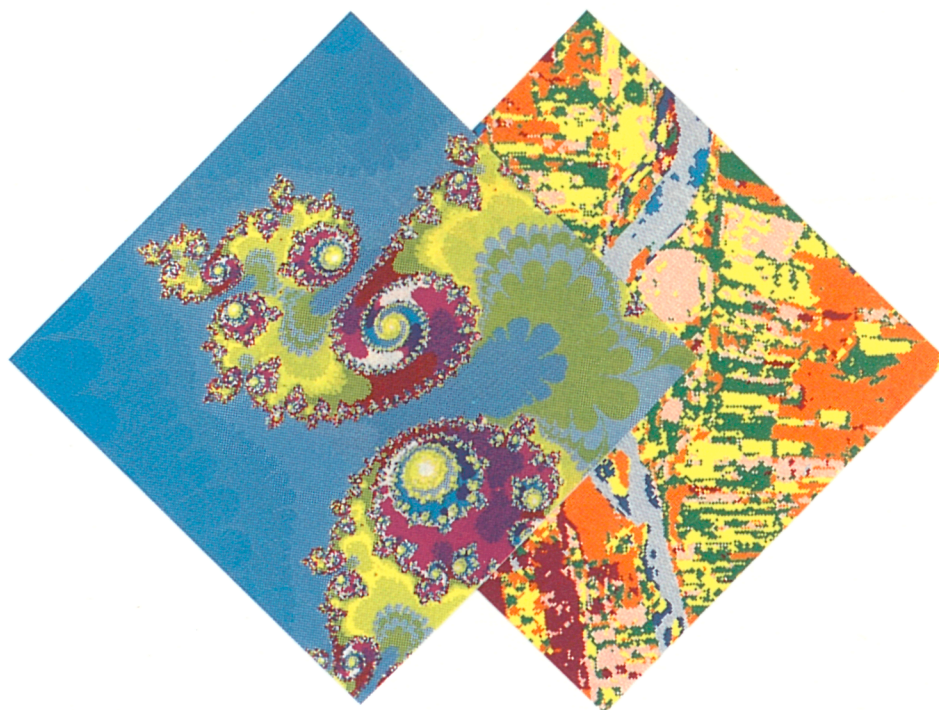


IMAGE UNDERSTANDING RESEARCH SERIES Vol. 1









---

INSTITUTE FOR REMOTE SENSING APPLICATIONS

# **FRACTALS IN GEOSCIENCE AND REMOTE SENSING**

Proceedings of a Joint JRC/EARSeL Expert Meeting  
Ispra, Italy 14-15 April 1994

*Edited by*

G.G. Wilkinson, I. Kanellopoulos and J. Mégier

*Organizing Committee*

J. Mégier, JRC Ispra

K. Seidel, ETH Zurich

G.G. Wilkinson, JRC Ispra

IMAGE UNDERSTANDING RESEARCH SERIES Vol. 1

Published by the  
**EUROPEAN COMMISSION**  
Directorate-General XIII  
Telecommunications, Information Market and Exploitation of Research  
L-2920 Luxembourg

**LEGAL NOTICE**

Neither the European Commission nor any person  
acting on behalf of the Commission is responsible for the use which might  
be made of the following information

Cataloguing data can be found at the end of this publication

Luxembourg: Office for Official Publications of the European Communities, 1995

© ECSC-EC-EAEC, Brussels • Luxembourg, 1995

*Printed in Italy*

# Acknowledgments

The chapters which appear in this book are all based on presentations at an Expert Meeting entitled '*Fractals in Geoscience and Remote Sensing*' which was held at the Joint Research Centre (JRC) of the European Commission, Ispra, Italy, on 14-15 April 1994. The meeting was jointly organised by the JRC and by the European Association of Remote Sensing Laboratories (EARSeL). The editors would like to acknowledge the assistance and co-operation of the many people who directly and indirectly contributed both to the success of the Expert Meeting itself and to the production of this volume.

First and foremost we would like to thank the authors themselves, not only for contributing to the extremely interesting and lively scientific meeting on which this volume is based, but also for producing the significant written contributions which form the material presented herein as a permanent record of their views, ideas, and results for a wider audience. We would also like to thank EARSeL for jointly sponsoring the meeting alongside the JRC and particularly Madeleine Godefroy, of the EARSeL Secretariat, for her assistance and patient handling of some of the more difficult logistical problems associated with convening an international meeting of this kind. We are also grateful to Dr. Tim Ellis (City University, London) for acting as a session chairman during the meeting. Thanks are also due to the many staff of the JRC who assisted in the organization of the meeting and in the production of this volume. Although it is difficult to single out particular individuals, Jeremy Wells of the JRC Reprographic Service merits a special mention for his expert management of the book production as does Karen Fullerton for her assistance with creating the cover images.

*The Editors*





# Contents

Introduction ( <i>The Editors</i> )	7
Chapter 1: Standard and Advanced Multifractal Techniques in Remote Sensing ( <i>D. Schertzer and S. Lovejoy</i> )	11
Chapter 2: An Evaluation of the Contribution of Fractals to Remote Sensing Problems ( <i>M. Raffy</i> )	41
Chapter 3: Fractal and Multi-resolution Techniques for the Understanding of Geo-Information ( <i>M. Datcu and K. Seidel</i> )	56
Chapter 4: Multifractal Analysis of Remotely Sensed Images ( <i>J. Lévy-Véhel</i> )	85
Chapter 5: How Bright is the Coast of Brittany? ( <i>S. Lovejoy and D. Schertzer</i> )	102
Chapter 6: Multifractals: Theory and Application to Image Texture Recognition ( <i>S. Fioravanti</i> )	152
Chapter 7: Mapping Spatial Variability in Landscapes: An Example Using Fractal Dimensions ( <i>S. de Jong</i> )	176
Chapter 8: Applications of the L-Systems for Canopy Reflectance Modelling with Monte Carlo Ray Tracing Technique ( <i>Y. Govaerts and M. Verstraete</i> )	211
Chapter 9: Fractal Modelling of Chernobyl's Radioactive Fallout Over Europe ( <i>G. Salvadori et. al.</i> )	237
Chapter 10: Fractals in Geosystems and Implications for Remote Sensing ( <i>L. Vasiliev</i> )	252
Chapter 11: Fractal-Based Evaluation of Relief Mapping Techniques ( <i>L. Polidori</i> )	277
Chapter 12: Characterisation and Imaging of Fractal Topography ( <i>W. G. Rees</i> )	298
Chapter 13: The Fractal Structure of Materials and Surfaces ( <i>G. Dietler</i> )	325
List of Participants	343



# Introduction

The word 'fractal' has become a familiar term in the world's scientific vocabulary in the last 10-15 years following the pioneering work of Benoit Mandelbrot and others. Mandelbrot and his followers effectively opened the world's eyes to something that others had noticed before but had not proceeded to explore in such depth nor to publicize with such conviction -this is the fact that many patterns in the natural world are not 'measurable' in the normal sense of the word. These patterns have an underlying spatial structure of considerable complexity based on a principle of great simplicity known as 'self-similarity'. On the theoretical front, fractals are now studied in many disciplines and work in the inter-related areas of non-linear dynamical systems theory, fractals, and chaos is now providing some of the most exciting advances this century both in mathematics and in our understanding of geophysical processes. But to a large extent, fractals are still associated by many people with exotic forms of computer-generated art and there is a large gap between studying pure fractal patterns in themselves and actually applying our understanding of them to real practical problems. Slowly it is being realised that in fact there are many uses for fractals in scientific applications especially when shapes, forms and patterns are being studied -and particularly when these shapes, forms and patterns come from nature itself.

Remote sensing is a discipline which concerns itself with the observation and monitoring of the state of the planet. In many cases, what is actually being observed consists of natural patterns in the spatial and temporal domains. Moreover, these patterns are often observed at a variety of different space scales. It is inescapable therefore that fractals could have much relevance for remote sensing. But so far, the number of practitioners in remote sensing who have tried, successfully or otherwise, to apply fractal analysis techniques to their data sets is extremely small. This is clearly a situation of some concern.

L. F. Richardson is credited with asking the question 'How long is the coastline of Britain?' to which it is now appreciated there can be many answers -it all depends on how you make the measurement. In operational remote sensing, the measurement of the area of natural features of the landscape can be the equivalent of measuring the coastline of Britain -but in a higher dimension (i.e. area instead of length).

One of the interesting problems in remote sensing is that two teams of

researchers supposedly measuring or mapping the same thing from space rarely come up with the same answers. Quantities such as total biomass, total area of forest, and net global albedo all fall into this category. This lack of precision or uncertainty is often seized upon by politicians who wish to stall efforts at changing the way we manage the planet. If fractal aspects of nature are in any way responsible for some of these uncertainties then it is clear they deserve much greater attention than hitherto in remote sensing. Hopefully further study of fractals will not only enable us to remove some of the uncertainties inherent in remote observation of the planet but will actually help us to integrate the massive volumes of data generated by different sensors and satellites at a wide range of different spatial scales. Indeed it is in this latter area that we might expect the most significant contributions of fractals to be.

Although on the ground a forest seen by the Landsat Thematic Mapper may be the same thing as the forest seen by the NOAA AVHRR instrument, or in the near future by the MODIS or MERIS instruments to be flown on the next generation of satellites, the actual observable and 'measurable' quantities that describe that forest are very different for the various sensors. Indeed it is not at all clear how measurements at such different spatial scales should be integrated. Perhaps the answer does in fact lie with fractals, although this view is not universally accepted. Interestingly, as this volume was being prepared for publication, a special issue of the *International Journal of Remote Sensing* (Vol. 15, no. 12) appeared devoted to the topic of scaling in remote sensing. That particular issue was edited by one of the authors who has contributed to this volume. In that issue, fractals were dismissed as a tool for the analysis of scale change in contradiction to many of the chapters which appear here. We seem to have arrived at a point where scale change issues are now being taken very seriously but a major argument appears to be emerging over which mathematical tools are needed to deal with them. Hopefully this volume will make a useful contribution to the growing debate.

The chapters which follow in this volume are all based on a small Expert Meeting on the subject of '*Fractals in Geoscience and Remote Sensing*' which was held at the Joint Research Centre in April 1994. The objective of this meeting was to gather together an international group of experienced researchers in the application of fractals to remote sensing and related disciplines and to give them a free hand to show their results, and share their experiences and ideas. Since the Joint Research Centre's own Institute for Remote Sensing Applications is now the largest institute dedicated to applying remote sensing in Europe and has responsibility for many large scale

international projects concerned with observing the environment both locally (in Europe) and globally, it was felt that this was the correct venue for this meeting.

Although the improved understanding and analysis of remote sensing data was the driving force behind the meeting, a few of the authors invited to the meeting and whose work has been included here have not worked in remote sensing. One of the reasons for this is that research on the use of fractals in describing or characterizing aspects of the natural world, such as surface topography, is relevant to remote sensing or at least might become so in the future. Hence some of the papers are concerned with topics which we have chosen to include under the generic name 'geoscience' in the title, even though our emphasis and objectives are very much concerned with the future of remote sensing. The reader will also notice that the chapters in this book have different styles and represent different mathematical approaches. It was felt when the meeting was set up that (a) the number of remote sensing specialists who use, understand, and value fractal methodologies is very small and (b) there is still little consensus on what analytical approaches to use. For this reason the authors were given the freedom to write in the style which they preferred and the results are here for the reader's perusal. Each chapter has been edited to ensure general conformity to the structure of the book, and in some cases chapters have been shortened by the editors to ensure a balance between the different sections, though we hope that we have succeeded to retain the full essence of the contributions of each of the authors whose expertise and depth of knowledge are represented here.

Interestingly, the expert meeting itself became extremely stimulating with some intense arguments. What rapidly became clear is that even amongst the people who have considerable experience of fractal techniques, there are still major differences of opinion about how to use them correctly or even about whether we should use them at all given the existence of other mathematical approaches for dealing with the same problems. One of the main conclusions which emerged was that modelling the natural world by single or 'mono' fractals was mostly not sufficient and that if we are going to use fractals in real applications then emphasis should now be given to 'multi' fractals. Overall it is clear that there are many problems still to be tackled in the application of fractal techniques to remote sensing, but they may have a key role in helping us to understand exactly what measurements from space really mean. Hence there is clearly a need to devote more research to the topic of fractals in remote sensing, primarily to decide if they have a real practical use, or if they should be more or less forgotten about whilst we concentrate on other more usable methodologies.

If this volume leads to more people (a) accepting that we can not simply ignore fractals in remote sensing (at least for the time being) and (b) taking up the challenge of trying to apply them, then it will have served its main purpose.

Finally, the opportunity is taken to inaugurate with this book the first volume of the Image Understanding Research Series. The idea of this series is to present state of the art reports at regular intervals on mathematical methodologies, emerging computational techniques and technological innovations, primarily in the European context, which hold promise for improved analysis and understanding of images acquired by remote sensing.

*The Editors*

Ispira, September 1994.



# Chapter 1

## Standard and Advanced Multifractal Techniques in Remote Sensing

*Daniel Schertzer\* and Shaun Lovejoy†*

### 1 Failure of classical approaches and the nonlinear variability of geophysics

Remote sensing of the Earth has often been considered as a very applied domain where no fundamental problems were expected, and where brute force applications of standard methods were expected to be quite adequate for handling the noisy geophysical signals. However, the failures of this approach are impressive: seemingly obvious notions such as “cloud cover <sup>1</sup>” and the accepted value of the albedo of the Earth turn out to be satellite resolution dependent, the water budget is “officially” known to no better than a factor of ten, “nowcasting” is more of field of research than an operational reality... Nowhere - even in its original field of map making - has it even approached its potential. Without a doubt, these troubles are related to a fundamental characteristic of geophysical fields: their extreme variability.

One obvious aspect of this extreme variability is that it is often associated with catastrophic events: earthquakes, tornadoes, flash floods, extreme temperatures, volcanic eruptions, etc. A fundamental characteristic of this variability - which turns out to be its major cause - is that it occurs over a very large range of scales. This range often extends from 10,000 km to 1mm in space, and from geological scales to milliseconds in time:

---

\*Laboratoire de Météorologie Dynamique, Université Pierre et Marie Curie, Paris

†Physics Department, McGill University, Montréal, Canada

<sup>1</sup>See the accompanying paper Lovejoy and Schertzer 1994

typical scale ratios are at least  $10^9$ , and for geophysical flows the corresponding Reynolds Number is typically of the order of  $10^{12}$  — so large that without any doubt the dynamics are all turbulent. Indeed, all geophysical processes show abundant evidence of nonlinear variability resulting from strong nonlinear interactions between different scales, different structures, and different fields. Standard approaches which invariably hypothesize homogeneity at the scale of observation are totally inadequate to deal with such a variability.

Over the last fifteen years, a whole new series of analysis and modelling techniques - at first fractal, then multifractal - have been developed for dealing with this variability. Many of these - such as box-counting or partition functions - have become quite standard and are already powerful enough that they are often considered adequate. After first discussing some of these “standard” techniques, we go on to insist on their limitations. From the point of view of geophysical and remote sensing, a basic limitation is the restriction of the techniques to treating single positive scalar fields whereas the physics involves many interacting fields each of which can be vector or tensor. However, even within the framework of positive scalars, the standard techniques are in a sense too general; they attempt to determine an infinite number of parameters (e.g. the entire dimension/codimension function). We shall show that the problem can be made tractable by exploiting the recent discovery of multifractal universality classes and by using especially designed analysis techniques. This paper is complementary to the accompanying Lovejoy and Schertzer 1994 chapter (designated LS94 below).

## 2 The scalar multifractal framework

### 2.1 Fractals and multifractals

Without any doubt, Fractal Geometry (Mandelbrot 1983) provides the simplest non-trivial example of scale invariance, and is appropriate for dealing with fractal sets. Unfortunately in geophysics we are much more interested in fields (e.g. temperature, wind, radiances etc.) and are rarely interested in geometrical sets. In order to illustrate the need to consider multifractal fields rather than Fractal Geometry we will consider the rain field, which is often of prime importance in geophysical remote sensing. Let us start by recalling the notion of fractal dimension by considering the number of occurrences of a given phenomenon over a wide range of scales. We will question below whether this notion of occurrence is in fact well posed and

relevant. If it is, and if the phenomenon of interest is scaling, then the number of occurrences ( $N_A(l)$ ) of an event at resolution scale  $l$  (in space and/or time) follows a power law<sup>2</sup>:

$$N_A(l) \approx \left(\frac{l}{L}\right)^{-D_F} \quad (1)$$

$D_F$  being the (unique) fractal dimension, generally not an integer, and  $L$  the (fixed) largest scale. For instance, Fig. 1 shows the records of rain events during the last 45 years in Dedougou (Hubert and Carbonnel, 1989). These authors show that the occurrence of rainy days during a certain time scale  $T$  is fractal, having a dimension  $D_F \approx 0.8$ , which accounts for the fact that the rain events on the time axis form a Cantor-like set. Amusingly, the wet season is often considered to last 7 months per year, and  $0.8 \approx \log 7 / \log 12$  (recall that the standard Cantor set is obtained by iteratively removing the (closed) middle section of the unit interval and has dimension  $\log 2 / \log 3$ ).

Numerous similar (mono-) fractal results can be obtained on different fields. However fields having different levels of intensity do not reduce to the oversimplified binary question of occurrence or non-occurrence of an event. For instance, in the case of rain we have to address the fundamental question: what is the rain rate at different scales? What is a negligible rainrate? Generalizations of fractal/scale invariance ideas well beyond geometry were desperately needed and appeared in 1983 when the dogma of a unique dimension was finally abandoned (Henstchel and Procaccia 1983, Grassberger 1983, Schertzer and Lovejoy<sup>3</sup> 1983).

However, it is already important to note that the notion of codimension ( $c$ ) (usually defined by  $c = D - D_F$ , where  $D$  is the dimension of the embedding space) can be considered to be at least as fundamental as the notion of fractal dimension  $D_F$ . Indeed,  $c$  can be directly defined as measuring the fraction of the space occupied by the fractal set  $A$  of dimension  $D_F$ . This can be seen by considering that a (randomly placed) ball  $B_l$  of size  $l$  has the following probability of intersecting  $A$ :

$$P(B_l \cap A) \approx \frac{N_A(l)}{N(L)} = l^{-c} \quad (2)$$

where  $N(l) \approx l^{-D}$  is the number of balls of size  $l$  necessary to cover the  $D$ -dimensional space in which the set  $A$  is embedded.

---

<sup>2</sup>Here and below the sign  $\approx$  means equality within slowly varying and constant factors

<sup>3</sup>The former references treated self-similar (isotropic) multifractals, while the latter treated the more general case of anisotropic multifractals using elliptical dimensions (see below)

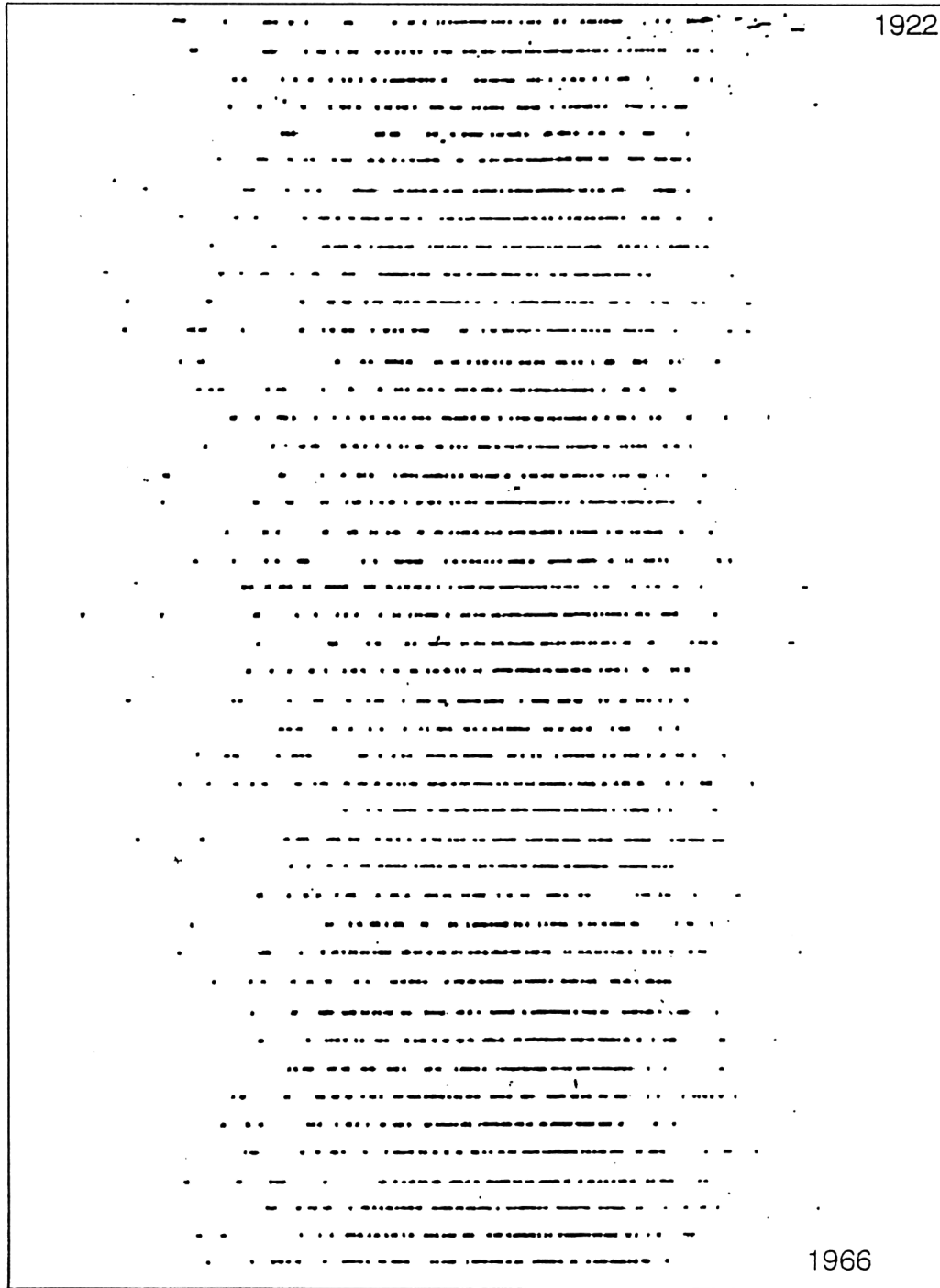


Figure 1: 45 years of daily rain rates in Dedougou (Burkina Fasso). Each line corresponds to one year of observation, and each black dot to a rainy day (Hubert and Carbonnel 1990). The rain events form Cantor-like sets of dimension  $D_F \approx 0.8$ . (The standard Cantor set is of dimension  $\log(2)/\log(3)$ ).

In fact, for multifractal fields, codimensions will be more fundamental and useful than dimensions, since they give intrinsic characterizations of the multifractal process. We will therefore use a codimension formalism (Schertzer and Lovejoy 1987, 1992) rather than the more popular dimension formalism developed for strange attractors (e.g. Halsey *et al.* 1986). One may note that the need of a codimension formalism has recently been implicitly acknowledged by Mandelbrot<sup>4</sup> (1991).

## 2.2 The extension to scalar multifractals

One obtains much more information about rainfall by looking not simply at its occurrence, but at its rate: a 1 mm daily rain rate is negligible compared to a 150 mm daily rain rate! For instance an analysis of the rain rate at Nimes (France) during a few years, and averaged over varying scales  $T$  (from a day to a year) shows great intermittency. Most of the time the rain is negligible, while sometimes it reaches 200 mm (228 mm in few hours, for the famous October 1988 catastrophe!) - in comparison the daily average is  $\approx 2.1$  mm. The variability was found to be so significant in this time series that Ladoy *et al.* (1991) found some evidence of the divergence of moments (a subject we will discuss more below) -especially considering the 1974–1988 Nimes time series (Ladoy *et al.* 1993). Qualitatively this variability is analogous to that of the energy flux cascade in turbulence (as displayed in fig. 2), an analogy which turns out to be quite profound.

## 2.3 Multiplicative cascade processes

It has become clear that the process transferring energy from larger to smaller scales in turbulence is a multiplicative process (Kolmogorov 1962, Obukhov 1962, Yaglom 1966, Novikov and Stewart 1964, Mandelbrot 1974): a random factor determines the fraction of the rate of energy transferred from one large eddy to one of its sub-eddies (as shown on fig. 4 for a two dimensional cut), larger structures are thus multiplicatively modulated by smaller ones. Consider iterating this construction and denote the scale ratio  $\lambda$  ( $= L/l$  where  $L$  is the larger scale and  $l$  the smallest resolved scale which corresponds to the spatial resolution of our field). As  $\lambda \rightarrow \infty$ , we observe singularities: at some points the field diverges (a singularity), whereas over most of the space it goes to zero (a regularity; for convenience we collectively call both types of behaviour “singularities”).

---

<sup>4</sup>The codimension function is essentially the same as the “Cramer function”

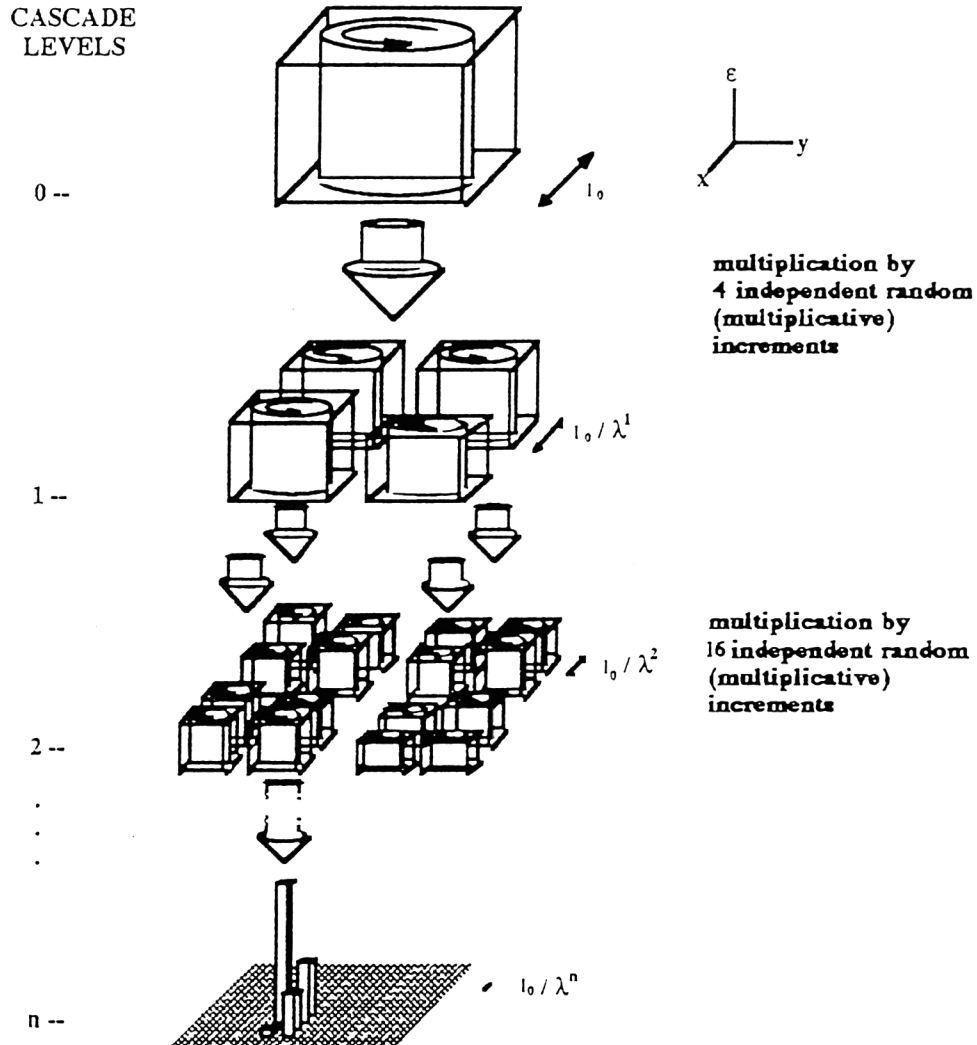


Figure 2: A schematic diagram showing a two-dimensional cascade process at different levels of its construction to smaller scales. Each eddy is broken up into four sub-eddies, transferring a part or all of its energy flux to the sub-eddies. In this process the flux of the field at large scales multiplicatively modulates the various fluxes at smaller scales, the mechanism of flux redistribution is repeated at each cascade step (self-similarity).



The simplest multifractal model of this genre is the  $\alpha$ -model (Schertzer and Lovejoy 1983, Levich and Tsvetkov 1985, Bialas and Peschanski 1986, Levich and Shtilman 1991...) obtained with a random two-state multiplicative factor: the only restriction is conservation of the ensemble average. If after  $n$  iterations of the multiplicative process,  $\epsilon_n$  is the value of the field (for example, the energy flux to smaller scales), we have the relation  $\epsilon_n = \mu\epsilon \epsilon_{n-1}$ , where  $\mu\epsilon$  is a random variable which can have two values with the probabilities :

$$\begin{aligned} Pr(\mu\epsilon = \lambda^{\gamma^+}) &= \lambda^{-c} & \text{strong sub-eddies}(\gamma^+ > 0) \\ Pr(\mu\epsilon = \lambda^{\gamma^-}) &= 1 - \lambda^{-c} & \text{weak sub-eddies}(\gamma^- < 0) \end{aligned} \quad (3)$$

$\gamma^+, \gamma^-, c$  are constrained so that the ensemble average  $\langle \mu\epsilon \rangle = 1$  (ensemble average conservation of  $\epsilon$ ). The (monofractal)  $\beta$ -model (Frisch *et al.* 1978) is obtained when  $\gamma^- = -\infty, \gamma^+ = c$ : the sub-eddies are dead or alive.  $c$  is the codimension of the (unique) support of turbulence of dimension  $D_F = D - c$ .

## 2.4 Bare and dressed quantities

Figures 3 and 4 show an example of an  $\alpha$ -model developed from a large scale to a small homogeneity scale: this is the “bare” cascade, which develops singularities when the homogeneity scale goes to zero. But our sensors (e.g. satellites) have not such a small resolution (the homogeneity scale is perhaps of the order of millimeters), and what we observe is an averaged field; these are the “dressed”<sup>5</sup> quantities in the sense that the observation hides or dresses the activity occurring on scales smaller than that of observation. On the contrary, in the same sense, a cascade whose development is limited to the scale  $\lambda$  is “bare” on this scale of observation: no smaller scale activity is hidden. Figs. 3 and 4 (especially 4) show that the small scale singularities which appear when we develop the cascade to the homogeneity scale may give overwhelming contributions to the larger scale fluctuations of the dressed quantities. These contributions can be so important that as we will see later, they may imply divergence of high order statistical moments, corresponding to “hard” multifractal behaviour.

## 2.5 Multifractal fields

In the  $\alpha$  model, pure singularities  $\gamma^+, \gamma^-$  (note: only when  $\gamma > 0$  we obtain singularities, otherwise they are regularities, but for convenience all

---

<sup>5</sup>The jargon “bare” and “dressed” are borrowed from the renormalization literature.

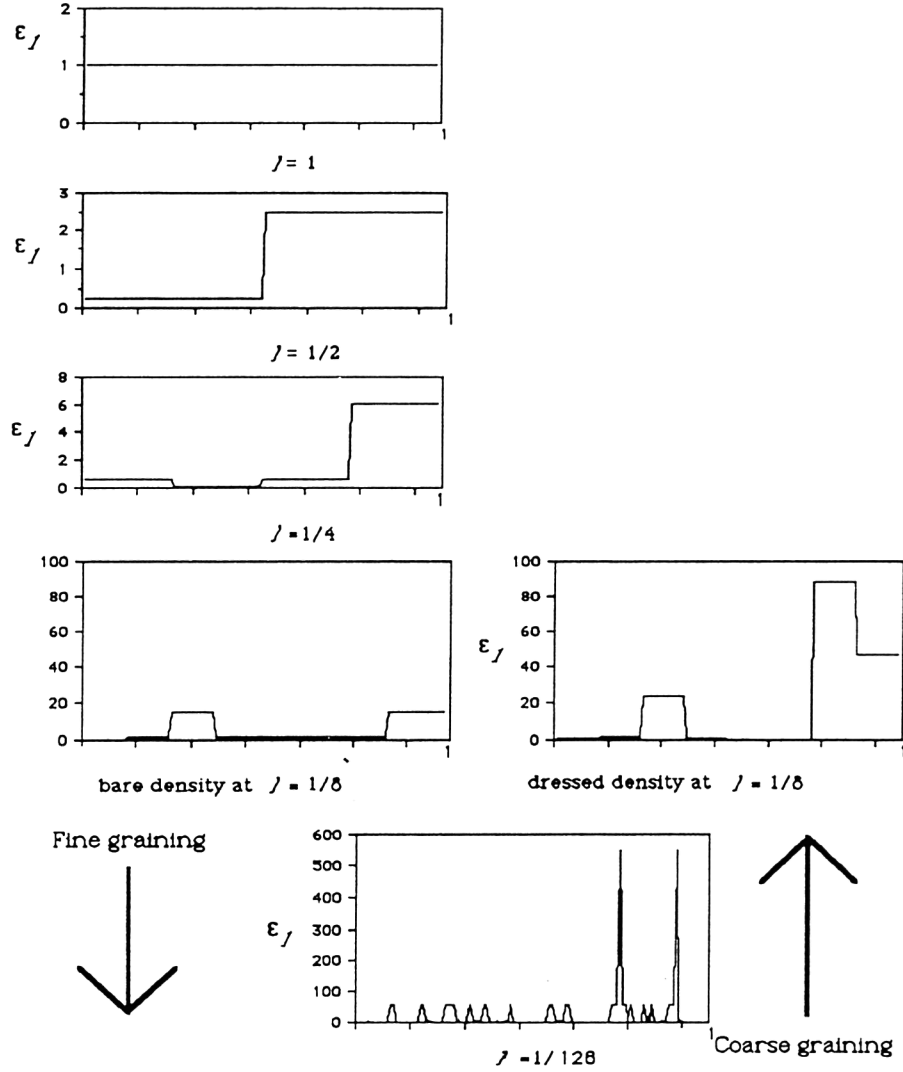


Figure 3: Illustration of the ‘bare’ and ‘dressed’ energy flux densities. The left hand side shows the step by step construction of a ‘bare’ multifractal cascade (the  $\alpha$ -model) starting with an initially uniform unit flux density. The vertical axis represents the density of energy  $\epsilon_\lambda$  flux to a smaller scale with its ensemble average conserved  $\langle \epsilon_\lambda \rangle = 1$ . At each step the horizontal scale is divided by two. The developing spikes are incipient singularities of various orders (characteristic of multifractal processes).

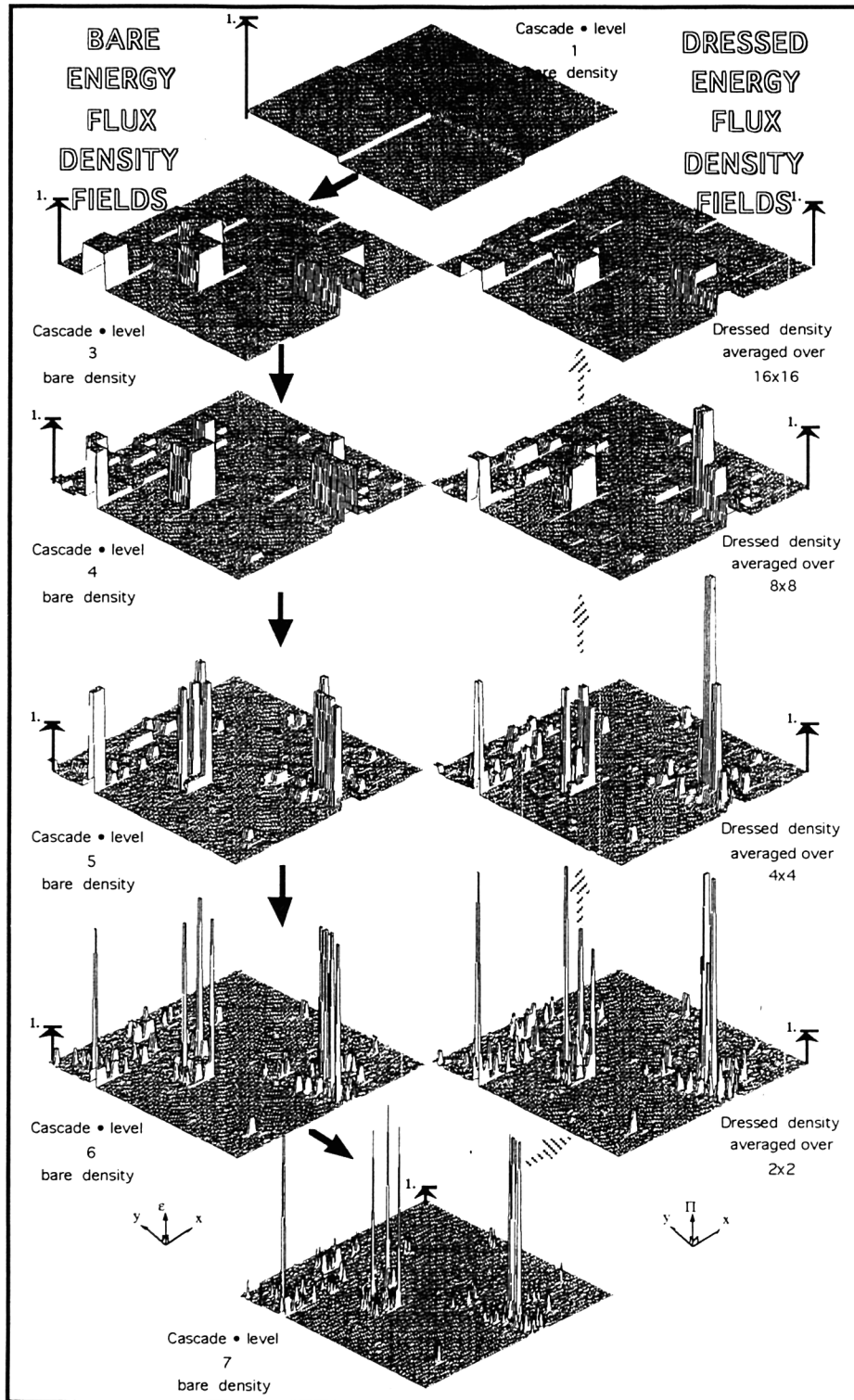


Figure 4: Illustration of the 'bare' and 'dressed' energy flux densities, for a two-dimensional cut.

the  $\gamma$  are called “singularities”) give rise to an infinite hierarchy of mixed singularities ( $\gamma^- \leq \gamma \leq \gamma^+$ ) ( $n^{\text{th}}$  step):

$$\begin{aligned}\gamma &= \frac{n^{+\gamma^+} + n^{-\gamma^-}}{n} \\ n^+ + n^- &= n; \\ Pr(n^+ = k) &= C_n^k \lambda^{-ck} (1 - \lambda^{-c})^{n-k}\end{aligned}\tag{4}$$

The probability density of the resulting field is given by :

$$Pr(\epsilon_n \geq (\lambda^n)^\gamma) \approx (\lambda^n)^{-c_n(\gamma)}\tag{5}$$

When  $n \gg 1$  :  $c_n(\gamma) \approx c(\gamma)$ , a function independent of  $n$ , and the probability density of the multifractal turbulent field  $\epsilon_\lambda$  (the field  $\epsilon$  at scale  $\lambda$ ) is given by (Schertzer and Lovejoy 1987):

$$Pr(\epsilon_\lambda \geq \lambda^\gamma) \approx \lambda^{-c(\gamma)}\tag{6}$$

When  $c(\gamma) < D$  ( $D$  being the space dimension), as already discussed (eq. 2),  $c(\gamma)$  is the (geometrical) codimension  $c(\gamma) = D - D(\gamma)$  corresponding to the (geometrical) fractal dimension  $D(\gamma)$  of the support of singularities whose order is greater than  $\gamma$ .

In the most interesting cases  $c(\gamma) \geq D$  the function  $c(\gamma)$  remains a (finite) codimension on an (infinite dimensional) probability space, see below. The multiple scaling behaviour of this field  $\epsilon$  at scale ratio  $\lambda$  can be also characterized by the corresponding law for the statistical moments (via a Laplace transform):

$$\langle \epsilon_\lambda^q \rangle \approx \lambda^{K(q)}\tag{7}$$

The relations between the turbulent notation used here and the strange attractor  $f_D(\alpha_D)$  and  $\tau_D(q)$  notation (the subscript  $D$  explicitly emphasizes the dependence of  $\alpha, f, \tau$  on the dimension of the observing space  $D$ ) is:  $f_D(\alpha_D) = D - c(\gamma)$  and  $\tau_D(q) = K(q) - (q - 1)D$  with  $\alpha_D = (D - \gamma)$ . The turbulence notation used is necessary when dealing with stochastic processes because  $\gamma, c, K$  are intrinsically contrary to  $\alpha_D, f_D, \tau_D$  which diverge with  $D \rightarrow \infty$ , it also avoids introducing negative (“latent” dimensions when  $c(\gamma) > D$  (Mandelbrot 1991).

Just as  $f(\alpha)$  is the Legendre transform (Parisi and Frisch 1985) of  $\tau(q)$ , so  $c(\gamma)$  is the transform of  $K(q)$ :

$$\begin{aligned}K(q) &= \max_\gamma (q\gamma - c(\gamma)) \\ c(\gamma) &= \max_q (q\gamma - K(q))\end{aligned}\tag{8}$$

These relations establish a one to one correspondence between orders of singularities and moments ( $q = c'(\gamma), \gamma = K'(q)$ ).

## 2.6 Some basic properties of multifractal fields

Multifractal fields, contrary to (mono-) Fractal Geometry, involve an infinite hierarchy of  $\gamma$ 's corresponding to an infinite hierarchy of  $c(\gamma)$ . Indeed, according to eq. 5, the hierarchy of codimensions may be obtained by thresholding the field and computing the fractal codimension of values greater than this threshold  $\lambda^\gamma$  (see fig 5). The codimension function  $c(\gamma)$  must

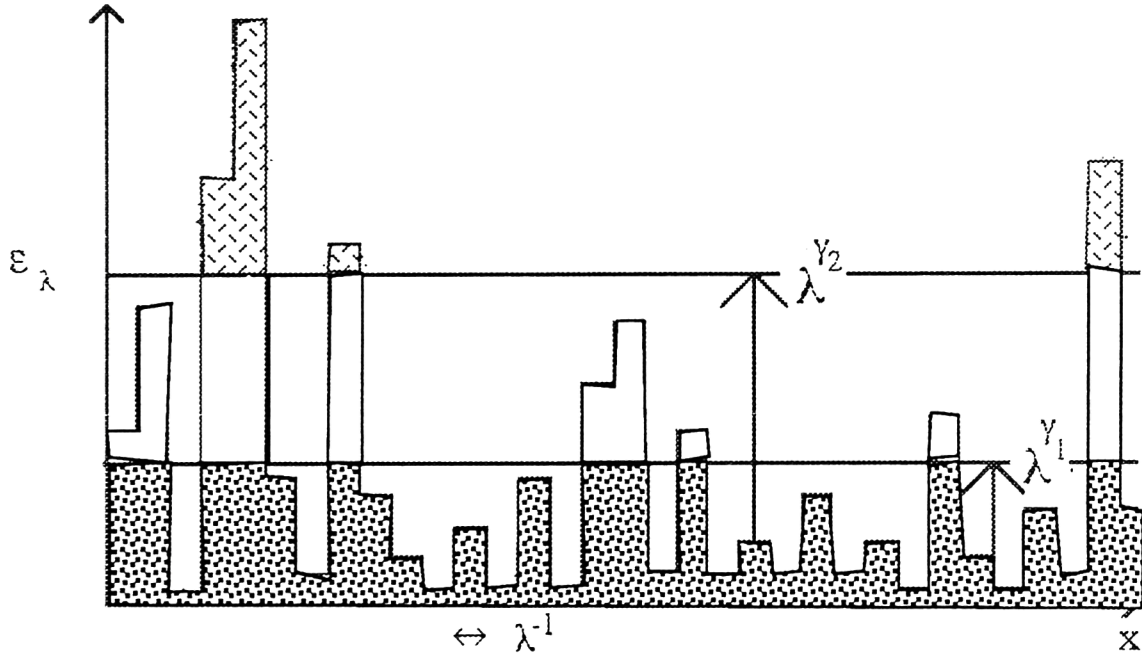


Figure 5: The importance of the threshold in analyzing a multifractal field: if  $\gamma_1 < \gamma_2$ ,  $D(\gamma_1) > D(\gamma_2)$ , and  $c(\gamma_1) < c(\gamma_2)$ : the codimension is an increasing function.

satisfy only a rather weak constraint (see fig. 6): not only should it be obviously an increasing function of  $\gamma$  (if  $\gamma_1 > \gamma_2$ ,  $Pr(\epsilon_\lambda \geq \lambda^{\gamma_1}) < Pr(\epsilon_\lambda \geq \lambda^{\gamma_2})$ , thus  $c(\gamma_1) > c(\gamma_2)$ ), but with  $K(q)$ , it must also be convex (Feller 1971).

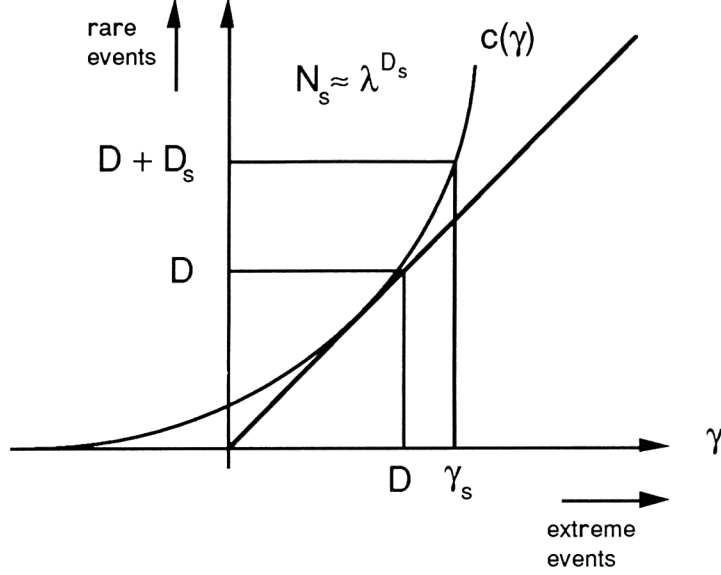


Figure 6: With larger and larger number of samples  $N_s$ , the maximum reachable singularity  $\gamma_s$  increases ( $N_s = \lambda^{D_s}$ ;  $c(\gamma_s) = D + D_s$ ; Schertzer and Lovejoy, 1989).

## 2.7 The sampling dimension $D_s$

Here we point out the utility of the notion of *sampling dimension*  $D_s$ . As we are always compelled to analyze finite samples, it is rather obvious that the highest singularities will rarely be present in a given sample. More precisely speaking, some of the singularities will almost surely not be present in a finite sample. Indeed, when we analyze only one sample/realization of the field on a dimension  $D$  at resolution  $\lambda$ , the largest singularity  $\gamma_s$  we can reach is given by  $c(\gamma_s) = D$ . More generally, if we are studying  $N_s$  samples, we can introduce the sample dimension  $D_s \neq 0$  (at resolution  $\lambda$ ) defined as  $N_s \approx \lambda^{D_s}$  (Schertzer and Lovejoy 1989, Lavallée 1991, Lavallée *et al.* 1991). This largest singularity increases with  $D_s$ , since its order is then given by  $c(\gamma_s) \approx D + D_s$  (see fig. 6), it corresponds to a moment of order  $q_s = c'(\gamma_s)$  where  $K(q)$  becomes (spuriously) linear. The sampling dimension  $D_s$  gives us a quantitative way to describe how larger samples enable us to explore more and more of the probability space, eventually attaining the rare singularities responsible of the wild behavior of experimental fields.



## 2.8 Classification of multifractal fields

Unfortunately most of the theoretical and corresponding empirical studies presuppose very restrictive calmness and regularity assumptions on multifractal fields. Such a limited view of multifractals is quite misleading. It is therefore a matter of some importance to reveal the full diversity of multifractality and classify the different types of possible multifractal fields. Indeed a purely geometric approach (without any reference to a stochastic process: Parisi and Frisch 1985, Paladin and Vulpiani 1987), presupposes that the singularities are bounded by  $\gamma_{\max}^{(g)}$ , the upper bound of geometrical singularities, with  $c(\gamma_{\max}^{(g)}) = D$  and  $\gamma_{\max}^{(g)} < D$ . Stochastic processes are generally capable of having singularities of all orders (i.e.  $c(\gamma) \geq D$  and  $\gamma > D$ ). However, conservation of the flux (e.g. energy flux in turbulence) may introduce a new constraint, which will depend on the type of conservation involved. If we assume microcanonical conservation (i.e. conservation on each realization, see: Benzi *et al.* 1984, Pietronero and Siebesma 1986, Meneveau and Sreenivasan<sup>6</sup> 1987, Sreenivasan and Meneveau 1988), then the singularities are bounded above by  $\gamma_{\max}^{(m)} = D$  (the superscript m corresponding to “microcanonical” -this bound is reached only for the extreme case in which for each step all the density of the flux is concentrated on a single subeddy (of volume  $\lambda^{-D}$ ), we may say that singularities remain “calm” and “soft”. As soon as we leave this restricted microcanonical framework to canonical conservation (i.e. ensemble conservation) we have some “wild” singularities  $\gamma > \gamma_{\max}^{(m)}$ , which can even be “hard” in the sense they are responsible of the divergence of moments -see below).

## 2.9 Divergence of moments, multifractal phase transitions and self-organized criticality

It is possible to show (Schertzer & Lovejoy, 1987) that the integration of  $\epsilon_{\lambda}^q$  over a set of dimension  $D$  diverges (for  $\lambda \rightarrow \infty$ ) when  $q > q_D$ ;  $q_D$  given by:  $K(q_D) = (q_D - 1)D$ ;  $q_D > 1$ . More precisely, consider the flux over a volume element  $B_{\lambda}$  (scale ratio  $\lambda$ ):

$$\Pi(B_{\lambda}) = \int_{B_{\lambda}} \epsilon d^{D_x} \quad (9)$$

where  $\epsilon = \lim_{\lambda \rightarrow \infty} \epsilon_{\lambda}$ . If we now consider  $\epsilon_{\lambda,D} = \Pi(B_{\lambda})/Volume(B_{\lambda})$  as a (dressed) estimate of the (bare)  $\epsilon_{\lambda}$  over the  $D$ -dimensional ball  $B_{\lambda}$ ; the two

---

<sup>6</sup>Their well known “ $p$  model” is in fact nothing more than a microcanonical restriction of the  $\alpha$  model discussed earlier

will have totally different statistical properties:

$$\langle \epsilon_\lambda^q \rangle < \infty \forall q; \langle \epsilon_\lambda, D^q \rangle = \infty, q \geq q_D (> 1) \quad (10)$$

This is the fundamental difference between the two quantities bare  $\epsilon_\lambda$  and dressed  $\epsilon_{\lambda,D}$ . One may note that the singular statistics (of dressed quantities) has been taken as a basic feature of Self Organized Criticality (Bak *et al.* 1987).

Divergence of moments of a random variable  $X$  ( $\langle X^q \rangle = \infty$  for  $q > q_D$ ) corresponds to a “hyperbolic” (algebraic) fall-off of the probability distribution:

$$Pr(X \geq s) \approx s^{-q_D} (s \gg 1) \Leftrightarrow \langle X^q \rangle = \infty \text{ for } q > q_D \quad (11)$$

The probability density obtained by differentiation is also hyperbolic, but with an exponent  $q_D + 1$ . The physical significance of divergence of moments is that when  $q < q_D$  the dressed moments are macroscopically determined whereas for  $q > q_D$  the moments will be microscopically determined depending crucially on the small scale details. It is possible to make a formal<sup>7</sup> analogy between conventional thermodynamics and multifractals; for example, the entropy corresponds to  $c(\gamma)$  and the temperature to  $1/q$ , the Massieu potential (the free energy divided by temperature), to  $K(q)$ . Therefore, this qualitatively new behaviour for  $q > q_D$  (low temperatures) can be considered as discussed in Schertzer and Lovejoy (1987) and Schertzer *et al.* (1993) Schertzer and Lovejoy 1994a: this corresponds to a first order multifractal phase transition, where the thermodynamic potential  $K(q)$  has a first order discontinuity at the critical temperature analog  $q_D^{-1}$ .

## 2.10 The three fundamental exponents: $H, C_1, \alpha$

It is already important to note that three parameters are sufficient to *locally* characterize (around the mean singularity) the infinite hierarchy of fractal codimensions  $c(\gamma)$ . Furthermore, this characterization turns out to be global under certain general hypotheses of universality we discuss in the next section. The three fundamental exponents are the following:

- **$H$**  describes the *deviation from conservation* of the flux:  $\langle \epsilon_\lambda \rangle \approx \lambda^{-H}$ .  $H = 0$  for conservative fields (for instance the energy flux in turbulence,  $\langle \epsilon_\lambda \rangle$  independent of  $\lambda$ ) whereas according to the Kolmogorov relation in real space  $\Delta v_\lambda \approx \epsilon \lambda^{1/3} \lambda^{-1/3}$  (where  $\Delta v_\lambda$  is the wind shear amplitude  $|v(x +$

---

<sup>7</sup>Only formal since we here considering systems out of equilibrium

$\lambda^{-1}) - v(x)|$  at scale ratio  $\lambda$ ), the wind shear is a non conservative field ( $H = 1/3$ ). When  $H > 0$  it is also a measure of the non-stationarity (statistical translational invariance) of the process<sup>8</sup>.

- $C_1$  describes the *mean inhomogeneity* as it is the codimension of the mean singularity:  $C_1 = c(C_1 - H)$ , in the case of conservative fluxes it is also the order of the mean singularity (and simultaneously the fixed point of  $c(\gamma)$ ).

- $\alpha$  represents the *degree of multifractality* measured by the convexity of  $c(C_1)$  around the mean singularity ( $C_1 - H$ ) measured by the radius of curvature:  $R_c(\gamma = C_1 - H) = 2^{3/2}\alpha C_1$  which increases with the range of singularities (starting from zero with the monofractal  $b$ -model). As shown below, in case of universal multifractals,  $\alpha$  is also the Lévy index of the generator and  $0 \leq \alpha \leq 2$ .

## 2.11 Universality by mixing of multifractal processes

The particularities of discrete models (based on integer scale ratios, e.g. the  $\alpha$ -model,  $p$  model) remain as the cascade proceeds to its small scale limit, if we simply iterate the model step by step with a fixed ratio of scale  $\lambda$ , we indefinitely increase the range of scales  $\Lambda \rightarrow \infty$  which already poses a non trivial mathematical problem (weak limit of random measures, see Kahane 1985). On the contrary, *keeping the total range of scale fixed and finite, mixing independent processes of the same type*. (by multiplying them, preserving certain characteristics, e.g. variance of the generator). and *then* seeking the limit  $\Lambda \rightarrow \infty$ : *a totally different limiting problem is obtained!* For instance, this may correspond to densifying the excited scales by introducing more and more intermediate scales. and seeking thus the limit of continuous scales of the cascade model. Alternatively, we may also consider the limit of multiplications of i.d.d. discrete cascades models.

In both cases, multiplying processes corresponds to adding generators:  $\epsilon_\lambda \approx \exp^{\Gamma_\lambda}$  where  $\epsilon_\lambda$  is the process and  $\Gamma_\lambda$  is the generator. If we seek *generators* which are *stable* and *attractive* under *addition*. (using the results on the second Laplace characteristic function  $K(q)$  equivalent to the free energy), we must consider (Schertzer and Lovejoy, 1987, 1989, Schertzer *et al* 1988, Fan, 1989) stable extremal Lévy noises with  $1/f$  spectra. which are characterized by a Lévy index  $\alpha$  :  $Pr(-\Gamma \geq s) \approx s^{-\alpha}$  ( $s \gg 1$ )  $\implies$  any  $q > \alpha$  :  $\langle (\Gamma)^q \rangle = \infty$ . Except for the gaussian exception  $\alpha = 2$ ,  $\alpha$  is the

---

<sup>8</sup>This should not be confused with the more restricted notion of 2nd order stationarity which depends only on the spectral exponent and which has no special significance for multifractal processes

order of divergence of moments of the generator. These generators yield the following *universal* expressions for the scaling function of the moments of the field  $K(q)$  and of the codimension function  $c(\gamma - H)$ :

$$\begin{aligned} c(\gamma - H) &= C_1 \left( \frac{\gamma}{C_1^\alpha} + \frac{1}{\alpha} \right)^{\alpha'} & \alpha \neq 1 : \\ c(\gamma - H) &= C_1 \exp \left( \frac{\gamma}{C_1} - 1 \right) & \alpha = 1 : \end{aligned} \quad (12)$$

$$\begin{aligned} K(q) - Hq &= \frac{C_1}{\alpha-1} (q^\alpha - q) & \alpha \neq 1 : \\ K(q) - Hq &= C_1 q \log(q) & \alpha = 1 : \end{aligned} \quad (13)$$

where  $(\frac{1}{\alpha} + \frac{1}{\alpha'} = 1$ , and for  $q = dc/d\gamma > 0$ ) and  $C_1$  is related to the coefficient  $C$  of the canonical Lévy measure  $dF$  by:

$$C_1 = C \Gamma \frac{(3 - \alpha)}{\alpha}; \quad dF = 1_{x>0} C (2 - \alpha) x^{-\alpha} \frac{dx}{x} \quad (14)$$

(here  $\Gamma$  is the usual gamma function and should not be confused with the generator. Figure 7 shows universal  $K(q)$  and  $c(\gamma)$  curves, with  $\alpha$  varying from 0 to 2.

The two functions  $K(q)$  and  $c(\gamma)$  are analytic, and depend only on the three parameters  $H, C_1$  and  $\alpha$ . The knowledge (either by measurements or from theoretical considerations) of these parameters is then enough to compute all the statistical properties of the field. The implicit hypothesis is that this field results from a universal process, hence these parameters are universal. The first,  $H$ , is often known theoretically and experimentally, and is therefore already recognized to be universal for many fields. The second,  $C_1$ , may perhaps slightly fluctuate with time and location (e.g. Tessier *et al.* 1993). In fact the most important parameter, the Lévy index  $\alpha$ , which is fundamental for the classification of the fields (see table 1) is the most likely to be universal. Some experimental results tend to confirm this assumption: at least for the temporal rate rain: five different experiments (Hubert *et al.* 1993) have (independently) estimated on different time periods, geographical locations, and for both rain gage accumulations and radar measurements the value  $\alpha = 0.5 \pm 0.05$  (see also Lovejoy and Schertzer, 1991, 1994).

## 2.12 Scaling anisotropy and Generalized Scale Invariance (GSI)

The standard picture of atmospheric dynamics is that of an isotropic 2-D large scale and an isotropic 3-D small scale, the two separated by a

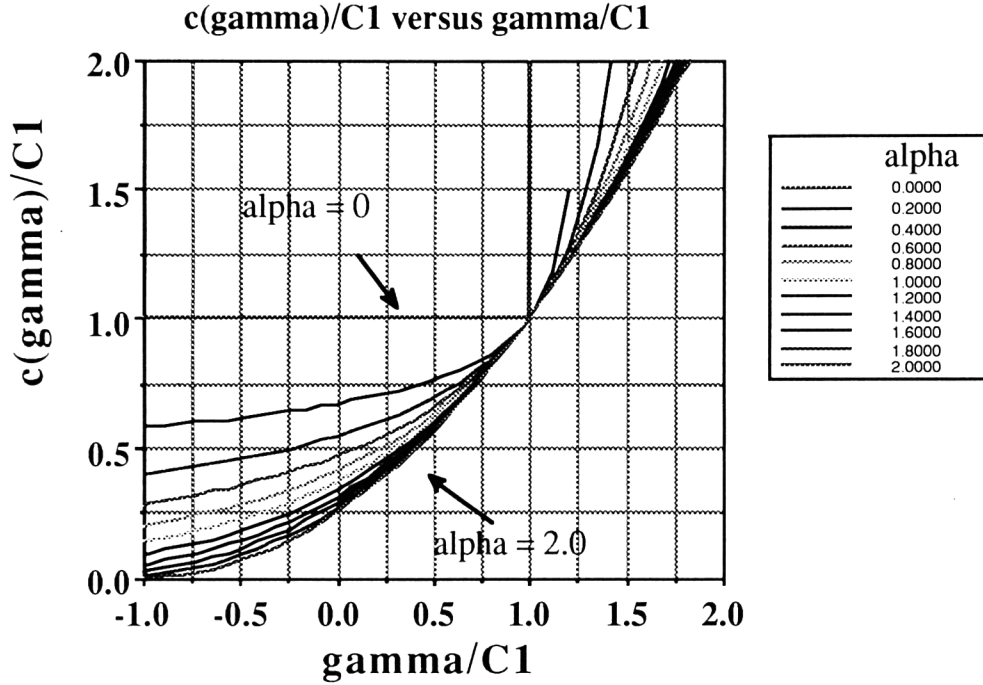


Figure 7: Universal (bare) singularities, codimension  $c(\gamma)/C_1$  corresponding to the five classes: from left to right  $\alpha = 2, 1.5, 1, 0.5, 0$ .

“meso-scale gap”. Mounting evidence now suggests that, on the contrary, atmospheric fields, while strongly anisotropic, are nonetheless scale invariant right through the meso-scale. The idea of generalized scale invariance (GSI), is to leave the artificial 2D/3D dichotomy and to postulate first scale invariance and then study the (unusual) remaining symmetries. The result is the “unified scaling model” of atmospheric dynamics (Lovejoy et al 1993) which is anisotropic but scaling throughout.

The specification of GSI requires a generator ( $G$ ) which can be a non-linear function (varying from point to point): data sets with very large ranges of scale will be needed, and even then, some simplifying approximations will be necessary. As a result of these difficulties the first empirical tests were studies of the compression (stratification) part of GSI associated with the trace of the generator (the elliptical dimension  $D_{el}$ ). The studies have specifically avoided the difficult differential rotation problem (see below) by concentrating on the vertical stratification (Schertzer and

<b>Data Type:</b>	Gauge: daily accumulation	Gauge: 6 minutes resolution	Gauge: daily accumulation	Gauge: daily accumulation	Gauge: 15 minutes resolution	Mean and standard deviation
<b>Location:</b>	Global network	Réunion Islands	Nîmes (France)	Dédougou (Burkina Fasso)	Alps (France)	
<b>No. of stations:</b>	4000	1	1	1	28	
<b>Duration:</b>	1 year	1 year	1 year	45 years	4 years	
$\alpha$ :	0.5	0.5	0.45	0.59	0.50	$0.51 \pm 0.05$
$C_1$ :	0.6	0.2	0.6	0.32	0.47	$0.44 \pm 0.16$
$\gamma_s$ :	0.84	0.36	0.83	0.57	0.72	$0.66 \pm 0.18$
<b>Reference:</b>	Tessier et al. 1993	Hubert et al.*	Ladoy et al. 1993	Hubert et al.*	Desuerosne et al.*	

Table 1: A comparison of various gauge estimates of  $\alpha, C_1, \gamma_0, \gamma_s$  over various time scales. Parameters were mostly estimated from PDMS (Probability Distribution/ Multiple Scaling) and the DTM (Double Trace Moment) techniques [Lavallée, 1991; Lavallée et al., 1991; Lovejoy and Schertzer, 1991; Schertzer and Lovejoy, 1991. \*=Private Communications]

Lovejoy 1983, 1985) who estimated  $D_{el} = 23/9 = 2.555\dots$  for the horizontal wind field,  $D_{el} = 2.22 \pm 0.07$  for the vertical stratification of rain, and  $D_{el} = 2.5 \pm 0.3$  in space/time for the rainfield (Lovejoy *et al.* 1987, Lovejoy & Schertzer 1991).

To go from one scale to another, we only need to specify the scale ratios (see LS94 for examples). We can here define a (semi) group of scale changing operators  $T_\lambda = \lambda^{-G}$  ( $G$  being the generator) which reduces the scale of vectors by scale ratio  $\lambda$  :  $B_\lambda = T_\lambda(B_1)$  is the ball of all vectors at scale  $\lambda$  (where the unit “ball”  $B_1$  defines all the unit vectors). Virtually the only other restriction on  $T_\lambda$  is that the  $B_\lambda$  are strictly decreasing ( $B_\lambda \supset B_{\lambda'}$  :  $\lambda < \lambda'$ ), hence the real parts of the (generalized) eigenvalues of  $G$  are all  $> 0$ .

Approximating  $G$  by a matrix leads to Linear GSI: when there are no

off-diagonal elements we obtain only differential stratification: “self-affine” fractals/multifractals. Off diagonal elements are associated with differential rotation and can be empirically estimated (for example, on cloud satellite images) with the help of the Monte Carlo Differential Rotation Technique (Pflug *et al.* 1993), and more recently, with the Scale Invariant Generator technique (Lewis 1993). For more discussion, see LS94.

### 3 Multifractal and multichannel radiance field: beyond scalar analysis and modelling

#### 3.1 Motivations

In remote sensing, one is primarily interested in obtaining information from radiances at different wavelengths on the *global* structure of the radiance field rather than studying the structure at each wavelength in isolation, the latter giving no information on the cross-scaling inter-relations. The corresponding multifractal multichannel analysis (implicitly considering each channel as a component of a radiance vector) is beyond the multifractal scalar framework discussed up until now. On the physics and modelling levels there is a corresponding need. Indeed, up until now the multifractal analysis and modelling of rain has relied on the simplifying hypothesis that the interaction between rain and the dynamics can be reduced to a scalar relationship (namely between their respective fluxes); this is fundamentally the reason why up until now, multifractal results have always been expressed in terms of scalar fields. Theoretically however, even in the simplest case of passive advection this relation is vectorial (the velocity field coupled with the concentration field via the gradient of the latter<sup>9</sup>). This situation is in a way paradoxical: classical methods, such as those used in GCM modeling, deal easily with this vectorial interaction but on a very limited range of scales, whereas scaling models readily deal with an infinite range of scales but avoid treating this vectorial interaction.

Below, we point out how the rather general framework of “Lie cascades” (Schertzer and Lovejoy 1993, 1994) allows us to analyze and generate multiplicative processes for vectorial and tensorial fields, and more generally rather abstract fields admitting a Lie group of symmetries. For remote sensing, it opens up the possibility of multifractal multichannel analysis by

---

<sup>9</sup>and not by a scalar relationship between their respective fluxes, as done for multifractal scalar cloud modelling (Wilson *et al.* 1991, Pecknold *et al.* 1993)

considering the multichannel field of radiance, i.e. the set of radiances in different wavelengths. Concerning the modelling, it opens a scaling and vectorial alternative to GCM techniques, since we then may consider the generator of the joint field  $(\underline{v}, R, I, \dots)$ , (= velocity, rain rate, radiance, etc.) which generates not only each component field, but also their (vectorial, tensorial, etc.) interrelations.

Before solving this problem, let us point out the difficulty. The main problem with a real cascade with alternating sign is that the set of real numbers is not algebraically closed, i.e. it doesn't satisfy the d'Alembert theorem; in particular positive numbers have 2 real square roots, negatives none. A rule related to this is the sign of products: products of the same sign give positive numbers, products of two opposite signs give negative results. As a consequence if we allow negative multiplicative factors, there are obviously some non-trivial problems in renormalizing a discrete real cascade by a factor 2 and conversely to introduce intermediate scales. . . More fundamentally, and especially when one considers a continuous process, a series of multiplications corresponds to an exponentiation of a sum, unfortunately an exponential of any real number is a positive number!

### 3.2 Complexification of a cascade as an example

By considering the algebraic closure of the real numbers (i.e. the set  $\mathcal{C}$  of the complex numbers) we should already be able to solve the above mentioned difficulties. For instance, the image of  $\mathcal{C}$  under exponentiation is  $\mathcal{C}$  itself. On the other hand, complex multiplication (with  $v (= x_1 + ix_2)$ ) corresponds to a particular linear transformation on  $\mathbb{R}^2$ , i.e. the conformal transformation which is a particular subgroup of (the set of all linear transformations on  $\mathbb{R}^2 : L(\mathbb{R}^2, \mathbb{R}^2)$ ) which can be identified with the product of rotation (angle  $\theta$ ) and dilation (ratio  $r$ ) ( $v = re^{i\theta}$ ).

$$v_\lambda = \exp(\Gamma_\lambda)v_1 \quad \text{where } v_\lambda, v_1 \in \mathcal{C}; \Gamma_\lambda \in \mathcal{C} \quad (15)$$

The significance of  $\Gamma_{R,\lambda} = Re(\Gamma_\lambda)$  and  $\Gamma_{I,\lambda} = Im(\Gamma_\lambda)$  are obvious:  $\Gamma_{R,\lambda}$  generates a non negative cascade process which modulates the amplitude of the modulus of  $v_\lambda$ , whereas  $\Gamma_{I,\lambda}$  gives the rotation of  $v_\lambda$ , hence the sign of its real part. We may specialize to the case where  $\Gamma_{R,\lambda}$  and  $i\Gamma_{I,\lambda}$  are independent stochastic processes with corresponding characteristic functions  $K_R(q), K_I(q)$ :

$$\langle v_{\lambda q} \rangle = \langle \exp(q\Gamma_{R,\lambda}) \rangle \langle \exp(iq\Gamma_{I,\lambda}) \rangle \langle v_{1q} \rangle = \lambda^{K_R(q)} \lambda^{K_I(q)} = \lambda K(q) \quad (16)$$



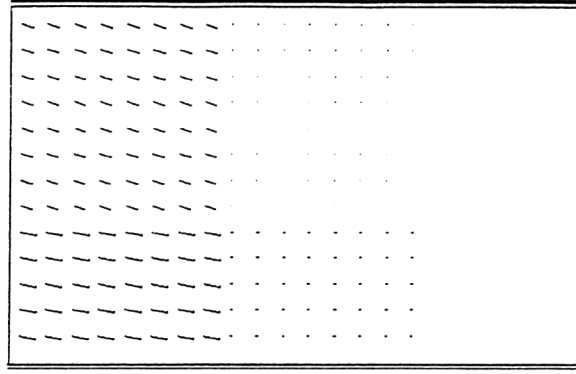
The characteristic function  $K(q)$  of the complex process is therefore simply:

$$K(q) = K_R(q) + K_I(q) \quad (17)$$

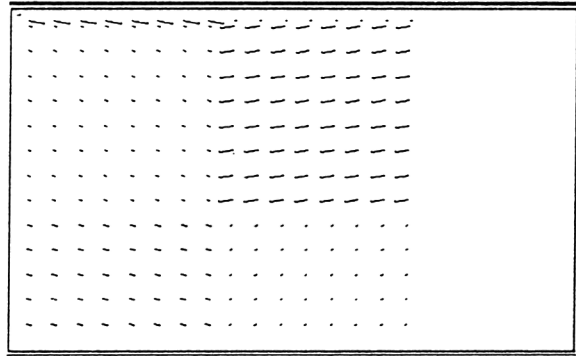
It is important to note that whereas  $K_R(q)$  is real for any real  $q$ ,  $K_I(q)$  is complex, being in general neither real nor pure imaginary. The condition of conservation ( $\langle v_\lambda \rangle = 1$ ) still corresponds to  $K(1) = 0$ , but not to  $K_I(1) = 0$ , i.e.  $\Gamma_R$  generates a non conservative process for the vector modulus. Let us consider as an example (Brethenoux *et al.* 1992) and as an illustration the discrete ( $\lambda_0$  being the fixed step scale ratio) so-called “lognormal” case, more properly speaking a Gaussian generator; where the real and imaginary exponential increments are  $\Gamma_{R,\lambda_0}$  and  $\Gamma_{I,\lambda_0}$  respectively will be Gaussian variables with variance  $\sigma_R^2$  and mean  $m_R$  (respectively  $\sigma_I^2$  and  $m_I$  for the imaginary case) which lead to a generalization of the scalar universal scaling function (with  $\alpha = 2$ ):

$$\begin{aligned} K_R(q) &= C_{1,R}(q^2 - q) + H_R q \\ K_I(q) &= -C_{1,I}(q^2 - q) + H_I q \\ K(q) &= C_1(q^2 - q) + H_q \\ C_{1,R} &= \frac{\sigma_R^2}{2} \\ C_{1,I} &= \frac{\sigma_I^2}{2} \\ C_1 &= C_{1,R} - C_{1,I} \\ H_R &= m_R - C_{1,R} \\ H_I &= im_I + C_{1,I} \\ H &= H_R + H_I \end{aligned} \quad (18)$$

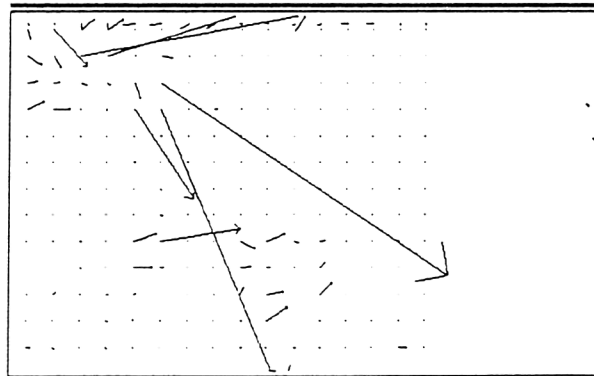
A conservative field is obtained with  $m_R = -C_1$  (i.e.  $\neq -C_{1,R}$ , as required to obtain a conservative cascade of modulus),  $m_I = 0$ . Figs. 8(a)-(d) give the first steps of the corresponding complex cascade. One may note that  $K(q)$  remains of the standard universal form even for complex  $q$ . Similar properties hold for Lévy processes when  $\Gamma_{R,\lambda}$  and  $\Gamma_{I,\lambda}$  are independently identically distributed. However,  $\Gamma_{R,\lambda}$  and  $\Gamma_{I,\lambda}$  need not have the same  $\alpha$  and there is no longer a requirement that  $\Gamma_{I,\lambda}$  should correspond to an extremal Lévy process, since  $K_I(q)$  for real  $q$  is the Fourier characteristic function of  $\Gamma_{I,\lambda}$  whereas  $K_R(q)$  remains the Laplace characteristic function of  $\Gamma_{R,\lambda}$ , and admits the usual the scalar universal form (eq. 13, with respectively  $H_R, C_{1,R}, \alpha_R$  instead of  $H, C_1, \alpha$ ). The rather more general universal



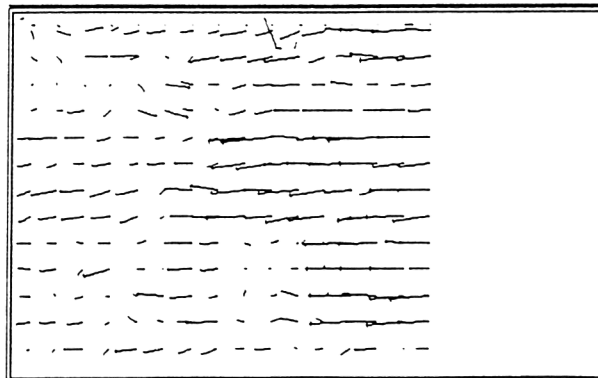
(a)



(b)



(c)



(d)

Figure 8: An example of a complex cascade with Gaussian generator ( $\alpha = 2$ ). (a) the (bare) field obtained at the first step. (b) the corresponding (complex) singularities, (c) the (bare) field obtained at the third step. (d) the corresponding (complex) singularities.

form <sup>10</sup> of  $K_I(q)$  is defined for all  $q$  (the  $\pm$  is the sign of  $q$ ). Note that  $\beta$  is the asymmetry parameter of the Lévy process  $\Gamma_{I,\lambda}$  and  $\beta = -1$  for an extremal Lévy process such as  $\Gamma_{R,\lambda}$ :

$$\begin{aligned} K_I(q) - H_{Iq} &= -\frac{C_{\pm I}}{\alpha-1}(|q|^{\alpha_I} - q); & (\alpha \neq 1); \\ K_I(q) - H_{Iq} &= -C_{\pm I}|q|\log|q| & (\alpha = 1) \end{aligned} \quad (19)$$

$$C_{\pm I} = C_I \left\{ \cos\left(\frac{\pi\alpha}{2}\right) \pm i\beta \sin\left(\frac{\pi\alpha}{2}\right) \right\} \Gamma^{\frac{(3-\alpha_I)}{\alpha_I}} \quad (\pm = \text{sgn}(q))$$

$C_I$  being the coefficient of the canonical Lévy measure  $dF$  defining  $\Gamma_{I,\lambda}$ . Fig. 9 shows the complex scaling analysis for a visible and infra red satellite image pair ( $v = I_V + iI_R$ ,  $I_V$  and  $I_R$  being respectively the visible and infra red radiances).

### 3.3 Vectorial processes and beyond: Lie algebra of generators

In the previous subsection, we extended scalar cascades to two component vector cascades by complexifying the cascade. Considering the linear transformations of the plane, we need not restrict our attention to conformal ones, which correpond to complex multiplications. More generally, we may consider non positive cascades as being components of more or less straightforward vectorial extensions of positive real processes:

$$v_\lambda = \exp(\Gamma_\lambda)v_1; \quad v_\lambda, v_1 \in \mathbb{R}^d, \Gamma_\lambda \in L(\mathbb{R}^d, \mathbb{R}^d) \quad (20)$$

the  $v$ 's being vectorial fields from  $\mathbb{R}^d$  to  $\mathbb{R}^d$ ,  $v_1$  being a homogeneous vectorial field (e.g. in the strictest sense:  $\forall y \in \mathbb{R}^d \quad v_1(x+y) = v_1(x)$ ). Just as in the positive scalar case, in order to obtain multiple scaling of the moments  $\Gamma_\lambda$  should be some band limited  $1/f$  noise although now we have a tensor scaling function  $K(q)$ :

$$\forall \lambda > 1 : \langle \exp(q\Gamma_\lambda) \rangle \approx \lambda^{K(q)}; \quad K(q) \in L(\mathbb{R}^d, \mathbb{R}^d) \quad (21)$$

and introducing the vectorial singularities  $\gamma$  and their codimensions  $c(\gamma)$ :

$$\forall \gamma \in \mathbb{R}^d, S_\lambda(\gamma) = \{v \in \mathbb{R}^d, v_i \geq \lambda^{\gamma_i} : \} \quad Pr(v_\lambda \in S_\lambda(\gamma)) \approx \lambda^{-c(\gamma)} \quad (22)$$

---

<sup>10</sup>which can be obtained with the help of appendix A of Schertzer and Lovejoy 1991.

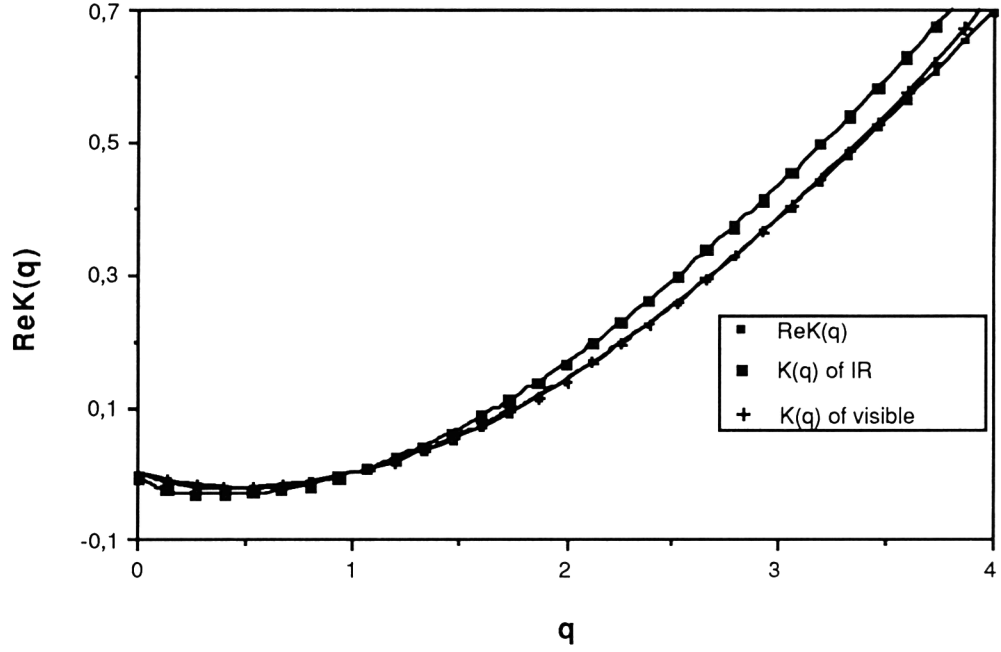


Figure 9: The moment scaling functions for a visible and infra-red satellite image pair ( $K_V(q)$ ,  $K_{IR}(q)$  respectively) at 8km resolution taken over the Montréal area as part of the RAINSAT automated satellite rain algorithm (each image is of 256 x 256 pixels). Also shown is the  $K_R(q)$  function described in the text which is obtained by considering the multi-scaling of the modulus of the vector (visible, infra-red). This gives partial information about the scaling interrelation between the two fields. Using the double trace moment (Lavallée 1991, Lavallée et al. 1993, we obtain  $\alpha_V = 1.7$ ,  $\alpha_{IR} = 1.75$ ,  $\alpha_R = 1.73$ ,  $C_{1,V} = 0.22$ ,  $C_{1,IR} = 0.20$ ,  $C_{1,R} = 0.25$  -accuracy of the estimates is  $\pm 0.2$ ). From Schertzer and Lovejoy, 1994b.

for conservative processes, we still have the same type of conservation law<sup>11</sup>:

$$\langle v_\lambda \rangle = \langle v_1 \rangle; \text{ i.e. } K(1) = 0 \in (\mathbb{R}^d) \quad (23)$$

In fact, independently of the representation of the  $v$  field and of the  $B_\lambda$  balls (as discussed about GSI), we are only using the (multiplicative) group properties related to the basic fact that scale ratios simply multiply. Such one-parameter groups can be obtained as the results of stochastic flows obtained from stochastic integrations (more precisely from Stratonovich integrations as discussed in Schertzer and Lovejoy, 1993) over infinitesimal (random) generators  $d\Gamma$  and  $dG$ . For instance, quaternions and Clifford algebra have been considered which yields already a richer structure than the conformal group. Originally (Schertzer and Lovejoy, 1991) such an integration was proposed only on  $T_\lambda$  in the case of the so-called nonlinear (random) GSI (Generalized Scale Invariance). Corresponding to the group property of the transformation of the field or of the space, there is a Lie algebra structure for the generators, i.e. there is a skew and distributive product  $[\cdot, \cdot]$  called the Lie bracket. The group properties of the statistical moments of the field or scale transformations correspond to the fact that the second characteristic function (cumulant generating function)  $K\lambda(q)$  generates (for the different values of  $q$ ) a Lie sub-algebra.

We now can study a remotely sensed data set which is invariant under different symmetries, not only scaling symmetries, by considering the Lie algebra of the generators. We are naturally lead to look for some universality properties, i.e. a kind of classification of the possible algebra. The answer is partially affirmative (Schertzer and Lovejoy 1994): the part corresponding to non scaling symmetries enters in the classical and universal Cartan classification (e.g. Sattinger and Weaver 1985) whereas the part corresponding to scaling symmetry is outside the classification and on the contrary admits a factorization.

## 4 Conclusions

In Schertzer and Lovejoy 1987, it was proposed that in many geophysical applications that scaling symmetries can be used as dynamical constraints in place of coupled nonlinear partial differential equations. This is the usual physical notion that a system is totally determined once all its symmetries

---

<sup>11</sup>which is a consequence of the Martingale property of the process (the conditional expectation at resolution scale  $\lambda$  of  $v_{\lambda'}(\lambda' > \lambda)$  is  $v_\lambda$ ) see Kahane, 1985.

are known. Since scaling arguments are so general and the phenomena so prevalent, it has become urgent to develop a formalism for handling scaling for coupled multifractal processes (e.g. vector cascades) as well as to restrict the generator of the scaling symmetries using additional symmetries. Both goals require the formalism of Lie cascades discussed here.

Not only have we shown that there is no fundamental reason to restrict cascade processes to positive (real) quantities, but there are very wide possible generalizations to rather abstract processes. As a consequence, it restates in a new way a potentially wider unity of Geophysics, as well as its remotely sensed analysis. At the same time it points out a quantitative way to classify the wide diversity of phenomena occurring over wide ranges of scale with the help of the classification of the corresponding Lie algebra. This classification will also enable us to discover new types of nonlinear interactions.

Immediate applications of the ideas discussed here include multifractal multichannel remote sensing analysis and the corresponding simulation of vector multifractals, and the scale invariant characterization of the interrelations of rain, cloud radiance and other fields. We gave a first example of the latter by analyzing the multiscaling of the vector moments of the joint visible and infra red cloud radiance fields from GOES satellite data. When this is extended to radar reflectivities of rain and rain gauge measurements, this resolution independent characterization of their interrelation can form the basis of resolution independent satellite rain algorithms, as well as for the resolution independent calibration of radars from rain gauges.

## 5 Acknowledgements

We thank G. Brosamlen, Y. Chiriginskaya, N. Desaulniers-Soucy, M. Duncan, F. Francis, H. Gaonach, C. Hooge, P. Hubert, P. Ladoy, A. Lazarev, D. Lavalle, C. Naud, S. Pecknold, F. Schmitt, for helpful comments, discussions and technical assistance.

## 6 References

- [1] P. Bak, C. Tang & K. Wiessenfeld (1987) Phys. Rev. Lett. 59, 381.
- [2] R. Benzi, G. Paladin, G. Parisi & A. Vulpiani (1984) J. Phys. A, 17, 3521.
- [3] A. Bialas & R. Peschanski (1986) Moments of rapidity distributions

- as a measure of short-range fluctuations in high-energy collisions, Nucl. Phys. B, B 273, 703-718.
- [4] G. Brethenoux, D. Mitrani, J. Dezani, D. Schertzer & S. Lovejoy (1992) Lie cascades: multifractal vectorial and tensorial multiplicative processes. EOS, 73, 14 supp., 57.
  - [5] A. H. Fan (1989) Chaos additif et multiplicatif de Lévy. C. R. Acad. Sci. Paris I. 308, 151.
  - [6] W. Feller (1968) An Introduction to Probability Theory and its Applications. Vol. I. J.Wiley & Sons, New York.
  - [7] W. Feller (1971) An Introduction to Probability Theory and its Applications. Vol. II. J.Wiley & Sons, New York.
  - [8] P. Grassberger (1983) Generalized dimensions of strange attractors. Phys. Lett., A 97, 227.
  - [9] T. C. Halsey, M. H. Jensen, L. P. Kadanoff, I. Procaccia & B. Shraiman (1986) Fractal measures and their singularities: the characterization of strange sets. Phys. Rev. A., 33, 1141.
  - [10] H. G. E. Hentschel & I. Proccacia (1983) The infinite number of generalized dimensions of fractals and strange attractors. Physica, 8D, 435.
  - [11] P. Hubert and J. P. Carbonnel (1989) Dimensions fractales de l'occurrence de pluie en climat soudano-sahélien. Hydrol. continent., 4, 3-10.
  - [12] P. Hubert, Y. Tessier, S. Lovejoy, D. Schertzer, P. Ladoy, J. P. Carbonnel & S. Violette (1993) Multifractals and Extreme Rainfall events. Geophys. Res. Lett. 20, 931-934.
  - [13] J. P. Kahane (1985) Sur le chaos multiplicatif, Ann. Sci. Math. Que., 9, 435.
  - [14] A. N. Kolmogorov (1962) A refinement of previous hypotheses concerning the local structure of turbulence in viscous incompressible fluid at high Reynolds number. J. Fluid Mech., 83, 349.
  - [15] P. Ladoy, S. Lovejoy & D. Schertzer (1991) Extreme fluctuations and intermittency in climatological temperatures and precipitation, in: Scaling, fractals and non-linear variability in geophysics, D. Schertzer & S. Lovejoy ed.s, 241-250, Kluwer.
  - [16] P. Ladoy, F. Schmitt, D. Schertzer & S. Lovejoy (1993) Variabilité temporelle multifractale des observations pluviométriques à Nîmes. C. R. Acad. Sci. Paris, II, in press.
  - [17] D. Lavallée (1991) Multifractal analysis, simulation techniques and turbulent fields, Ph.D. Thesis, McGill Univ., Physics Dept., Montreal (Canada).
  - [18] D. Lavallée, D. Schertzer & S. Lovejoy (1991) On the determination of the codimension function. Scaling, fractals and non-linear variability in

- geophysics, D. Schertzer & S. Lovejoy ed.s, 99-110, Kluwer.
- [19] E. Levich & E. Tzvetkov (1985) Helical inverse cascade in three-dimensional turbulence as a fundamental dominant mechanism in meso-scale atmospheric phenomena, *Phys. Rep.*, 128, 1-37.
  - [20] E. Levitc & I. Shtilman (1991) Helicity fluctuations and coherence in developed turbulence. *Nonlinear Variability in Geophysics: Scaling and Fractals*, D. Schertzer & S. Lovejoy ed.s, Kluwer Academic Press, Dordrecht-Boston, 13-30.
  - [21] S. Lovejoy, D. Schertzer and A. A. Tsonis (1987) Functional box-counting and multiple elliptical dimensions in rain, *Science*, 235, 1036.
  - [22] S. Lovejoy & D. Schertzer (1991) Multifractal analysis techniques and the rain and cloud fields from  $10^{-3}$  to  $10^6$  m. *Nonlinear Variability in Geophysics: Scaling and Fractals*, D. Schertzer & S. Lovejoy ed.s. Kluwer Academic Press, Dordrecht-Boston. 111-144.
  - [23] S. Lovejoy and D. Schertzer (1994) How bright is the coast of Brittany? (this volume).
  - [24] S. Lovejoy & D. Schertzer (1994) Multifractals and rain. In *New Uncertainty Concepts in Hydrology and Hydrological modelling*. Ed. A. W. Kundzewicz, Cambridge University Press. in press.
  - [25] S. Lovejoy, D. Schertzer, P. Silas. Y. Tessier & D. Lavallée (1993) The unified scaling model of the atmospheric dynamics and systematic analysis of scale invariance in cloud radiances. *Annales Geophysicae*, 11, 119-127.
  - [26] B. B. Mandelbrot (1983) *The fractal geometry of nature*. Freeman. S. Francisco.
  - [27] B. B. Mandelbrot (1974) Intermittent turbulence in self-similar cascades: divergence of high moments and dimension of the carrier. *J. Fluid Mech.*, 62, 331.
  - [28] B. B. Mandelbrot (1991) Random multifractals: negative dimension and the resulting limitation of the thermodynamic formalism. in *Turbulence and stochastic processes*, Eds. J. C. R. Hunt, O. M. Phillips & D. Williams, The Royal Society.
  - [29] C. Meneveau & K. R. Sreenivasan (1987) Simple multifractal cascade model for fully developed turbulence. *Phys. Rev. Lett.*, 59, 13, 1424.
  - [30] E. A. Novikov & R. Stewart (1964) Intermittency of turbulence and spectrum of fluctuations in energy-dissipation, *Izv. Akad. Nauk. SSSR. Ser. Geofiz.*, 3, 408.
  - [31] A. Obukhov (1962) Some specific features of atmospheric turbulence. *J. Geophys. Res.*, 67, 3011.
  - [32] G. Paladin & A. Vulpiani (1987) *Phys. Rev. Lett.*, 156, 147.



- [33] G. Parisi and U. Frisch (1985) A Multifractal Model of Intermittency, In, *Turbulence and Predictability in Geophysical Fluid Dynamics and Climate Dynamics*, Ed.s. M.Ghil et al., North Holland, New York, 84.
- [34] S. Pecknold, S. Lovejoy, D. Schertzer, C. Hooge, J. F. Malouin (1993) The simulation of universal multifractals. *Cellular automata: prospects in astrophysical applications*, Ed.s J. M. Perdang, A. Lejeune, World Scientific, p 228-267.
- [35] L. Pietronero & A. P. Siebesma (1986) Self-similarity of fluctuations in random multiplicative processes. *Phys. Rev. Lett.*, 57, 1098.
- [36] K. Pflug, S. Lovejoy & D. Schertzer (1993) Generalized Scale Invariance. Differential rotation and cloud texture: analysis and simulation. *J. Atmos. Sci.*, 50, pp.538-553.
- [37] D. H. Sattinger and O. L. Weaver (1985) *Lie groups and algebras with applications to physics, geometry and mechanics*, Springer-Verlag, 215pp.
- [38] D. Schertzer and S. Lovejoy (1983) The dimension of atmospheric motions. *Preprints. IUTAM Symp. on turbulence and chaotic phenomena in fluids*, 141-144. Kyoto, Japan.
- [39] D. Schertzer & S. Lovejoy (1985) The dimension and intermittency of atmospheric dynamics, *Turbulent Shear Flow 4*, B. Launder ed., Springer, 7.
- [40] D. Schertzer and S. Lovejoy (1987a) Physical modelling and analysis of rain and clouds by anisotropic scaling multiplicative processes, *J. Geophys. Res.*, 92, 9693.
- [41] D. Schertzer, S., Lovejoy, R. Visvanthan, D. Lavallée and J. Wilson (1988) Universal multifractal in turbulence fractal aspects of materials: disordered systems, Eds. D. A. Weitz, L. M. Sander, B. B. Mandelbrot, pp. 267-270, *Materials Research Society*, Pittsburg.
- [42] D. Schertzer & S. Lovejoy (1989) Nonlinear variability in geophysics: multifractal analysis and simulations. *Fractals: Physical Origin and Consequences*, Ed. L. Pietronero, Plenum, New York, 49.
- [43] D. Schertzer & S. Lovejoy (1991) Nonlinear geodynamical variability: multiple singularities, universality and observables. *Scaling, fractals and non-linear variability in geophysics*, D. Schertzer & S. Lovejoy ed.s, Kluwer Academic Press, Dordrecht-Boston, 41-82.
- [44] D. Schertzer and S. Lovejoy (1992) Hard and soft multifractal processes, *Physica A*, 185, 187.
- [45] D. Schertzer, S. Lovejoy and D. Lavallée (1993) Generic multifractal phase transitions and self-organized criticality. *Cellular Automata:*

prospects in astronomy and astrophysics, Ed.s J. M. Perdang & A. Lejeune, World Scientific, Singapore.

- [46] D. Schertzer and S. Lovejoy (1993) Scaling and multifractal processes, Lecture Notes of the NVAG3 conference, Cargèse, Corsica, Sept. 10-17.
- [47] D. Schertzer and S. Lovejoy (1994a) Multifractal generation of self-organized criticality, in Fractals in the natural and applied sciences Ed. M. M. Novak, Elsevier, North-Holland, 325-339.
- [48] D. Schertzer and S. Lovejoy (1994b) From scalar cascades to Lie cascades: joint multifractal analysis of rain and cloud processes. Space/time Variability and Interdependence for Various Hydrological Processes. Ed. R. A. Feddes, Cambridge University Press, in press.
- [49] K. R. Sreenivasan & C. Meneveau (1988) Singularities of the equations of fluid motion. Physical Review A. 38 12, 6287.
- [50] Y. Tessier, S. Lovejoy and D. Schertzer (1993) Universal multifractals: theory and observations for rain and clouds, J. Appl. Meteor.. 32. n. 2. 223.
- [51] J. Wilson, S. Lovejoy and D. Schertzer (1991) Physically based cloud modelling by scaling multiplicative cascade processes. Scaling. fractals and non-linear variability in geophysics. D. Schertzer and S. Lovejoy ed.s, 185-208, Kluwer.
- [52] A. M. Yaglom (1966) The influence of the fluctuation in energy dissipation on the shape of turbulent characteristics in the inertial interval. Sov. Phys. Dokl., 2, 26.

## Chapter 2

# An Evaluation of the Contribution of Fractals to Remote Sensing Problems

*Marcel Raffy\**

### 1 Introduction

More than 100.000 papers using fractal ideas have been published to date. For this evaluation of prospective ideas it is thought to be of little use to present yet another discourse on the subject, but rather to evaluate the relevance of the theory to progress on the problems posed by remote sensing of the Earth.

For such an evaluation, it is necessary to consider the problem of fractals from outside of its own conceptual frame. Therefore we must not discuss, for example, the comparison between simple fractals and multifractals to represent an object but the status of fractals within the framework of modelling activities in general.

The first part of this chapter concerns the definition of what should be required from a model. The notion of model is considered in many different ways in the scientific literature. In [1] for example, a model is a set of equations or inequalities which describe the state of a system. This definition is too restrictive for our topic since it does not allow the possibility to discuss the merits of the actual statement of equations in itself but only the merits of one set of equations compared to another one for the description of a process. We adopt the point of view of R. Thom [2] and J. L. Casti [3] which is general enough for our purpose.

The discussion in section 2 leads to various criteria required for a relevant modelling activity. Then, we evaluate these criteria with respect to the

---

\*Groupement Scientifique de Télédétection Spatiale, Strasbourg, France

fractal fields close to the topic of remote sensing and we look at the main problems posed by remote sensing today.

## 2 The modelling activity

“At the beginning was inquisitiveness”, says Asimov [4]. This can be the foundation of Science. Let us consider a ‘thing’  $T$  which presents us with some sort of mystery. In other words, we have one or a set of questions  $Q$  about it. Consequently, we are interested in the answer(s)  $A$  to these questions (Fig. 1). If  $A$  is not obvious then we must simplify the system

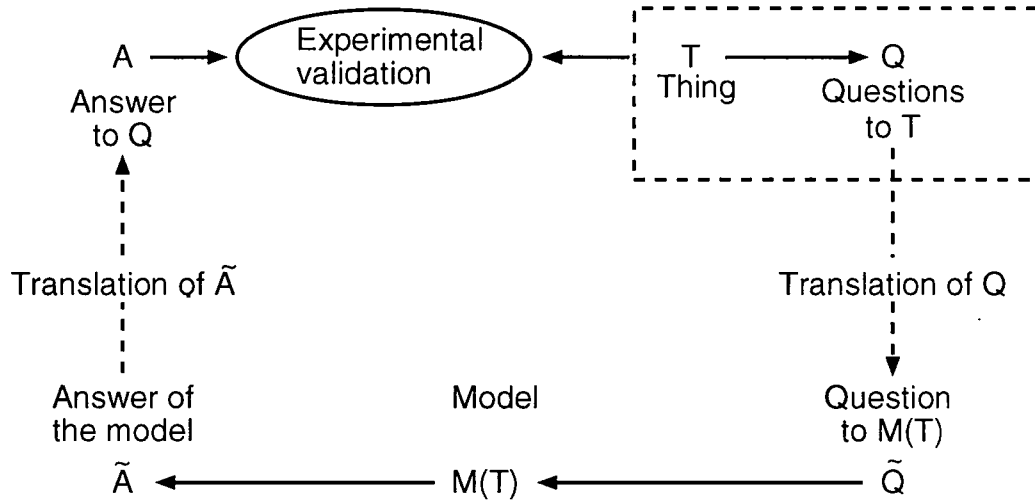


Figure 1: The schematic role of a model

composed of  $T$ ,  $Q$  and  $A$ , in such a way as to reduce our degree of inquisitiveness about  $T$ . The necessity of modelling comes from the fact that we need to have an answer through a schematic description of  $T$  that can be processed by our brain (and our mind). This schematic description  $M(T)$  of  $T$  must be built in such a manner that the question  $Q$  will have a relevant translation  $\tilde{Q}$  on the image (or model)  $M(T)$  of  $T$ .

This scheme is very general since  $T$  can be any object which can be observed: a person, a group of persons, and in particular, any object considered as “scientific”. Let us remark that the latter type is not so easy to distinguish from the “non-scientific” objects without cultural arguments [2], [5].

**Example 1:** The thing  $T$  is the error in the transmission of a computational message on a line. The question  $Q$  arises: “Is it possible to have a predictable irregularity in relation to the physical support of the transmission line?”. The model  $M(T)$  proposed by Berger and Mandelbrot [6] is the “hyperbolic distribution”  $Prob(U \geq u) = u^{-D}$  of the successive intervals of size  $U \geq u$ . This model is a good analogue of the actual observation  $T$  of the errors. On the basis of the morphological analogy between a set of actual intermissions and the simulated one given by the hyperbolic distribution, the hope is to link the constant  $D$  to a particular characteristic of the line. Thus, the question  $\hat{Q}$  to the model would be: “what is the value of  $D$ ?” and  $\hat{A}$ : “we therefore have such a physical property of the line”.

Let’s first remark that  $D$  does not lead to  $A$  but can help to give  $A$  on the basis of good simulations provided by  $M(T)$ . Furthermore, we remark on the very strong morphological analogy between  $T$  and  $M(T)$ , even if the analogy is not an easy concept to define with accuracy.

The general concept of analogy is not in fact easy to define with accuracy. Nevertheless, one can imagine that if the computer simulation  $M(T)$  of the physical frequencies of the errors is a good (symbolic) analogue of  $T$ , then we can lean on this analogy to give us an accurate translation of  $\hat{A}$ . This is a very general analysis. A systematic analogy between  $T$  and  $M(T)$  is given by demonstration models, so often used in physics.

A high degree of analogy between  $T$  and  $M(T)$  is nevertheless not sufficient an argument for the efficiency of the model to lead to  $A$ , as example 2 below will show.

**Example 2:** In primitive populations,  $M(T)$  was a fetish doll representing an enemy  $T$ . On the basis of this (symbolic) analogy, the witch-doctor carried out various actions on the doll, with the aim of weakening or destroying the enemy. The analogy is symbolic, as is the computer simulation of the errors in transmission lines.

As in example 1, the role of morphological analogy is strong. Nevertheless, the ability of the model to give  $A$  is not measured by the analogy between  $T$  and  $M(T)$ , but by the experimental validation of  $M$  to lead to  $A$ . If an experiment on  $T$  leads to a confirmation of the answer  $A$ , then the model  $M$  works for the question posed (Fig. 1).

Hence, the morphological analogy between  $T$  and  $M(T)$  is not sufficient. Furthermore it is not necessary at all in the modelling activity.

**Example 3:** As a particular case of the previous scheme, there is the concept of models as a set of equations or inequalities, generally considered

by physicists. Let us consider the dynamics of a fluid as  $T$ . The model  $M(T)$  of the Navier-Stokes equations leads to the answer  $\tilde{A}$  to the question  $Q$ : “what is the state of  $T$  at a time  $t$ , at a point  $P$  within the fluid?”. In this case  $\tilde{Q}$  is: “what are the initial and boundary conditions?”. The strength of this model, always confirmed by experience, does not take its relevancy from any analogy between  $T$  and  $M(T)$  but from the physical analysis of the process and its mathematical expression.

While the morphological analogy between  $T$  and  $M(T)$  is not necessary to have a relevant model, the following principle is necessary: *The question must be prior to the model.* A model has a sense only with respect to a question. Indeed a model can be good for one question, it can be bad for another one.

**Example 4:** The fractional Brownian motion (FBM) is a good model for the question of realistic computer simulations of the Brownian walk at any scale. The morphological analogy between  $T$  and  $M(T)$  is strong. nevertheless the FBM model is totally irrelevant in answer to the question of the energy required for the Brownian walk, since we obtain an infinite energy for a particle to follow a nowhere differentiable path.

To conclude this section, we observe that:

- a- The scheme of figure 1 is a very general frame to interpret the modelling activity.
- b- The main principle is that the question must determine the model and not the other way round.
- c- The morphological analogy between  $T$  and  $M(T)$  is neither sufficient nor necessary to be efficient. The model can have a very high degree of morphological analogy with  $T$  or a very low one.

### 3 Quality of a model; Fractal models

For a given thing and question  $Q$  about it, a model  $M(T)$  will be called efficient if the scheme of figure 1 is satisfied with an acceptable experimental validation. For a given question  $Q$  the set  $M_Q$  of efficient models can be empty, have one element, a finite or an infinite number of elements. Within  $M_Q$ , we may distinguish various classes and, if necessary, we may have to select one of them. This can be the case for economic considerations, for example.

We will consider another classification of models based on their “quality” which can be defined as follows.

A first natural idea is to consider that a model of the Set  $M_Q$  is good if its answer is in good agreement with the experiment. For a given degree of accuracy of this agreement, we may have a certain number of models. For example, for the study of the heat diffusion in a homogeneous medium, we may propose a demonstration model  $M_1$  of the medium with sensors leading to the temperature evolution within the medium and the heat equations  $M_2$ . They may have the same accuracy. Now, to compare these two models, one may propose the “degree of surprise” as a quality criterion. This is exactly the opposite to the degree of analogy detailed in section 2. Here, the degree of surprise of  $M_2$  is much greater than that of  $M_1$ .

**Example 5:** Let us suppose that we are interested in  $T$  = the agressivity of a dog. We want to know how both anger and fear operate. Zeeman [7] proposes for  $M(T)$ , the study of a path in a folded surface. The degree of analogy is very low for this model. Therefore, the degree of surprise is high.

**Example 6:** For the study of the reflectance of vegetation, various teams in remote sensing work on ray-tracing methods over some plants morphologically simulated by the computer. The degree of analogy of these models is very high, while their degree of surprise is very low.

Finally, we can define the quality of a model by the following parameter:

$$\rho = \frac{\epsilon}{a} \quad (1)$$

where:  $\epsilon$  = degree of agreement with experiment,  $a$  = degree of analogy between  $T$  and  $M(T)$ .

Despite its mathematical form,  $\rho$  cannot be numerical. Indeed while we can imagine a numerical value for  $\epsilon$ , such as the difference between  $A$  and the experimetal values,  $a$  is certainly not easy to quantify. Nevertheless,  $\rho$  can be a good tool for the definition of large classes of models.

## 4 Fractal models

Giving a global view of fractals in a few words poses an immense problem. There is no doubt that this section will be partial and subject to debate, but its relation with the previous section is nethertheless clear. Let us first describe the large classes of applications of fractal ideas.

### **(a) Mathematical aspects:**

These works follow mainly the notions developed by Hausdorff [8], (for example, [9] to [12] ). One of their important effects can be interpreted as the geometrical point of view of measure theory, as opposed to the topological one developed by Lebesgue. A new interest for iteration processes and attractions appeared (for example, [13],[14]) relative to point (b)-I below. In connection with  $C'$ , iteration processes have also been developed by M. Barnsley [15].

Some mathematical aspects of Navier-Stokes equations have been developed around the Hausdorff dimension of attractors. [16]

### **(b) Physical aspects:**

**(b)-I** -Self-similarity is not new to physics. The study of critical properties of phase transitions and the formulation of the renormalization group approach has essentially covered this question [17]. [18]. Fractals bring to this field a new geometrical point of view. Fractal dimensions are not just critical exponents but very strongly related to them.

**(b)-II** -For phase transitions and percolation problems. geometrical aspects and probabilistic ones have often been studied (for example. [19] to [23]).

**(b)-III** -Chaotic phenomena gain geometrical points of view with the fractal properties of (strange) attractors in the space phase (for example. [24] to [28]).

**(b)-IV** -Diffusion processes simulated by random walks of particles situated on discrete lattices give fractal fronts in good agreement with observations [28], [29].

**(b)-V** -From Mandelbrot [30], [31] and Frish and Parisi [32]. problems of turbulence and fluid motion are at the origin of many papers on fractals (for example [33],[34]).

Let us remark that the problems encountered in (b)-III and (b)-IV are well modelled by the diffusion and Navier-Stokes equations. This supposes a degree of smoothness of the solutions which must satisfy these partial differential equations. So, fractals could be presumed to be a poor tool for these problems.

The success of fractals in diffusion processes appears at the very small scales where particles, submitted to random walks interact with the irregularities of the medium. While the diffusion equations take into account global mean values, the fractal description links probability and potentials. Here, as in example 1, this success is due to the high degree of morphological analogy between  $T$  and  $M(T)$ .



For fluid problems, fractals are related to the singularities of the Navier-Stokes equations which can define what is turbulence. The success of fractals is mainly based on the fact that in this field, any geometrical information is interesting, since little is known about these singularities.

**(b)-VI** -Growth processes. This field which contains the older field of aggregate processes [35] leads to this new general concept very strongly based on computer simulations of random walks [36].

**(b)-VII** -Chemistry of heterogeneous media approached in [37] and surfaces in colloids in [38].

### **(c) Images and computing:**

The strong support for any use of fractals is the computer. The expansion of the ideas on fractals would not have been possible twenty years ago, even with the great talent of B. Mandelbrot. Let us note here that while the computer is necessary for the development of most of these ideas in many fields, it is also the origin of many papers specific to computer representation of objects.

In the field of images new techniques have appeared for the simulation of natural morphologies. The important “Collage theorem” of Barnsley [15] leads to a lot of algorithms for landscapes [39] vegetation, [40] and connects attractors to images. The artistic aspects of fractal images is pointed out by many authors [41], [42].

### **(d) Applications:**

By application we mean all relevant subject matters encountered other than those fields previously mentioned in paragraphs a, b, c, such as geology [43], geography and botany ([31], [44], [45], [46]), oceanography [47], meteorology ([33], [48]), urbanism, [49], psychology [50], music [51], etc... Few have not been reached by the attractive ‘fractal speak’.

**Remark:** This attractiveness in itself is an interesting study of the sociology of scientists and its evolution due to the pressure of publishing. This aspect, apparently outside of the scope of our topic must be pointed out, since the very great number of papers on a subject can, at first glance, over-estimate the depth of the subject while it can just be due to a greater accessibility to paper production.

Scientific productivity in applications is much larger than the previous sections. The domains currently related to remote sensing are essentially

- Geology: roughness, relief and dimension, breaks in direction and size

- Geography: many various fields where hydrology is an important one for structure studies
- Oceanography, meteorology: often related to turbulence aspects, the fractal approach in these domains is often distinguishable from others by the similarity to the paragraph (b)-IV type approach
- Urbanism: shapes with aggregate simulations
- Botany: plant morphology

## 5 Fractal models in applications

We have mentioned the well known exceptional activity arising from the use of fractals in applications (the term applications has the same meaning in this section as in point (d) above). This activity confirms the great intuition of Mandelbrot and a few others before him, mainly developed by himself. that the Hausdorff dimension is omnipresent in nature. If we observe this activity with respect to the scientific modelling activity, two points appear.

### 5.1 The principle *b* of modelling (section 2) is very often not respected

On page 404 of [31], Mandelbrot presents a drawing of Jean Effel which shows president De Gaulle in front of journalists at a press conference. He says: “ Please, Mr. journalists, pose your questions to my answers”. This drawing presented as a joke by Mandelbrot (and Effel!) has unfortunately become a reality in many cases, in the applications of fractals. In other words, the questions appear after the model, when the question must select the appropriate model. The consequences, at least, are that the relevance of the question is quite random with respect to the topic and the coherency of the system  $(T, Q, M(T))$  is suspect.

In many cases, the scheme of figure 1 is reduced to that in figure 2. The model is just an algorithm built to deliver a dimension. So what? Where is the question? Where is the thematic progress?

If one doesn't want to analyse the production on the subject, then there is an external proof of the weakness of the use of fractals in the applications. Let us suppose that fractals have suddenly, since 1975, led to many solutions of thematic problems in applications. So, how is it possible to understand that so many researchers in all the disciplines, were blocked, until a simple

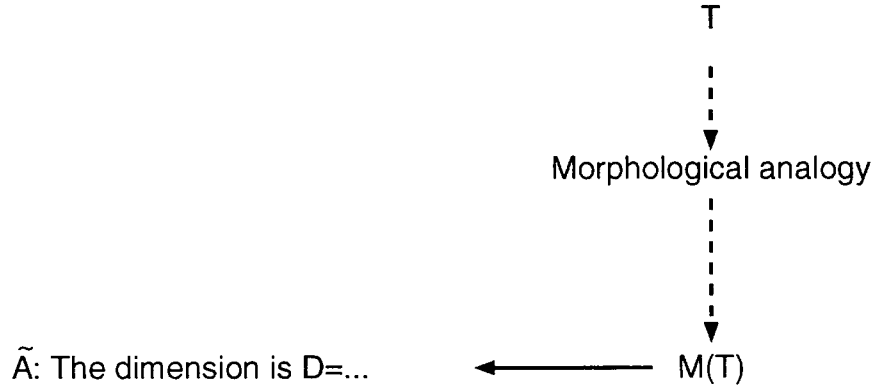


Figure 2: Scheme of the unsatisfactory behaviour in many modelling activities

log-log plot solved their problems ? The answer is certainly contained in figure 2 and the remark of section 4(d).

## 5.2 The quality ratio $\rho$ is weak.

The degree of surprise defined by equation (1) which is the modelling increase of value towards the answer, is in general very weak. The main reason is the high degree of the morphological analogy between  $T$  and  $M(T)$  in the applications of fractals.

**Remark:** Let us recall that the morphological (generally computer) copy of an object is not the understanding of a process involving the object (see examples given previously, especially number 4). In most cases, the actual thematic problems lie in most cases in the understanding of the processes, as will be detailed for remote sensing, in the following section.

For example, the fractal perimeter-area dimension of  $1.35 \pm 0.05$  computed for rain fronts is far from any meteorological explanation of the reason for this value. In many regions, the geologists have calculated dimensions of the relief. From what geological processes are these dimensions issued? The examples are plentiful.

Even if the imitation of a shape can help us to progress in the mod-

elling of the process, the work involved seems much too laborious a routine of programming work than of research work, and finally the result is the morphology which was anticipated (see example 6).

## 6 The fundamental questions of remote sensing

The pluri-disciplinary questions encountered in remote sensing of the Earth are mainly based on the important fact that the observed processes taking place at the Earth's surface do not have the same description in situ and from space. The principal questions are orientated around the following fields in which we do not take directly into account the fundamental problems posed by instrument progress.

- A- The energetic equilibrium of our planet
- B- The understanding of vegetation dynamics
- C- The prospection of natural resources
- D- The understanding of the density of human occupation of the surface and its equilibrium with the surroundings.

These questions lead to an infinite number of questions and sub-questions. Each of them has a great number (finite or not) of associated models. Nevertheless, it is possible to list a few examples of the types of question referred to. However, fractals do not seem to be the obvious direction to take first in any case.

**Point A:** *The energetic equilibrium of our planet.*

**Q:** Is it possible to obtain separately (hourly, daily, monthly,...) the dynamics of the sensible and latent heat fluxes at the earth's surface from space measurements and standard meteorological measurements ?

Sub-Q1 How do we obtain the global surface temperature? (What is the global emissivity ?)

Sub-Q2 Is radar measurement useful for the determination of the latent heat flux?

Sub-Q3 Is it possible or necessary to have models for the surface roughness (aerodynamic or thermal) at large scale for the previous problem? (Here, fractals can be useful, but one can also evaluate the distance to go from the fractal models of roughness to answer such questions.)

**Remarks:**

These questions have not been yet resolved, even on surfaces without crop cover. The important difficulty is the experimental validation of any modelling in this field.

**Point B:** *The understanding of vegetation dynamics.*

The main questions concern two points: desertification and yield.

**Q1:** Is it possible to detect from space indices of desertification?

Sub-Q1 How do we optimise the high frequency low resolution data and the low frequency high resolution data to answer the previous question?

**Q2:** Is it possible to quantify from space the biomass and its dynamics?

Sub-Q1 Is it possible to link satellite measurements to the density of cover (cultivated types, natural types)?

**Remarks:**

Progress is being made in finding the solutions to these questions, nevertheless, two difficulties remain:

- The progress concerns species type by type and cannot be applied to large scale regions.
- The difficulty of validation remains.

**Point C:** *The prospection of natural resources.*

**Q:** Is it possible to identify minerals in place and quality?

Sub-Q1 Are there optimal spatial resolutions for the various minerals ?  
Same question for spectral resolution.

Sub-Q2 Is the relief (combined with present satellite data) able to define preferential zones for such and such type of minerals?

Sub-Q3 What instrumental propositions is it possible to make with respect to radar developments?

Sub-Q4 Is the thermal band useful via the thermal inertia of the surface?  
How do we obtain this parameter from surface temperature dynamics?

**Point D:** *The understanding of the density of human occupation of the surface and its equilibrium with the surroundings.*

**Q:** Is it possible to manage human behaviour from space as we hope to do with vegetation?

Sub-Q1 How to obtain the density of population? What are the best sensors for that?

Sub-Q2 What socio-economic parameters are obtainable from space?

**Remark:**

These questions have not yet been seriously approached.

## 7 Conclusion

Remote sensing is in need of modelling. A great number of surface processes must be understood especially with respect to the very considerable range of scales between in situ description and space observation. Even if in some fields closely related to turbulence phenomena or to vegetation cover, (multi-) fractals can be an interesting geometrical description, the work done with fractals is still far from modelling the process involved in remote sensing. The main reason is that too much importance is given in these activities to the computer morphological simulation of the objects often taken as an aim. We consider that, if in some sense, clouds, ocean, vegetation... present fractal properties in their geometry, the physics of such geometrical objects is yet to be understood. The physics of electromagnetism, thermodynamics, fluid mechanics, which are the bases of the processes in remote sensing are known classically in homogeneous media. What happens in fractal media? For example what is the behaviour of the electromagnetic field in a fractal cloud? Such are the questions where fractals can play a role in remote sensing. The fascination of computer image production has often diverted the community away from the summits which it needs to climb. Physics is not contained in geometry.

## References

- [1] Dautray R., Lions J. L., Analyse mathématique et calcul numérique, Masson, 1987.
- [2] Thom R., Modélisation et scientificité. In Elaboration et justification des modèles, application en biologie, Maloine, 1979.
- [3] Casti, J. L., Reality Rules, John Wiley, 1992.
- [4] Asimov I., Asimov's New Guide to Science, Basic Books Inc., New York, 1984.
- [5] Thom. R., Morphogénèse et Imaginaire, CIRCE, lettres Modernes éd. 1978.
- [6] Berger J. M., Mandelbrot B., A New Model for the Clustering of Errors on Telephone Circuits. IBM J. of Research and Development 7, 224-236, 1963.
- [7] Zeeman E.C., Catastrophe Theory: Selected Papers, Addison-Wesley, Reading, MA, 1977.
- [8] Hausdorff F., Dimension und Ausseres. Mass. Math. Ann., 79, 1919.
- [9] Kahane J. P., Le Chaos Multiplicatif, C.R. Acad. Sc. Paris 301, 1985.
- [10] Kahane J. P., Peyrière J., Sur certaines Martingales de Benoît Mandelbrot. Advances in Math. 22, 1976. [11] Falconer, Fractal Geometry, John Wiley, 1990.
- [12] Tricot C., Courbes et Dimension Fractale, Springer-Verlag, 1993.
- [13] Douady A., Osterle J. Dimension de Hausdorff des Attracteurs. CRAS, 290, 1980.
- [14] Gumowski I., Mira C., Dynamique Chaotique: Transformations Ponctuelles - Transition: Ordre-Désordre. Cepadues ed. Toulouse, 1980.
- [15] Barnsley M., Fractals Everywhere, Academic Press, 1988.
- [16] Constantin P., Foias C., Temam R., Attractors Representing Turbulent Flows. Memoirs of the Amer. Math. Soc., no. 134, 1985.
- [17] Amit D.-J., Field Theory, The Renormalization Group and Critical Phenomena, Mc Graw Hill Int., 1978.
- [18] Toulouse G., Pfeuty P., Introduction au Groupe de Renormalisation et ses Applications, Presses Univ. de Grenoble, 1975.
- [19] Stauffer D., Introduction to Percolation Theory. Taylor and Francis, London, 1985.
- [20] Mackay R. S., A Renormalization Approach to Invariant Aides in Area-Preserving Maps, Order in Chaos, North-Holland, 1983.
- [21] Shenker S. J., Quasiperiodicity in Dissipative Systems: A Renormalization Group Analysis, Order in Chaos, North-Holland, 1983.

- [22] Pietronero L., Tosatti E., Fractals in Physics, North-Holland, Amsterdam, New York, 1986.
- [23] Pietronero L., Order and Chaos in Non-Linear Physical Phenomena, Lindqvist N., ed., Plenum Publ. New York-London 1987.
- [24] Grebogi C., McDonald S. W., Ott E., Yorke J., Final State Sensitivity: An Obstruction to Predictability, Phys-letters, vol 99A, n 9, 1983.
- [25] Farmer J. D., Ott E., Yorke J., The Dimension of Chaotic Attractors, Physica, 7D, North-Holland 1983.
- [26] Davies P. (ed), The New Physics, Cambridge Univ. Press, 1993.
- [27] Bergé, Pomeau Y., Vidal C. L'Ordre Dans Le Chaos, Vers une Approche Déterministe de la Turbulence, Hermann, 1984.
- [28] Gouyet J-F., La Physique des Fractals, Masson, 1992.
- [29] Sapoval B., Rosso M., Gouyet J. F., The Fractal Nature of a Diffusing Front and the Relation to Percolation, J. Phys. Lett., 46. 149-156. 1985.
- [30] Mandelbrot B., Les Objets Fractals, Flammarion, 1975.
- [31] Mandelbrot B., The Fractal Geometry of Nature, Freeman. San Francisco, 1982.
- [32] Frisch U., Parisi C., On the Singularity Structure of Fully Developed Turbulence. Turbulence and Predictability in Geoph. Fl. Dyn. and Clim. Dyn. (ed. M. Ghil, R. Benzi and C. Parisi, North-Holland. New York), 84, 88, 1985.
- [33] Schertzer D. and Lovejoy S., The Dimension and Intermittency in Atmospheric Dynamics. Turbulent Stream Flow. IV. Ed. B. Lauder, New-York, Springer, 1984.
- [34] Ledrappier F., Some Relations between Dimension and Lyapounov Exponents. Comm. Math. Phys., 81, 1981.
- [35] Julien R., Les Phénomènes d'Aggrégation et Les Aggrégats Fractals, Ann. des Télécom. Paris, tome 41, 1986.
- [36] Vicsek T., Fractal Growth Phenomena, World Scientific, 1992.
- [37] Avnir D., The Fractal Approach to Heterogeneous Chemistry. John Wiley, 1989.
- [38] Le Méhauté A., Héliodore F., Chabassier G., Electromagnetic Waves in Fractal Media, Progress in Electromagnetism, Res. Symp., Boston, July 1989.
- [39] Jürgens H., 3D Rendering of Fractal Landscapes, in Fractal Geometry and Computer Graphics, Springer-Verlag, 1992.
- [40] Peitgen H. O., Saupe D., The Science of Fractal Images, Springer-Verlag, 1988.
- [41] Peitgen H. O., Richter P. H., The Beauty of Fractals, Springer-Verlag, Berlin, 1986.



- [43] Turcotte D. L., Fractals and Chaos in Geology and Geophysics, Cambridge Univ. Press, 1992.
- [44] Ross J., Marshak A., Monte Carlo Methods, in Photon-Vegetation Interactions. Springer-Verlag, 1991.
- [45] Verhoef W., Light Scattering by Leaf Layers with Application to Canopy Reflectance Modelling: The SAIL Model, Rem. Sens. of Environment, 16. 125-141.
- [46] Dauzat J., Hautecoeur O., Simulation des Transferts Radiatifs sur Maquettes Informatiques de Couverts Végétaux, 5th. Intl. Coll. on Phys-Meas. and Signatures in Remote Sensing, Courchevel, 1991.
- [47] Rothrock D. A., and Thorndike A. S., Measuring the Sea Ice Floe Size Distribution, J. Geophys. Res. 89 (C4) : 6477-6486, 1984.
- [48] Lovejoy S., The Area-Perimeter Relation for Rain and Cloud Areas, Science. 216. 185-187, 1982.
- [49] Batty M., Cities as Fractals: Simulating Growth and Form. A. J. Crilly (ed.). Springer-Verlag, 1991. Verlag, 1991.
- [50] Schroeder M., Fractals, Chaos, Power Laws, Freeman, New-York, 1991.
- [51] Voss R. F., Random Fractal Forgeries, NATO-ASI vol. F 17, Springer-Verlag, 1985.

# Chapter 3

## Fractal and Multi-resolution Techniques for the Understanding of Geo-Information

*Mihai Datcu\* and Klaus Seidel†*

### 1 Introduction

The high complexity of remotely sensed images and measurements provided by the last generation of sensors demands new techniques for scene understanding and analysis. The similarity of fractal and real world objects was observed and intensively studied from the very beginning. Fractal geometry became a tool for computer graphics and data visualization in the simulation of the real world. In order to perform visual analysis and comparisons between natural and synthetic scenes several techniques have been developed. After a period of qualitative experiments fractal geometry began to be used for objective and accurate purposes: modelling image formation processes, generation of geometrically and radiometrically accurate synthetic scenes and images, evaluation of the characteristics of relief, determination of the surface roughness, analysis of textures. The recent progress in the mathematical formulation of the behaviour of  $1/f$  processes, in utilization of wavelets to make evidence of scale dependent features of nonstationary processes and the developments in hierarchic stochastic processes open a new perspective for the processing and interpretation of a large class of non-stationary multi-dimensional signals.

---

\*German Aerospace Research Establishment (DLR), Oberpfaffenhofen, D-82234, Wessling, Germany [On leave from Polytechnic University, Bucharest, Romania]

†Swiss Federal Institute of Technology, ETH, Institute for Communication Technology, CH-8092, Zurich, Switzerland

## 2 Elements of fractal geometry

A discussion of the field of fractals obviously embraces an enormous field [1]. The primary concern of this chapter is thus with the presentation of the elementary ideas necessary to understand applications of fractal geometry in geo-processing [2]. Fractal geometry deals with the behaviour of sets of points  $S$ , in the  $n$ -dimensional space  $R^n$ .

$$S \subset R^n \quad (1)$$

For the addressed applications  $S$  is a curve, a surface or an image intensity field. Therefore  $n$  is restricted to 1, 2 or 3. But several applications, such as multispectral data analysis, ask for representation of data in a higher dimensional space [3].

### 2.1 Self-similarity and self-affinity

Mandelbrot defined a fractal as a shape made of parts similar to the whole in some way [4]. The definition is qualitative, but not ambiguous, as it looks at first glance. The main characteristic of a fractal is its self-similarity [5]. A set is called self-similar if it can be expressed as a union of sets, each of which is a reduced copy of the full set. More generally a set is said to be self-affine if it can be decomposed into subsets that can be linearly mapped into the full set. If the linear mapping is a rotation, translation or isotropic dilatation the set is self-similar. Self-similar objects are particular cases of self-affine ones.

$$\{\text{SELF-AFFINE}\} \supset \{\text{SELF-SIMILAR}\} \quad (2)$$

A fractal object is self-similar or self-affine at any scale. If the similarity is not described by deterministic laws stochastic resemblance criteria can be found. Such an object is said to be statistically self-similar. Natural fractal objects are statistically self-similar. A statistically self-similar fractal is by definition isotropic. To have a more precise, quantitative, description of the fractal behaviour of a set, a measure and a dimension are introduced [6]. The rigorous mathematical description is done by the Hausdorff measure and dimension [7,8].

### 2.2 Hausdorff dimension

Let  $S$  be a set of points in the  $n$  dimensional space  $R^n$ . The topological dimension of the space is  $n$ , where  $n$  is an integer. Choose also a real

number  $r$  inferior to  $n$ .

$$S \subset R^n; 0 \leq r \leq n \quad (3)$$

Consider further the cover  $H_\delta^r$  of the set  $S$  with sets  $U_i$  of limited diameter  $|U|$ :

$$H_\delta^r(S) = \inf \left\{ \sum_i |U_i|^r / 0 < |U_i| < \delta \right\} \quad (4)$$

$$|U| = \sup \{ |x - y| / x, y \in U \} \quad (5)$$

The infimum is evaluated over all coverings of  $S$  by a collection of sets with diameters at most  $\delta$ . The set  $\{U_i\}$  is countable or finite.  $H_\delta^r$  increases as  $\delta$  decreases to zero. By decreasing  $\delta$  the restrictions on the allowable coverings of the set  $S$  are increasing. The  $r$ -dimensional Hausdorff measure  $H^r(S)$  of the set  $S$  is defined:

$$H^r(S) = \lim_{\delta \rightarrow 0} H_\delta^r(S) \quad (6)$$

To exemplify: if  $S$  is a smooth curve,  $U_i$  can be a linear stick of length  $\delta$  and  $H^1(S)$  is the length of the curve, if  $S$  is a smooth surface,  $U_i$  can be a disk of diameter  $\delta$  and  $H^2(S)$  is the area of the surface. The Hausdorff measure generalizes the definition of length, area, volume.  $H_\delta^r(S)$  gives the volume of a set  $S$  as measured with a ruler of  $\delta$  units. A figure with finite length will have zero area, and a finite area will be covered by a curve of infinite length. Based on these observations and particular cases, two properties of the Hausdorff measure will be introduced. If the  $r$ -dimensional Hausdorff dimension of the set  $S$  is higher than zero, then the  $p$ -dimensional Hausdorff measure of the set  $S$  is infinite, for  $p$  less than  $r$ . If the  $r$ -dimensional Hausdorff measure of the set  $S$  is bounded, then the  $p$ -dimensional Hausdorff measure of the set  $S$  is zero, for  $p$  greater than  $r$ . The value of the parameter  $r$  for which the  $r$ -dimensional Hausdorff measure of the set jumps from zero to infinite is called the *Hausdorff dimension*,  $dim_H$ , of the set  $S$ .

$$\begin{cases} H^r(S) > 0 ; \forall p < r ; H^p(S) = \infty \\ H^r(S) < \infty ; \forall p > r ; H^p(S) = 0 \end{cases} \quad (7)$$

$$\begin{cases} dim_H S = \sup \{ r / H^r(S) = \infty \} \\ dim_H S = \inf \{ r / H^r(S) = 0 \} \end{cases} \quad (8)$$

A set is said to be fractal if its Hausdorff dimension strictly exceeds its topological dimension:

$$dim_H S > n \quad (9)$$

Numerical evaluation of Hausdorff dimension is difficult because of the necessity to evaluate the infimum of the measure over *all* the coverings of the set of interest. That is the reason to look for another definition for the dimension of a set.

### 2.3 Minkowski dimension

The Minkowski dimension [6] allows the evaluation of the fractal feature of a set. First the parallel set  $E_S(\delta)$  of the set  $S$  is introduced:

$$E_S(\delta) = \{x \in R^n / d(x, S) \leq \delta\} \quad (10)$$

The parallel set  $E_S(\delta)$  of the set  $S$  is the set including all the points of the space that are closer than a given constant  $\delta$  to the points of the set  $S$ . The Minkowski dimension of the set  $S$ , is:

$$\aleph(s) = \limsup_{\delta \rightarrow 0} \left\{ n - \frac{\log V_n(E_S(\delta))}{\log(\delta)} \right\} \quad (11)$$

$V_n$  represents the volume in the  $n$  dimensional space  $R^n$ . In contrast to the box counting dimension or the Hausdorff dimension, to compute the Minkowski dimension one must not search for an optimal cover of the set  $S$ .

Computing the volume of the parallel sets for different values of the radius  $d$ , and plotting these values in log-log coordinates, one will obtain a straight line if the set has fractal behaviour. The Minkowski dimension is computed as the topological dimension of the space,  $n$  minus the slope of the straight line. The similarities in the structure of the set  $S$  are detected by evaluating the volume of the associated parallel set for different scales defined by  $d$ .

### 2.4 Box counting dimension

The box counting dimension allows the evaluation of the dimension of sets of points spread in an  $n$ -dimensional space and also gives possibilities for easy algorithmic implementation. Given a set of points  $S$ , in an  $n$ -dimensional space  $R^n$  and  $N_\delta$  is the least number of sets of diameter at most  $\delta$  that cover  $S$ , the box counting dimension,  $dim_B$ , is defined as:

$$dim_B S = \lim_{\delta \rightarrow 0} \frac{\log N_\delta(S)}{-\log(\delta)} \quad (12)$$

Depending on the geometry of the box and the modality to cover the set, several box counting dimensions can be defined: 1) the least number of closed balls of radius  $\delta$  that cover  $S$ , 2) the least number of sets of diameter at most  $\delta$  that cover  $S$ , 3) the least numbers of cubes of side  $\delta$  that cover  $S$ , 4) the number of cubes of the lattice of side  $\delta$  that intersect  $S$ , 5) the largest number of disjoint balls of radius  $\delta$  centered in  $S$  [8]. The equivalence of these definitions was proved. Also it was proved that these dimensions are inferior bounded by the Hausdorff dimension [7].

The relation of the scale properties of a fractal to the box counting dimension's definition can be seen from an example. Consider a fractal self-similar contour  $f(x, y)$ ,  $f(\alpha x, \alpha y)$  is statistically similar to  $f(x, y)$ ;  $\alpha$  is the scaling factor. The number of boxes of dimension  $\delta_x, \delta_y$  necessary to cover the set represented by the points of  $f(x, y)$  is  $N$ , and the number of boxes of dimension  $\alpha\delta_x, \alpha\delta_y$  required to cover the set is  $N_\alpha$ . If the set is self-similar, as previously supposed, the ratio  $N_\alpha/N$  will be a constant. The logarithm of this constant is proportional to the fractal dimension of the set.

If a statistically self-affine fractal is considered it will be non-isotropic. At different scales  $f(x, y)$  will be statistically similar to  $f(\alpha x, \alpha^H y)$ .  $H$  is the Hausdorff dimension, and  $\alpha$  is the scaling factor. The boxes must be scaled differently in the  $x$  and  $y$  directions, with  $\alpha$  and  $\alpha^H$  respectively. The ratio  $N_\alpha/N$  is also a constant proportional to the fractal dimension of the set.

## 2.5 Other dimensions

Several further definitions for the dimension of a set have been introduced. All these definitions, as the previous ones, have a common goal: to show the self-similarity or self-affinity of the set. As an immediate consequence all definitions are based on a multiscale evaluation of a certain measure. For example:

**the  $P(m, L)$  dimension** [9], is the probability to have  $m$  points within a box of size  $L$ . The expected number of boxes to cover the set  $N(L)$  is:

$$N(L) = \sum_{m=1}^N \frac{1}{m} P(m, L) \quad (13)$$

and the regression of  $N$  versus  $L$  in log-log plot gives a straight line if the set is fractal. The slope of the line is the fractal dimension of the given set.

**Space scale filtering**, the self-similarity or self-affinity properties of sets are scale relative, that is why one can deal with the change of the scale

of the set instead of the change of magnitude of the ‘stick’ used for the estimation of the dimension. For evaluation of the fractal dimension of a signal,  $\phi$ , a multi-resolution approach is used [10]. The signal is smoothed using a bank of Gaussian filters having different variance  $\sigma$ .

$$\Phi(\bar{x}, \sigma) = \int_{-\infty}^{\infty} \varphi(\bar{\xi}) \frac{1}{\sigma\sqrt{2\pi}} e^{-\frac{(x-\bar{\xi})^2}{2\sigma^2}} d\bar{\xi} \quad (14)$$

The regression of the ‘length’ of the signal,  $\Phi$  measured with a fixed ‘stick’, plotted in log-log as a function of the variance of the applied filter will be a straight line. The slope of the line gives the fractal dimension.

**Covering-blanket method**, is used for the estimation of the fractal dimension of contours, surfaces or image intensities [11]. The concept of the covering-blanket is based on the analysis of a multiscale construction. For a surface, as an example the upper, and lower bounding surfaces are to be generated. The covering-blanket is defined by the band of thickness  $2\varepsilon$ , created by the two secondary functions. The multiscale analysis will be done for different values of  $\varepsilon$ . The estimation of the fractal dimension involves taking the logarithm of the difference of the upper and lower bounding surfaces divided by the scale factor  $\varepsilon$ , and fitting a line to it in a log-log plot, as a function of scale.

**Power-spectrum method**, is based on the property of fractal functions to have a negative power-law shaped power-spectrum function [12]. The Fourier transform is used to derive the power-spectrum and a linear regression is used in log space to derive the fractal dimension.

**Wavelet transform of fractals**. Both fractals and wavelets, as a main characteristic, allow scale to be made explicit [13]. The wavelet transform  $Wf$  of a function  $f(x)$  is its decomposition on an orthogonal basis of functions. The basis functions are generated from a parent function  $y$  using dilatations of factor  $a$ , and translations with vector  $b$  [14].

$$Wf(a, b) = \int_{-\infty}^{\infty} f(x) \sqrt{a} \Psi(a(x - b)) dx \quad (15)$$

The wavelet transform encodes patterns occurring at different scales in a uniform way. It means that by considering a fractal and computing its wavelet transform one can derive the fractal dimension [15].

### 3 Fractals synthesis

#### 3.1 Brownian process

To generate fractal objects several techniques have been developed: deterministic fractals are synthesised using iterative equations, cellular automata, or L-systems; stochastic fractals are obtained by Brownian process simulation, using  $1/f$  filtering methods, random-midpoint displacement or modified L-systems. Natural landforms are well represented by fractals derived from the Brownian process description [16]. Consider, in the one-dimensional case, a random process  $X(t)$ . If the Probability Density Function PDF, of the consecutive sample is Gaussian the process is called Brownian.

$$\begin{aligned} X(t_{n+1}) - X(t_n) &= x(t_n) \quad t_{n+1} - t_n = t \\ p(x, t) &= \frac{1}{\sqrt{4\pi St}} \exp\left(-\frac{x^2}{4St}\right) \end{aligned} \quad (16)$$

The Brownian motion describes as Gaussian the displacement of a particle in one time interval [17]. The displacement is an independent variable.  $S$  is a constant: the diffusion coefficient, it models the ‘spread’ of a particle trajectory in Brownian motion. To study the scale behaviour, the Brownian process will be sampled at intervals  $\Theta = kt$ . The PDF of the consecutive samples difference, for the new process, will be derived.

$$\Theta = kt; \quad \zeta = t\sqrt{k} \quad p(\zeta, \Theta) = \frac{1}{\sqrt{k}} p(x, t) \quad (17)$$

The newly derived PDF at the scale  $\Theta = kt$  is also Gaussian and differs by a constant from the original process PDF. The Brownian process is statistically self-affine. The affinity is in the statistic of the differences of consecutive samples at any scale. Wiener introduced a random function to describe the displacement of particles in Brownian motion. The difference of consecutive samples is extracted from a Gaussian distribution and is proportional to a power function of the sampling period [4].

$$X(t_{n+1}) - X(t_n) \approx grv |t_{n+1} - t_n|^H \quad (18)$$

Where  $grv$  is a Gaussian Random Variable, and  $H = 1/2$ . The process is self-affine. Mandelbrot generalized the random function of Wiener and introduced the concept of fractional Brownian motion, changing the exponent  $H$  to be any real number in the interval  $(0,1)$ . The new random function was denominated  $B_H(t)$ . The previously presented random functions give a



basis for the generation of fractals in one dimension or in an  $n$ -dimensional space. The random functions can be represented in  $n$ -dimensions simply by the substitution of time in a space  $n$ -tuple of coordinates [18]. Voss introduced the successive random addition algorithm [16]. In order to generate a fractional Brownian curve the variance of the increments of the position must be:

$$V(t) = E[X(t) - X(0)]^2 = |t|^{2H} \sigma_0^2 \quad (19)$$

In the first iteration the increments of the process are to be extracted from a Gaussian distribution of variance  $\sigma = 1$ . In the  $n$ -th iteration the displacements (midpoints) are interlaced between the previous step points, and are extracted from a Gaussian distribution of variance:

$$\sigma_n^2 = \left(\frac{1}{2}\right)^{2H} \sigma_{n-1}^2 \quad (20)$$

## 3.2 Spectral method

The power spectral density  $S$ , of a self-affine fractal is a negative power law shaped function [19].

$$S(f) \approx 1/f^\beta \quad (21)$$

The fractal dimension  $D$  is related to the  $\beta$  coefficient [16]:

$$D = T + (3 - \beta)/2 \quad (22)$$

where  $T$  is the topological dimension. As a direct consequence of this property the Fourier transform is one of the main tools for the generation of fractal objects.

## 3.3 L-systems

The three dimensional structure of plants is probably most realistically modelled using L-systems [20]. A formal set of rules specify how the plants develop in different stages. It is important to develop algorithms which by means of a reduced set of parameters can control the variability of ‘synthetic’ vegetation. The L-system is constructed starting with a string called an axiom, and in the first step substituting every symbol of the string in accordance to a given set of rules. The process is repeated iteratively. It is essential to note that all the symbols in the string are changed simultaneously. This is a major difference compared with a formal language where the parser is applied sequentially. Applying the previous procedure the defined

object grows preserving the same structure at larger scales. More generally than plant modelling, the L-systems can describe almost any fractal object or at least their finite approximations. The work of Lindermayer was oriented mainly to graphic representation and considering the evolution of the field this issue was continued. The theory of L-systems developed into several new techniques: bracketed L-systems, graph theoretic trees using strings with brackets [21]; data base amplification [2], simulation of development of real plants; the axial tree [23], a notion which complements the graph-theoretical concept and makes it closer to natural vegetation models; context-sensitive L-systems, that model the possible interaction of component elements. The techniques for plant models generation was enhanced using combined methodology of L-systems and iterated function systems IFS [24].

## 4 Multiresolution analysis and synthesis of $1/f$ fractal processes

A large diversity of fractal processes can be defined. One of the most important class of random fractals is considered to be  $1/f$  processes [25, 26]. These processes model a huge spectrum of natural and man-made phenomena. The recently developed mathematical methods for the representation of  $1/f$  processes increased their impact in applications such as signal and image processing.

Several models describe the  $1/f$  process. One class, exemplified by fractional Brownian motion, is based upon a fractional integral formulation. Other models are in the category of infinite order *ARMA* processes class. Recently stochastic multiscale and scale recursive models have been developed [27, 28]. The power spectrum of the  $1/f$  processes is

$$S(\omega) = \frac{\sigma^2}{|\omega|^\gamma} \quad (23)$$

for a given range of the ‘gamma’ parameter. In terms of spectral analysis Equation 23 is not integrable and actually does not represent a valid power spectrum [29]. The  $1/f$  random processes are self-similar, (Eq. 24 and 25):

$$x(t) = a^{-H} x(at) \quad (24)$$

$$S(\omega) = |a|^\gamma S(a\omega) \quad (25)$$

characterized by a long term correlation structure with polynomial decay that can not be represented by classical time series models. An example is the correlation function of fractional Brownian motion:

$$R(t, \tau) = \frac{\sigma_H^2}{2} (|t|^{2H} + |\tau|^{2H} - |t - \tau|^{2H}) \quad (26)$$

$$\sigma_H^2 = \Gamma(1 - 2H) \cos \frac{(\pi H)}{\pi H} \quad (27)$$

The processes are generally non-stationary but stationary when passed through time invariant linear filters. The non-stationarity of the process is related to the time dependent analysis, and the self-similarity is related to the scale-dependent analysis [30]. In terms of frequency characterization a  $1/f$  process when filtered by an ideal bandpass filter yields a wide-sense stationary random process with finite variance and having a power spectrum as in Equation 23, with

$$\gamma = 2H - 1$$

This gives the mathematical frame to justify and accept former frequency synthesis methods for fractal synthesis with the natural bandpass assumption: the available data length limits the knowledge at low frequencies and the sampling interval limits the access to details at high frequencies. Sample functions of fractional Brownian motion have fractal behaviour for

$$0 \leq H \leq 1 \quad 1 \leq \gamma \leq 3$$

being characterized by the Hausdorff-Besicovitch dimension  $D = 2 - H$  (for one dimensional case). A limitation of the fractional Brownian motion is that it does not provide models for  $1/f$  processes with

$$\gamma < 1 \quad \gamma > 3 \quad \gamma = 1$$

The multi-resolution approach considers a decomposition of the signal space in nested sequences of approximation spaces [31]. The wavelet based multi-resolution is characterized to have similar resolution approximation in all time intervals and at all scales. Because  $1/f$  processes simultaneously exhibit both statistical scale invariance and a particular time invariance behaviour the wavelet transform constitutes a natural analysis and synthesis tool for these processes.

The importance of the wavelet transform in the field of non-stationary  $1/f$  processes can be compared with the importance of the Fourier transform in the field of stationary process. The wavelet transform applied to the  $1/f$  processes has the same role as a Karhunen-Loeve expansion [15].

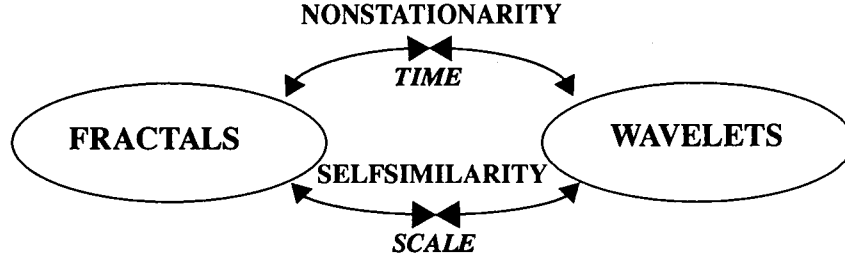


Figure 1: Interrelationships between fractals and wavelets

As a generalization a nearly  $1/f$  process was introduced via wavelet based synthesis [15,25]. The process  $x(t)$ :

$$x(t) = \sum_m \sum_n x_n^m \Psi_m^n(t) \quad (28)$$

$$\frac{\sigma_L^2}{|\omega|^\gamma} \leq S(\omega) \leq \frac{\sigma_H^2}{|\omega|^\gamma} \quad (29)$$

is obtained from a collection of mutually uncorrelated zero-mean random variables  $x$ , of variance

$$\text{var}(x_n^m) = \sigma^2 2^{-\gamma m} \quad (30)$$

for any orthonormal wavelet basis with a given degree of regularity and  $S$  the time averaged spectrum. In figure 1 the interrelations between fractals and wavelets are shown. As a result referring to the analysis of  $1/f$  processes it was shown that the orthonormal wavelet expansion of such a process produces coefficients weakly correlated in contrast with the strong correlation of the original process. The wavelet coefficients are in a wide sense stationary at each scale and an ‘across scale stationarity’ is also verified. For a fractal process the ratio of the energy of the detailed signal at different scales is a constant, logarithmically related to the fractal dimension.

The wavelet transform defines a bridge between the rich class of multi-scale stochastic processes and the fractional Brownian process. An isotropic

stochastic process is indexed by the nodes of an homogeneous tree. The homogeneity is related to the ‘across scale stationarity’. A horizontal level in the tree is associated to a fixed scale resolution. The multiscale stochastic processes are described by a scale recursive model. The model can be interpreted as a generalization of the midpoint displacement technique for generation of Brownian motion. The technique assumes a dyadic partition of the unit interval and adding samples extracted from a random number generator according to the joint probability distribution implied by the Brownian motion model.

The construction can be further modelled as a sequence of interpolations at a scale to the power of 2. For a linear spline interpolation the process can be interpreted as nonorthogonal multiscale approximation using the triangular ‘hat’ functions which are the integral of the Haar wavelet. At any level in the multi-resolution representation each state is a linear combination of its parents plus an independent noise. The latter advances in the description of  $1/f$  noise, hierarchic stochastic processes and multi-resolution representation give a new perspective in the analysis and synthesis of a large class of non-stationary signals. The diagram in figure 2 presents the direction of possible further developments.

## 5 Applications

### 5.1 Incomplete data simulation

To deal with incomplete data, in the image formation process, fractal geometry can be used when models are unknown. The proved self-similarity or self-affinity of the landforms and land cover structures are used. In figure 3 the synthesis technique is shown. The lack of geometric data encoded in Digital Elevation Models (DEM) and radiometric information is supplemented using fractal objects. The data fusion from real satellite images with synthetic images creates a new approach in model based image understanding. The model is expressed in terms of the geometry and radiometry of the synthetic images. The concept of identity declaration by physical modelling is considered.

Many of the early applications of fractal geometry were involved in finding methods for the generation of pleasant visual aspect images for computer graphic representations. More recently realistic looking landscapes have been synthesised for flight simulators or relief visualization of other planets [1, 26], and more precise simulations of the landforms are derived

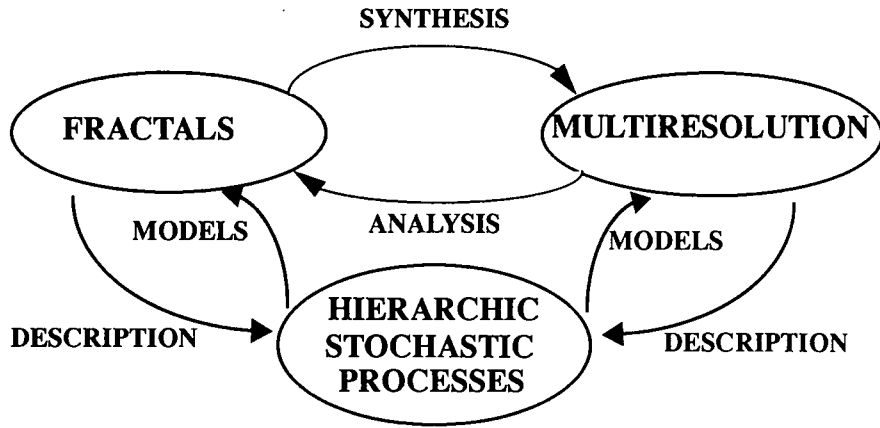


Figure 2: Direction of possible further developments

with the aim to build models to be used in feature evaluation for further correlation with characteristics of the natural relief [32]. Geomorphology and soil science require terrain models with peculiar characteristics for other simulations: water erosion process, drainage basin topology, surface water flow, river course erosion, wind mass transport effects, deforestation, volcanic lava flow [33, 34]. One of the benefits in cartography from fractal simulation is the possibility to generate synthetic digital elevation models at a variety of scales and terrain roughness which can be used as test areas for the performance of the algorithms for digitizing simulated cartographic maps [35]. The techniques frequently used for the generation of synthetic DEMs are the ‘mid point displacement’, and the simulation of the  $1/f$  noise. A Gaussian white noise is filtered using a  $1/f^\beta$  shaped transfer function. The output signal is a self-affine fractal having the fractal dimension  $D = T + (3 - \beta)/2$ .  $T$  is the topologic dimension of the space [36]. Figure 4 shows two synthetic DEMs having different fractal dimension. The surfaces are presented as Lambertian surfaces illuminated from the S-E direction. The left hand image, 6a, due to the fractal behaviour, can be

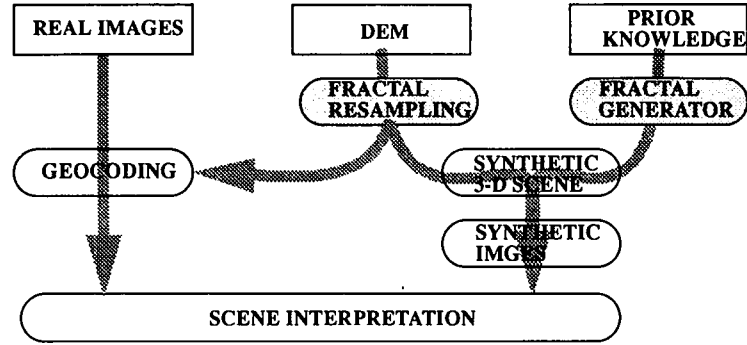


Figure 3: Incomplete data simulation

considered as any rescaled subwindow from the right hand image, 6b. The surface is self-affine, in the statistical sense. The ‘lakes’ in the right hand image are obtained from the intersection of a plane with the surface. The contours of the lakes are fractal lines having the fractal dimension  $D - 1$  [37].

Available DEMs are generally limited in resolution. The resolution is given by the constant of the support grid for the height data. Applications such as: relief visualization, image formation modelling for remote sensors, high resolution contour mapping etc. require accurate DEMs. A higher resolution can be obtained by a resampling process: to add new samples in a higher resolution grid. If functional resampling is used the resulting DEM has an unrealistic smooth aspect. It has been experimentally proved that natural relief has fractal behaviour for a certain range of scales [33, 38]. The fractal resampling process uses this prior information: the similarity of landforms for several spatial scales. The fractal resampling is accomplished in two steps: the analysis of the real DEM for evaluation of the fractal dimension and local variance of the height field, and the fractal interpolation [39]. The fractal interpolation increases the resolution of the DEM in steps of 2. The statistical resemblance of the synthesised samples is obtained using the random addition method of Voss [16]. An example is presented in figure 5: a 100m. resolution DEM resampled to 50m. The surface

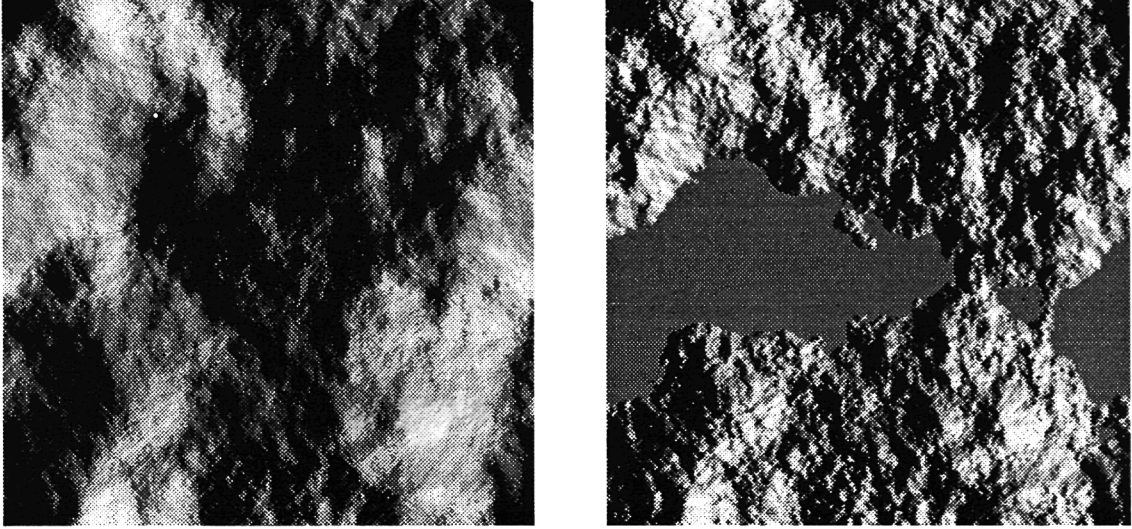


Figure 4: Synthetic fractal DEMs presented as Lambertian surface illuminated from the south east direction

is presented as a Lambertian one, lit from the south-east direction. The visual appearance is more realistic. The generation of synthetic images with the aim of enhancing the performance of classification of remotely sensed images is one of the topics of interest [40]. The fractal resampling can not be applied below a given scale. Gravity and diffusion processes or, vegetation cover break the continuity in similarity, and other models must be applied [41].

## 5.2 Multiresolution approach in image synthesis

Surface visualization is limited in accuracy for at least two reasons: the limited resolution of the geometrical description, incomplete knowledge and imperfect simulation of the light scattering process. For surfaces having fractal behaviour any ‘facet’ or interpolated representation means a cut in the similarity. A multi-resolution approach is used to derive an accurate model [42]:

1. At the macro-scale the scene is described by the knowledge of the



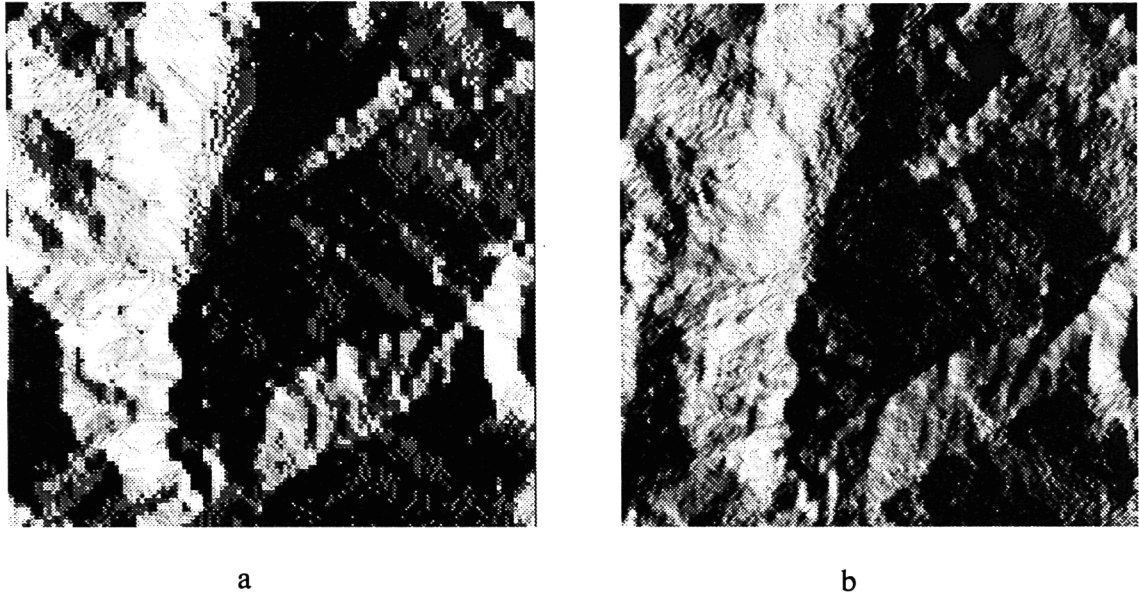


Figure 5: DEM, (a) 100m. resolution, (b) 50m. resolution -fractally resampled

surface geometry.

2. A meso-scale is introduced relative to the spatial resolution of the sensor. The pixel intensity is dependent on the local geometry, on the local roughness of the surface at a resolution higher than the sensor's geometrical resolution, and on the reflectance behaviour of the surface at the next finer scale. Thus the sensed intensity is the result of a nonlinear spatial operator. This spatial operator models the image formation process of the specific sensor.

3. At the micro-scale the facets of the surface are characterized by reflectance functions. They are generally obtained by statistical, experimental or on a heuristic basis. The realism and accuracy of the synthetic images is determined by the model of local light scattering. A general scattering function for unpolarized light is a function of four variables and the Bidirectional Reflectance Function, BRF [43].

At the micro-scale the BRF can be approximated from simple models

of light scattering. The model is dependent on three physical parameters describing the surface appearance: diffuseness, specularity and interreflection characteristics. At the meso-scale the previously presented models and the sensor description are considered. The image formation process is simulated. The sensor is represented by a non-linear spatial operator. In the usual case the operator is a spatial convolution of the surface reflectance with the point spread function of the sensor followed by a non-linear transform.

If the sensor resolution is lower than the resolution of the surface, the intensity of one pixel is modelled by the integral of all scattered intensities of the microfacets weighted by the sensor's point spread function. A virtual radiometric experiment can be carried out for a given sensor and microgeometry of the surface. In figure 6a the imaging geometry for a rough surface is presented. Each microfacet is characterized by the surface optical attributes and its geometry, the local normal vector  $\bar{n}$ . The sensor and light source positions are specified respectively by the vectors  $\bar{r}$  and  $\bar{l}$ . An area of 32 x 32 microfacets was imaged from a sensor placed at the nadir with variable incident illumination. The resulting images are displayed in figure 6b. The last scene is a perspective view of the imaged surface (3D). Using the information from these images the albedo and BRF have been computed, and with prior knowledge of the sensor characteristics the accurate pixel intensities have been modelled. The experiment explains the difference in radiometry of the images in figure 3. After fractal resampling the local roughness increases and the BRF is modified. The experiment was applied for vegetation cover radiometric evaluation. A three dimensional plant model was developed using generalized L-systems [44].

To take into account the exact surface roughness and to calculate the actual scattering cross-section the Kirchhoff solution must be found. The validity of the Kirchhoff solution was intensively studied [45]. In the solution of scattering from fractal surfaces, the wavelength is considered as a yardstick. The solution is derived for relative space-scale to wavelength ratios [45]. The results find applicability to synthetic aperture radar (SAR) imagery of sea surface or rough terrain.

The intrinsic similarity of fractal surfaces for an infinite range of scales makes an accurate visualization impossible. Applying the previously presented models, and using the knowledge of the surface geometry at the meso-scale and the sensor model, complex and more accurate reflectance functions have been obtained. The virtual radiometric experiment was applied for fractal surfaces.

Figures 7 a, b, and c show the dependence of the sensed intensity on

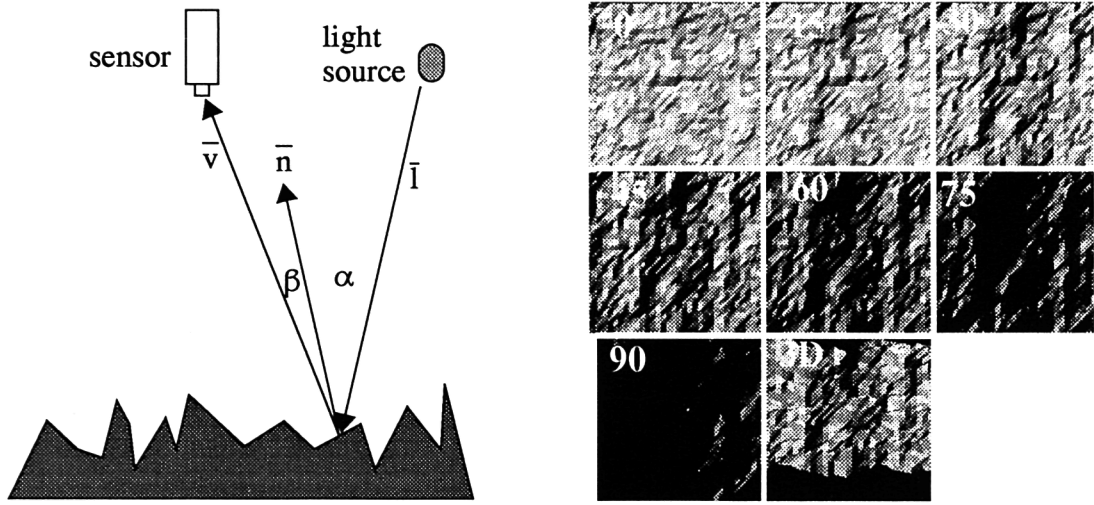


Figure 6: Imaging geometry, rough surface imaged for different incident light positions; 0, 15, 30, 45, 60, 75, 90 degrees, and 3D view

the roughness,  $\gamma$ , and on the incidence light angle,  $\alpha$ , for three different assumptions of the micro-scale facet appearance: diffuse (a), diffuse and specular (b), and diffuse, specular, and interreflections (c). Note the highest roughness is given for low values of  $\gamma$  (highest fractal dimension). In figure 8 fractal surfaces are shown in macro-scale representation with diffuse and specular appearance. Figure 8a is generated with the appearance of the microfacets described by the diagram in figure 7a, and image 8b with the reflectance function as shown in figure 7b.

### 5.3 Application in understanding remotely sensed scenes by optical sensors

Data fusion in synthetic images, and the modelling of incomplete knowledge using fractal objects, is further demonstrated in a remote sensing application. The aim is to segment the snow covered areas in rough mountainous regions. This results in a new method for the rejection of topographic

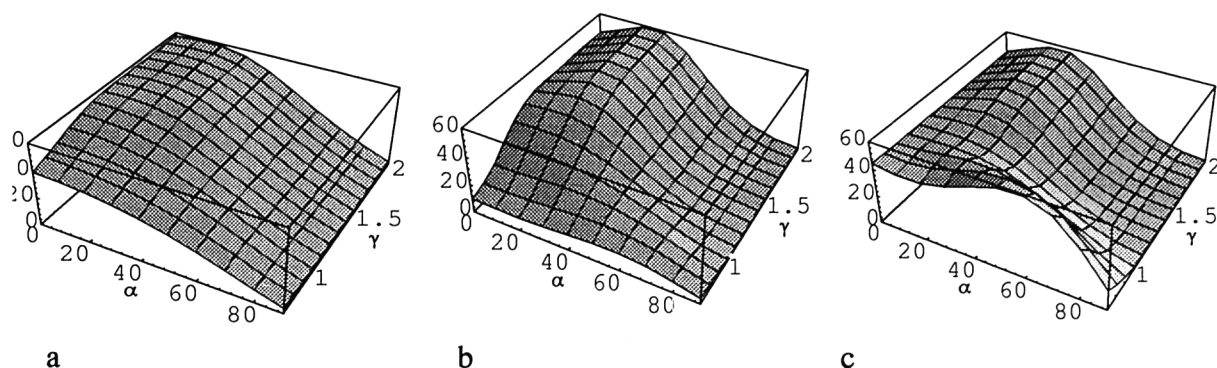


Figure 7: Reflectance functions

influences in the radiometry. The importance of topographic effects on the radiometric behaviour of the remotely sensed imagery increases for at least two reasons: the higher spatial resolution in the latest generation of satellite sensors, and the extension of remote sensing applications to rough mountainous areas. The higher spatial resolution of aerial imagery makes the analysis more sensitive to local terrain roughness. Interpretation of mountainous regions, faces one with difficulties during classification due to shadow areas and diffuse and indirect secondary lighting. The existing methods for the alleviation of topographical effects are based on models for light scattering that are local, implying that the model does not take into account the spatial resolution of the sensor, and the DEM resolution.

The previously deduced results in the virtual radiometric experiments have been used as a basis for a physical model for multisensor image and data fusion. Digital Elevation Models of adequate resolution are available. This makes attractive the idea of geometrically modelling of the satellite images. Modelling refers to the geometry, to the radiometry of the imaged scene, and the simulation of the image formation process, the sensor and illumination models [46].



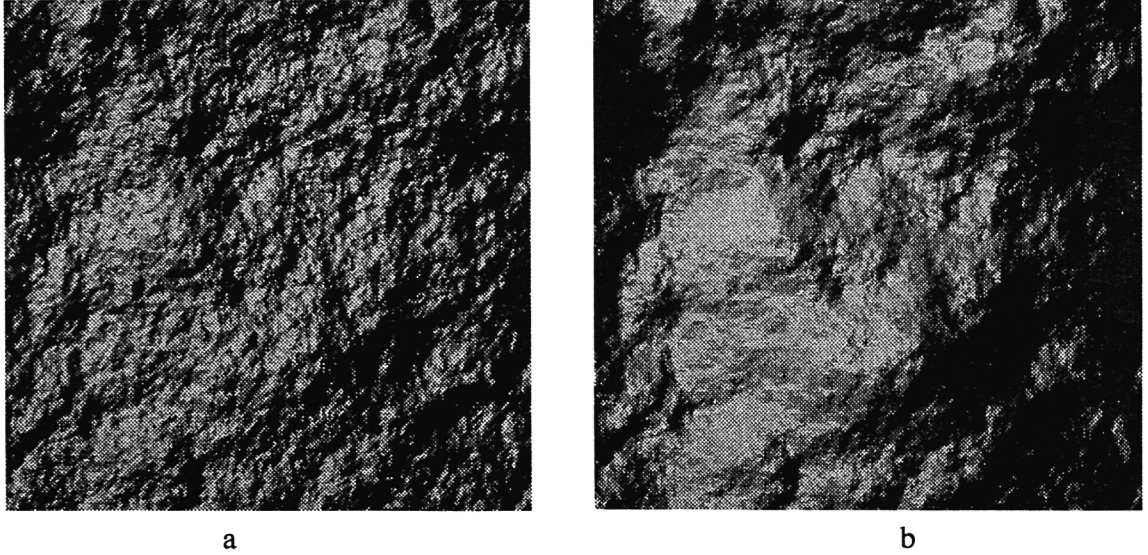


Figure 8: Fractal surface visualization: (a) Lambertian BRF (b) BRF embedding multiscale information

To alleviate the influences of the topography in a satellite image of a rough mountain area, synthetic images have been generated. For this experiment a Landsat-TM scene, band 4 (figure 9), was used. The spatial resolution of the sensor is approximately 30m. The data and knowledge fused in the synthetic image are: the geometry of the terrain, the sensor model, the sun position and an illumination model, and the multi-resolution assumption in image formation. The geometry is described by a Digital Elevation Model known on a 10m. rectangular grid. The sensor was modelled by a convolution operator. The sun elevation and azimuth at the date and time of image acquisition are used. The illumination model is defined for directly lit and shaded areas. Parallel illumination, illumination by interreflections, and diffuse light are considered. At the micro-scale, 10m. resolution, the surface is assumed to be described by diffuse, specular reflections and interreflections. At the meso-scale, 30m. resolution, the sensor model was used to deduce the pixel intensity. In figure 9 are shown: (a) the perspective view of the DEM, (b) the synthetic image modelling the

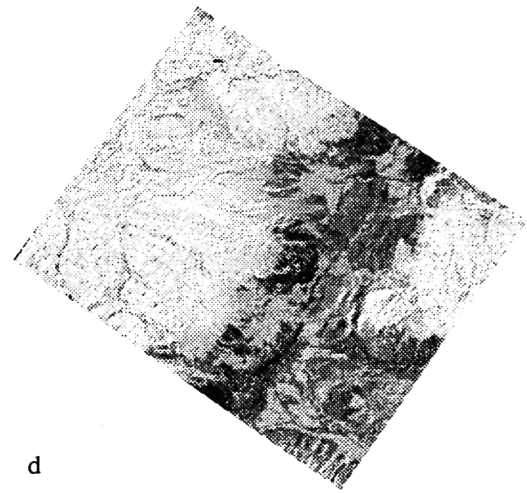
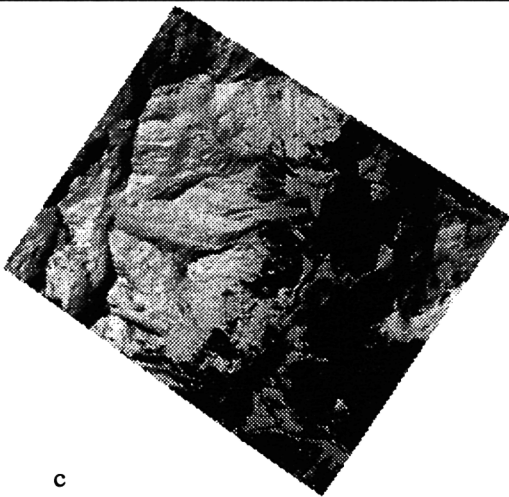
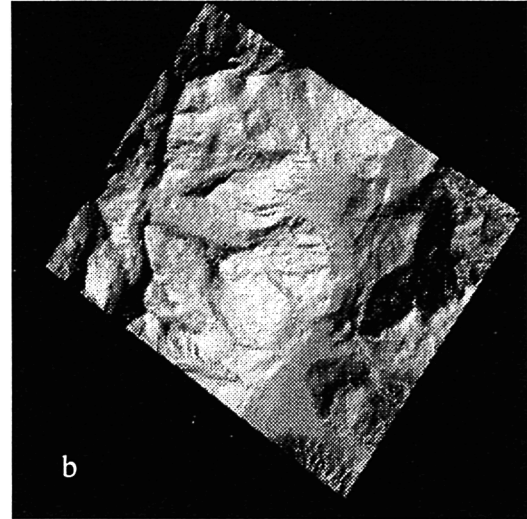
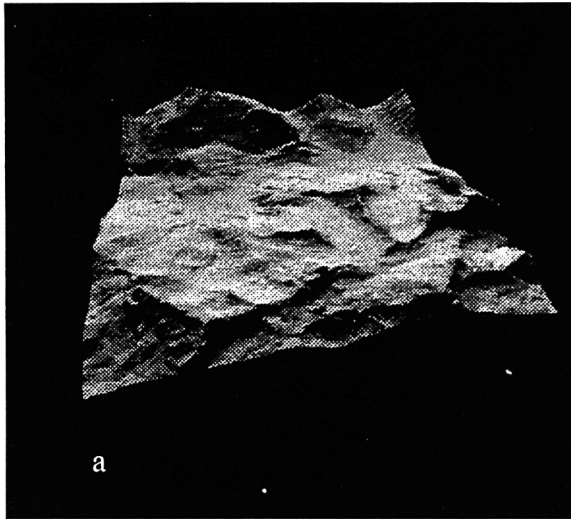


Figure 9: (a) DEM, perspective view, (b) synthetic image (c) Landsat TM image (d) radiometric correction of topography influences

snow cover, this image can be interpreted as a visualization of the fused data, (c) the Landsat-TM band 4 scene, and (d) the segmentation of the snow cover in the previous image. The radiometry of the synthetic image models rough surfaces covered by snow. Due to the more complete model specification, the accuracy obtained in snow cover segmentation is superior to other methods [47]. The presented algorithm describes the image formation process for directly lit and shadow areas, using the multi-resolution approach.

## 5.4 Applications in Synthetic Aperture Radar image processing

The rough structure of many natural surfaces is reflected in a corresponding roughness of the pixel intensity of the imaged scene. The image is textured. If the surface is a fractal one, its image (the set of pixel intensities) will be also a fractal having the same dimension [18]. The idea is to use fractal geometry, the fractal dimension, as a feature to characterize the textures. A fractal transform is defined: an image is mapped into another image that has as pixel intensity the values of the fractal dimension derived for a moving window overlapped on the original picture. It is necessary to state here several observations: one can derive a large class of very different objects having the same fractal dimension, real structures have fractal behaviour for several ranges of scale, and it could be possible that the similarity is respected only for a very low number of scales, the natural scenes when imaged are very often corrupted by strong noise, the sampling and quantification process destroy the scale invariant patterns. Several algorithms have been derived to enhance the discriminatory power of the fractal transform: multiple resolution techniques [48], lacunarity [49], local fractal dimension [10], dendritic analysis [50].

The rough aspect of the Synthetic Aperture Radar (SAR) images rises difficult problems in scene segmentation. The presence of the speckle phenomenon affects the performance of the algorithms for texture classification. In the mean time the filters applied to reduce the speckle noise change the texture features. The fractal dimension seems to be a promising global parameter for the classification of SAR images [51, 52, 53]. In figure 10, a SAR (ERS-1) image and its fractal transform are presented. The fractal transform was locally evaluated using the  $P(m,L)$  definition of the dimension. The urban area is segmented. Taking into account the previous observations referring to the difficulties to interpret the values of the various dimensions, the fractal transform is generally used as a feature in connection with other

parameters. Better results on the application of the fractal transform are reported in the segmentation of images obtained from optical sensors and in the classification of the terrain roughness and geological features [55,56,57].

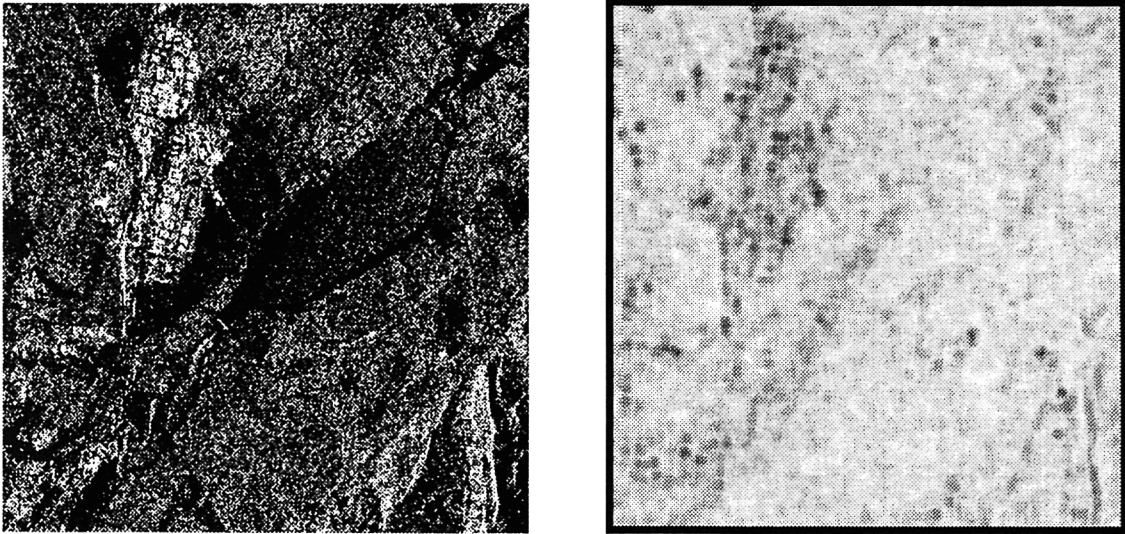


Figure 10: Fractal transform: urban area segmentation in SAR scene

The fractal random process models have been used in synthesis [58], analysis and segmentation of clutter in high resolution polarimetric synthetic aperture radar (SAR). The fractal dimension of a preprocessed SAR image was evaluated using the power spectrum scaling algorithm. The clusters have been separated by a Maximum Likelihood classifier based on a Gaussian assumption applied to the fractal transformed image [59].

## 5.5 Miscellaneous

The algorithms derived in the previously presented results exploit the property that the coefficients of a suitable wavelet transform can be modelled as sets of mutually independent random variables having a specific geometric scale to scale variance progression. The algorithms implemented in this as-



sumption are performance and compositionally efficient. Results have been obtained in implementing a whitening filter for  $1/f$  processes, Bayes detection, Maximum Likelihood parameter estimation, and smoothing of  $1/f$  processes corrupted by Gaussian stationary noise [60]. A fractal deconvolution method was implemented for the analysis of aeromagnetic data. An iterative deconvolution procedure are used to recover the fractal innovation from data [61].

Particular topics in signal and image processing are the interpretation of undersampled periodicities, sampling with unevenly spaced intervals and noisy sparse data. Such data sets are difficult to process using conventional methods. Fractal algorithms derived from the theory of dynamic systems and chaos provide an alternative to classical techniques [62]. Several of the experimental algorithms are: analysis of Poincaré sections, analysis of multi-dimensional phase space object using the Radius of Gyration Exponent (ROGE), the Artificial Insymetration Patterns (AIP), the Lyapunov Spectra, the R/S analysis and the Maximum Entropy method. These methods do not require any physical background of the analysed data set, but if such a foundation of the signal generator process exists, this is a strong premise to guarantee the robustness of the analysis. These techniques could be classified as ‘model based’. Fractal signal coding is a field that gives promising results and could be a basis for a further perspective development for the representation of geo-information. The premises are in the fractal similarity of natural scenes and in the necessity to store or transmit huge volumes of data generated in geosciences.

Fractal signal coding aims at the identification of a fractal or a set of fractals that are a best fit for a given signal and are represented in fewer bits than the original data. The fractal coding can be a feature extraction method but the main goal is data compression [63]. The mathematical basis for the fractal signal compression is in the theory of Iterated Function Systems (IFS) and the Collage Theorem. The principle of the algorithms lies in the field of block coding and vector quantization. The implementations, due to their high computational complexity demand fast searching algorithms and recently the use of Genetic Algorithms (GA) has been considered.

## 6 Conclusions

The field of fractals developed as an interdisciplinary area between branches of mathematics and physics and found applications in different sciences and engineering fields. In geo-information interpretation the applications devel-

oped range from simple verifications of the fractal behavior of natural land structures, to simulations of artificial landscapes and classification based on the evaluation of the fractal dimension, to advanced remotely sensed image analysis, and scene understanding and to accurate geometric and radiometric modelling of land and land cover structures. The multi-resolution signal analysis and synthesis, mainly based on the theory of wavelets has created a new perspective in the understanding of the stochastic fractals. The advances in modelling non-stationary and self-similar  $1/f$  processes has opened a new direction in signal processing. The hierarchical representation of stochastic processes come as an algorithmic support creating a bridge connecting the statistic and deterministic approaches in analysis and synthesis. The models provide efficient scale recursive techniques for statistical signal processing allowing a trade-off between accuracy and complexity.

Referring to the computational effort, fractal analysis generally asks high complexity algorithms. Both wavelets and hierarchical representation now allow implementation of 'fast' algorithms or 'parallel' ones. As a consequence new operational applications can be expected. Another application direction is developing from the multi-resolution approach applied to accurate image synthesis. The physical model based method can be used for the simulation of unknown data. Prior parametric radiation scattering models and fractal geometric assumptions are encapsulated in the model at a sub-pixel scale. The results obtained for the modelling of vegetation and snow cover are promising and the research is directed towards model refinements and algorithmic improvements. The topic is in the frame of data fusion applied for remotely sensed image understanding. The archiving and transmission of remotely sensed images demand high performance compression algorithms. Data compression can benefit from the theory of fractals through signal and image representation using IFS.

Two topics in data fusion have been presented, the utilization of fractal geometry for the simulation of incomplete data, and the data and knowledge fusion in synthetic images. The method introduced is an extension of the physical model inference in data fusion. The scene identification is accomplished by a second level of fusion of real and synthetic images. The multi-resolution approach in image synthesis is used to accurately represent and visualize surfaces with fractal nature. The similarity of fractal and real worlds is used as a basis for incomplete knowledge modelling, and the results are applied for remotely sensed image processing. Better results have been obtained in the alleviation of the radiometric effects induced by the topography in the imagery of rough terrain regions.

## 7 References

- [1] H.-O. Peitgen, H. Jurgens, D. Saupe, Chaos and fractals: new frontiers of science, Springer-Verlag, 1992.
- [2] D. L. Turcotte, Fractals and chaos in geology and geophysics, Cambridge University Press, 1992.
- [3] N. Dodd, Multispectral texture synthesis using fractal concepts, IEEE Tr. PAMI, Vol. 9, No. 5, 1987.
- [4] B. B. Mandelbrot, The fractal geometry of nature, W. H Freeman, New York, 1982.
- [5] M. Hata, Topological aspects of self-similar sets and singular functions, in: Fractal Geometry and Analysis, NATO ASI Series, Vol. 346, Kluwer Academic Publishers, 1991.
- [6] S. Baldo. Introduction a la topologie des ensembles fractals, Ecole polytechnique de Montreal. 1990.
- [7] J. Belair. S. Dubuc (Editors), Fractal Geometry and Analysis, NATO ASI Series, Vol. 346, Kluwer Academic Publishers, 1991.
- [8] K. Falconer, Fractal Geometry, Mathematical Foundations and Applications. Wiley and Sons, 1992.
- [9] R.F. Voss, Random fractals: Characterisation and measurements, in: Scaling Phenomena in Disordered Systems, (Ed.: P. Pynn, A. Skjeltrep) Plenum 1986.
- [10] U. Mussigmann, Texture analysis using fractal dimension, in: J. L. Encarnacao, H.-O. Peitgen, G. Saks, G. Englert, Fractal Geometry and Computer Graphics, Springer-Verlag, 1992.
- [11] G. A. Edgar, Measure, topology, and fractal geometry, Springer, 1990
- [12] R. F. Voss, Random fractals forgeries, in: Fundamental algorithm in computer graphics (Ed.: R.A. Earnshaw), Springer-Verlag, 1985.
- [13] G. C. Freeland, T. S. Durrani, On the use of the wavelet transform in fractal image modelling, IEE Colloquium on: The Application of Fractal Techniques in Image Processing Dec. 1990.
- [14] S. G. Mallat, A Theory for Multiresolution Signal Decomposition: The wavelet Representation, IEEE Tr. on PAMI, Vol. 11, No. 7, July 1989.
- [15] G. W. Wornell, A Karhunen-Loeve-like Expansion of  $1/f$  Processes via Wavelets, IEEE Tr. on Inf. Theory, Vol. 36, No. 4, July 1990.
- [16] R. F. Voss, Fractals in Nature: from characterisation to simulation, in The Science of Fractals Images (Ed.: H. Peitgen, D. Saupe) Springer-Verlag, 1988.
- [17] J. Feder, Fractals, Plenum, 1988
- [18] A. P. Pentland, Fractal-Based Description of Natural Scenes, IEEE Tr.

PAMI, Vol.6, No.6, Nov. 1984.

- [19] B. B. Mandelbrot, *Les objets fractals*, Flammarion, 1989.
- [20] P. Prusienkiewicz, J. Hanan, *Lindenmayer Systems, Fractals, and Plants*, Springer-Verlag, 1989.
- [21] A. Lindenmayer, Mathematical model for cellular interaction in development, *Journal of Theoretical Biology*, No.18, 1968.
- [22] H. F. Smith, A garden of fractals, in: H.-O. Peitgen, J. M. Henriques, L. F. Penedo (Editors), *Fractals in the Fundamental and Applied Sciences*, North-Holland, 1991.
- [23] F. P. Preparata, R. T. Yeh, *Introduction to Discrete Structures*, Addison-Wesley, 1973.
- [24] A. R. Smith, Plants, fractals, and formal languages. *Computer Graphics*, 18(3), 1984.
- [25] G. W. Wornell, Wavelet-Based representations of the  $1/f$  Family of fractal Processes, *Proc. of IEEE*, Vol. 81, No.10, Oct. 1993.
- [26] G. A. Mastin, P. A. Watterberg, J. F. Mareda, Fourier Synthesis of Ocean Scenes, *IEEE CG and A*, March 1987.
- [27] M. R. Luetttgen, W. C. Karl, A. S. Willsky, R. T. Tenney, Multiscale Representation of Markov random Fields, *IEEE Tr. on Signal Processing*, Vol. 41, No. 12, Dec. 1993.
- [28] B. Claus, Multiscale Statistical signal Processing: Identification of a Multiscale AR Process from a Sample of an Ordinary Signal. *IEEE Tr. on Signal Processing*, Vol. 41, No. 12, Dec. 1993.
- [29] P. Flandrin, On the Spectrum of Fractional Brownian Motion. *IEEE [Tr. on Information Theory]*, Vol. 35, No. 1, January 1989.
- [30] P. Flandrin, Wavelet Analysis and Synthesis of Fractal Brownian Motion, *IEEE Tr. on Information Theory*, Vol. 38, No. 2, March 1992.
- [31] G. Strang, Wavelets and Dilatation Equations: A Brief Introduction. MIT Numerical Analysis Report 89-9, August 1989.
- [32] K. Clarke, Scale-Based Simulation of Topographic Relief. *The American Cartographer*, Vol.15, No.5, April 1988.
- [33] M. Goodchild, The fractional Brownian process as a terrain simulation model, *Modelling and Simulation Conference*, Pittsburgh, Pa. 1982
- [34] M. Datcu, B. Dugnol, A. Lana, Relief erosion - animation. Dept of Mathematics, University of Oviedo, Spain, 1991.
- [35] N. Yokoya, K. Yamamoto, N. Funakubo, Fractal-Based Analysis and Interpolation of 3D, Natural Surface Shapes and Their Application to Terrain Modelling, *CVGIP*, 46, 1989.
- [36] H.-O. Peitgen, J. M. Henriques, L. F. Penedo (Editors), *Fractal in the Fundamental and Applied Sciences*, North-Holland, 1991.

- [37] A. P. Pentland, Fractal-Based Description of Natural Scenes, IEEE Tr. PAMI, Vol.6, No.6, Nov. 1984.
- [38] M. Goodchild, Fractals and the Accuracy of Geographical Measures, Mathematical Geology, Vol.12, No.2, 1980.
- [39] L. Polidori, J. Chorowicz, Modelling Terrestrial Relief with Brownian Motion: Application to Digital Elevation Data Evaluation and Resampling, EARSeL Symposium, Graz, 1990.
- [40] K. Seidel, M. Datcu, Model based image analysis for remotely sensed images, Geotechnica'93, Koln, May 5-8, 1993.
- [41] K. Clarke, D. Schweitzer, Measuring the Fractal Dimension of Natural Surfaces Using a Robust Fractal Estimator, Cartography and Geographic Information Systems, Vol.18, No.1, 1991.
- [42] S. H. Westin, J. R. Arvo, K. E. Torrance, Predicting Reflectance Functions from Complex Surfaces, Computer Graphics, Vol. 26, July 1992.
- [43] J. Arvo (Ed.), Graphic Gems II, Academic Press, Inc., 1991
- [44] B. Goel, I. Rosenthal, R. L. Thompson, A Computer Graphic Based Model for Scattering from Objects of Arbitrary Shapes in the Optical Region Int. J. Remote Sensing, Feb. 1990.
- [45] D. L. Jaggard, X. Sun, Scattering from fractally corrugated surfaces, J. Opt. Soc. Am. A, Vol 7, No. 6, 1990.
- [46] M. Datcu, F. Holecz 1993: Generation of synthetic images for the alleviation of radiometric influences induced by the topography, SPIE OE/Aerospace Sensing Orlando, 1993.
- [47] B. I. Naugle, J. D. Lashlee, Alleviating Topographic Influences on Land-Cover Classifications for Mobility and Combat Modeling, Photogrammetric Engineering and Remote Sensing. Vol. 58, No. 8, 1992.
- [48] S. Peleg, Multiple resolution texture analysis and classification, IEEE Tr. PAMI, 6, No. 4, 1985
- [49] J. M. Keller, S. Chen, Texture Description and Segmentation through Fractal Geometry, CVGIP, 45, 1989.
- [50] P. Hanusse, P. Guillaud, Dendronic Analysis of Pictures, Fractals and other Complex Structures, in: J. L. Encarnacao, H.-O. Peitgen, G. Saks G. Englert, Fractal Geometry and Computer Graphics, Springer-Verlag, 1992
- [51] S. Dellepiane, D. D. Giusto, S. B. Serpico, G. Vernazza, SAR image recognition by integration of intensity and textural information, Int. J. Remote Sensing, 1991, Vol.12, No.9.
- [52] N. M. Allinson, M. Lawson, Accurate Texture Characterisation Using Fractal Techniques, IEE Colloquium on: The Application of Fractal Techniques in Image Processing, Dec. 1990.

- [53] A. Schistad, A. K. Jain, Texture analysis in the presence of speckle noise, IGRASS'92
- [54] L. Polidori, J. Chorowicz, R. Guillande, Description of Terrain as a Fractal Surface, and Application to Digital Elevation Model Quality Assessment, Photogrammetric Engineering and Remote Sensing, Vol.57, No.10, Oct.1991.
- [55] J. Huang, D. Turcotte, Fractal image analysis: application to the topography of Oregon and synthetic images, J. Opt. Soc. Am. A, Vol 7, No. 6, 1990.
- [56] G. Ramstein, M. Raffy, Analysis of the structure of radiometric remotely sensed images, Int. Jurnal Remote sensing, Vol. 10, No.6, 1989.
- [57] G. Ramstein, structures spatiales irregulieres dans les images de teledection, Ph.D. These, Univiversite Strasbourg I, 1989.
- [58] M. Datcu, Model for SAR images, SPIE Aerospace Sensing. Orlando Fl. 1992.
- [59] C. V. Stewart, B. Moghaddam, K. J. Hintz, L. M. Novak, Fractal Brownian Motion Models for Synthetic Aperture Radar Imagery Scene Segmentation, Proc. IEEE, vol.81, No.10, Oct.1993.
- [60] C. Jones, P. G. Earwicker, S. Addison, S. Watson, Multiresolution Decomposition of Fractal Images, IEE Colloquium on: The Application of Fractal Techniques in Image Processing Dec. 1990.
- [61] M. E. Gregotski, O. Jensen, Fractal Modeling Techniques for Spatial Data, IEEE Tr. on Geoscience and Remote Sensing, Vol.31, No.5. Sept. 1993.
- [62] J. W. Handley, H. M. Jaenisch, C. A. Bjork, L. T. Richardson, R. T.Carruth, Chaos and Fractal Algorithms Applied to Signal Processing and Analysis, Simulartion, Vol. 60, No.1, 1993.
- [63] A. E. Jacquin, fractal Image Coding: A review, Proc. of IEEE, vol. 81, no.10, Oct. 1993.

# Chapter 4

## Multifractal Analysis of Remotely Sensed Images

*Jacques Lévy-Véhel\**

### 1 Introduction

Images of the earth obtained through SPOT or SAR sensors often exhibit irregularities at all scales, due to the presence of both texture information and different kinds of correlated noise. It is known that, in such contexts, fractal analysis may provide interesting insight into the fine structure of the studied phenomena. More precisely, multifractal tools can be successfully used to process the complex repartitions of the measures given by remote sensors. Several problems may be (partially) solved:

- image restoration: noise removal algorithms can be designed based on the fact that certain types of noise have well defined multifractal spectra
- edge based image segmentation: the local Hölder exponents associated with certain types of measures react very differently when computed on edges and on smooth or slightly textured zones
- textured based image segmentation: when strongly textured regions are present in the image, a more robust approach is to compute global multifractal parameters based on a partition function

We thus have available several tools which, when used in conjunction, allow a semi-automatic processing of images, and make it possible to detect various features such as edges, homogeneous textured regions, or to perform

---

\*INRIA, Rocquencourt, France

global tasks such as the detection of certain kinds of changes in an image. We present here mostly the method for singularity detection, and show some results using edge based or texture based segmentation.

## 2 Classical approach to image segmentation

We restrict ourselves here to the problem of image segmentation: segmentation means that we want to extract from the image a compact description in terms of edges and/or regions. Thus, we do not tackle the problem of higher level interpretations such as recognition for instance.

Essentially, image segmentation consists in finding all the characteristic entities of an image: these entities are either described by their contours (edge detection) or by the region where they lie (region extraction). These two approaches are dual, but their algorithms are very different, and, unfortunately, most of the times lead to different segmentation results.

### 2.1 Edge detection

It is by far the most widely used approach. The crux of most classical methods is the assumption that edges usually corresponds to local extrema of the gradient of the grey levels in the image. In this setting, one then has to tackle the problem of computing some kind of ‘derivative’ of a noisy discrete signal.

Let  $I(x, y)$  be the image (noisy) signal. An edge is defined by its type: a step edge is a 0<sup>th</sup>-order discontinuity of  $I$ , a roof-edge is a 1<sup>st</sup>-order discontinuity of  $I$ , ... Let  $G(I)$  be the gradient of  $I$ . The problem reduces to the determination of a filter yielding a good approximation of  $G$ . Under some assumptions on the nature of the noise, it may be shown that the problem is equivalent to that of finding an optimal linear filter  $f$  such that:

$$G = (I * f)' = I * f'$$

In order words, we start by smoothing the discrete image data  $I$  by convolving it with  $f$ , and then compute the gradient by differentiating the smoothed signal. Edge points are then defined to be the local maxima of the gradient’s norm in the gradient’s direction. Using additionnal criteria, one can derive expressions for optimal filters. A frequently used one is:

$$f(x) = -ce^{-\alpha|x|}\sin(wx) \quad \text{or} \quad f(x) = -cxe^{-\alpha|x|} \quad (\text{Canny-Deriche filter})$$



It is also possible to refine the method using a multiresolution scheme: the original image undergoes a series of successive smoothings, and, at each step, some characteristic points (maxima of the transform) are computed. These points are then used in collaboration through a propagation method to describe more robustly and accurately the edges [12].

## 2.2 Region extraction

The idea here is to separate the image into regions that verify a given uniformity criterion. If we are dealing with very simple images, the criterion might just be that all points belonging to a certain region must have the same grey level. However, in general, images include textured zones, and one has to solve the much harder problem of texture discrimination. For more complete discussion, see [15, 11].

## 3 Basics of the multifractal theory

We define here our notations and briefly recall some basic facts about the multifractal theory [1, 2, 3, 4, 13, 14].

Let  $\mu$  be a Borel probability measure on  $[0, 1] \times [0, 1]$ . Let  $\nu_n$  be an increasing sequence of positive integers, and define:

$$I_{i,j,n} = \left[ \frac{i}{\nu_n}, \frac{i+1}{\nu_n} \right] \times \left[ \frac{j}{\nu_n}, \frac{j+1}{\nu_n} \right]$$

We consider the following quantities:

$$\tau_n(q) = \frac{1}{\log \nu_n} \log \sum_i^* \sum_j^* \mu(I_{i,j,n})^q$$

where  $\sum^*$  means that the summation runs through those indices  $(i, j)$  such that  $\mu(I_{i,j,n}) \neq 0$ . When the limit exists, we set:

$$\lim_{n \rightarrow \infty} \tau_n(q) = \tau(q)$$

We then define  $f_l(\alpha)$  as the following Legendre transform of  $\tau(q)$  :

$$f_l(\alpha) = \inf_{q \in \mathbb{R}} (\alpha q - \tau(q))$$

On the other hand, we consider the sets:

$$E_\alpha = \left\{ (x, y) \in [0, 1] \times [0, 1] / \lim_{n \rightarrow \infty} \frac{\log \mu(I_n(x, y))}{\log \nu_n} = \alpha \right\}$$

with

$$I_n(x, y) = \{I_{i,j,n} / (x, y) \in I_{i,j,n}\}$$

$\alpha$  is the local Hölder exponent at point  $(x, y)$ , and we define  $f_h(\alpha)$  as the Hausdorff dimension of  $E_\alpha$ .

Finally, we consider the following double limit:

$$f_g(\alpha) = \lim_{\varepsilon \rightarrow 0} \lim_{n \rightarrow \infty} \frac{\log N_n^\varepsilon(\alpha)}{\log \nu_n}$$

where:

$$N_n^\varepsilon(\alpha) = \text{card}\{I_{i,j,n} / \alpha_n(I_{i,j,n}) \in [\alpha - \varepsilon, \alpha + \varepsilon]\}$$

and  $\alpha_n$  is the coarse grained Hölder exponent of  $\mu$  at  $I_{i,j,n}$ :

$$\alpha_n(I_{i,j,n}) = \frac{\log \mu(I_{i,j,n})}{\log \nu_n}$$

A central concern of the multifractal theory is to compare the three descriptions of the singularities of the measure, namely the ‘spectra’  $(\alpha, f_l(\alpha))$ ,  $(\alpha, f_g(\alpha))$  and  $(\alpha, f_h(\alpha))$ . This has important applications. Indeed,  $\tau(q)$ , and thus  $f_l(\alpha)$ , is usually much easier to compute on experimental data than the other spectra:  $\tau(q)$  is obtained by averaging over many ‘boxes’ and then taking the limit.  $f_g(\alpha)$  is more difficult to evaluate, both theoretically and practically, especially on real noisy data, since pointwise computations are necessary. As for  $f_h(\alpha)$ , it is even much more complex, since the computation of a Hausdorff dimension is typically very involved.

Under very general assumptions, it has been proven that [1]:

$$f_h(\alpha) \leq f_l(\alpha)$$

It is also possible to prove that in general [8]:

$$f_g(\alpha) \leq f_l(\alpha)$$

For certain special classes of measures, including multinomial measures, we have an equality:

$$f_n(\alpha) = f_g(\alpha) = f_l(\alpha)$$

when all quantities are the same, we simply denote them  $f(\alpha)$ .

In the case of multinomial measures,  $f(\alpha)$  is a bell-shaped curve. This shape is also observed for a number of natural phenomena. However, this is in no way a general property, as one can prove that any ruled function can be the spectrum of a multifractal function (see [5]), or capacity (see [8]).

Other ‘special’ features of  $f$  may appear depending on the construction of the measure, as for instance negative values (see [13]). In general, it is easy to construct a measure for which  $f_l(\alpha)$  is strictly greater than  $f_g(\alpha)$  and  $f_h(\alpha)$ . We shall call the assumption that  $f_g = f_h = f_l$  the ‘strong assumption’, and the assumption that  $f_g = f_h$  the ‘weak assumption’.

## 4 Application to image analysis

### 4.1 Definition of the measures

Though fractal geometry was introduced a long time ago in image analysis, it is not yet used extensively [16, 10].

Some authors have used the fractal dimension to perform texture classification and image segmentation, others have used higher order dimensions or measures, such as correlation or lacunarity [6, 9], to refine the results and have obtained some interesting results. Very few papers have been devoted to the use of multifractals in image analysis [11], although we believe that approaches based on the computation of the fractal dimension are largely unfounded. This approach assumes that the 2D grey level image can be seen as a 3D surface, or, equivalently, that the grey levels can be assimilated to a spatial coordinate on the  $z$ -axis. This assumption has no theoretical basis, since the scaling properties of the grey levels are generally different from those of the space coordinates. Instead, we should look at the grey levels as a measure, laid upon a generally compact set, totally inhomogeneous to space coordinates. This leads to a multifractal analysis.

A natural choice is to define the measure  $\mu$  as the sum of intensities of pixels in the measured region. This measure will be useful, but it will not be sufficient for a fine description of the image. One possibility is then to define other types of functions of the grey levels, and to apply the multifractal analysis to them. Since the notion of resolution is of great importance in image analysis, we find it more appropriate to work with set functions than with point functions. However, it occurs that those functions that are relevant in our field are not in general measures, but rather capacities. Lack of space prevents us from presenting the extension of the multifractal analysis to capacities, thus we refer the interested reader to [8] and just define the capacities that we will need.

We introduce ‘*max*’, ‘*min*’ and ‘*iso*’ capacities of a region  $\Omega$ . If  $\Omega^*$  is the subset of  $\Omega$  where intensity is non-zero, and  $p(i)$  is the intensity of the point  $i$ , we define:

$$\mu_{max}(\Omega) = \max_{i \in \Omega} p(i) \text{ and } \mu_{min}(\Omega) = \min_{i \in \Omega} p(i) \quad (1)$$

If  $G(\Omega)$  is the geometrical centre of  $\Omega$ , we define:

$$\mu_{iso}(\Omega) = \text{Card}\{i \in \Omega / p(i) = p(G(\Omega))\} \quad (2)$$

The exponents computed with those capacities give different information on the singularities encountered:  $\alpha_{max}$  and  $\alpha_{min}$  only depends on the height of the singularity,  $\alpha_{iso}$  only depends on the kind of singularity, and  $\alpha_{sum}$  depends on both height and kind of the singularity.

## 4.2 Edge detection using multifractal characterizations

### 4.2.1 Introduction

The approach here is, in some sense, inverse to the classical one explained in section 2: instead of smoothing the discrete data in order to be able to compute some derivatives, we stay with our initial discrete values and quantify the singularity around each point; we then characterize an edge point as a point having a given value of singularity.

This procedure is based on the idea that, in some cases, it might be impossible to recover an underlying continuous process from the discrete data (if such a process exists ...). Thus it seems more natural to directly model the sampled signal. The advantage is that we do not lose or introduce any information by smoothing. The drawback is that we may well be much more sensitive to noise. This is why we have to define several capacities. Using jointly the local information provided by  $\alpha$  and the global one contained in  $f(\alpha)$ , we are able to construct an operator on the image whose main features are the following ones: it is idempotent (it detects its own result), it reacts differently to different types of singularities (provided that the noise is not too important), and no tuning parameters are needed, as soon as the type and the amplitude of the noise are known. As a drawback, since a more complex analysis of the image is made, the computations are not as fast as with gradient-based edge detectors. A few minutes are needed to analyse a  $512 \times 512$  image.

### 4.2.2 Computation of the singularity exponents

We study the behaviour of the singularity exponents for *sum*, *max*, *min* and *iso* capacities on simplified models of step-edge, corner, line and plane.

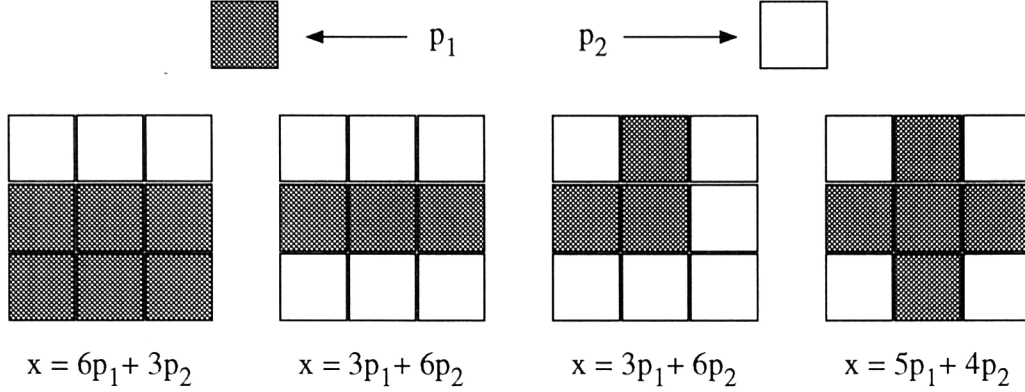


Figure 1: Step-edge, line, corner line, and corner models. Note that the line and the corner line model give the same capacity so they will not be distinguished further

Figure 1 describes those singularities. There are only two values for the gray levels:  $p_1$ , the level of the point of interest, and  $p_2$ , the level of the background. We will denote  $V(i)$  the  $i \times i$  squared neighbourhood centred on the pixel of interest, and  $V^*(i)$  as  $V(i)$  minus the pixel of interest.

We stress a very important point here: it is obvious that the objects we consider are far from being ‘fractals’, or even ‘multifractals’. However, our approach does **not** at any point make such an assumption. All we do is suppose that the defined capacity does have a Hölder exponent at each point (a rather weak assumption). This makes it possible to compute a multifractal spectrum, whether the capacity is multifractal or not. Of course, strictly speaking, the spectra corresponding to all of our models reduce to the point (2,2), thus we do not have multifractal behaviour. The fundamental idea here is that we are not interested in getting the ‘real’ spectrum, but rather to verify that, if we use a certain procedure of estimation, the ‘spectrum’ associated with a typical image will allow a description of the local singularities. In other terms, we are not interested in absolute quantities (the ‘true’ spectrum), but rather in evidencing differences between estimated spectrum associated with different sets of images.

$\alpha$  is computed as the estimation of the slope of  $\log \mu(V(i))$  versus  $\log i$ , with  $i = 2n + 1$ ,  $n = 0 \dots$ . The maximal size of neighbourhoods is related to localization of computation. If we use little neighbourhoods, for instance

$i \leq 3$ ,  $\alpha$  will react to localized singularities, if we use larger neighbourhoods,  $\alpha$  will react to more widespread singularities. If we consider a computing neighbourhood  $V(3)$ , it is possible to derive explicitly the probability law of  $\alpha$  in some cases, for instance when the noise is additive gaussian or uniform. The calculations are simple but rather tedious, and the formulas are quite long, thus we only give here one for information:

**Law of  $\alpha$  (sum measure), for a gaussian additive noise of variance  $\sigma$ :** the singularity is characterised by  $n$  ( $n$  equals 9 for a smooth region, 6 for a step, 4 for a corner, 3 for a line), and  $s_1 = \frac{p_1}{\sigma}$  et  $s_2 = \frac{p_2}{\sigma}$ :

$$\left\{ \begin{array}{l} f_1(\alpha) = \frac{1}{9}(3^{2\alpha} - 2 \cdot 3^\alpha + 9) \\ S(n) = n s_1 + (9 - n s_2) \\ f_2(\alpha) = -\frac{2}{9}S(n)3^\alpha + \frac{2}{9}(S(n) + 3^\alpha s_1) - 2s_1 \\ f_\alpha(\alpha) = \frac{6\sqrt{2}\log 3 \cdot 3^\alpha}{\pi f_1(\alpha)} \exp\left(-\frac{1}{16}S^2 - \frac{9}{16}s_1^2 + \frac{1}{8}S(n)s_1\right) \times \\ \quad \left(-\frac{8}{9} - \frac{\sqrt{\pi}f_2(\alpha)}{3\sqrt{f_1(\alpha)}} \exp\left(\frac{9f_2(\alpha)^2}{64f_1(\alpha)}\right) \operatorname{erf}\left(\frac{3f_2(\alpha)}{8\sqrt{f_1(\alpha)}}\right)\right) \end{array} \right.$$

Observation of plots of different laws show that there is nearly no chance of confusion between the different types of singularity when the amount of noise is not too large, and that the *max* and *min* capacities are more robust to uniform noise.

### 4.2.3 Results

Edges detected by Canny-Deriche filtering can be irregular, and edges detected by the multifractal exponent are far less sensitive to noise. In figure 2, we can see the detection of a line blurred with uniform noise. The line is detected with a fair accuracy by the multifractal exponent, and not at all by Canny's filter: we should here have used a specific filter for lines. However, the same multifractal exponent is able to detect both step-edge and line.

Figure 3 shows a comparison on a natural scene. It can be seen that the multifractal exponent is able to detect small details accurately. The most remarkable aspect is the accuracy of the detection of the corners of the

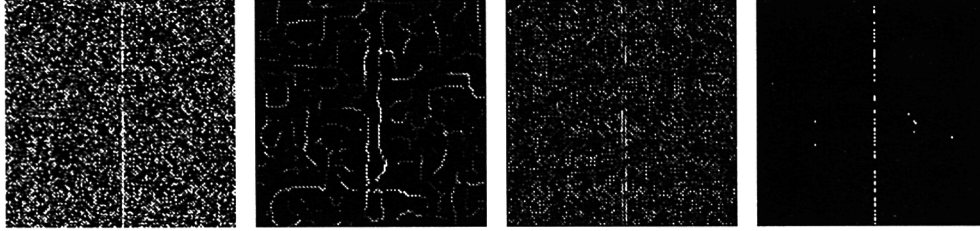


Figure 2: Comparison of Canny edge detection approach and multifractal exponent approach. From left to right: blurred line; Canny edge result with large bandwidth; Canny edge result with small bandwidth; edge detected with *iso* capacity 9 grey levels on  $V(3)$

door and of the limits of the bush, when Canny's edge method only gives good results in the presence of a step. Finally, figure 4 shows the result of using the multifractal method on a SPOT image of a region of France. The remarkable feature here is that all lines are detected even when the contrast is very low (see for instance the part of the river passing through the town).

#### 4.2.4 Use of $f(\alpha)$

In the images presented so far, the use of  $\alpha$  computed with well chosen capacities has proven to be sufficient. However, this will not always be the case. In this section, we indicate how the use of  $f(\alpha)$  can help us refine our image description. Let us consider figure 5.

On the left, anyone would see three edges, that are easily detected by any edge detector. On the right, we have done nothing else than triple the number of lines in the image. Of course, it is still possible to interpret this image as being composed of nine edges, but most people would prefer to talk of a binary texture. However our local computation of exponent  $\alpha$  would be the same in both situations.

Here appears another characteristic feature of an edge: an edge does not only correspond to a certain type of singularity in the images, or to an extremum of the gradient (local characterization), but also to a 'rare' event, in some sense that has to be defined. In other words, if too many 'edges' are detected in a portion of an image, then the human visual system will have a

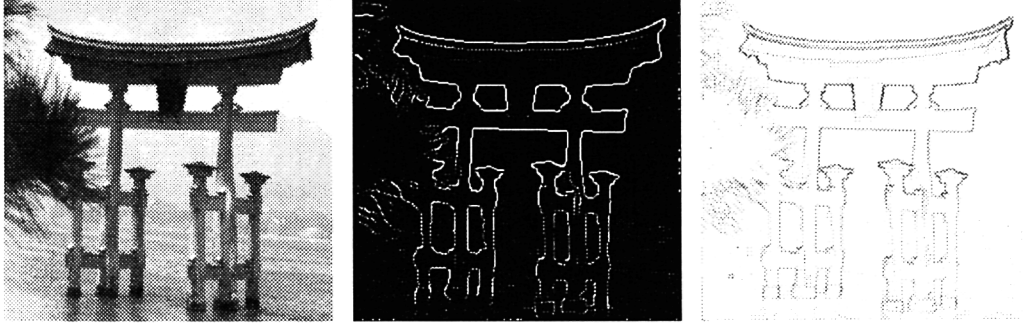


Figure 3: Comparison of Canny edge detection approach and multifractal approach on natural scene. From left to right: original image; Canny edge detection result; multifractal exponent computed with *min* capacity on  $V(3)$

tendency to talk of a textured zone, rather than of a concentration of edges. This is where we can use the  $f_g(\alpha)$  characterization. Remember that  $f_g(\alpha)$  measures, loosely speaking, how rare or frequent an event of singularity  $\alpha$  is.

Now if we assume that  $f_g(\alpha)$  and  $f_h(\alpha)$  are equal (weak assumption), we may assess how ‘rare’ a smooth edge is, because a smooth edge point will belong to a set  $E_\alpha$  whose dimension is one. We simply use here the connection between geometry and probability provided by the assumption made on the two spectra. The general line of reasoning is the following one: from a geometrical point of view, a point with prescribed singularity belongs to a set of given  $f_h(\alpha)$ . If the weak assumption holds, then  $f_g(\alpha)$  is also given, and we know the probability of finding such a point in the image at a given resolution (this means that all the quantities are computed at this resolution).

In this sense, we may precisely say how an edge, for instance, is characterized both by a given singularity value (local condition) and by the fact that it is a rare event (global condition). To illustrate this, we show in figure 6 the points of figure 3 (original image) where  $f(\alpha) \approx 1$  (one can verify that we get most edge points of the original image), and the points belonging to the sets  $E_\alpha$  (there might be several such  $E_\alpha$  sets) such that  $f(\alpha) \approx 2$  (we keep here all the points lying inside regions). These ideas can be used more rigorously in a probabilistic setting. The general frame-





Figure 4: Left: initial SPOT image, right: edge detection result using *max* capacity [original satellite data copyright SPOT Image / CNES]

work is that of Bayesian optimisation. We restate the problem as follows: at a given point  $(x, y)$  in the image, we look for the most probable couple  $(t, \lambda)$ , where  $t$  is the type of singularity and  $\lambda$  the relative height of singularity at  $(x, y)$ . Let us denote by  $A$  the vector of computed local Hölder exponents at point  $(x, y)$ , with different measures or capacities. Typically,  $A = (\alpha_{min}, \alpha_{max}, \alpha_{sum}, \alpha_{iso})$ . As is usual in image analysis, we use Bayes rule to write:

$$Pr((t, \lambda)/A) = \frac{Pr(A/(t, \lambda))Pr(t, \lambda)}{Pr(A)}$$

and we look for the couple  $(t, \lambda)$  that maximizes the left hand side of the above equality. This is equivalent to maximizing the product  $Pr(A/(t, \lambda)) \times Pr(t, \lambda)$ , since  $Pr(A)$  is a constant here. Thus we have to evaluate two quantities: the conditional probability of a vector of Hölder exponents given

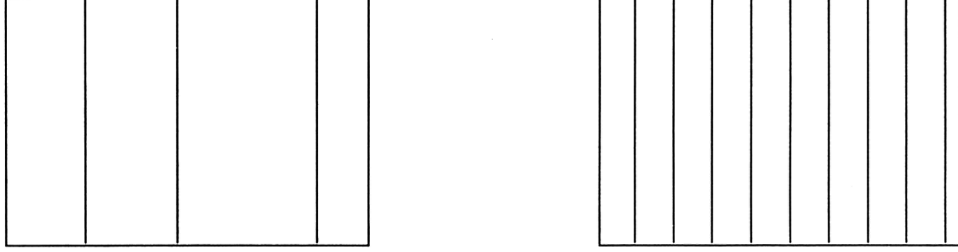


Figure 5: Left: some edges, right: a texture

a singularity, and the prior probability of a given singularity.

#### **Computation of the conditional probability**

This probability is difficult to compute theoretically, and only the cases of uniform noise with  $A = (\alpha_{max}, \alpha_{sum})$  or  $A = (\alpha_{min}, \alpha_{sum})$  have been completed (see [7]). In the general case, one has to perform computer simulations to obtain the conditional laws.

#### **Computation of the prior probability**

Two cases have to be considered: when the point does not lie in a smooth region, it is reasonable to assume that  $t$  and  $\lambda$  are independant. Thus:

$$Pr(t, \lambda) = Pr(t)Pr(\lambda)$$

On the other hand, we know that the *iso* capacity reacts only to the type of the singularity, and that the *max* capacity reacts only to the relative height of the singularity. In our case, we even have an equivalence between  $(t, \lambda)$  and the coarse grained Hölder exponents, which allows us to write:

$$Pr(t \in T) = Pr(\alpha_{iso}^n \in A_i)$$

$$Pr(\lambda \in \Lambda) = Pr(\alpha_{max}^n \in A_m)$$

where we have used a superscript  $n$  to indicate that the coarse grained exponents are computed at resolution  $n$ . The sets  $T, A_i$  and  $\Lambda, A_m$  are related by expressions that can be derived explicitly.

To evaluate  $Pr(t, \lambda)$ , we thus need only to evaluate the two spectra  $f_g(\alpha_{iso})$  and  $f_g(\alpha_{max})$ . This can be done directly on the data, using an approach described in [7].

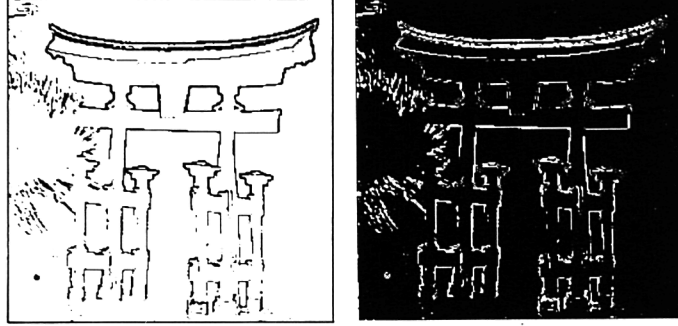


Figure 6: Left: image of points (in white) whose  $f(\alpha) = 1.93$ ; right: image of points (in white) whose  $f(\alpha) = 1.1$

Finally, when  $(x, y)$  lies in a smooth region, another approach using only  $(\alpha_{min}, \alpha_{max})$  has to be used.

Results obtained with this approach are presented on an aerial photograph (figure 7). A blurring with Gaussian noise of variance 0.1 has first been preformed, then the method explained above has been applied at three successive resolutions. Finally, a propagation algorithm has been used.

Using the same line of reasoning, it is also possible to perform texture segmentation. We only show here a result on a SPOT image of the region of Montpellier, France (figure 8), where the aim was to recognize four types of textured zones: sea, fields, dense towns and semi-urban area. Even though the results are far from being perfect, we see that the method was able to localize most of the regions.

Finally, we mention that, using more complex capacities, comparable results have been obtained on SAR images.

## 5 Conclusion

In this work, we have demonstrated that the use of a multifractal characterization of image points can help to solve the problem of segmentation. Our experiments show that, in several cases, this approach gives at least as good results as the classical ones. Much more work is needed in this direction, but these preliminary results show that the  $(\alpha, f(\alpha))$  approach might be able to build a bridge between the two so far unconnected methods of edge detection and region extraction.

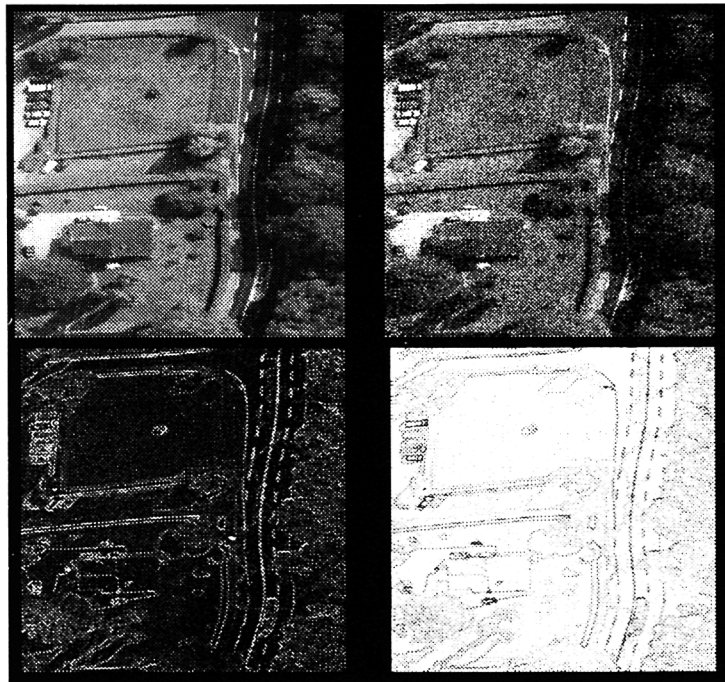


Figure 7: Top left: original image; top right: blurred image; bottom left: all non-smooth points; bottom right: smooth points



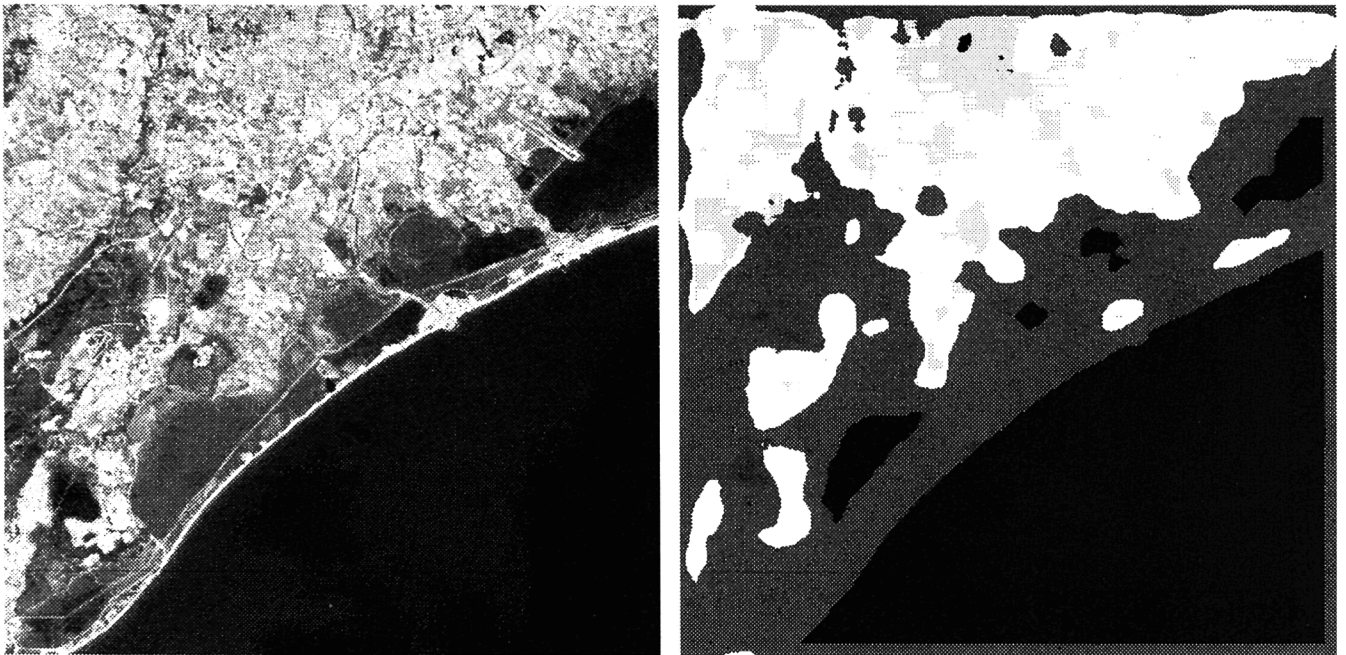


Figure 8: Left: original SPOT image (Montpellier region); right: texture based segmentation [original satellite data copyright SPOT Image / CNES]

## References

- [1] G. Brown, G. Michon, and J. Peyrière. On the multifractal analysis of measures.
- [2] U. Frisch and G. Parisi. Turbulence and predictability in geophysical fluid dynamics and climate dynamics, page 84. M. Ghil, R. Benzi and G. Parisi, Amsterdam (Holland), 1895.
- [3] H. G. E Hentschel and I. Procaccia. The infinite number of generalized dimensions of fractals and strange attractors, *Physica* 8D, 1983.
- [4] I. Procaccia. The characterization of fractal measures as interwoven sets of singularities: global universality at the transition to chaos. Technical report, Department of Chemical Physics, The Weizmann Institute of Science, Rehovot 76100, Israel, 1986.
- [5] S. Jaffard. Construction de fonctions multifractales ayant un spectre de singularités prescrit. *C.R. Acad. Sci. Paris*, pages 19-24, 1992. T. 315, Srie I.
- [6] James M. Keller, Susan Chen, and Richard M. Crownover. Texture description and segmentation through fractal geometry. *CVGIP*, 45:150-166, 1989.
- [7] J. Lévy-Véhel, P. Mignot, and J.-P. Berroir. Multifractal image analysis. Preprint.
- [8] J. Lévy-Véhel, P. Mignot, and R. Vojak. Analyse multifractale de capacités. Preprint.
- [9] J. Lévy-Véhel. About lacunarity, some links between fractal and integral geometry, and an application to texture segmentation. In *ICCV*, 1990.
- [10] J. Lévy-Véhel. Fractal probability functions: an application to image analysis. In *CVPR*, 1991.
- [11] J. Lévy-Véhel, P. Mignot, and J. P. Berroir. Multifractals, texture, and image analysis. In *CVPR*, 1992.
- [12] S. Mallat and W. L. Hwang. Singularity detection and processing with wavelets, *IEEE Trans. on Information Theory*, 38(2), March 1992.

- [13] B. B. Mandelbrot. A class of multinomial multifractal measures with negative (latent) values for the dimension  $f(\alpha)$ . In Fractals (Proceedings of the Erice meeting ). L. Pietronero, New York, 1989.
- [14] B. B. Mandelbrot. Fractal measures (their infinite moment sequences and dimensions) and multiplicative chaos: early works and open problems. Technical report, Physics Department, IBM Research Center/Mathematics Department, Harvard University, Cambridge, MA 02138, USA. 1989.
- [15] O. Monga. An optimal region growing algorithm for image segmentation. International Journal of Pattern Recognition and Artificial Intelligence. 1(3), December 1987. Paris, France.
- [16] S. Peleg, J. Naor, R. Hartley, and D. Avnir. Multiple resolution texture analysis and classification. IEEE, PAMI-6(4), July 1984.

# Chapter 5

## How Bright is the Coast of Brittany?

*Shaun Lovejoy\* and Daniel Schertzer†*

### 1 Introduction

#### 1.1 Fractal sets and multifractal measures

As long ago as 1913, Jean Perrin noted that the usual notions of measurement were perhaps not adequate for answering the seemingly simple question ‘How long is the coast of Brittany?’<sup>1</sup>, and Steinhaus (1954) noted that rivers were ‘not rectifiable’<sup>2</sup>. It wasn’t until many decades later that a clear answer became at all accepted. It now seems obvious that there is ‘something’ fractal about a coastline, hence today, even laymen understand that the length depends fundamentally on the resolution at which it is measured.

If there is no unique (scale independent) length of a coastline, then why should there be a unique fractional cloud cover (forest cover) etc? Indeed, over the last decade, it has been noticed that as the resolution of satellites improves, the estimates of global albedo are consistently declining. Estimates of fractional cloud cover are also known to decline -sometimes

---

\*Physics Department, McGill University, Montréal, Canada

†Laboratoire de Météorologie Dynamique, Université Pierre et Marie Curie, Paris

<sup>1</sup>Mandelbrot, 1967, building on Richardson’s 1961 scaling analyses suggested that a fractal dimension was the appropriate characterization of the scaling

<sup>2</sup>‘...the left bank of the Vistula, when measured with increased precision would furnish lengths ten, hundred and even thousand times as great as the length read off a school map. A statement nearly adequate to reality would be to call most arcs encountered in nature as not rectifiable. This statement is contrary to the belief that not rectifiable arcs are an invention of the mathematicians and that natural arcs are rectifiable: it is the opposite that is true...’ Steinhaus, 1954. To prove his point, Steinhaus 1962 shows a (fractal) Peano curve



precipitously- with improved resolution. Indeed, Gabriel et al. 1988, have shown that the effect is systematic no matter what brightness thresholds are used to estimate the cloud fraction<sup>3</sup>. Similarly, the resolution dependence of the coastline has now been generalized to all topographic level sets (not just sea level); Lovejoy and Schertzer 1990 have shown the same effect on regions exceeding various altitudes on the earth. How is it therefore that the analogous conclusion - now obvious for coastlines - has not been drawn for remotely sensed radiances? A partial answer to this question may be that remote sensing deals with measures and their integrals over various resolutions ('pixel elements'), not with geometric points of sets (such as the borderline between zones above and below sea level). While the framework necessary for dealing with the latter has been around for quite some time (see especially Mandelbrot 1983), the corresponding multifractal framework necessary for dealing with measures and fields, is little over ten years old (1983). In the following, we argue that there is now ample theoretical and empirical evidence for recognizing this resolution dependency as a basic aspect of remote sensing. Its implications must be fully pursued in the development of resolution independent remote sensing algorithms.

This chapter will review a small part of what is a mushrooming field, aiming to give a brief synopsis of different aspects of a large body of work. Several more pedagogical introductions to multifractals are now available, see especially Schertzer and Lovejoy 1994a. In a companion paper (Schertzer and Lovejoy 1994b, hereafter labeled SL94), we concentrate on more recent advances in multifractals and how they can be used in remote sensing.

## 1.2 Clouds

Before considering multifractals and multifractal analyses (which involve an exponent function rather than a unique exponent values), we will give some examples of the scaling of some basic geophysical fields (clouds, wind and Earth's surface) using standard energy spectra ( $E(k)$  for the energy at wavenumber  $k$ ). Scale invariance implies invariance under 'zooms', the simplest of which is the isotropic zoom  $\underline{x} \rightarrow \lambda \underline{x}$  (see section 4 for generalizations), hence  $\underline{k} \rightarrow \lambda^{-1} \underline{k}$ . Invariance will be associated with power laws:

$$E(k) \approx k^{-\beta} \quad (1)$$

---

<sup>3</sup>They even used statistical hypothesis testing to show that resolution independent cloud brightness fractions did not exist for any significant brightness levels

since only power laws retain their form under zooms (in section 4, we shall see that more precisely, they have the required group properties). We shall see that the spectral exponent  $\beta$  is related to a single value of the moment function  $K(q)$  (defined in section 2):  $\beta = 1 - K(2)$  (the value 2 because spectra are second order statistics).

There has long been uncertainty over the exact type and range of scaling in the atmosphere. Since the 1950's the basic model postulated isotropic two dimensional turbulence at large scales, and isotropic three dimensional turbulence at large scales, the two being separated by a hypothetical 'meso-scale' gap or 'dimensional transition' (supposedly at about 10km, the scale height of the mean pressure). The recognition of scale invariance as a basic dynamical symmetry principle ('Generalized Scale Invariance', Schertzer and Lovejoy 1985a,b) in the 1980's made the standard model seem quite ad hoc since it was much simpler to postulate scaling, but without the restriction to isotropy. The resulting 'unified scaling model' (Lovejoy et al. 1993, Chiriginskaya et al. 1994, Lazarev et al. 1994) seems to be very close to the measurements (see fig. 1 for a schematic diagram). Indeed, figs. 2, 3 show some recent aircraft and radiosonde spectra indicating that through the entire atmosphere in the vertical (and right through the meso-scale in the horizontal), that the scaling is well obeyed, although the exponents are quite different in the two directions (defining an 'elliptical dimension'  $\approx 23/9$ , see section 4).

In order to clarify the situation in the horizontal, (specifically to augment the number of samples of large structures so as to obtain good statistics) satellite radiances are analyzed in fig. 4 with no evidence of a break in the horizontal scaling over at least the range  $\approx 300\text{m}$  to  $\approx 4000\text{km}$ . Since the cloud radiances are nonlinearly coupled with the dynamics, the absence of a break in the radiances will reflect the absence of a break in the dynamics. To extend this range to smaller scales, figs. 5, 6 show that the corresponding cloud liquid water content is scaling over at least the range  $\approx 5\text{m}$  to  $\approx 330\text{km}$ . Recent results on rain (Lovejoy and Schertzer 1990) extend the latter limit down to millimeter scales and it has long been known that atmospheric turbulence is scaling from dissipation scales of less than millimeters to much larger scales. These findings (combined with many others, see Lovejoy et al. 1993 for a review) make it likely that the atmosphere is scaling over the entire meteorologically significant range.

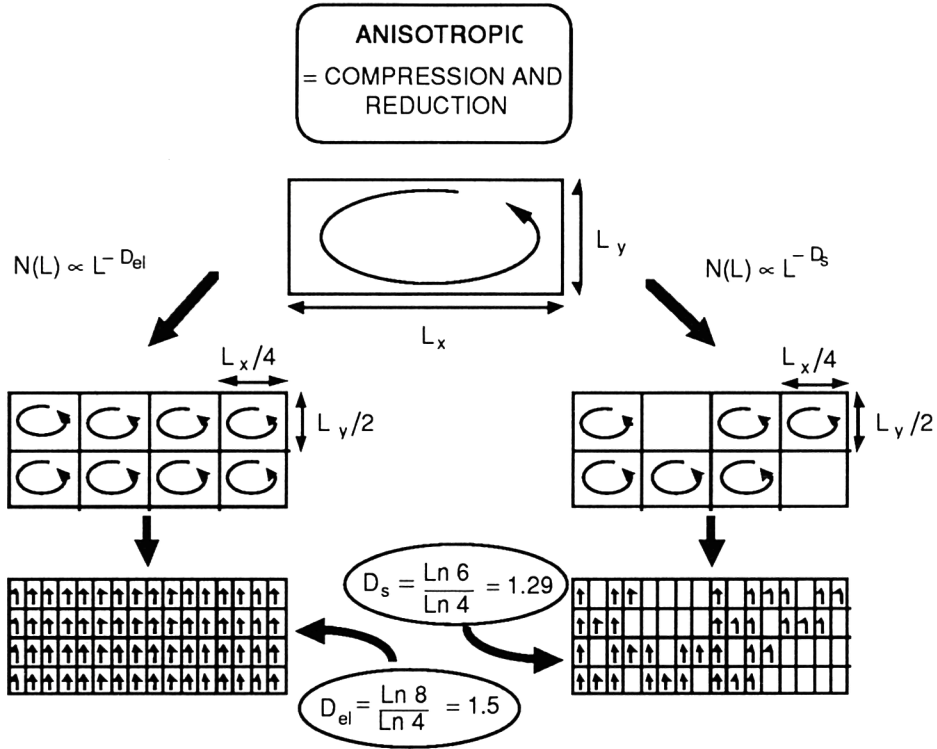


Figure 1: Anisotropic cascade scheme showing how the vertical cross-section of a large (horizontally flattened eddy) gets broken into smaller sub-eddies in a scaling anisotropic manner. The elliptical dimension used here is  $3/2$  (from Lovejoy and Schertzer 1986.)

### 1.3 Surfaces

The other field fundamental for remote sensing is the Earth's surface. It has long been known (Venig-Meiniz, 1951) that the topography has a power law spectrum over wide ranges. However, during the 1980's the scaling properties and limits were somewhat obscured when attempts were made using inappropriate monofractal analysis techniques to fit the multifractal topography (see below) into monofractal frameworks. For example, debates arose around which was the most appropriate value of the supposedly unique fractal dimension of altitude isolines. Research has shown that there is no unique value; the fractal dimension systematically decreases for higher and higher altitude thresholds. This implies that the monofractal frame-

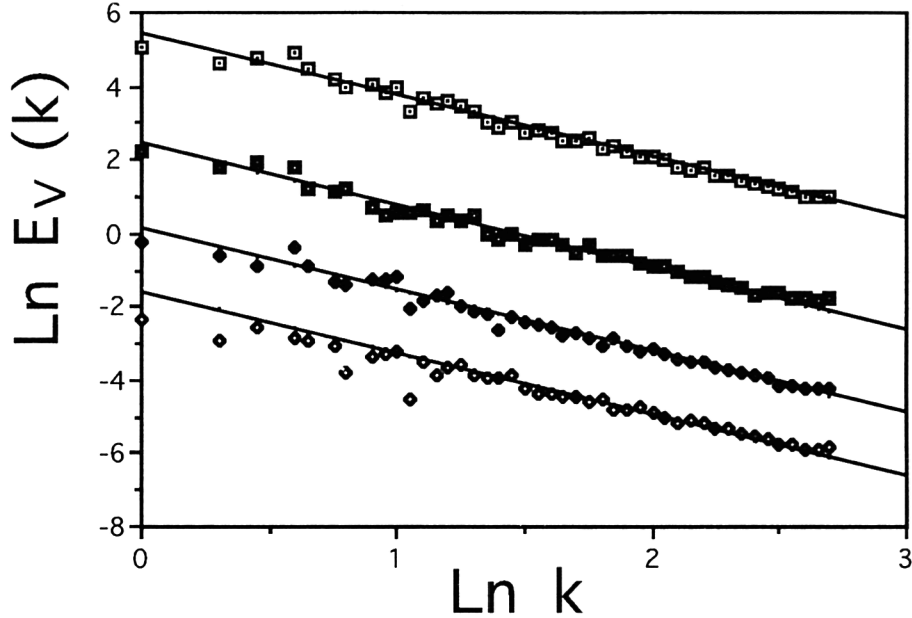


Figure 2: The spectrum of temperature fluctuations. Top: average over the 3 air craft data sets taken roughly at one year interval in the tropics (each contains 10 samples). Below: 3 individual spectra obtained by averaging over the 10 samples. The absolute slopes are close to Corssin-Obukhov value  $5/3$ :  $\beta_v = 1.68 \pm 0.05$  over the frequencies range  $\omega_0/20 - \omega_0/20480$  ( $\omega_0 = 8\text{Hz}$ ). From Chiriginskaya et al. 1994.

work of self-affine surfaces (which cannot handle multiple dimensions) is inappropriate.

When surfaces are remotely sensed, there is usually no simple or direct relation between the physical surface or atmospheric parameters and the observed radiances. Below we will argue with examples, that serious exploitation of remotely sensed data requires the use of multifractal models of the radiation/matter interactions. For the moment, we consider another example: ice surfaces observed by airborne Synthetic Aperture Radar (SAR); fig. 7 shows the result at different wavelengths and polarizations. Full treatment of these correlated multifractals requires (complex) Lie cascades (see section 5, the accompanying text, and Schertzer and Lovejoy 1994).

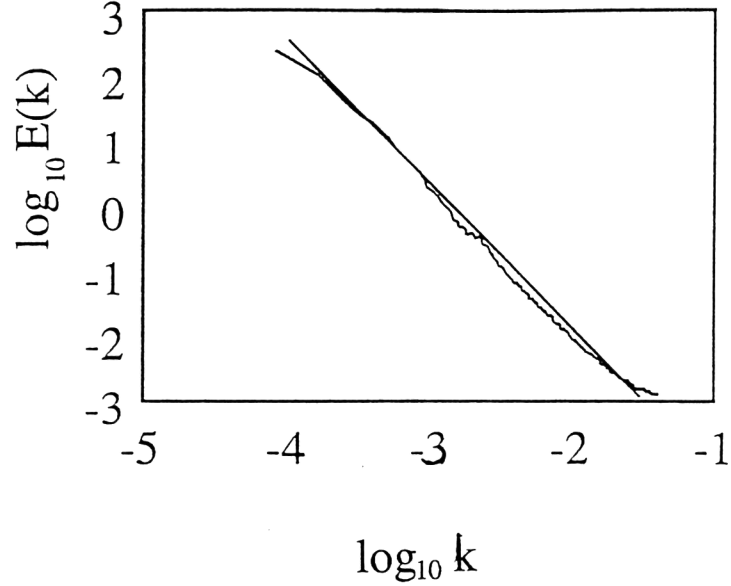


Figure 3: The mean spectrum of 280 radiosondes at 50m resolution, over a total depth of 13.3km, taken in the tropics (same experiment as fig. 2). The straight line is the theoretical line (Bogliano-Obhukhov scaling) with  $H_v = 3/5$ ;  $\beta_v = 2.20$ . The scaling is well respected throughout the entire thickness of the atmosphere.

## 2 Properties of Multifractals

### 2.1 Discussion

The full implications of nonlinear dynamics coupled with scaling have only begun to be grasped in the last few years. It is now increasingly clear that this generally leads to multifractal behaviour (see e.g. Schertzer and Lovejoy 1991). Multifractals have highly singular small scale limits; they do not converge in the sense of functions, but only weakly, in the sense of measures. Although at first sight this may seem to be an academic distinction, it is in fact fundamental. When multifractal fields are measured by remote or in situ sensors whose temporal or spatial resolution is much lower than that of the intrinsic variability of the phenomenon (which can easily be of the order of millimeters and milliseconds), then the result is a low resolution function whose properties depend fundamentally (in precise

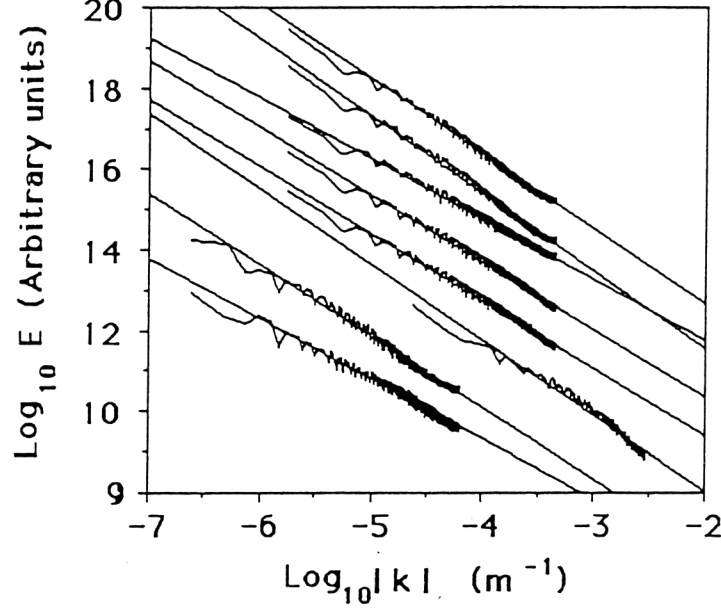


Figure 4: Average power spectrum for satellite images grouped according to the satellite and the frequency range of the images (from bottom to top): LANDSAT (visible)  $\beta = 1.7$ , GOES (visible)  $\beta = 1.4$ , GOES (infra-red)  $\beta = 1.7$ , Nimbus-9 (channel 1 to 5)  $\beta = 1.67, 1.67, 1.49, 1.91, 1.85$ . (See Tessier et al. 1993b, Lovejoy et al. 1993).

power law ways) on the resolution.

Denote the ratio of the largest (e.g. satellite image) scale by  $L$ , and the smallest (e.g. single pixel) scale by  $l$ , and the ratio  $\frac{L}{l} = \lambda (> 1)$ . We can then denote the field of interest (e.g. satellite radiance) at resolution  $l$  by  $\varepsilon_\lambda$  which will have the following ‘multiscaling’ behaviour (Schertzer and Lovejoy 1987):

$$Pr(\varepsilon_\lambda \geq \lambda^\gamma) \approx \lambda^{-c(\gamma)} \quad (2)$$

where  $Pr$  indicates ‘probability’,  $\gamma$  is the ‘order of singularity’ associated with the threshold value  $\varepsilon_\lambda$ , and  $c(\gamma) \geq 0$  is the corresponding ‘codimension’. As the resolution ( $\gamma$ ) is increased, the satellite will see more and more small bright regions; for a scale invariant field,  $\gamma$  is the correct way to remove the systematic resolution dependencies. Similarly,  $c(\gamma)$  indicates how the histograms of brightness values will change with resolution, and provides the appropriate way of removing the scale dependence of the his-

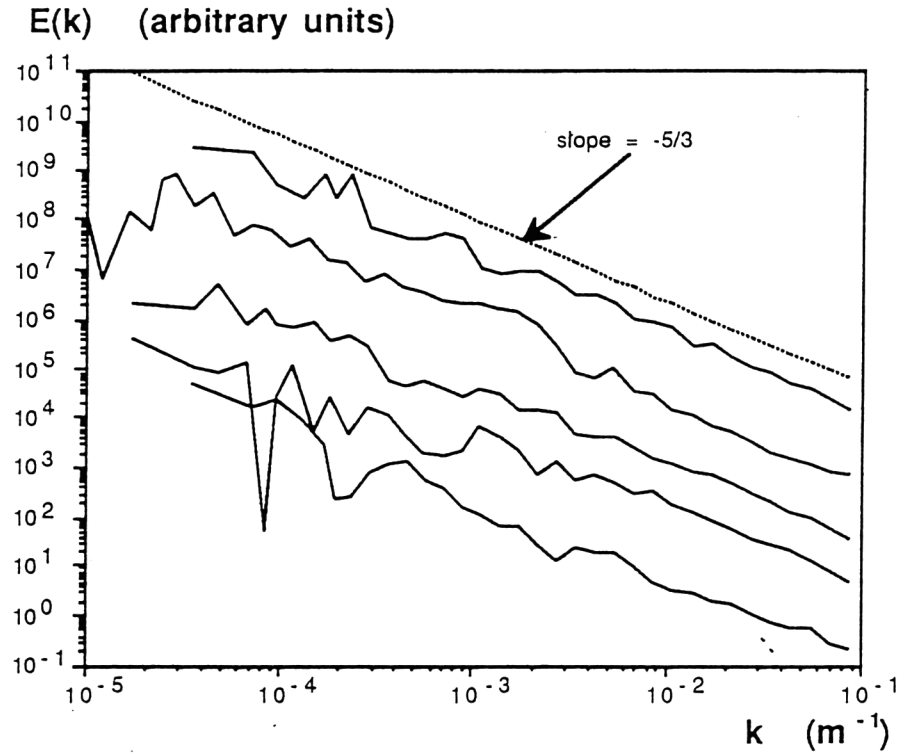


Figure 5: Power spectrum of 5 different aircraft liquid water concentration data sets (averaged to 10 points per magnitude on the  $k$ -axis, resolution  $\approx 5\text{m}$ ). All the sets are very well scaling and have absolute slopes close to the theoretical value for passive scalars  $\beta = \frac{5}{3}$  (straight line on top of graph). In order to avoid overlapping of the different curves, the lines were offset vertically. Number of data sets from top to bottom with vertical offset given in brackets: 4 ( $10^5$ ), 3 ( $10^4$ ), 1 ( $10^2$ ), 2 ( $10^1$ ), 5. From Brosamlén et al. 1994.

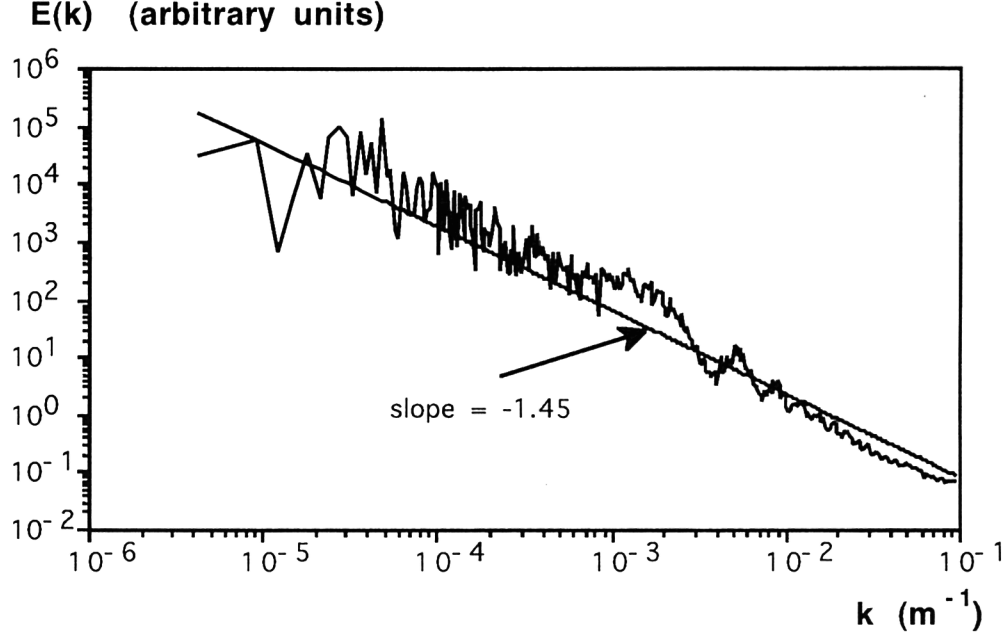


Figure 6: Aircraft liquid water concentration data sets power spectrum (averaged to 100 points per magnitude on the  $k$  axis). This shows a remarkably good scaling right through the meso-scale ( $\approx 10\text{km}$ , the graph covers the range of  $\approx 10\text{m}$  to  $\approx 300\text{km}$ ). From Brosamlén et al. 1994.

tograms. The behaviour indicated in eq. 2 will of course break down for large enough  $\lambda$  (small enough  $l$ , often of the order of millimeters), but over its range of validity, it represents a very strong effect since  $\varepsilon_\lambda$  and the probabilities will respectively diverge and converge as  $\lambda$  increases. When,  $c(\gamma) < D$  ( $D$  being the dimension of the observing space;  $=2$  for images)  $c(\gamma)$  is the (geometrical) codimension  $c(\gamma) = D - D(\gamma)$  corresponding to the (geometrical) fractal dimension  $D(\gamma)$  of the support of singularities whose order is greater than  $\gamma$ . The basic physical model for such behaviour are cascade processes in which the large scale multiplicatively modulates the smaller scales, in a mechanism that repeats from one scale to another over a very large range. Note that for the moment, we consider only isotropic scale changes associated with self-similar multifractals, full treatment of geophysical fields requires Generalised Scale Invariance (GSI, Schertzer and Lovejoy 1985a,b, 1989, 1991) which involves anisotropic scale changes and



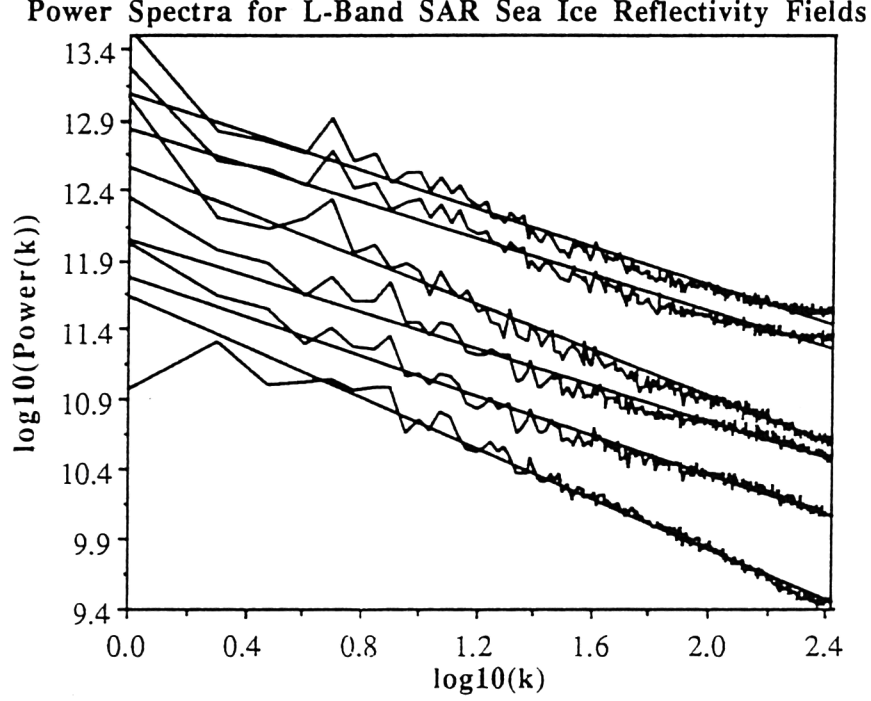


Figure 7: Power spectra of synthetic aperture radar data of two scenes (512 x 512 points each) of sea ice at 12.5m resolution showing that the scaling is well respected, especially in the HV polarization in both the SAR C-band data scenes (from top to bottom, the curves are HH, VV and HV for scene 1 and HH, VV and HV for scene 2 respectively. They were offset by 0.5 in the vertical so as to not overlap. From Francis et al. 1994.

is necessary to account for the ‘texture’ and ‘morphology’ of structures (see e.g. Pflug et al. 1993 for a recent study of cloud texture and type and section 4).

The multiple scaling behaviour of this field  $\varepsilon$  at scale ratio  $\lambda$  ( $=\frac{L}{l}$  the ratio of the largest scale  $L$  to the scale  $l$ ) can be also be characterized by the corresponding law for the statistical moments (via a Laplace transform):

$$\lambda^{K(q)} = \langle \varepsilon_\lambda^q \rangle = \int \lambda^{q\gamma\lambda - c(\gamma)} d\gamma \quad (3)$$

(the symbol ‘ $\langle . \rangle$ ’ indicates statistical averaging). All satellite and radar measurements of the atmosphere or surface which obey eq.s 2, 3 are strongly dependent on the characteristics of the sensor (via the ratio  $\gamma$ ); they are

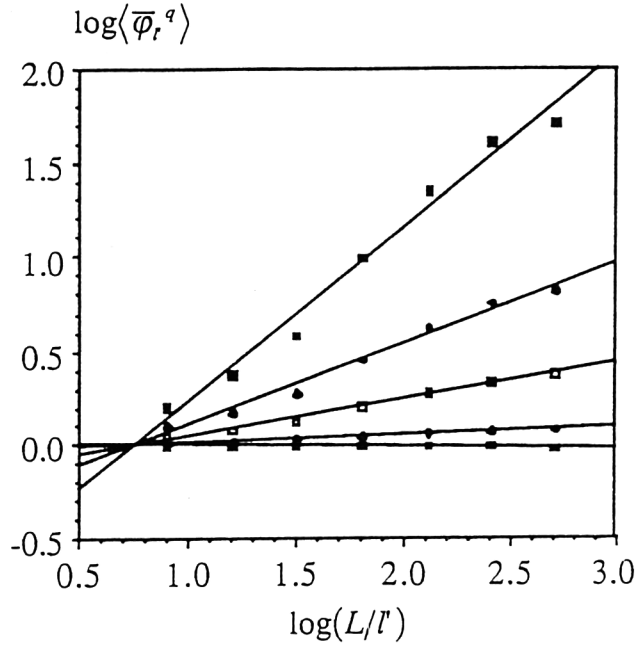


Figure 8: The scaling behaviour of the statistical moments of the Deadman's Butte data is illustrated here by the straightness of the curves of the  $\log\langle\bar{\phi}_l^q\rangle$  as functions of  $\log(L/l)$ , with  $L$  the largest scale in the Digital Elevation Model: from bottom to top  $q = 0.5, 1.5, 2.5, 3.5$  and  $5$ . The slopes correspond to the scaling exponent  $K(q)$ . From Lovejoy et al. 1994c.

not pure functions of the state of the atmosphere or surface that we are measuring. Since detailed comparisons of remote measurements at different resolutions are seldom made, workers in the field are only just starting to realize the importance of these resolution effects. What we propose is the systematic development of new resolution-independent algorithms for calibrating and exploiting remotely sensed data. This will also involve a systematic characterization of the types and limits of scaling of the various fields.

Some examples of multiscaling of the moments are shown in fig. 8 which shows the scaling of the moments of the quantity  $\phi$  (the quantity corresponding to  $\varepsilon$ ) for the topography at Deadman's Butte, and fig. 9 shows the corresponding  $K(q)$  function. Monofractal topographies (such as those of the celebrated monofractal landscapes illustrating Mandelbrot's book), would be linear. Below, we indicate how to quantify this degree of

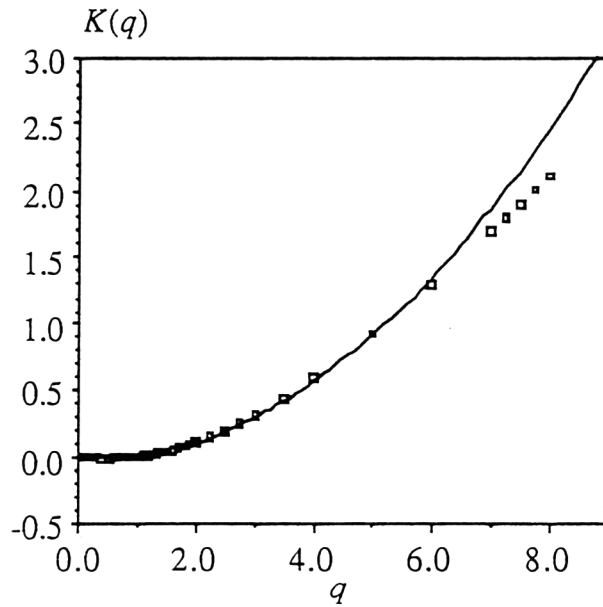


Figure 9: The scaling exponent  $K(q)$  against  $q$  for the Deadman's Butte data (see figs. 8). The continuous curve is the theoretical universal multifractal fit with  $\alpha = 1.9$ ,  $C_1 = 0.05$  (see eq. 9) For  $q > 6$ , the asymptotic behavior of  $K(q)$  becomes linear. This is a second order multifractal phase transition predicted from the finite sample size. From Lovejoy et al. 1994c.

multifractality more precisely with the help of universal multifractals.

## 2.2 A few properties

In general, knowledge of the probability distributions is equivalent to knowledge of all the statistical moments of a process; in multifractals, this relationship is particularly simple. In eq. 3, only the maximum exponent dominates in the integral, and the (Laplace) transform relating the moments and probabilities reduces to a Legendre transform for the exponents (Parisi and Frisch 1985).

$$K(q) = \max_{\gamma}(q\gamma - c(\gamma)) \quad c(\gamma) = \max_q(q\gamma - K(q)) \quad (4)$$

These relations establish a one to one correspondence between orders of singularities and moments ( $q = c'(\gamma)$ ,  $\gamma = K'(q)$ ). Both the codimension function  $c(\gamma)$  and the moment scaling exponent  $K(q)$  are convex. Note that in practice, the maximum order of singularity available in a sample is bounded simply due to the finite sample size; the resulting restrictions on the  $\gamma$  in the above maximization, are associated with multifractal phase transitions as discussed in SL94.

Various types of multifractals exist; and they can profitably be classified according to their highest order of singularity (see Schertzer et al. 1991, and Schertzer and Lovejoy 1992). Unfortunately, those which have been most extensively studied; the geometric multifractals in strange attractors, or the microcanonical multifractals often used as a framework for analysing turbulence (e.g. the celebrated 'p model', Meneveau and Sreenivasan, 1987), are artificially restricted so that high order singularities cannot occur. In contrast, the general 'canonical' multifractals generically produced by cascade processes do not suffer from these restrictions. In canonical multifractals, the existence of occasional 'hard' (very violent) singularities leads to quite different behaviour for the (theoretical) process without the small scale interactions ('bare' properties), and for the same process with the small scale interactions ('dressed' properties). The latter are the result for example when cascade processes proceed down to infinitely small scales and are then integrated over finite scales (for example by a remote sensor). The dressed  $\varepsilon_{\lambda}$ , will generally display the phenomenon of divergence of high order statistical moments, and are discussed in more detail in SL94.

### 2.3 Universal multifractals

One of the most fruitful physical ideas is that of universality; that of all the complex details of a process, that -if it is repeated sufficiently often for example over a wide enough range of scales - that only a few of the details will actually matter. Each resulting ‘universality class’ has a basin of attraction which determined by all the set of parameters which give the same limiting behaviour. In multiplicative process and multifractals, the question of universality has a long history, much of it being connected with the ‘law of proportional effect’ and lognormal distributions. Unfortunately, for various technical reasons (discussed in more detail in SL94), for several years, an anti-universality prejudice developed in the multifractal literature. The absence of universality would have dire implications for the very possibility of using multifractals for anything since it would mean that an infinite number of theoretical parameters would be needed to specify every multifractal process (e.g. the entire  $c(\gamma)$  or  $K(q)$  function). Similarly, the corresponding empirical characterization would also be impossible. Fortunately, stable, attractive universality classes do exist for multifractal processes, a fact that is being increasingly recognized (Schertzer and Lovejoy 1987, 1989, Fan 1989, Brax and Peschansky 1991, Kida 1991, Dremin 1994 etc.).

Multiplying processes corresponds to adding generators. We seek *generators* which are *stable* and *attractive* under *addition*. Considering for the moment only stationary (conservative) multifractals, these generators yield the *universal* expressions (Schertzer and Lovejoy 1987, 1989) for the scaling function of the moments of the field  $K(q)$  and of the codimension function  $c(\gamma)$ :

$$c(\gamma) = C_1 \left( \frac{\gamma}{C_1 \alpha'} + \frac{1}{\alpha} \right) \alpha' \quad \alpha \neq 1 \quad (5)$$

$$K(q) = \frac{C_1}{\alpha - 1} (q^\alpha - q) \quad \alpha \neq 1 \quad (6)$$

where  $(\frac{1}{\alpha} + \frac{1}{\alpha'}) = 1$ , and when  $\alpha < 2$ , for  $q = c'(\gamma) > 0$ .  $\alpha$  is the Levy index of the generator and characterizes the degree of multifractality. The  $\alpha = 2$  case corresponds to the maximal degree of multifractality and the bare  $\alpha = 2$  multifractal has lognormal probabilities. The  $\alpha = 0$  case corresponds to the monofractal minimum.  $C_1$  is the codimension of the mean and characterizes the sparseness of the mean field.  $H$  is the degree of nonconservation and characterizes the degree of nonstationarity of the process. Note that the lognormal multifractals are compatible with the lognormal phenomenology of geophysics.

## 2.4 The degree of non-stationarity: the Hurst exponent $H$

Most fields observed in nature are not conserved, i.e. the average of the observed quantity at scale  $\lambda$  (denoted here by  $\langle \rho_\lambda \rangle$ ) is not equal at different scales. This requires the introduction of a third<sup>4</sup> universal multifractal parameter  $H$  (the ‘Hurst’ exponent) which measures the degree of nonstationarity in the process; it is also a measure of the conservation of the field over different scales (as the cascade proceeds to smaller scales), e.g.  $H = 0$  is a conserved or stationary multifractal<sup>5</sup>. For many analysis techniques it is necessary to isolate the underlying conserved quantity (see below).

To understand this better, consider the relatively well studied case of passive scalar advection. If cloud droplets were passive scalars, i.e. transported by the wind without interacting with it, one obtains the Corrsin-Obhukhov law for passive scalars (Obhukhov 1949, Corrsin 1951):

$$\Delta \rho_\lambda = \phi_\lambda^{\frac{1}{3}} \lambda^{-\frac{1}{3}} \quad (7)$$

$$\phi_\lambda = \chi_\lambda^{\frac{3}{2}} \varepsilon_\lambda^{-\frac{1}{2}} \quad (8)$$

where  $\varepsilon_\lambda$  is the turbulent energy flux and  $\chi_\lambda$  is the passive scalar variance flux<sup>6</sup> at scale ratio  $\lambda$ . Eq. 7 indicates that  $H = 1/3$ .  $\Delta \rho_\lambda = \rho(x + \lambda^{-1}L) - \rho(x)$  is the density fluctuation at scale  $\lambda$ . Without intermittency,  $\chi_\lambda$  and  $\varepsilon_\lambda$  are constants (have trivial scale dependency) with (scaling) intermittency then  $\chi_\lambda$  and  $\varepsilon_\lambda$  will be multifractal and  $\phi_\lambda$  will obey eqs. 2, 3. More generally, since liquid water is not really passive (for example it is associated with latent heat release which modifies the velocity field) we may still consider that the characteristic fluctuations  $\Delta \rho_\lambda$  are scale invariant and write the scaling for the density  $\rho$  as:

$$|\Delta \rho|_\lambda \approx \phi_\lambda^\alpha \lambda^{-H} \quad (9)$$

---

<sup>4</sup>Davis et al. 1994 have proposed characterizing multifractals with just *two* parameters ( $C_1, H$ ); these are clearly only sufficient to determine the tangent of  $K(q)$  near  $q=1$ , i.e. the best *mono* fractal approximation. To discuss any *multi* fractal characterization, at least three parameters are necessary,  $\alpha$  is the natural choice

<sup>5</sup>If  $H > 0$  the process is nonstationary i.e. it is statistically translationally invariant. A more restricted notion of stationarity (second order stationarity) depends on the value of  $\beta$  (a process is second order stationary if  $\beta < 1$ ). The distinctions between true stationarity (discussed here) and second order stationarity (which has no special significance for multifractals) have sometimes been forgotten (e.g. Davis et al. 1994)

<sup>6</sup>Note that as indicated Corrsin-Obhukov scaling involves quasi steady fluxes; these boundary conditions are totally different from those of point dispersion pollutants

where  $\phi_\lambda$  has the conserved property  $\langle \phi_\lambda \rangle = \text{constant}$  (independent of scale). Since we have as yet no proper dynamical theory for the liquid-water distribution in the atmosphere, we do not know the appropriate fields  $\phi_\lambda$  nor the corresponding value of  $a$ . However, changing the value of  $a$  corresponds essentially to changing the parameter  $C_1$ , (Schertzer and Lovejoy 1994), without loss of generality, we therefore set it equal to 1.

### 3 Multifractal analysis and simulation techniques

#### 3.1 Summary of multifractal data analyses

Table 1 summarizes some recent studies of universal multifractal characteristics of various fields, many of them remotely sensed. Most of these estimates were obtained using the Double Trace Moment (DTM) technique (Lavallé 1991). This method is based a generalization of the above obtained by first raising the field at the smallest available resolution (indicated by  $\Lambda$ ) to the power  $\eta$ , then degrading to resolution  $\lambda$  before averaging over the  $q$ th power of the result:

$$\langle (\varepsilon_\Lambda^\eta)_\lambda^q \rangle = \lambda^{K(q,\eta)} \quad (10)$$

Since we are considering the normalized  $\eta$  powers, the  $q, \eta$  scaling exponent function is related to the usual exponent by:

$$K(q, \eta) = K(q\eta) - qK(\eta) \quad (11)$$

The usefulness of the double trace moment technique becomes apparent when it is applied to universal multifractals since in this case, we have the following:

$$K(q, \eta) = \eta^\alpha K(q, 1) \quad (12)$$

i.e.  $\log K$  vs.  $\log \eta$  will be linear over the region where the above holds. Since eq. 12 is strictly true only for bare moments, the finite sample and/or divergence of moments will cause it to break down for large  $q, \eta$  ( $q$  or  $q\eta > q_s$ ). At small  $\eta$ , it can also break down due to the presence of noise or zero values. Figs. 10, 11, 12 give some examples on surfaces.

Table 1 contains a more complete list including universality parameters, sampling limits, critical orders and singularities of divergence (corresponding to ‘hard’ multifractals and Self-Organized Critical structures; see SL94), as well as the effective dimension of dressing (see SL94 for more details).

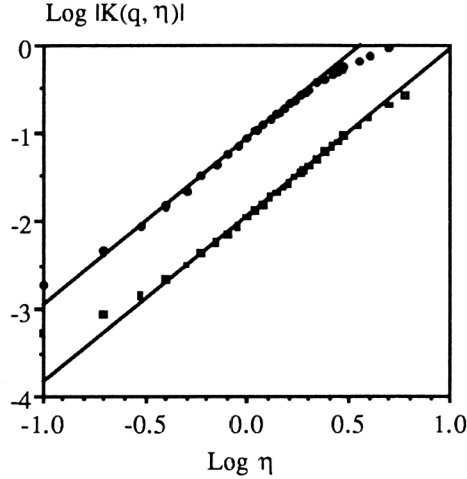


Figure 10: The curves of  $\log |K(q, \eta)|$  as functions of  $\log \eta$ , for the Deadman's Butte data. From top to bottom  $q$  takes the values 2 and 0.5. All the curves are parallel as predicted by universality eq. 12. The evaluation of their slopes, with  $\eta$  taking values between en 0.5 and 2.4, gives the following values of  $\alpha$  :  $1.90 \pm 0.1$  and  $1.89 \pm 0.1$ . The values of  $C_1$ , obtained by solving the expression for  $\log \eta = 0$  intercept given by  $\log |K(h, l)|$  and using eq. (12), are respectively:  $0.044 \pm 0.05$  and  $0.045 \pm 0.05$ . The consistency between the estimates of  $\alpha$ ,  $C_1$  for various values of  $q$ , are good indications that they are accurate. For values of  $\eta$  too high or too low, the curve  $K(q, \eta)$  becomes (fairly) constant, and these values of  $\log |K(q, \eta)|$  must not be considered to estimate  $\alpha$ . From Lavallée et al. 1993.

Two aspects are worth noting. First, almost all of the  $\alpha$  values are  $> 1$ , hence the corresponding processes are 'unconditionally hard', i.e. for any finite  $D$ , a finite  $q_D$  exists; some moments will diverge. Self-organized criticality therefore seems to be prevalent and  $\gamma_D$  gives a quantitative measure of the intensities of the self-organized critical structures. Second, we see that  $C_1$  is often smaller than  $H$  (see. e.g. topography or turbulence), hence the multifractality - while being nearly maximal according to the observed value of  $\alpha$  - will nevertheless not be too pronounced unless we consider the extreme events; monofractal models can therefore



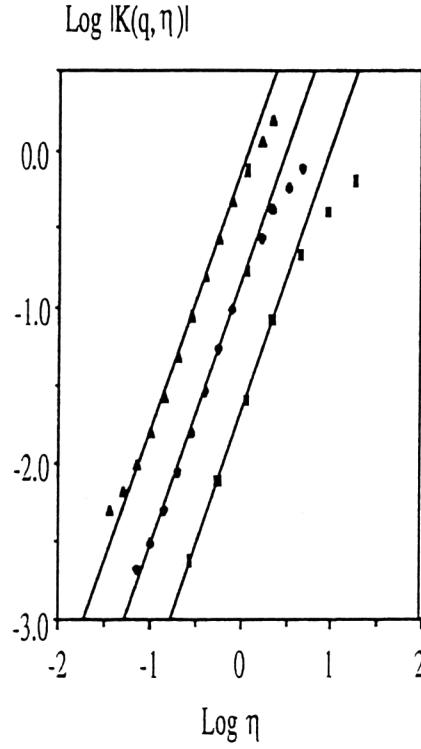


Figure 11: Same as fig. 10 but for the French topography at 1km resolution. From top to bottom  $q$  takes the following values: 4, 2 and 0.5. All the curves are parallel as predicted by eq. (12). The estimates of the slope for  $q = 4$ , with  $\eta$  taking values between 0.1 and 0.5, gives  $\alpha = 1.67 \pm 0.1$ . The same analysis for  $q = 2$  and 0.5 (with  $\eta$  taking values between 0.12 and 1.1 in the first case and between 0.3 and 2.3 in the second), yield respectively  $\alpha = 1.69 \pm 0.1$  and  $1.7 \pm 0.1$ . The values of  $C_1$ , obtained by solving the expression for the  $\log \eta = 0$  intercept given by  $\log |K(q, l)|$  and using eq. 12, are respectively:  $0.078 \pm 0.05$ ,  $0.076 \pm 0.05$  and  $0.076 \pm 0.05$ . Here also the values of  $\alpha$ ,  $C_1$  determined are independent of the  $q$  values. From Lavallée et al. 1993.

Field	Type	$\alpha$	$C_1$	$H$	$q_D$	$q_s^{c2}$	$\gamma_D$	$D$	Range of scales
Radiation fields	Clouds, Visible, Infra red <sup>a</sup>	1.35	0.15	0.3-0.4 <sup>b</sup>	>5	6.8	—	—	160m→4000km
	Clouds Microwave <sup>b1</sup>	1.35	0.10	0.3-0.5 <sup>b</sup>	—	9.2	—	—	10km→2000km
Rain	Rain Radar reflectivity <sup>c</sup>	1.35	0.30	0.0	1.1-2 <sup>d</sup>	4.1	0.6-0.8	0.4-0.5	30m→64km
	Rain Raingauge, horizontal <sup>c</sup>	1.35	0.20	0.0	3 <sup>e</sup>	5.5	0.8±0.1	0.40	50km→4000km
	Rain Raingauge, time series <sup>f</sup>	0.5-0.7	.45-.60	0.0-0.1	2.5-3 <sup>g</sup>	2.7-4	.75±.1	0.65±.15	8 minutes→16 days <sup>h</sup>
Rivers	Daily streamflow <sup>i</sup>	1.45±.3	0.2±.1	-0.1±.1	2.5±.5	2.5-4	0.6	0.3±.1	1month→30 years
Turbulent velocity	Wind (tunnel, time) <sup>j</sup>	1.30	0.06	.33	—	8.7	—	—	1ms→1s
	Wind atmos. (time) <sup>k</sup>	1.45	0.07	.33	7.5±1	6.3	-0.1±.03	0.20±.03	1ms→1s
	Wind atmos. (horizontal) <sup>l</sup>	1.35±.07	0.068±.01	0.33±.03	7.0±1	7±0.5	-0.1±.02	0.22±.03	12m→12km
	Wind atmos. (vertical) <sup>m</sup>	1.85±.05	.076±.01	0.6±.1 <sup>n</sup>	5±0.2 <sup>o</sup>	4±0.2	0.07±.03	0.33±.03	50m→14km
Temperatures	Climatological Temperatures	1.4 <sup>o2</sup>	0.06 <sup>o2</sup>	0.25 <sup>o3</sup>	5 <sup>o3</sup>	6.5	0.0	0.2	4→4,000years
	Temperature (atmos, time) <sup>p</sup>	1.20	0.04	0.30	5 <sup>q</sup>	15	-0.2	0.1	0.1s→1000s
	Temperature, atmos. (hor.) <sup>s</sup>	1.25±.06	0.04±.01	33±.03 <sup>s2</sup>	5.5 <sup>s3</sup>	13	-0.2	0.10±.02	12m→12km
Turbulent scalars	Pollution (Seveso) <sup>t</sup>	1.2	0.8	-0.2	3 <sup>t2</sup> , 5 <sup>t3</sup>	2.1	1.5-2	1.5-1.9	30m→5km
	Cloud liquid water (hor.) <sup>u</sup>	2.00±.01	0.07±.01 <sup>v</sup>	0.28±.03 <sup>v</sup>	2.2±0.1 <sup>v1</sup>	3.8±0.1	-0.08±.05	0.15±.01	5m→330km
Measuring Networks	Density of stations <sup>w</sup>	0.8	0.3	0.0	3.6	11	0.6	0.6	200km→20000 km
Surfaces	Sea Ice (radar) <sup>x</sup>	1.85±.05	0.01±.01	-.15±.05	>5	17	—	—	50m→25km
	Ocean surface (0.95μm) <sup>y</sup>	1.1	0.25	0.35	3 <sup>z</sup>	6.6	0.2	0.6	1m→50m
	Topography <sup>aa</sup>	1.8±.1	0.06±.01	0.5±.02	>5	7±0.5	—	—	50m→1000km
	Rock fracture surfaces <sup>ab</sup>	1.5	0.09	0.85	—	8	—	—	50μm→5cm
Astrophysics	Galactic luminosity <sup>bb</sup>	1.2±0.4	1.3±0.1	0.0	1.35 <sup>bc</sup>	1.5±0.1	1.8±0.1	1.5±0.1	0.1→100 <sup>o</sup>
Solid Earth	Seismicity <sup>cc</sup>	1.1	1.35	0.0	0.9 <sup>dd</sup>	1.4	1.2	1.1±.1	2km→1000km
	Geomagnetic field <sup>ee</sup>	1.9	0.3	0.75	1.4	2.7	-0.14	0.4	400m→100km
Physiology	Low frequency speech <sup>ff</sup>	2.0	0.1	-0.35	—	3.2	—	—	0.1s→1000s

Table 1: Empirical estimates of universal multifractal parameters.

## Key to Table 1

- [a] Tessier et al. 1993a; see also Lovejoy et al. 1993
- [b] The value of  $H$  depends slightly on the wavelength band used.
- [b1] At 19, 21, 37GHz., Lavallée et al. 1993, the value of  $H$  depends slightly on the wavelength band used.
- [c] Tessier et al. 1993a.
- [c2] Calculated for a single realisation;  $D_s = 0$ .
- [d] Schertzer and Lovejoy 1987, Duncan et al. 1993, Lovejoy 1981 obtained  $q_D \approx 1.66$  for integrals of reflectivity of isolated storms
- [e] Tessier et al. 1993a, using a global raingauge network, correcting for the multifractal sparseness of the network
- [f] Tessier et al. 1993a, Ladoy et al. 1993 obtain similar values for the global network and Nimes respectively (for 12, 24 hour resolution respectively). Other similar values were obtained in Réunion and Dédougou, Hubert et al. 1993. Nguyen et al. 1993 find the slightly higher  $\alpha$ , smaller  $C_1$  in various locations near Montréal.
- [g] Segal 1979 found a value of  $2.5 \pm 0.5$  for 50 stations, 10 years of data at 5 minute resolution.
- [h] Using a very large data base, Olsson 1994 finds similar values in Lund, Sweden, over periods of 8 minutes to 1 week.
- [i] Tessier et al. 1993c, 50 rivers.
- [j] Schmitt et al. 1992a, note that the theoretical (Kolmogorov) value of  $H$  is  $1/3$ .
- [k] Schmitt et al. 1993, 1994.
- [l] Chiriginskaya et al. 1994.
- [m] Lazarev et al. 1994, radiosondes.
- [n]  $H$  was first estimated using Jimspheres, by Endlich and Mancuso 1968, and confirmed by Adelfang 1971, and Schertzer and Lovejoy 1985. The theoretical (Bogliano-Obhukov) value of  $H$  is  $3/5$ .
- [o] The value of  $q_D$  was first estimated in Schertzer and Lovejoy 1985.
- [o2] F. Schmitt, S. Lovejoy, and D. Schertzer, analysis of Greenland ice core oxygen isotope ratios (in preparation).
- [o3] Lovejoy and Schertzer 1986, analysis of hemispheric temperatures and ice core paleotemperatures.
- [p] Schmitt et al. 1992b, the theoretical value for  $H$  is  $1/3$  if it is approximated as a passive scalar.
- [q] This value was estimated for daily temperatures at individual stations (Lovejoy and Schertzer 1986a), regional averages (Ladoy et al. 1986).
- [s] Chiriginskaya et al. 1994.

- [s2] The theoretical value (passive scalar approximation) is  $1/3$ .
- [s3] In the vertical, Schertzer and Lovejoy 1985 estimate  $H=0.9$ ,  $q_D=3.3$  apparently for the potential temperature in the range 50m-6km.
- [t] Salvadori et al. 1994.
- [t2] This value was estimated for  $UF_6$  tracer fluctuations by Visvanathan et al. 1991.
- [t3] This value was estimated for  $CO_2$  fluctuations over wheat fields Austin et al. 1991.
- [u] Brosamlén et al. 1994.
- [v] Davis et al. 1994 obtained similar values for  $H$ ,  $C_1$  with a smaller data set. The theoretical value (passive scalar approximation) is  $1/3$ .
- [v1] Due to the symmetry of the  $\alpha=2$  multifractal, the same value of  $q_D$  is obtained for  $1/\text{liquid water density}$ .
- [w] Using the global meteorological measuring network, considering the station density as a multifractal, Tessier et al. 1993, 1994
- [x] Synthetic aperture radar, 10, 30cm wavelengths, all polarizations, Francis et al. 1994.
- [y] Tessier et al. 1993b.
- [z] Kerman 1993.
- [aa] Deadman's Butte Wyoming, 50m-25km; France 1km-1000km; Lavallée et al. 1993a.
- [ab] F. Schmitt, private communication.
- [bb] Garrido et al. 1994.
- [bc] Schertzer et al. 1993.
- [cc] Hooge et al. 1993, 1994.
- [dd] This is the well-known Gutenberg-Richter exponent, first estimated by Gutenberg-Richter 1944, and is somewhat variable, the value cited here is for the Parkfield region.
- [ee] Lovejoy et al. 1994.
- [ff] Larnder et al. 1992.

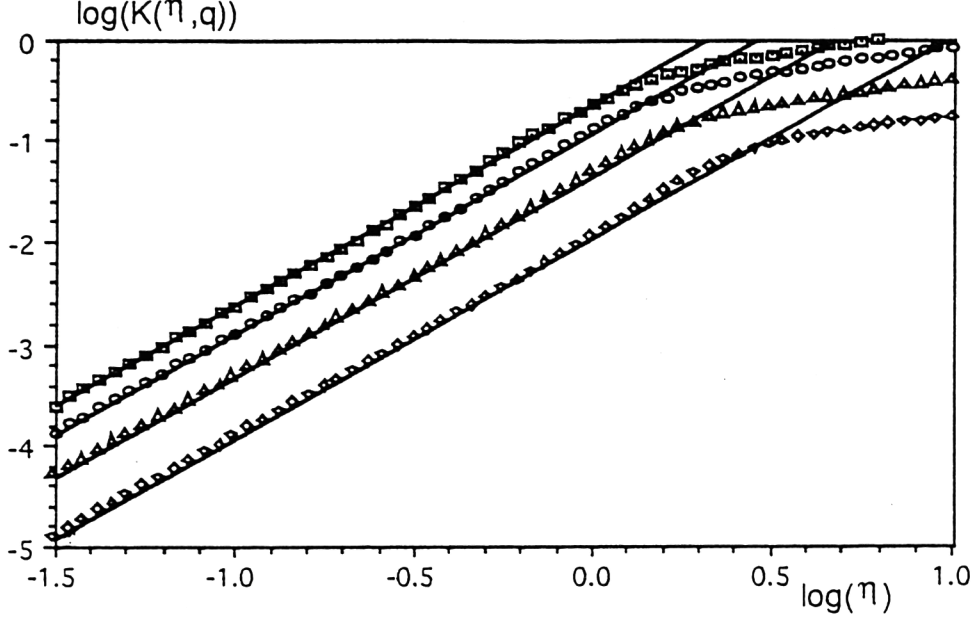


Figure 12:  $K(q, \eta)$  as a function of  $\eta$  on  $\log_{10} - \log_{10}$  scales, for the values (top to bottom)  $q = 2.5, 2.0, 1.5, 0.75$ . As expected for universal multifractals, the curves are linear and parallel for a certain range of the moments  $\alpha$ . The parameter  $\alpha$  can be identified as the slope of the straight line parts of the curves, whereas  $C_1$  is the value of the straight line at the intersection  $\eta = 0$ . From Brosamlen et al. 1994.

### 3.2 Isotropic (self-similar) simulations of universal multifractals

We now indicate briefly how to exploit the universality (and the measured  $H$ ,  $C_1$ ,  $\alpha$  parameters) to perform multifractal simulations. The first multifractal models of this type were discussed in Schertzer and Lovejoy 1987, and Wilson et al. 1991 give a comprehensive discussion including many practical (numerical) details. In particular, the latter describes the numerical simulation of clouds and topography, including how to iteratively ‘zoom’ in, calculating details to arbitrary resolution in selected regions. Pecknold et al. 1993 give a number of improvements and include more systematic results (including those shown here). Although we will not repeat these details, enough information has been given in the previous sections to un-

derstand how they work.

First, for a conserved (stationary) multifractal process  $\phi_\lambda$  we define the generator  $\Gamma_\lambda = \log \phi_\lambda$ . To yield a multifractal  $\phi_\lambda$ , it must be exactly a  $1/f$  noise, i.e., its spectrum is  $E(k) \approx k^{-1}$  (this is necessary to ensure the multiple scaling of the moments of  $\phi_\lambda$ ). To produce such a generator, we start with a stationary gaussian or Levy ‘subgenerator’. The subgenerator is a noise consisting of independent random variables with either gaussian ( $\alpha=2$ ) or extremal Levy distributions (characterized by the Levy index  $\alpha$ ), whose amplitude (e.g., variance in the Gaussian case) is determined by  $C_1$ . The subgenerator is then fractionally integrated (power law filtered in Fourier space) to give a  $k^{-1}$  spectrum. This generator is then exponentiated to give the conserved  $\phi_\lambda$  which will thus depend on both  $C_1$  and  $\alpha$ . Finally, to obtain a non conserved process with spectral slope  $\beta$ , the result is fractionally integrated by multiplying the Fourier transform by  $k^{-H}$  where  $H$  is given in eq. 9. The entire process involves two fractional integrations and hence four FFT’s.  $512 \times 512$  fields can easily be modelled on personal computers (they take about 3 minutes on a Mac II), and  $256 \times 256 \times 256$  fields (e.g., space-time simulations of dynamically evolving multifractal clouds) have been produced on a Cray-2 (Brenier 1990, Brenier et al. 1990).

Figures 13-18 inclusive show series of one dimensional simulations with various parameters.

It is apparent from them that  $C_1$  is the measure of the sparseness of the field: the higher the  $C_1$ , the fewer the field values corresponding to any given singularity. (Because the field is normalized, the spikes are higher for the fields with higher  $C_1$ ). It is also again apparent that the higher  $\alpha$  fields are dominated by a few large singularities.

## 4 Elements of Generalized Scale Invariance (GSI)

### 4.1 Discussion

The usual approach to scaling is first to posit (statistical) isotropy and only then scaling, the two together yielding self-similarity. Indeed this approach is so prevalent that the terms scaling and self-similarity are often used interchangeably! Perhaps the best known example is Kolmogorov’s hypothesis of ‘local isotropy’ from which he derived the  $k^{-\frac{5}{3}}$  spectrum for the wind fluctuations. The GSI approach is rather the converse: it first posits scale invariance (scaling), and then studies the remaining non-trivial

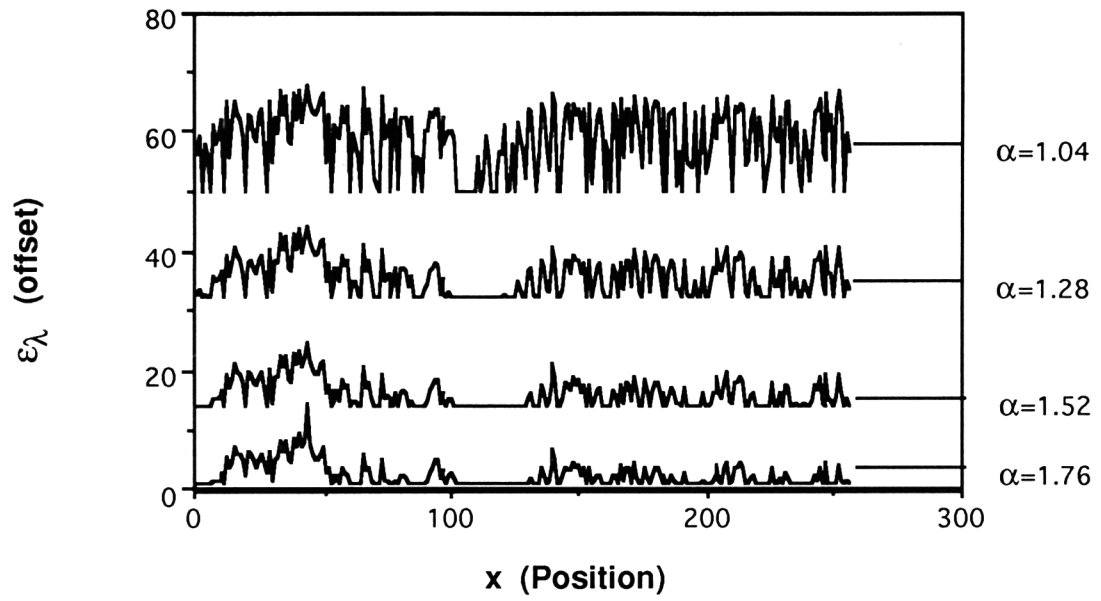


Figure 13: One-dimensional simulation of length 256, with  $C_1 = 0.9$  and varying  $\alpha$ . These simulations have been vertically offset so as not to overlap. From Pecknold et al. 1993.

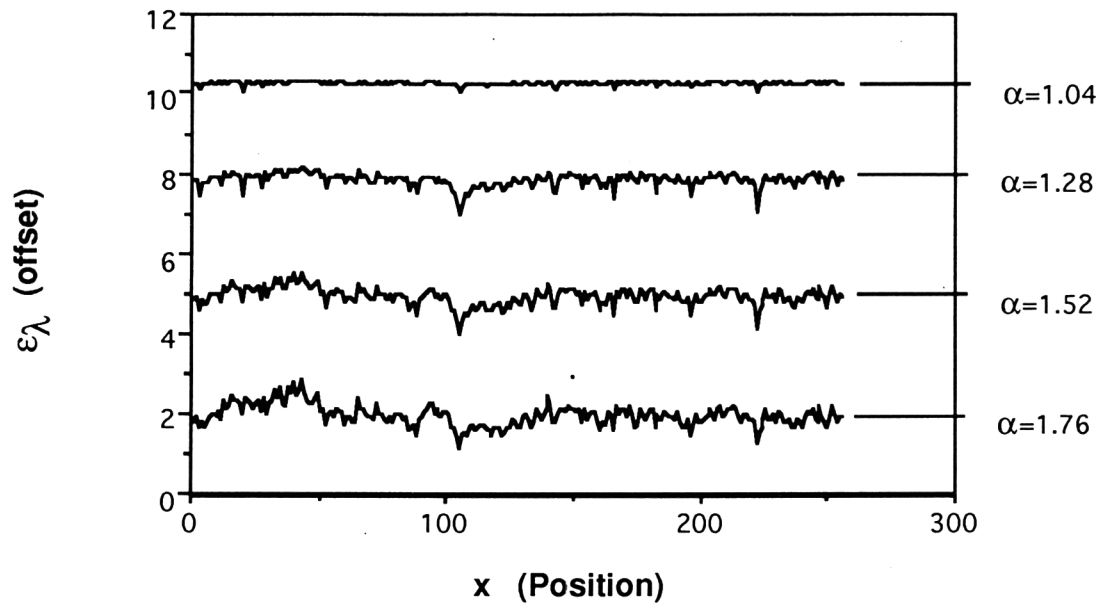


Figure 14: One-dimensional simulation of length 256, with  $C_1 = 0.01$  and varying  $\alpha$ . These simulations have been vertically offset so as not to overlap. From Pecknold et al. 1993.



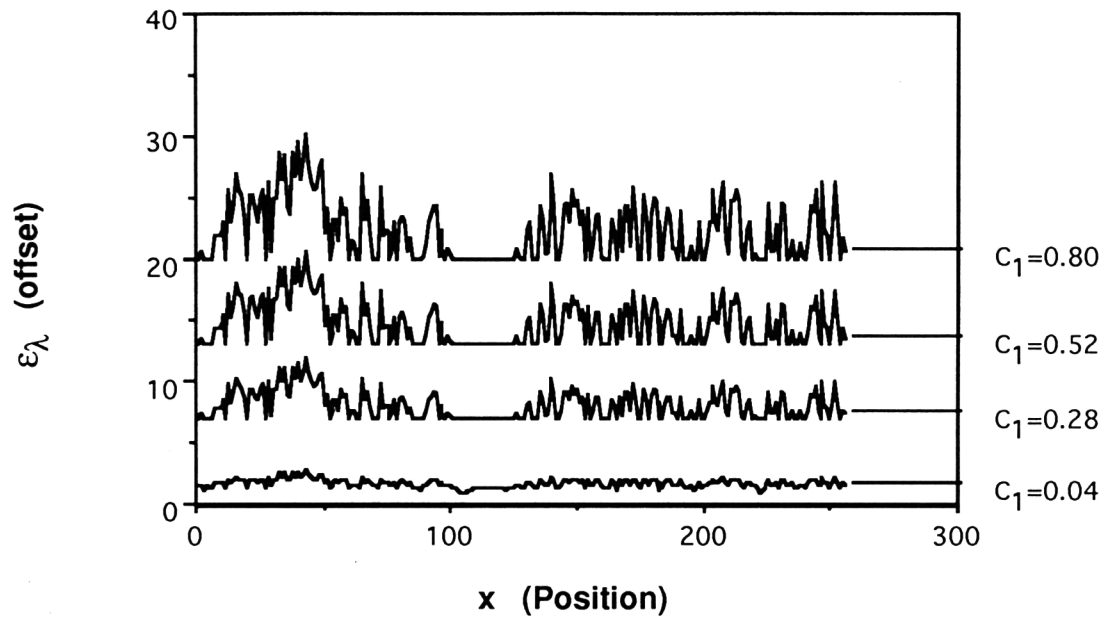


Figure 15: One-dimensional simulation of length 256, with  $\alpha = 1.4$  and varying  $C_1$ . These simulations have been vertically offset so as not to overlap. From Pecknold et al. 1993.

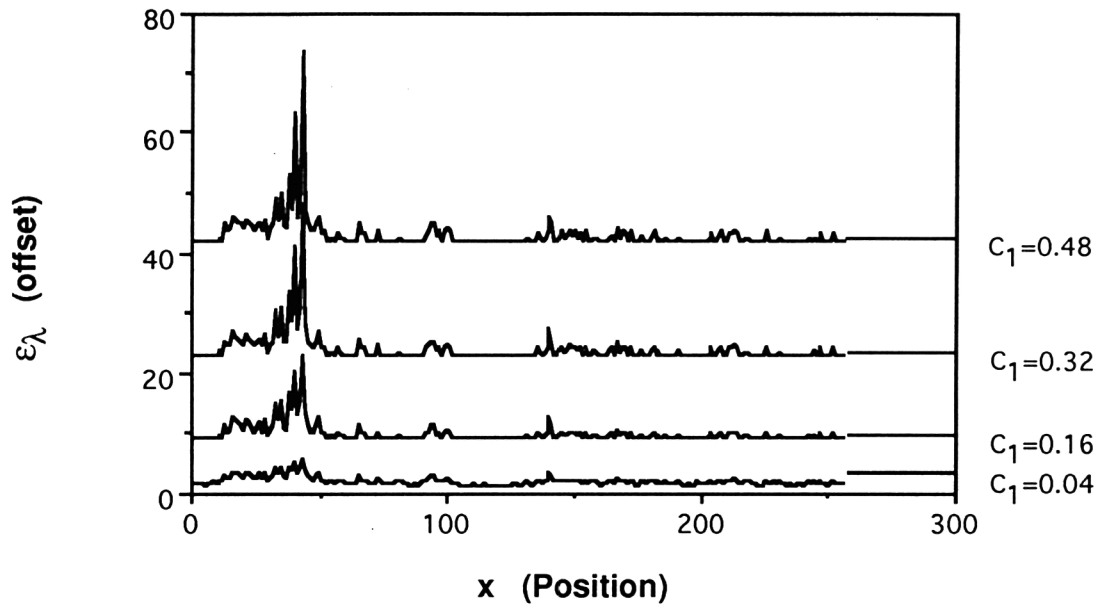


Figure 16: One-dimensional simulation of length 256, with  $\alpha = 2.0$  and varying  $C_1$ . These simulations have been vertically offset so as not to overlap. From Pecknold et al. 1993.

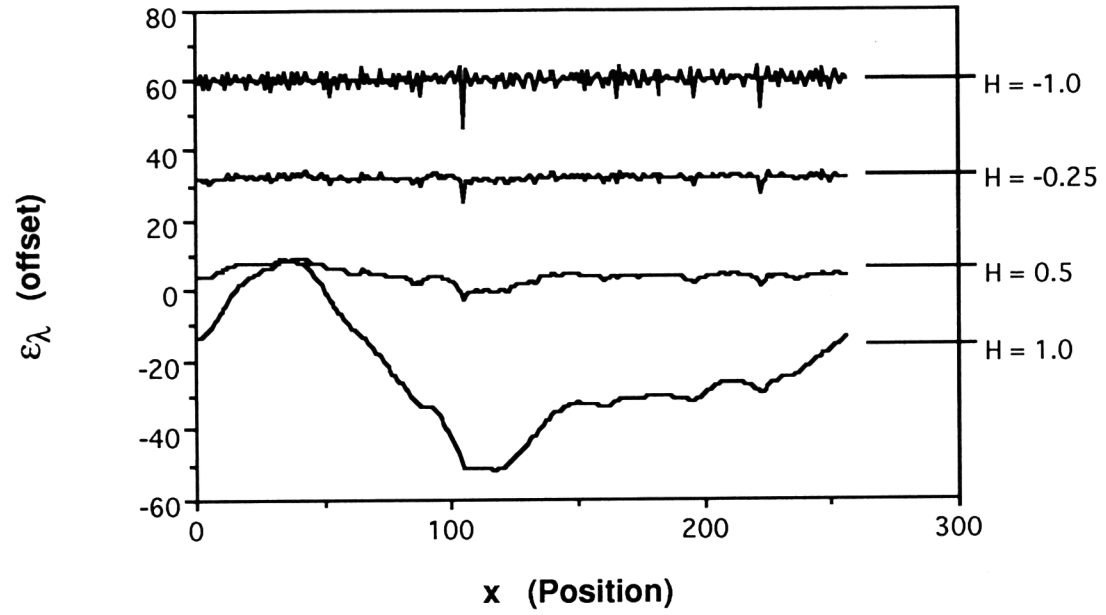


Figure 17: One-dimensional simulation of length 256, with  $\alpha = 1.8$  and  $C_1 = 0.02$ , fractionally integrated with varying  $H$  (non-conservation parameter). These simulations have been vertically offset so as not to overlap. From Pecknold et al. 1993.

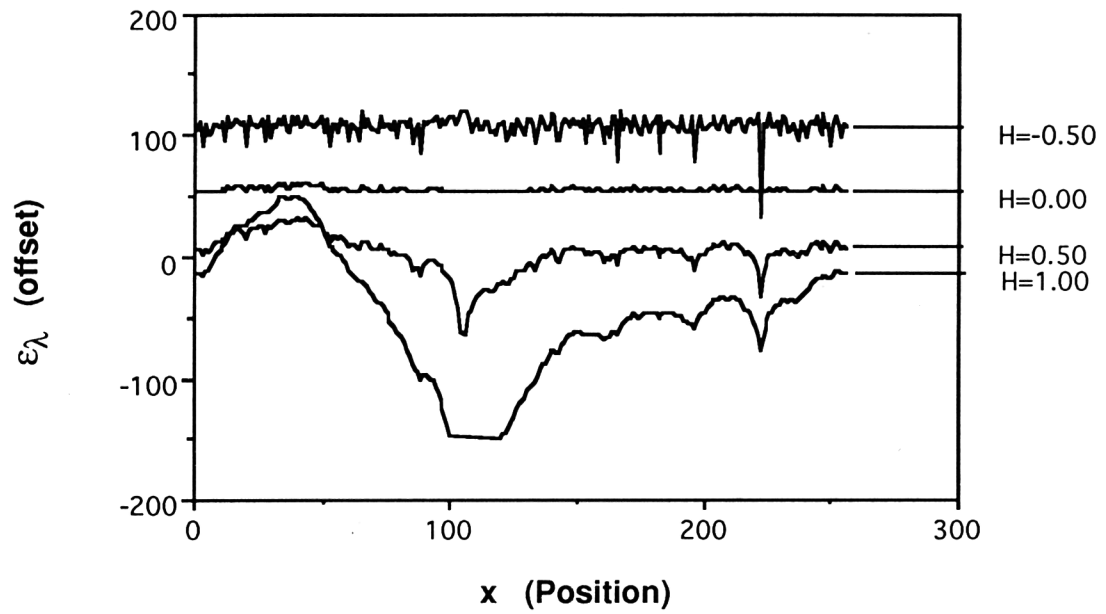


Figure 18: One-dimensional simulation of length 256, with  $\alpha = 1.5$  and  $C_1 = 0.4$ , fractionally integrated with varying  $H$  (non-conservation parameter). These simulations have been vertically offset so as not to overlap. From Pecknold et al. 1993.

symmetries. For instance, fig. 1 gives a (scaling) anisotropic version of the usual isotropic cascade scheme (in which the rectangles in fig. 1 would be replaced by squares). One may easily check that this type of anisotropy - which reproduces itself from scale to scale - does not introduce any characteristic scale. The straightforward generalization of scaling shown in fig. 1 involving scaling anisotropy in a fixed direction is called 'self-affinity'. As far as we know this anisotropic scheme (Schertzer and Lovejoy 1983) seems to be the first explicit model of a physical system involving a fundamental self-affine fractal mechanism.

## 4.2 The basic elements of GSI

Consider scale invariance under, isotropic dilations/contractions (e.g., simple reductions):  $\lambda^{-1}B = T_\lambda B$  where  $T_\lambda$  is a scale changing operator. In our example,  $T_\lambda = \lambda^{-1}\mathbf{1}$  where  $\mathbf{1}$  is the identity matrix. This means that if  $\mathbf{x}_1$  is an element in  $B$  then  $\mathbf{x}_\lambda = T_\lambda \mathbf{x}_1$  (again, in the previous example  $T_\lambda = \lambda^{-1}\mathbf{1} \Rightarrow \mathbf{x}_\lambda = \lambda^{-1}\mathbf{x}_1$ ). The subscripts on  $\mathbf{x}$  indicate the scale. In generalized scale invariance (GSI),  $T_\lambda$  can be much more general than isotropic dilations. Fig. 19 shows a generalized 'blow' down of the acronym 'NVAG' showing how the reduction is combined with stretching and rotation. In general, a scale invariant system will be one in which the small and large scales are related by a scale changing operation that involves only the scale ratios; there is no characteristic size. In what follows we outline the basic elements necessary for defining such a system: we follow closely the development in Schertzer and Lovejoy 1985b.

To be completely defined, GSI needs more than a scale changing operator; it also requires a definition of the unit scale, as well as a definition of how to measure the scale. These three basic elements can be summarized as follows:

(i) The unit ball  $B_1$  which denotes all the unit vectors. If an isotropic ball (e.g., circle or sphere) exists, we call the corresponding scale the 'spheroscale'. For simplicity we often assume this - indeed direct evidence for this exists in many satellite cloud pictures, but it is not strictly necessary (and at least in some cases not at all true!).

(ii) The scale changing operator  $T_\lambda$  which transforms the scale of vectors by scale ratio  $\lambda$ .  $T_\lambda$  is the rule relating the statistical properties at one scale to another and involves only the scale ratio (there is no characteristic 'size'). This implies that  $T_\lambda$  has certain properties. In particular, if and



Figure 19: A generalized blow-down with increasing  $\lambda$  of the acronym 'NVAG'. If  $\mathbf{G} = \mathbf{I}$ , we would have obtained a standard reduction, with all the copies uniformly reduced converging to the centre of the reduction (thanks to S. Pecknold, G. Lewis). Here the parameters determining  $\mathbf{G}$  are  $c = 0.3$ ,  $f = -0.5$ ,  $e = 0.8$  (see section 4), and each successive reduction is by 28

only if  $\lambda_1 \lambda_2 = \lambda$ , then

$$B_\lambda = T_{\lambda_1} B_{\lambda_2} = T_{\lambda_2} B_{\lambda_1} \quad (13)$$

i.e.,  $T_\lambda$  has the group properties (see fig. 20):

$$T_{\lambda_2} T_{\lambda_1} B_1 = B_\lambda = T_{\lambda_1} T_{\lambda_2} B_1 \quad (14)$$

Hence  $T_\lambda$  is a one parameter multiplicative group  $\Rightarrow T_\lambda = \lambda^{-G}$ , where  $G$

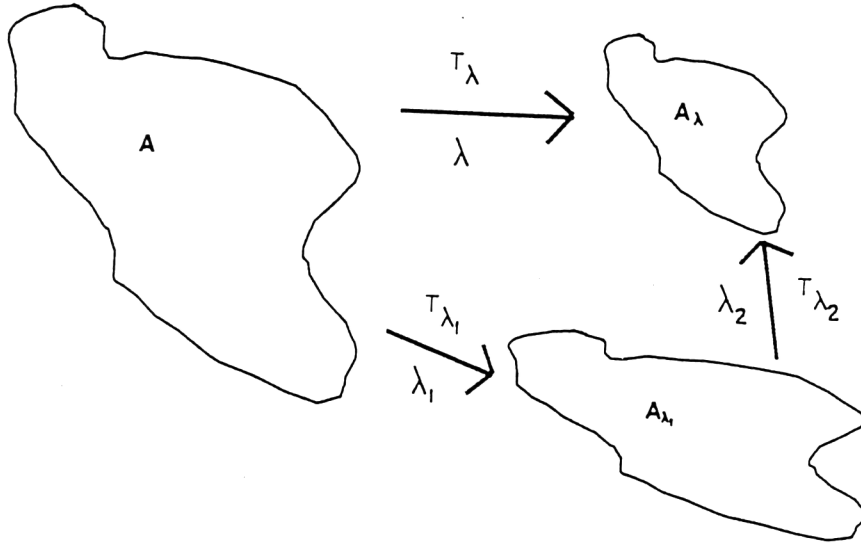


Figure 20: Illustration of the group property of the scale changing operator. From Schertzer and Lovejoy 1994.

is the generator of the group. We use the negative sign since in future we will be only interested in reductions by factor  $\lambda$  since we shall see that in turbulent cascades, energy flux is transferred from large to small scales ( $T_\lambda$  will *reduce* sizes by factor  $\lambda$ ). We will not require that inverse operators  $T_\lambda^{-1} = T_{\lambda^{-1}}$  exist, hence we really only have a semi-group (the inverse will however usually exist if  $G$  is a matrix).

### 4.3 Linear GSI and differential rotation: the example of the Coriolis force

In the atmosphere, one expects differential rotation (associated with the Coriolis force  $\Omega \wedge \mathbf{v}$ , associated for example with cloud texture) as indicated

above. This can be modelled by a matrix  $G$  with off-diagonal elements. To understand this, we decompose  $G$  into quaternions (or equivalently, Pauli matrices):

$$G = d\mathbf{1} + e\mathbf{I} + f\mathbf{J} + c\mathbf{K} \quad (15)$$

where

$$\mathbf{1} = \begin{bmatrix} 1 & 0 \\ 0 & 1 \end{bmatrix}, \quad \mathbf{I} = \begin{bmatrix} 0 & -1 \\ 1 & 0 \end{bmatrix} \quad (16)$$

$$\mathbf{J} = \begin{bmatrix} 0 & 1 \\ 1 & 0 \end{bmatrix}, \quad \mathbf{K} = \begin{bmatrix} -1 & 0 \\ 0 & 1 \end{bmatrix} \quad (17)$$

These matrices satisfy the following anticommutation relations:

$$\{\mathbf{I}, \mathbf{J}\} = 0, \quad \{\mathbf{I}, \mathbf{K}\} = 0, \quad \{\mathbf{J}, \mathbf{K}\} = 0 \quad (18)$$

Writing  $u = \ln \lambda$  and  $a^2 = c^2 + f^2 - e^2$  we obtain:

$$T_\lambda = \lambda^{-G} = \lambda^{-d} \lambda^{(G-d\mathbf{1})} = \lambda^{-d} \left[ \mathbf{1} \cosh(au) - (G - d\mathbf{1}) \frac{\sinh(au)}{a} \right] \quad (19)$$

When  $a^2 < 0$ , the above formula holds but with  $|a|$  replacing  $a$  and ordinary trigonometric functions rather than hyperbolic functions. The case  $a^2 > 0$  corresponds to domination by stratification, whereas  $a^2 < 0$  to domination by rotation. Examples of both balls and trajectories (the locus of points  $\mathbf{r}_\lambda = \mathbf{T}_\lambda \mathbf{r}_1$ , obtained by  $\lambda$  varying with  $\mathbf{r}_1$  fixed) are shown in fig.21. To take into account the spatial variation of anisotropy, the generator can be taken to be a nonlinear function, or even stochastic (fig. 22).

## 5 Multifractal simulations for solving problems in remote sensing, some examples

### 5.1 Resolution independent algorithms

We are rarely able to directly remotely sense the fields of interest. Typically, a satellite will observe radiances associated with a field and then (often complex) semi-empirical algorithms are used to try to infer the various physical characteristics from the radiances. Above we argued that such algorithms must at a minimum explicitly take the resolution into account, preferably removing it entirely so as to obtain sensor independent algorithms. Ultimately however, a full understanding of the relationship



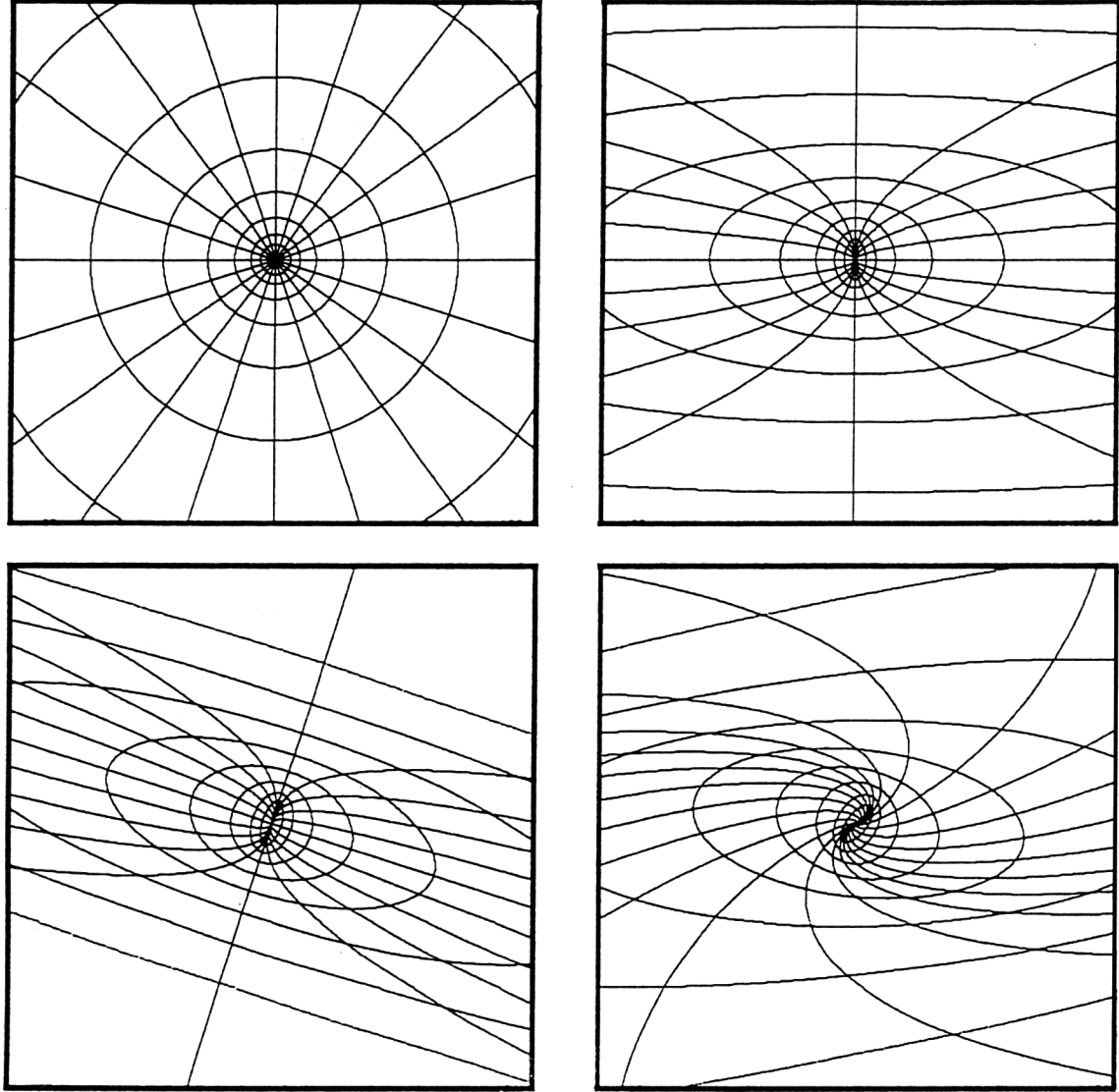


Figure 21: Examples of balls and trajectories for linear GSI with sphero-scale. Isotropic case:  $c = 0.0$ ,  $f = 0.0$ ,  $e = 0.0$  (top left); self-affine case:  $c = 0.35$ ,  $f = 0.0$ ,  $e = 0.0$  (top right); stratification dominant case ( $a^2 > 0$ ) with no rotation:  $c = 0.35$ ,  $f = 0.25$ ,  $e = 0.0$  (bottom left); rotation dominant case ( $a^2 < 0$ ):  $c = 0.35$ ,  $f = 0.25$ ,  $e = 0.6$  (bottom right). For all cases  $d = 1$  with sphero-scale at 30 units (pixels) out of a total of 512. From Lewis 1993.

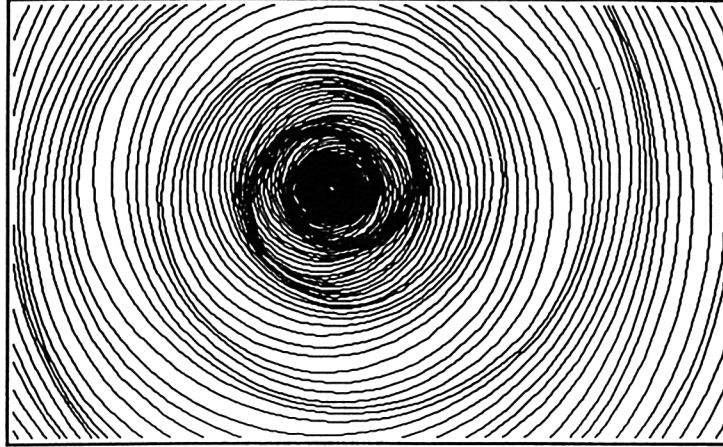


Figure 22: Deterministic non-linear GSI with a stochastic generator. Schertzer and Lovejoy, 1991.

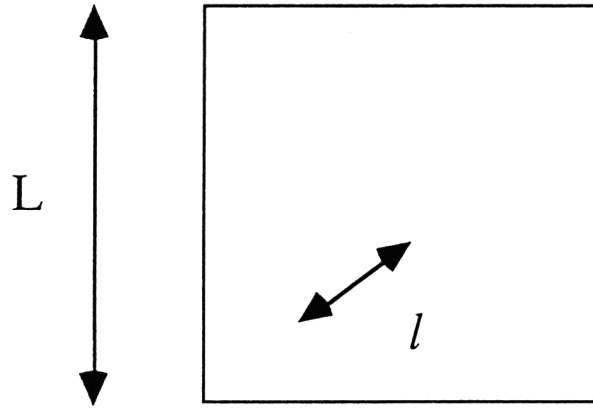
between the remotely sensed and underlying physical field will only be possible as the result of explicit multifractal modelling of the radiation/matter interaction. Our efforts in this direction have been especially aimed at studying these issues in the rain and cloud fields since radar data of rain and satellite data of clouds are probably the data sets with the widest range of spatial and temporal scales available anywhere.

## 5.2 Scattering statistics in multifractal clouds

We have argued that over wide ranges, atmospheric fields may be expected to display strong multifractal variability. In a series of papers (Gabriel et al. 1986, Lovejoy et al. 1988, Lovejoy et al. 1990, Gabriel et al. 1990, Davis et al. 1990), we argued that scaling models involving ‘monofractal’ clouds do in fact already display interesting and realistic radiative properties. In particular, formulae for asymptotically optically thick clouds were derived and were shown to provide straightforward explanations for the ‘albedo paradox’. Davis et al. 1991a,b obtained some early results on more realistic multifractal clouds, including theoretical formulae for small distance behaviour, as well as supercomputer simulations. Cahalan 1989, 1994 and Barker and Daies 1992 studied optically thin monofractal clouds and Evans

1993 performed numerical simulations on optically thin multifractal clouds.

Here we give a glimpse at some more recent results which may provide the basis for systematic study of radiative transport in multifractal media. Specifically, we indicate how formulae analogous to eqs. 2, 3 for the multifractal optical density field arise for radiative properties. Consider the following definitions:



$k$  = extinction coefficient [ $m^2 kg^{-1}$ ]

$\langle \rho \rangle$  = mean cloud density [ $kgm^{-3}$ ]

$l$  = random photon path distance [ $m$ ]

$L$  = size of cloud [ $m$ ]

$l_m$  = mean free path (m.f.p.) of a photon in the equivalent homogeneous cloud =  $(k\langle \rho \rangle)^{-1}$  [ $m$ ]

$x = \frac{l}{L} = l^{-1}$  random photon distance, (fraction of cloud)

$\tau_p = \frac{l}{l_m}$  = random photon distance, (no. of m.f.p.'s =  $kx$ )

$\lambda = \frac{L}{l}$  = scale ratio  $\leq \Lambda$ , ( $\Lambda$  = maximum cascade resolution)

$\kappa = \frac{L}{l_m}$  = extinction parameter = no. of m.f.p.'s across cloud = mean optical depth = extinction coefficient in units such that  $L = 1, \langle \rho \rangle = 1$ .

Detailed analysis (Lovejoy et al. 1994b) of radiative transfer in multifractal clouds indicates that in a cloud whose large scale mean optical depth is  $\kappa$  that the photon optical path statistics can be described by a formalism extremely similar to the multifractal density statistics but with  $\kappa$  playing

the role of resolution  $\lambda$ . First, the optical distance between

$$\tau(l) = \int_l k \rho_\Lambda(z') dz' = k \rho_{l,d} l \quad (20)$$

where we have written  $\rho_l$  for the average density at resolution  $l$ . Using the above notation, we obtain:

$$\tau = \frac{\rho_\lambda}{\langle \rho \rangle} \lambda^{-1} \frac{L}{l_m} = \lambda^{\gamma-1} \kappa \quad (21)$$

which is the optical thickness over a distance  $l$  through a singularity of order  $\gamma$ . The direct (unscattered) transmission  $T$  across this distance is thus:

$$T(l) = e^{-\tau(l)} \quad (22)$$

Since the transmittance is the probability distribution for photon path lengths, we can average over the singularities, and obtain:

$$Pr(l' > l) = \langle T(l) \rangle = \langle e^{-\tau(l)} \rangle \quad (23)$$

Take  $\tau_p$  as the dimensionless photon path and write it as a function scaling with an ‘order of singularity  $\gamma_p$ ’ defined as follows:

$$\tau_p = \kappa^{\gamma_p} = \frac{l}{l_m} = \kappa x = \kappa \lambda^{-1} \quad (24)$$

or:

$$\lambda = \kappa^{(1-\gamma_p)} \quad (25)$$

We can now obtain a multifractal scattering formalism in which the extinction coefficient  $\kappa$  takes the place of the scaling parameter  $\lambda$ . Instead of the codimension function  $c(\gamma)$  of the singularities of the cloud density  $\gamma$  we rather talk about an analogue codimension function  $c_p(\gamma_p)$  which describes how the single photon path distance singularity  $\gamma_p$  varies with the extinction coefficient:

$$Pr(\tau_p \geq \kappa^{\gamma_p}) = Pr(l' > l) \approx \kappa^{-c_p(\gamma_p)} \quad (26)$$

$$\langle \tau_p^{q_p} \rangle \approx \kappa^{K_p(q_p)} \quad (27)$$

and anticipate that the two will be linked by a Legendre transform as in the standard multifractal case. The mean transmission in equation 23 is

obtained by averaging over the singularities, using eq. 2 to obtain the probability density of  $\gamma$ :

$$\kappa^{-c_p(\gamma_p)} \approx \langle T(\gamma, \lambda) \rangle = \int_{-\infty}^{\infty} e^{-\tau(\gamma, \lambda)} p(\gamma, \lambda) d\gamma \quad (28)$$

$$= \int_{-\infty}^1 e^{-\kappa \lambda^{\gamma-1}} \lambda^{-c(\gamma)} d\gamma = \int_{-\infty}^1 \kappa^{-\frac{\kappa \gamma \tau}{\log \kappa} - c\left(1 - \frac{1-\gamma \tau}{1-\gamma_p}\right)(1-\gamma_p)} d\gamma_\tau \quad (29)$$

where we have introduced the tranformation of variables:

$$1 - \gamma = \frac{1 - \gamma_\tau}{1 - \gamma_p} \quad (30)$$

In the lognormal case, the above integral can be done exactly; more generally, we can use the method of ‘moving maximum’ to obtain an asymptotic estimate of the integral by considering where the maximum occurs. This method will work as long as the latter is well-defined. This in turn hinges upon the existence of a solution to the following equation obtained by equating the  $\gamma_\tau$  derivative to zero:

$$\kappa^{\gamma_\tau} = -c'(\gamma) = -q \quad (31)$$

where the  $q$  is the Legendre conjugate of  $\gamma$ , it is the corresponding moment of the density distribution. We see immediately, that some  $c' < 0$ , must exist, i.e some negative moments must exist. While this seems rather general, in fact for universal multifractals, it is only true of the lognormal multifractal, all other universals have divergent moments for all negative moments. Assuming that the moments do exist, we obtain two families of codimension and moment scaling functions; their mutual relations are given in table 2.

Photon statistics	Cloud statistics
$q$	$= -q + K(q)$
$K_p(q_p) = \max_{\gamma_p} [q_p \gamma_p - c_p(\gamma_p)]$	$= K(q) = \max_{\gamma} [q \gamma - c(\gamma)]$
$1 - \gamma_p$	$= \frac{1}{1-\gamma}$
$c_p(\gamma_p) = \max_q [q \gamma_p - K_p(q_p)]$	$= \frac{c(\gamma)}{1-\gamma} = \frac{\max_q [q \gamma - K(q)]}{1-\gamma}$

Table 2: Summary of relations between multifractal cloud and photon scattering exponents

To give an example of the above, consider the  $\alpha = 2$  (lognormal multifractal). We have:

$$c(\gamma) = C_1 \left( \frac{\gamma}{C_1} + 1 \right)^2 \quad (32)$$

$$c_p(\gamma_p) = \frac{(1 - (1 + C_1)(1 - \gamma_p))^2}{4C_1(1 - \gamma_p)} \quad (33)$$

$$K(q) = C_1(q^2 - q) \quad (34)$$

$$K_p(q_p) = q_p - \frac{\sqrt{(1 + C_1)^2 + 4C_1q_p} - (1 + C_1)}{2C_1} \quad (35)$$

Numerics have shown (Brosamlén 1994) that these formulae are accurate even for clouds with mean optical thickness of the order of 4-10. Since the  $K_p(q_p)$  function is linear in homogeneous clouds, and the above  $K_p(q_p)$  function is close to linear -especially near  $q_p = 0$  which corresponds (see table 2) to the most probable photon path and singularity, we can use the above to approximately ‘renormalize’ the cloud, obtaining an effective extinction parameter:

$$\kappa_{\text{eff}} \approx \kappa^{\frac{1}{1+C_1}} \quad (36)$$

This result quite accurately predicts the numerical estimates of transmission through multifractal clouds discussed in the next section, and the exponent is the same as that obtained for anomalous diffusion in lognormal multifractals (also below). In a forthcoming paper (Lovejoy et al. 1994), we give many more details and extensions to multiple scattering.

Finally, a full understanding of the cloud radiation interaction involves a detailed understanding of the relation between cloud and radiation singularities. This is the subject of a paper by Naud et al. 1994.

### 5.3 Visible light scattering in multifractal clouds

To further understand the relations between the cloud and radiation fields, we seek to statistically relate the multifractal singularities of the various fields. From a numerical point of view, this is very demanding. Monte Carlo techniques avoid this problem, but require enormous numbers of simulated photons in order to yield good estimates of the internal cloud fields.

In optically thick clouds, photons undergo many scatterings and the details of the scattering phase function is not too important (according to the monofractal studies - Lovejoy et al. 1990, Gabriel et al. 1990, Davis et al. 1990 - it will affect prefactors, not exponents). In order to concentrate study on the effect of inhomogeneity, and to simplify calculations, a

two dimensional system was studied with phase functions which only permit scattering through 90 degrees; (discrete angle -DA- radiative transfer) the radiances decouple into non-interacting families with only four radiance directions each (details in Davis et al. 1991a). The phase functions were position independent; for simplicity we used isotropic DA phase functions. For validation purposes, the calculations were made using both Monte Carlo and relaxation techniques. The four radiances were then used to calculate the total radiance, the vertical and horizontal fluxes, as well as a component characterizing the anisotropy of the field. By varying the extinction coefficient, we were able to study the effect of increasing cloud thickness, optical thicknesses between 12 and 195. The calculations were performed on large (1024 x 1024 point grids using the Cray-2. at Palaiseau, France. The main conclusions were:

(1) Horizontal fluxes were typically less than 10 radiance fields were close to plane parallel, even though globally the radiative response was far from plane parallel.

(2) The anisotropic component was often very large; this points to the importance of ‘streaming’ or ‘channelling’ of photons through the more tenuous regions. It also indicates that the diffusion approximation will be poor even in optically thick clouds.

(3) The overall transmittances were compared with those of equivalent plane parallel clouds and with those obtained using the independent pixel approximation (each column independent).

The agreement was generally poor, although the independent pixel approximation was much better than the plane-parallel approximation. Such effects could readily account for the ‘albedo paradox’ (divergences of factors of ten or more between plane parallel and in situ estimates of cloud liquid water).

## 5.4 Diffusion on multifractals

The simplest nontrivial transport process in multifractals is diffusion and the diffusion equation is often taken as a simplified radiative transport model. Using this approximation, and taking  $J$  as the total intensity and  $D(\underline{x})$  as the (multifractal) diffusion constant, we have:

$$\nabla \cdot (D(\underline{x}) \nabla J) = \frac{\partial J}{\partial t} \quad (37)$$

where again, the diffusion constant is related to the cloud properties via:

$$D(\underline{x}) = \frac{1}{k\rho(\underline{x})} \quad (38)$$

where (as above)  $k$  is the extinction coefficient, and  $\rho(\underline{x})$  is the multifractal cloud density. In one dimension, many aspects are particularly simple. For example, the steady state  $J$  is a multifractal since:

$$\frac{\partial}{\partial x} \frac{1}{k\rho(x)} \frac{\partial J}{\partial x} = 0 \quad (39)$$

which implies:

$$\frac{\partial J}{\partial x} = k\rho(x) \quad (40)$$

i.e.  $J(x)$  will be multifractal with conservation parameter  $H$  (see eq. 9) increased by one (since  $J$  is an integral order one of the density, and  $H$  specifies the degree of fractional integration necessary to obtain the field from a conserved multifractal). The time dependent case is less straightforward, but still can be solved -at least in 1-D - (for details, see Silas et al. 1994). Because of the scaling, we anticipate that for photon random walks, the distance  $r$  after time  $t$  will vary as:

$$\langle r^q(t) \rangle = t^{S(q)} \quad (41)$$

where  $S(q)$  is the walk scaling exponent. Since the walk is an additive (monofractal) process,  $S(q)$  will be linear, defining as usual the ‘walk dimension’  $d_w$  we have:

$$S(q) = \frac{q}{d_w} \quad (42)$$

In one dimension, Silas et al. 1994 obtain the following result which (when applicable, i.e.  $K(-1)$  is finite), is believed to be exact:

$$d_w = 2 + K(-1) \quad (43)$$

In the above, the dressed scaling exponent  $K$  is used; since this is always positive,  $d_w > 2$ , hence the photon walk is subdiffusive (‘normal’ diffusion has  $d_w = 2$ ; here, the photon gets partially ‘trapped’ between large singularities, this subdiffusive behaviour was noted in a numerical example studied by Meakin 1987). Eq. 43 shows that as expected from the monofractal behaviour of the path, only a single multifractal singularity is important for the walk ( $\gamma_{cr} = K'(-1)$ ). Indeed, the critical role of this singularity can be considered to produce a dynamical ‘phase’ transition, since truncating the high multifractal singularities ( $\gamma$ ) has no effect on the transport. As long as  $\gamma > \gamma_{cr}$ , the transport is anomalous, becoming ‘normal’ discontinuously for  $\gamma < \gamma_{cr}$ .



## 5.5 Radar reflectivity of multifractals ‘speckle’

Radar remote sensing of sea ice, ocean or land surface or rain involves inhomogeneities due to multifractal structures that extend down below not only radar pulse volumes but also below microwave wavelengths (Lovejoy and Schertzer 1990a,b, Duncan et al. 1993). This leads to the ‘speckle’ phenomenon whereby small changes in look angle will be associated with large changes in intensity. It also implies that the usual way of removing this effect (by assuming subpulse volume statistical homogeneity and hence incoherent scattering) will lead to systematic errors. To correct the standard theory for these effects, we can model the reflector as a multifractal distribution of dielectrics. In the simplest case appropriate for rain, a scalar approximation is sufficient for most purposes since the scattering from drops is nearly isotropic. Other situations such as sea ice will involve multifractal distributions of dielectric tensor and will require the formalism of Lie cascades (Schertzer and Lovejoy 1993).

Actually, even for the scalar case basic results can be obtained using complex (Lie) cascades, since the radar detects a (complex) Fourier component. To see this consider a one (spatial) dimensional distribution of radar scatterers  $\sigma_\Lambda(x, t)$ , varying in time, with an inner (dissipation scale)  $\Lambda^{-1}$ , the radar number is  $k/2$  (the factor 2 is for simplicity; it will take into account the round trip distance to the scatterers), and the pulse volume is length  $\lambda^{-1}$ . We will be taking the outer scale of the process to be 1, hence we will be interested in  $\lambda > 1$ . Similarly, we will use units such that the velocity is unity (it is assumed to be independent of scale, we use isotropic space/time). The spatial average of the amplitude of the reflected wave is:

$$A_\lambda(k) = \frac{1}{\lambda^{-1}} \int_0^{\lambda^{-1}} e^{ikx} \sigma_\Lambda(x) dx \quad (44)$$

If we consider  $e^{ikx} \sigma_\Lambda(x)$  ( $k < \Lambda$ ) as a complex (bare) cascade quantity, then, for  $\lambda \ll k < \Lambda$ ,  $A_\lambda(k)$  is simply a dressed complex cascade. Using results on complex cascades, we obtain

$$Re(K_A(q)) = K_\sigma(q) + qC_{1,R} \quad (45)$$

where only  $C_{1,R} = Re(K_A(1))$  remains to be determined. This result has been tested numerically by Duncan 1993, Duncan et al. 1994 and indicated that the statistics of the cross-section field ( $\sigma, K_\sigma(q)$ ) and the modules of the amplitude ( $|A|, Re(K_A(q))$ ) are the same except for a term linear in  $q$  which represents a scale dependent bias. By using space-time transformations, it is also possible to model the temporal behaviour of the reflectivity field. Duncan et al. 1994 shows excellent agreement is found with rain data.

## 6 Conclusions

We have summarized a growing body of work indicating that - as theoretically predicted - due to underlying nonlinear but scale invariant dynamics, that many geophysical fields are multifractal over substantial ranges of scale. This implies that they are strongly dependent on the resolution at which they are observed and that remote sensing algorithms must systematically remove these effects if sensor independent measurements of geophysical fields are to be obtained.

We also summarized the basic properties of multifractals. Although the properties of multifractals are more fully discussed in the accompanying paper SL94, we concentrate on the discovery of universal multifractals. In particular universality classes exist in which most of the details of the details of the dynamics are ‘washed out’ leaving a dependence on just three basic universal parameters. Without such universality classes, multifractals would be sensitive to an infinite number of model parameters and would have little use. We summarised the empirical evidence for these two distinct properties in over 20 geophysical fields (many of them remotely sensed).

We also indicated that since scale invariance is a dynamical symmetry principle, it may be expected to hold widely; however, the scale changing operator will generally not be isotropic, hence we do not expect to observe self-similar multifractals and estimates of the generator of the scale changing operator using the Scale Invariant Generator technique confirm this. However, by allowing for very general (even stochastic) generators, we can take into account the observed texture and morphology of geophysical processes.

We also showed how to simulate multifractal fields, and we examined some of their properties. We argued that a full understanding of the relation between physically interesting quantities, and the remotely sensed radiances will require the use of such models, and we illustrated these ideas on radiative and diffusive transport, as well as on the problem of radar speckle.

## 7 Acknowledgments

We thank G. Brosamlén, Y. Chiriginskaya, A. Davis, N. Desaulniers-Soucy, M. Duncan, F. Francis, H. Gaonac’h, C. Hooge, P. Hubert, P. Ladoy, A. Lazarev, D. Lavallée, C. Naud, S. Pecknold, F. Schmitt, J. Todeschuk, and B. Watson for helpful comments, discussion and technical assistance.

## 8 References

- [1] Adelfang, S. I. 1971, On the relation between wind shears over various intervals, *J. Atmos. Sci.*, 10, 138.
- [2] Austin, L. B., Austin, G. L., Schuepp, P. H., Saucier, A. 1991, Atmospheric boundary layer variability and its implication for CO<sub>2</sub> flux measurements. In *Non-linear Variability in Geophysics: Scaling and Fractals*. Kluwer, D. Schertzer and S. Lovejoy ed.s, pp. 269-278.
- [3] Bak, P., Tang, C. and Wiessensfeld, K. 1987, Self-Organized Criticality: An explanation of  $1/f$  noise. *Phys. Rev. Lett* 59, 381-384.
- [4] Barker H. W. and Davies, J. A. 1992, Solar Radiative Fluxes for Stochastic, Scale-invariant Broken Cloud Fields, *J. Atmos. Sciences*, 49, 1115-1126.
- [5] Brax, P. and Pechanski, R. 1991, Levy stable law description on intermittent behaviour and quark-gluon phase transitions. *Phys. Lett. B* 253, 225-230.
- [6] Brenier, P. 1990, Simulation dynamique multifractale des nuages, Master's thesis, Ecole Nationale supérieure de techniques avancées, Paris, France.
- [7] Brenier, P., Schertzer, D., Sarma, G., Wilson, J. and Lovejoy, S. 1990, Continuous multiplicative cascade models of passive scalar clouds. *Annales Geophysicae* 8 (special edition), 320.
- [8] Brosamlen, G., 1994, Radiative transfer in lognormal multifractal clouds and analysis of cloud liquid water data, MSc. thesis, McGill University, 69pp.
- [9] Brosamlen, G., Lovejoy, S. and Schertzer, D. 1994, Multifractal analysis of cloud liquid water over the range 5m to 330 km: a new test of the unified scaling model. (submitted to *J. Atmos. Sci.*).
- [10] Cahalan, R. F. 1989, Overview of fractal clouds, paper presented at RSRM'87, *Advances in Remote Sensing*, 371-389, edited by A. Deepak et al., A. Deepak, Hampton, Va.
- [11] Cahalan, R. F. 1994, Bounded cascade clouds: albedo and effective thickness, *Nonlinear processes in Geophysics*, 2/3, 156-167.
- [12] Chigirinskaya, Y., Schertzer, D., Lovejoy, S., Lazarev, A. and Ordanovich, A. 1994, Unified multifractal atmospheric dynamics tested in the tropics Part 1: horizontal scaling and self organized criticality, *Nonlinear Processes in Geophysics*, 2/3, 105-114.
- [13] Davis, A., Lovejoy, S., Gabriel, P., Schertzer, D. and Austin, G. L. 1990, Discrete angle radiative transfer. Part III: numerical results on homogeneous and fractal clouds. *J. Geophys. Res.* 95, 11729-11742.

- [14] Davis, A., Lovejoy, S. and Schertzer, D. 1991a, Discrete angle radiative transfer in a multifractal medium, Ed. V. V. Varadan, SPIE, 1558, 37-59.
- [15] Davis, A., Lovejoy, S. and Schertzer, D. 1991b, Radiative transfer in multifractal clouds. In *Non-linear variability in geophysics: Scaling and Fractals*. Kluwer, Schertzer, D. and Lovejoy S. (ed.s), pp. 303-318.
- [16] Davis, A., Marshak, A., Wiscombe, W. and Cahalan, R. 1994, Multifractal characterization of nonstationary and intermittency in geophysical fields: observed, retrieved or simulated, *J. Geophys. Res.*, 99, 8055-8072.
- [17] Dremine, I. M., 1994, Fractality and the anomalous dimension of Quantum Chromodynamics, *Fractals in the natural and applied sciences*, M. M. Novak Ed. 101-108.
- [18] Duncan, M. R. 1993, The universal multifractal nature of radar echo fluctuations, PhD. thesis, McGill University, 220pp.
- [19] Duncan, M. R., Lovejoy, S. and Schertzer, D. 1994, Multifractals and the radar observer's problem, (submitted to *J. Atmos. Sci.*)
- [20] Duncan, M. R., Lovejoy, S., Fabry, F. and Schertzer, D. 1993, Radar measurement scales and nonuniformity in the rainfield. The 2nd Inter. Symp. on Hydrological Appl. of Weather Radar, Univ. of Hannover, Sept. 7-10th.
- [21] Endlich, R. M. and Mancuso, R. L. 1968, Objective analysis of environmental conditions associated with severe thunderstorms and tornadoes. *Mon. Wea. Rev.* 96, 342-350.
- [22] Evans, K. F., 1993, A general solution for stochastic radiative transfer, *Geophys. Res. Lett.*, 20, 19, 2075-2078.
- [23] Fan, A. H., 1989, Chaos additif et multiplicatif de Levy. *C.R. Acad Sci. Paris I*, 308, 151-154.
- [24] Francis, F., 1993, Multifractal characteristics of sea ice from SAR imagery. 3rd year report, Physics, McGill University.
- [25] Gabriel, P., Lovejoy, S., Austin, G. L. and Schertzer, D. 1986, Radiative transfer in extremely variable fractal clouds, 6th conference on atmospheric radiation, 230-234, AMS, Boston.
- [26] Gabriel, P., Lovejoy, S., Schertzer, D. and Austin, G. 1988, Multifractal analysis of resolution dependence in satellite imagery. *J. Geophys. Res.* 93, 1373-1376.
- [27] Gabriel, P., Lovejoy, S., Davis, A., Schertzer, D. and Austin, G. L. 1990, Discrete angle radiative transfer. Part II: renormalization approach to scaling clouds. *J. Geophys. Res.* 95, 11717-11728.
- [28] Gaonac'h, H., Lovejoy, S. and Stix, J. 1992, The resolution dependence

- of basaltic lava flows and their fractal dimensions. *Geophys. Res. Lett.* 19, 785-788.
- [29] Garrido, P., Lovejoy, S. and Schertzer, D. 1993, Universal multifractals and the large scale structure of the universe, (in preparation).
  - [30] Hooge, C., 1993, Earthquakes as a space-time multifractal process, MSc thesis, McGill University, 152pp.
  - [31] Hooge, C., Lovejoy, S., Schertzer, D., Schmitt, F. and Malouin, J. F. 1994, Multifractal phase transitions: the origin of self-organized criticality in earthquakes, *Nonlinear Proc. in Geophys.* (in press).
  - [32] Hubert, P., Tessier, Y., Lovejoy, S., Schertzer, D., Ladoy, P., Carbonnel, J. P. and Violette, S. 1993, Multifractals and extreme rainfall events. *Geophys. Res. Lett.* 20, 931-934.
  - [33] Kerman, B., 1993, A multifractal equivalent of the Beaufort scale for sea-state. *Geophys. Res. Lett.*, 20, 297-300.
  - [34] Ladoy, P., Schertzer, D. and Lovejoy, S. 1986, Une étude d'invariance locale-regionale des temperatures, *La Météorologie*, 7, 23-34.
  - [35] Ladoy, P. Schmitt, F., Schertzer, D. and Lovejoy, S. 1993, observations pluviométriques à Nimes, *C. R. Acad. des Sciences*, 317, II, 775-782.
  - [36] Larnder, C., Desaulniers-Soucy, N., Lovejoy, S., Schertzer, D., Braun, C. and Lavallée, D. 1992, Universal multifractal characterization, and simulation of speech, *Int. J. Bifurcation and Chaos*, 2, 715-719.
  - [37] Lavallée, D. 1991, Multifractal techniques: analysis and simulations of turbulent fields. Ph.D. thesis, McGill University, Montreal, Canada.
  - [38] Lavallée, D., Lovejoy, S., Schertzer, D. and Ladoy, P. 1993a, Nonlinear variability and landscape topography: analysis and simulation. *Fractals in Geography*, ed.s L. De Cola and N. Lam, 171-205.
  - [39] Lavallée, D., Jourdan, D., Gautier, C., and Hooge, C. 1993b, Universal multifractal properties of microwave satellite data. *Proc. of Hydrofractals*, '93, p. 21-26.
  - [40] Lazarev, A., Schertzer, D., Lovejoy, S. and Chigirinskaya, Y. 1994, Unified multifractal atmospheric dynamics tested in the tropics: part II, vertical scaling and Generalized Scale Invariance, *Nonlinear Processes in Geophysics*, 1, 115-123.
  - [41] Lewis, G. 1993, The Scale Invariant Generator technique and scaling anisotropy in geophysics. MSc. thesis, McGill University (110pp).
  - [42] Lovejoy, S. 1981, Analysis of rain areas in terms of fractals, 20th conf. on radar meteorology, 476-484, AMS, Boston.
  - [43] Lovejoy, S. and Schertzer, D. 1986, Scale invariance in climatological temperatures and the spectral plateau. *Annales Geophys.*, 4B, 401-410.

- [44] Lovejoy, S. and Schertzer, D. 1986, Scale invariance, symmetries, fractals and stochastic simulations of atmospheric phenomena, *Bulletin of the Amer. Meteor. Soc.*, 67, 21-32.
- [45] Lovejoy, S. and Schertzer, D. 1989, Fractal clouds with discrete angle radiative transfer. I.R.S. 88, Eds. C. Lenoble and J. F. Geylyn, Deepak publishing, 99-102.
- [46] Lovejoy, S. and Schertzer, D. 1990, Fractals, rain drops and resolution dependence of rain measurements, *J. Appl. Meteor.*, 29, 1167-1170.
- [47] Lovejoy, S. and Schertzer, D. 1990a, Multifractals, universality classes, satellite and radar measurements of clouds and rain. *J. Geophys. Res.*, 95, 2021-2034.
- [48] Lovejoy, S., Gabriel, P., Davis, A., Schertzer, D., and Austin, G. L. 1990b, Discrete angle *J. Geophys. Res.*, 95, 11699-11715.
- [49] Lovejoy, S., Schertzer, D., Silas, P., Tessier, Y. and Lavallée, D. 1993, The unified scaling model of the atmospheric dynamics and systematic analysis of scale invariance in cloud radiances, *Annales Geophysicae*, 11, 119-127.
- [50] Lovejoy, S., Schertzer, D., Hooge, C. and Todeschuk, J. 1994a, Multifractal analysis of aeromagnetic data (in preparation for *Geophys. Res. Lett.*)
- [51] Lovejoy, S., Watson, B., Brosamlen, G. and Schertzer, D., 1994b, A multifractal formalism for scattering statistics in multifractal clouds (prepared for *J. Stat. Phys.*)
- [52] Lovejoy, S., Lavallée, D., Schertzer, D. and Ladoy, P. 1994c, The  $l^{\frac{1}{2}}$  law and multifractal topography, submitted to *Nonlinear Proc. in Geophys.*
- [53] Mandelbrot, B. 1967, How long is the coastline of Britain? Statistical self-similarity and fractional dimension. *Science*, 155, 636-638.
- [54] Mandelbrot, B. 1983, *The Fractal Geometry of Nature*, Freeman, San Francisco.
- [55] Meakin, P. 1987, Random walks on multifractal lattices, *J. Phys. A*, 20, L771-L777.
- [56] Meneveau, C. and Sreenevasan, K. R. 1987, Simple multifractal cascade model for fully developed turbulence. *Phys. Rev. Lett.*, 59, 13, 1424-1427.
- [57] Naud, C., Schertzer, D. and Lovejoy, S. 1994, Analysis and simulation of radiative transport in multifractal disordered media, *Stochastic models in geosystems*, Ed. W. A. Woyczynski, Institute of Mathematics and its Applications (in press).
- [58] Nguyen, V. T. V., Pandley, G. R. and Rousselle, J. 1993, Estimation

- of missing short-duration rainfalls using data measured at longer time scales. Proc. of the 6th Inter. Conf. on Urban Storm Drainage, September 12-17, 1993, Niagara Falls, Ontario, Canada, Vol. 1, Edited by J. Marsalek, and H. C. Torno, pp. 170-175.
- [59] Olsson, J. 1994, Estimation of multifractal parameters for a high-resolution rainfall time series, *Nonlinear Processes in Geophysics* (submitted).
  - [60] Parisi, G., and Frisch, U. 1985, A multifractal model of intermittency. *Turbulence and predictability in geophysical fluid dynamics and climate dynamics.*, 84-88, Eds. M. Ghil, R. Benzi, G. Parisi, North-Holland.
  - [61] Pecknold, S., Lovejoy, S., Schertzer, D., Hooge, C. and Malouin, J. F. 1993, The simulation of universal multifractals. *Cellular Automata: Prospects in astrophysical applications*, Eds. J. M. Perdang, A. Lejeune, World Scientific, pp. 228-267.
  - [62] Perrin, J. 1913, *Les Atomes*, NRF-Gallimard, Paris.
  - [63] Pflug, K., Lovejoy, S. and Schertzer, D. 1993, Generalized Scale Invariance, differential rotation and cloud texture: analysis and simulation, *J. Atmos. Sci.*, 50, 538-553.
  - [64] Ratti, S. P., Salvadori, G., Gianini, G., Lovejoy, S. and Schertzer, D. 1994, A Universal multifractal approach to intermittency in high energy physics, *Z. Phys. C61*, 229-237.
  - [65] Richardson, L. F. 1961, The problem of contiguity: an appendix of statistics of deadly quarrels. *General Systems Yearbook*, 6, 139-187.
  - [66] Salvadori, G., Ratti, S. P., Belli, G., Lovejoy, S. and Schertzer, D. 1994, Multifractal objective analysis of Seveso ground pollution. *Toxicol. and Environ. Chem.* 43, 63-76.
  - [67] Saucier, A. 1992, Effective permeability of multifractal porous media, *Physica A*, 183, 381- 397.
  - [68] Schertzer D. and Lovejoy, S. 1985a, The dimension and intermittency of atmospheric dynamics, *Turbulent Shear flow* 4, 7-33, B. Launder ed., Springer.
  - [69] Schertzer, D. and Lovejoy, S. 1985b, Generalised scale invariance in turbulent phenomena *Physico-Chemical Hydrodynamics Journal*, 6, 623-635.
  - [70] Schertzer, D. and Lovejoy, S. 1987, Physically based rain and cloud modelling by anisotropic, multiplicative turbulent cascades. *J. Geophys. Res.*, 92, 9692-9714.
  - [71] Schertzer, D. and Lovejoy, S. 1989, Nonlinear variability in geophysics: multifractal analysis and simulations. *Fractals: their physical origins and properties*, Pietronero ed., Plenum Press, New York, 49-79.

- [72] Schertzer, D. and Lovejoy, S. 1991a, Scaling, fractals and non-linear variability in geophysics, Kluwer, 318pp.
- [73] Schertzer, D. and Lovejoy, S. 1991b, Nonlinear geodynamical variability: multiple singularities, universality and observables. In: Scaling, fractals and non-linear variability in geophysics, D. Schertzer and S. Lovejoy ed.s, Kluwer, 41-82.
- [74] Schertzer, D., Lovejoy, S., Lavallée, D. and Schmitt, F. 1991, Universal hard multifractal turbulence, theory and observations. Nonlinear Dynamics of Structures, R. Z. Sagdeev et al. ed.s, World Scientific, 213-235.
- [75] Schertzer, D. and Lovejoy, S. 1992, Hard and soft multifractal processes: Physica A, 185, 187- 194.
- [76] Schertzer, D. and Lovejoy, S. 1993, Multifractal generation of self-organized criticality, In: Fractals in the natural and applied sciences, M. M. Novak, ed., Elsevier North-Holland, 325-339.
- [77] Schertzer, D., Lovejoy, S. and Lavallée, D. 1993, Generic multifractal phase transitions and self-organized criticality. In: Cellular automata: prospects in astrophysical applications, J. M. Perdang and A. Lejeune, ed.s, World Scientific, pp. 216-227.
- [78] Schertzer, D. and Lovejoy, S. 1994a, From scalar cascades to Lie cascades: joint multifractal analysis of rain and cloud processes. In: Space/time Variability and Interdependence for Various Hydrological Processes, R. A. Feddes, ed., Cambridge University Press, in press.
- [79] Schertzer, D. and Lovejoy, S. 1994b, Multifractals and turbulence: fundamentals and applications, World Scientific (in press).
- [80] Schertzer, D. and Lovejoy, S. 1994c, Standard and advanced multifractal techniques in remote sensing (this volume).
- [81] Schmitt, F., Lavallée, D., Schertzer D. and Lovejoy, S. 1992, Empirical determination of universal multifractal exponents in turbulent velocity fields, Phys. Rev. Lett., 68, 305-308.
- [82] Schmitt, F., Schertzer, D., Lovejoy, S. and Brunet, Y. 1994, Estimation of universal multifractal indices for atmospheric turbulent velocity fields. Fractals, 3, 568-575.
- [83] Schmitt, F., Schertzer, D., Lovejoy, S. and Brunet, Y. 1994, Empirical study of multifractal phase transitions in atmospheric turbulence, Nonlinear Processes in Geophysics, 2/3, 95-104.
- [84] Segal, B. 1979, High-intensity rainfall statistics for Canada, no. CRC 1329-E, Ottawa (Ontario), Canada.
- [85] Silas, P. K., Lovejoy, S. and Schertzer, D. 1993, Single phase diffusion in multifractal porous rock, Proceedings of Hydrofractals '93, p1-6.



- [86] Steinhaus, H. 1954, Length, shape and area. *Colloquium Mathematicum*, 3, 1-13.
- [87] Steinhaus, H. 1962, *Mathématiques en instantanés*, Paris, Flammarion.
- [88] Tessier, Y., Lovejoy, S. and Schertzer, D. 1993a, Universal fractals in rain and clouds: theory and observations, *J. Appl. Meteor.*, 32, 223-250.
- [89] Tessier, Y., Lovejoy, S., Schertzer, D., Lavallée, D. and Kerman, B. 1993b, Universal multifractal indices of the ocean surface at far red wavelengths, *Geophys. Res. Lett.*, 20, 1167-1170.
- [90] Tessier, Y., Hubert, P., Carbonnel, J. P., Lovejoy, S. and Schertzer, D. 1993c, Phase transitions and universal multifractals in river flows. *Proceedings of Hydrofractals '93*, A1-A6.
- [91] Tessier, Y., Lovejoy, S. and Schertzer, D. 1994, The multifractal global raingauge network: analysis and simulation, (*J. Appl. Meteor.*, in press).
- [92] Venig-Meinesz, F. A. 1951, A remarkable feature of the Earth's topography. *Proc. K. Ned. Akad. Wet. Ser. B Phys. Sci.*, 54, 212-228.
- [93] Visvanathan, R., Weber, C. and Gibart, P. 1991, The stochastic coherence and the dynamics of global climate models and data. In *Non-linear variability in geophysics: Scaling and Fractals*. Kluwer, D. Schertzer and S. Lovejoy ed.s, pp. 269-278.
- [94] Wilson, J., Lovejoy, S. and Schertzer, D. 1991, Physically based cloud modelling by scaling multiplicative cascade processes. *Scaling, fractals and non-linear variability in geophysics*, D. Schertzer and S. Lovejoy ed.s, 185-208, Kluwer.

# Chapter 6

## Multifractals: Theory and Application to Image Texture Recognition

*Stefano Fioravanti\**

### 1 Introduction

In recent years, the use of fractal geometry in image processing has grown, especially for texture characterization. In particular, the fractal dimension employed as a descriptor of natural object surfaces has been widely investigated, with good performance [18], [15]. However, as discussed in [2], the fractal dimension is not an optimal tool for fully characterizing textures. To overcome the drawbacks of the single fractal dimension, fractal geometry has to be extended, and the  $q$ -th order fractal dimensions introduced. So, one has to deal with the concept of *multifractality*.

As pointed out elsewhere [9], the multifractality spectrum function  $D(q)$  allows one to characterize efficiently natural textures, even if they are quite similar. Such a function shows some interesting properties, which will be presented and discussed in the following.

### 2 $H$ -dimension, box-dimension, and fractal dimension

Usually, when people think about a set and its dimension, they think about its topological dimension. From Euclidean geometry, we know that the topological dimension is equal to 1 for a line segment, 2 for a surface, 3 for

---

\*Dipartimento di Ingegneria Biofisica ed Elettronica, Università degli Studi di Genova, Italy

a cube, and so on. Moreover, the area of a segment is null while its length is finite and different from zero, as is the volume occupied by a surface.

But there are bounded sets with topological dimensions equal to 1, infinite lengths, and null areas. Hence, one can envisage a new kind of dimension, i.e. a real (and not integer) dimension between 0 and 1, for which, if one found a measure concept linked to such a real dimension, the measure of the set is finite and different from zero. This is the basic concept of the Hausdorff-Besicovitch dimension (briefly, *H*-dimension). Mandelbrot gave the following definition of a fractal set: *A fractal set is, by definition, a set for which the H-dimension is strictly greater than its topological dimension* [14].

Let consider a line *L* that has to be measured in the different topological dimensions; to measure its length  $M_1$  (i.e., the measure in the dimension 1), the line can be broken into rectilinear segments or covered by balls, disks, or other structural elements with length  $\delta$ . This results in

$$M_1 = \lim_{\delta \rightarrow 0} N(\delta)\delta \quad (1)$$

where  $N(\delta)$  is the number of segments that are needed to cover the line (see Figure 1).

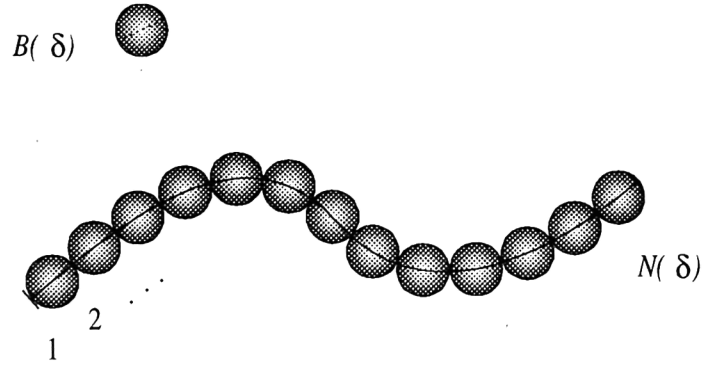


Figure 1: Line covering.

Analogously, for its area  $M_2$ , one can cover the line with small boxes with side  $\delta$ , so obtaining

$$M_2 = \lim_{\delta \rightarrow 0} N(\delta)\delta^2 \quad (2)$$

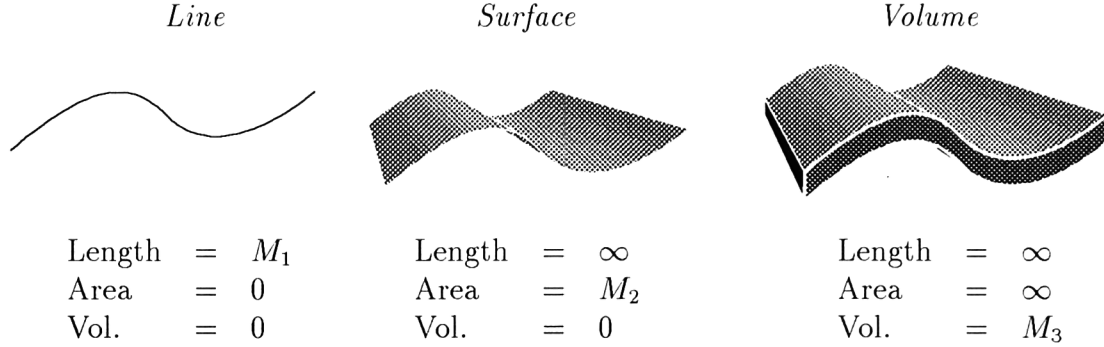


Figure 2: Length, area and volume measures.

and so on (see Figure 2). By generalizing, one can imagine that the measure of a set in the  $d$  dimension is

$$M_d = \lim_{\delta \rightarrow 0} N(\delta) \delta^d \quad (3)$$

The box-dimension  $D_b$  of such a set is then that value of  $d = D_b$  for which such a limit is finite and different from zero, i.e.

$$M_d = \begin{cases} +\infty & \text{if } d < D_b \\ 0 & \text{if } d > D_b \end{cases} \quad (4)$$

If the limit of  $M$  is a finite non-null number, for  $\delta$  small enough one can make the following approximation

$$N(\delta) \approx k \delta^{-D} \quad (5)$$

so allowing us to obtain the box-dimension  $D_b$

$$D_b = \lim_{\delta \rightarrow 0} \frac{\log N(\delta)}{\log \delta} \quad (6)$$

The box-dimension  $D_b$  so defined is valid in every  $E$ -dimensional metric space and is commonly called the *fractal dimension*  $D$  of the set.

### 3 Multifractality and the binary multiplicative process

Multifractality is a property relevant to objects with subsets whose fractal dimensions do not equal the global one. So, to characterize the multifractality of a set, one has to find the spectrum of the fractal dimensions of

the subsets which are different from that of the global set; in short, the multifractality spectrum.

Let us suppose we have a segment  $S$  of size  $s_S = 1$ , over which a set of  $P$  points is distributed. Let us divide the segment into  $N = 2^n$  equal parts; let  $N_i$  be the number of points contained in the  $i$ -th partition, and  $\mu_i$  the percentage contained in it. In other words,  $\mu_i = N_i/P$ . If we consider  $P$  and  $n$  to be increasing to infinite, the set

$$M = \{\mu_i\}_{i=0}^N \quad (7)$$

contains all the information about the distribution of the points over  $S$ . Let us now consider a process (i.e. a binary multiplicative process) that generates a distribution of points. These  $P$  points are distributed as follows:

1. divide  $S$  into two equal parts and distribute over each a different percentage of the initial population (i.e.  $\mu_0, \mu_1$ , where  $\mu_0 + \mu_1 = 1$ );
2. repeat recursively the above procedure for each subpart of the segment; in other words, re-distribute the population present over that sub-segment over the two halves.

At the  $n$ -th iteration the following  $M$  set, characteristic of the distribution, is obtained

$$M = \{(\mu_0)^n, (\mu_0)^{n-1}\mu_1, \dots, (\mu_1)^n\} \quad (8)$$

By counting the intervals over which it is distributed a portion of the population equal to  $\rho_k$ , where

$$\rho_k = \mu_0^{n-k} \quad (9)$$

they result to be

$$N(k) = \binom{n}{k} \quad k \in (0, \dots, n) \quad (10)$$

As we have to calculate the limit for  $(n, P)$  tending to infinity, it is useful to define  $\xi = \frac{k}{N}$  and solve the equations as a function of such a variable. Hence

$$N(\xi) = \binom{n}{n\xi} \quad (11)$$

and

$$\rho_\xi = (\mu_0^{1-\xi} \mu_1^\xi)^n \quad (12)$$

Let us consider now the set of intervals (sets) with population  $\rho_\xi$ , called  $S_\xi$ , and look for its fractal dimension

$$M_d(S_\xi) = \lim_{\delta \rightarrow 0} \sum_{S_\xi} \delta^d = \lim_{\delta \rightarrow 0} N(\xi) \delta^D = \begin{cases} 0 & d > D(\xi) \\ +\infty & d < D(\xi) \end{cases} \quad (13)$$

By computing such a limit with  $\delta = 2^{-n}$  (with  $n \rightarrow +\infty$ ), and by using the Stirling relation

$$n! \approx \sqrt{2\pi n}^{(n+1)/2} e^{-n} \quad (14)$$

one obtains

$$N_n(\xi) \approx \frac{1}{\sqrt{2\pi n \xi(1-\xi)}} e^{-n[\xi \log \xi + (1-\xi) \log(1-\xi)]} \quad (15)$$

and

$$D(\xi) = f(\xi) = -\frac{\xi \log \xi + (1-\xi) \log(1-\xi)}{\log 2} \quad (16)$$

It is possible to observe how the sets  $S_\xi$  characterize the distribution of points over  $S$ , as all of them are sets of points with the same densities and

$$S = \bigcup_{\xi} S_\xi \quad (17)$$

Moreover, even if the fractal dimension of  $S$  is equal to 1 (it is a segment), the fractal dimensions  $D(S_\xi)$  assume values between 0 and 1; each sub-set has its own fractal dimension, and from this originates the concept of multifractality.

The parameter  $\xi$  is used not so much in the literature; as suggested by Mandelbrot too, it is better to use the Lipschitz-Holder exponent  $\alpha$ , whose definition comes from

$$\rho_\xi = \delta^\alpha \quad (18)$$

By considering  $\delta = 2^{-n}$ , one obtains

$$\alpha = \frac{\log \rho_\xi}{\log \delta} = \frac{\xi \log \rho_\xi + (1-\xi) \log(1-\rho_\xi)}{\log 2} \quad (19)$$

It should be noted that  $\alpha$  is defined in  $[\alpha_m, \alpha_M]$ , as  $\xi \in [0, 1]$

$$\begin{cases} \alpha_m &= -\frac{\log(1-\rho_\xi)}{\log 2} \\ \alpha_M &= -\frac{\log(\rho_\xi)}{\log 2} \end{cases} \quad (20)$$

Moreover, there is a linear biunivocal correspondance between  $\alpha$  and  $\xi$ , which allows us to express everything as a function of  $\alpha$ , that is

$$S = \bigcup_{\alpha} S_{\alpha} \quad (21)$$

and

$$f(\alpha) = f[\alpha(\xi)] \quad (22)$$

is the fractal dimension associated with the set  $S_{\alpha}$ .

## 4 The function $\tau(q)$

When analyzing discrete sets (i.e., digital images), the simplest way to manage them is offered by the so-called *box-counting* method, which consists in dividing the sets into boxes. However, in such a way, one loses much information contained in the set; as a matter of fact, one loses information about the distribution of points.

To overcome such a drawback it is necessary to consider not only the boxes covering the set, but also the masses that they contain. Hence, to each box is associated a quantity

$$\mu_i = \frac{N_i}{N} \quad (23)$$

where  $N$  is the total number of points in the set, and  $N_i$  is the number of points contained into the  $i$ -th box. Hence, one has the set  $M$

$$M = \{\mu_i\}_{i=0}^B \quad (24)$$

where  $B$  is the number of boxes that are needed to cover the set. Moreover

$$D_b = \lim_{\delta \rightarrow 0} \frac{\log B}{\log \delta} \quad (25)$$

is the box-dimension of  $S$ .

In order to weight differently the subset of  $S$ , depending on the masses contained in the boxes, one has to not only measure  $S$  but also to compute

$$M_d(q, \delta) = \sum_{i=0}^{N(\delta)} \mu_i^q \delta^d = N(q, \delta) \delta^d \quad (26)$$

where

$$\lim_{\delta \rightarrow 0} M_d(q, \delta) = \begin{cases} 0 & d > \tau(q) \\ +\infty & d < \tau(q) \end{cases} \quad (27)$$

It follows that, in the computation of the box-dimension,

$$\tau(q) = -\lim_{\delta \rightarrow 0} \frac{\log [N(q, \delta)]}{\log \delta} \quad (28)$$

In this way, depending on the values of  $q$ , the different subsets have different weights; this fact can also be evidenced by the behaviour of  $\tau(q)$  at the boundaries of the existence range.

If the maximum and minimum values assumed by the densities are indicated by  $\mu_m$  and  $\mu_M$ , and  $N_m$  and  $N_M$  the number of boxes in the same cases, the infinite limit

$$\lim_{q \rightarrow -\infty} \tau(q) \approx -\lim_{\delta \rightarrow 0} \lim_{q \rightarrow -\infty} \frac{\log \sum_{i=0}^{N_m} \mu_i^q}{\log \delta} = \lim_{\delta \rightarrow 0} \lim_{q \rightarrow -\infty} q \frac{\log N_m}{\log \delta} \quad (29)$$

behaves as a straight line. By considering the derivative of  $\tau(q)$

$$\frac{d\tau(q)}{dq} = -\lim_{\delta \rightarrow 0} \frac{\sum_i \mu_i^q \log \mu_i}{\log \delta - \sum_i \mu_i^q} \quad (30)$$

its limits are

$$\begin{aligned} \lim_{q \rightarrow -\infty} \frac{d\tau(q)}{dq} &= -\lim_{\delta \rightarrow 0} \frac{\log \mu_m}{\log \delta} = -\alpha_M \\ \lim_{q \rightarrow +\infty} \frac{d\tau(q)}{dq} &= -\lim_{\delta \rightarrow 0} \frac{\log \mu_M}{\log \delta} = -\alpha_m \end{aligned} \quad (31)$$

Moreover,  $\tau(0)$  is the fractal dimension of the set under examination, and  $\tau(1) = 0$  as the  $\{\mu_i\}$  are normalized to the unit interval.

In the case of the quaternary multiplicative process used before, it is possible to find out the analytical form of  $\tau(q)$  when  $\delta = 2^n$

$$N(d, \delta) = \sum_{k=0}^n \binom{n}{k} p^{qk} (1-p)^{q(n-k)} = [p^q + (1-p)^q]^n \quad (32)$$

from which

$$\tau(q) = \frac{\log [p^q + (1-p)^q]}{\log 2} \quad (33)$$

In Figure 3, the behaviour of the  $\tau(q)$  function in this case is shown.



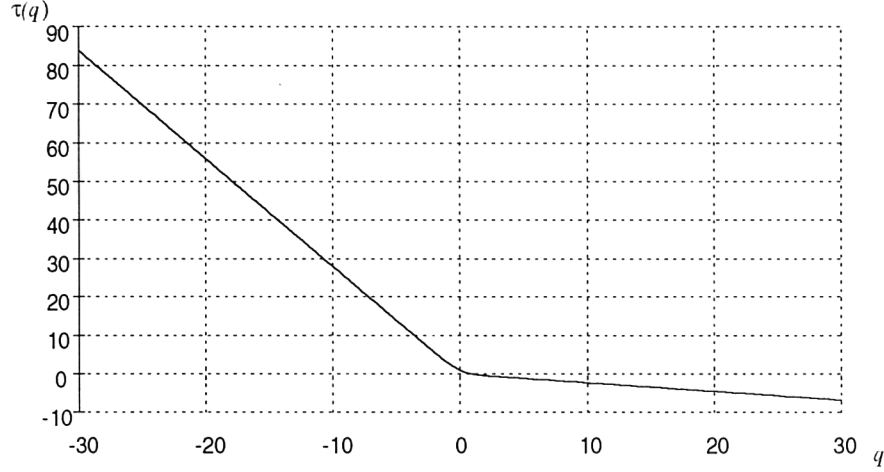


Figure 3:  $\tau(q)$  behaviour.

## 5 Links between $\tau(q)$ and $f(\alpha)$

The function  $\tau(q)$  is linked to the  $f(\alpha)$  one defined before;  $\tau(q)$  defines a set  $S$  that can be expressed as in (21), with  $\alpha$  chosen among the allowed values.

From the definition of  $\alpha$ , one knows that to that variable correspond the boxes  $\mu_\alpha$  so that

$$\mu_\alpha = \delta^{-\alpha} \quad (34)$$

and that the set of these boxes has, for  $\delta \rightarrow 0$ , a fractal dimension equal to  $f(\alpha)$ . By calling  $N(\alpha, \delta)$  the number of boxes that are needed to cover the set  $S_\alpha$ , with  $\alpha \in (\alpha, \alpha + d\alpha)$ , this number results to be, if  $\delta$  is sufficiently small,

$$N(\alpha, \delta) = \rho(\alpha) \delta^{-f(\alpha)} d\alpha \quad (35)$$

where  $\rho(\alpha)$  is the number of sets from  $S_\alpha$  to  $S_{\alpha+d\alpha}$ .

From its definition,  $M_d(q, \delta)$  is found to be equal to the summation of  $\mu_i^q$ , and consequently, in the continuous case,

$$M_d(q, \delta) = \int \rho(\alpha) \delta^{-f(\alpha)} \delta^{\alpha q} d\alpha = \int \rho(\alpha) \delta^{-[f(\alpha) - \alpha q - d]} d\alpha \quad (36)$$

In the limit for  $\delta \rightarrow 0$ , the integral behaves as the maximum on  $\alpha$  of the argument; of this one, the factor  $\rho(\alpha)$  remains bounded, as it does not depend on  $\delta$ , and then the dominant term is  $\alpha(q)$ ; so that, when  $\alpha = \alpha(q)$ ,

$$\frac{d}{d\alpha} [q\alpha - f(\alpha)] = 0 \quad (37)$$

and, for this value,

$$M_d(q, \delta) = K \delta^{-[f(\alpha) - \alpha q - d]} \quad (38)$$

Then

$$\tau(q) = f[\alpha(q)] - q\alpha(q)$$

If we differentiate with respect to  $q$ , we obtain that, when  $\alpha = \alpha(q)$ ,

$$\begin{aligned} \frac{d\tau(q)}{dq} &= \frac{df(\alpha)}{d\alpha} \frac{d\alpha(q)}{dq} - q \frac{d\alpha(q)}{dq} - \alpha(q) \\ &= \frac{d\alpha(q)}{dq} \left[ \frac{df(\alpha)}{d\alpha} - q \right] - \alpha(q) \\ &= -\alpha(q) \end{aligned} \quad (39)$$

Hence, there is a relation between  $\tau(q)$  and  $f(\alpha)$ , which can be expressed in a parametric form as

$$\tau(q) = f[\alpha(q) - q\alpha(q)] \quad (40)$$

$$\alpha(q) = -\frac{d\tau(q)}{dq} \quad (41)$$

## 6 The $q - th$ order generalized fractal dimensions $D(q)$

If one wants a function which is constant over an  $E$ -dimensional space, and equal to  $E$ , one has to use the function  $D(q)$ , introduced in [10]. Such a function results defined as

$$D(q) = \frac{\tau(q)}{1 - q} \quad (42)$$

With this kind of definition, in order to obtain a continuous function and defined over  $q \in \mathfrak{R}$ , it is necessary to manage differently the point  $q = 1$

$$\lim_{q \rightarrow 1} D(q) = -\lim_{\delta \rightarrow 0} \lim_{q \rightarrow 1} \frac{1}{1 - q} \frac{\log \sum_i \mu_i^q}{\log \delta} = -\lim_{\delta \rightarrow 0} \frac{\sum_i \mu_i \log \mu_i}{\log \delta} \quad (43)$$

by using l'Hospital's Rule. Hence, it is possible to make the function continuous by defining  $D(q)$  as follows

$$D(q) = \begin{cases} \frac{\tau(q)}{1 - q} & q \neq 1 \\ -\lim_{\delta \rightarrow 0} \frac{\sum_i \mu_i \log \mu_i}{\log \delta} & q = 1 \end{cases} \quad (44)$$

Moreover, the value assumed in 1 is the measure of the entropy of the distribution divided by  $\log \delta$ , a quantity well known in information theory, as well as in physics. From the definition of  $D_1$  it follows that, if it exists and it is finite, by calling  $H$  the entropy of the mass distribution,

$$H \approx -D_1 \log \delta \quad (45)$$

By considering an  $E$ -dimensional space over which is distributed a population of points in an uniform way, and by dividing the space into  $N = \delta^{-E}$  cells, each cell contains a portion of points equal to  $\mu_i = \delta^E$ . In this way it follows that:

$$N(q, \delta) = \delta^{(q-1)E} \quad (46)$$

and then

$$D(q) = -\frac{1}{1-q} \lim_{\delta \rightarrow 0} \frac{\log \delta^{(q-1)E}}{\log \delta} = E \quad (47)$$

From the definition, it follows that  $D(q) : \mathfrak{R} \rightarrow \mathfrak{R}$  and that, by using the same approach as for  $\tau(q)$

$$\lim_{q \rightarrow -\infty} D(q) = \lim_{\delta \rightarrow 0} \lim_{q \rightarrow -\infty} \frac{1}{1-q} \frac{\log \sum_i \mu_i^q}{\log \delta} = \alpha_M \quad (48)$$

Analogously

$$\lim_{q \rightarrow +\infty} D(q) = \alpha_m \quad (49)$$

Moreover,  $D(0)$  is the fractal dimension of the set, by assuming, by definition, the value equal to  $\tau(0)$ . Hence, the function  $D(q)$  is not increasing, has horizontal asymptotes to the infinite, is always positive, and, when  $q = 0$ , equals the fractal dimension of the set.

If we consider once again the case of the binomial multiplicative process, it is possible to compute this function in an analytical way, resulting in:

$$D(q) = \frac{\log [p^q + (1-p)^q]}{(1-q) \log 2} \quad (50)$$

It is constant if and only if  $p = \frac{1}{2}$ ; otherwise, it has a behaviour like the one in Figure 4.

## 7 Texture-signal analysis and fractals

By considering an image as a surface in a 3D domain (see Figure 5), where  $z$  represents the grey level, one can intuitively deduce the link between the

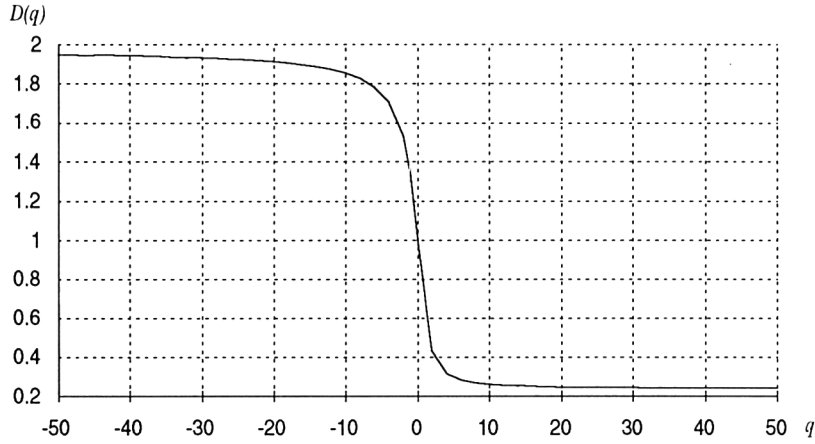


Figure 4:  $D(q)$  behaviour for binomial process.

roughness of such an object and its fractal dimension [14]. In short, a rough surface takes up a space of topological dimension larger than 2, and higher roughnesses are of larger dimensions, that is, close to 3. The concept of fractal dimensions expresses such idea in a quantitative way.

Several approaches to estimate the fractal dimension of real textures have been proposed in the literature. They can be subdivided in three main categories, according to their theoretical bases: statistical methods, frequential methods, and measure-based methods. To the first category belong methods based on the assumption that data can be modeled by the fractional Brownian motion (FBM), and that try to extract the statistical parameters that rule the FBM process [18], [13].

The second category includes techniques based on the analysis of the Fourier spectrum of the image signal, modelled like an  $\frac{1}{f}$  process [12]. In particular, in [18] the relation between the spectrum behaviour and the fractal dimension is proven and exploited.

The last ones exploit the links between some measures and the size of partitioning elements used for the estimation; to this category belong the blanket technique [17], which is based on the  $M_k$  measures (that is, length, area, volume, etc.), and the variation one [5], [6]. In particular, the last approach is very interesting for situations in which the estimation results are not dependent on the signal extent and on the partitioning elements' shape; as a matter of fact, they adopt a new structural element that is invariant under multiplication of all  $z$ -coordinates by a constant.

A class of measure-based techniques is based on the box-dimension concept [14]; for instance, the algorithms described in [11] and [19] exploit such

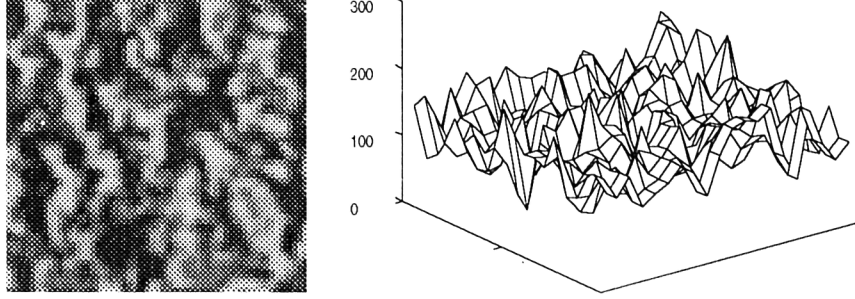


Figure 5: An image as a 3D surface.

a concept. The work in [11] is based on the work of Voss [20], where an original method is proposed to estimate  $N(\delta)$  over sets generated by a function  $y = f(\mathbf{x})$ , where to each vector  $\mathbf{x}$  corresponds one and only one value of  $y$ . In particular, Voss demonstrates that

$$N(\delta) \propto \sum_m \frac{1}{m} P(m|\delta) \quad (51)$$

where  $P(m|\delta)$  is the probability of finding  $m$  points within a box of side  $\delta$  centered on a generic point of the set under examination. By substituting such a property, one obtains the following expression of box-dimension

$$D = -\lim_{\delta \rightarrow 0} \left\{ \frac{1}{\log \delta} \log \left[ \sum_m \frac{1}{m} P(m|\delta) \right] \right\} \quad (52)$$

The box-dimension computed this way is not dependent on the grid, as in the box-counting method, and the resulting  $N(\delta)$  is a real number. However, roughness is not an exhaustive feature for describing textures. Various examples of structures of the same  $D$  but appearing very different to the human observer can be found (see Figure 6).

For instance, let us consider a fractal curve obtained by merging two curves of different fractal dimensions. The  $D$  of the resulting curve is equal to the greater  $D$  of the two starting curves and can be expressed as

$$D = -\lim_{\delta \rightarrow 0} \frac{\log [N_1(\delta) + N_2(\delta)]}{\log \delta} \quad (53)$$

As  $N_1(\delta) = \delta^{-D_1}$  and  $N_2(\delta) = \delta^{-D_2}$ , when  $\delta$  is sufficiently small, the expression for  $D$  is

$$D = -\lim_{\delta \rightarrow 0} \frac{\log (\delta^{-D_1} + \delta^{-D_2})}{\log \delta} = \max\{D_1, D_2\} \quad (54)$$

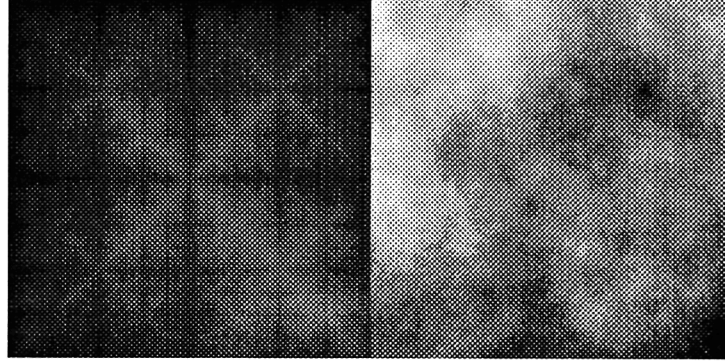


Figure 6: Takagi's and Brownian surfaces with  $D = 2.5$ .

This demonstrates that single and multiple fractal objects cannot be distinguished by measuring their fractal dimensions only. To obtain a more detailed description of a fractal object, it is necessary to use additional parameters that characterize different subsets. In other words, one has to introduce the  $q$ -th order generalized fractal dimensions [10], so dealing with the multifractal theory [8].

## 8 Multifractals for digital image processing

The definition of generalized fractal dimension described in the previous paragraphs supplies a method for estimation based on the concept of box-dimension and box-counting. However, as demonstrated in [5], although very simple to use, the box-counting method has many drawbacks that make it not so attractive for discrete signal processing. In particular, the results are strongly dependent on the origin of the partitioning grid. Hence, a different definition of  $D(q)$  is used that extends the method introduced by Voss to estimate the fractal dimension (see equations 53–54). By following the Voss approach, it is possible to extend the concept of  $d$ -measure  $M_d(\delta)$ , to  $q$ -th order momenta, as

$$M_d(q, \delta) = \sum_m m^q P(m|\delta) \delta^d = N(q, \delta) \delta^d \quad (55)$$

and to compute the  $q$ -th order fractal dimensions

$$D_v(q) = \begin{cases} \frac{1}{q} \lim_{\delta \rightarrow 0} \frac{\log[\sum m^q P(m|\delta)]}{\log \delta} & q \neq 0 \\ \lim_{\delta \rightarrow 0} \frac{\sum_m [(\log m) P(m|\delta)]}{\log \delta} & q = 0 \end{cases} \quad (56)$$

It can be demonstrated that, in the case of point distributions where each point has a unique mass  $\frac{1}{N_t}$ , where  $N_t$  is the number of points of the whole set, the latter definition of  $N_t$ , named  $D_V(q)$ , is equivalent to the former

$$D(q+1) = D_V(q) \quad (57)$$

The concepts defined in the previous section are based on the hypothesis that the analyzed sets are continuous or dense (that is, made up of infinite quantities of points). Under this assumption, it is possible to reach measuring-scale dimensions that are infinitesimal. Moreover, these sets fit the multifractal model at all scales, that is, it is possible to define a multifractal measure [7].

In the case of real structures, it is mandatory to define a different and approximated multifractal model to estimate the function  $D(q)$ . In other words, a model must be defined for a given range of scales, and a tool for parameter estimation must be provided. This has also been suggested in [18] for the estimation of the single fractal dimensions of real objects (that is, objects with finite resolutions).

Let us consider a set  $S$  that complies with the multifractal model  $\hat{D}(q)$  if, for a small  $\delta$  value (i.e.,  $\delta \ll s_S$ , where  $s_S$  is the set size), there exist  $(\delta_m, \delta_M)$  such that

$$N(q, \delta) \approx k_q \delta^{q\hat{D}(q)} \quad (58)$$

where  $\delta \in (\delta_m, \delta_M)$ . When  $\delta_m = 0$ , we deal with a fractal set and

$$\hat{D}(q) = D(q) \quad (59)$$

as can easily be demonstrated using the previous equations.

Now it is possible to estimate  $\hat{D}(q)$  through a linear regression in the bilogarithmic plane, that is,

$$\log \delta = x; \quad \log N(q, \delta) = y \quad (60)$$

$$y = \log k_q + q\hat{D}(q)x \quad (61)$$

In this way, the linear regression is applied to samples in the linear region, and  $\hat{D}(q)$  is estimated. However, this implies that, in order to estimate the fractal dimension, it is necessary to detect the range  $(\delta_m, \delta_M)$  over which (60) is linear in the same bilogarithmic plane as defined above. The algorithm for the estimation of  $(\delta_m, \delta_M)$  depends on the exploited multifractal measure and will be described in the next paragraph.

## 9 Multifractal texture measures

It is possible to define different multifractal measures related to a generic signal  $f(\mathbf{x})$ ,  $f : \mathbb{R}^E \rightarrow \mathbb{R}$ . One can take into account the signal graph, that is a multidimensional  $(E + 1)$  surface, or consider the image as an optical bi-dimensional mass distribution.

### 9.1 Multidimensional digitized surfaces

In this case, one can keep the roughness information provided by the fractal dimension (see Figure 5). However, in this case, the main problem in the estimation arises from the fact that a digital image is a discrete set of points resulting from the sampling of a continuous function. This discretization process gives rise to a drawback for negative  $q$  values; in this case, small masses predominate over large ones, and, for small  $\delta$  values, the measures of small masses are less accurate.

As showed in Figure 7, this drawback produces in the bi-logarithmic plane defined by equations (60–61) two linear regions with two different slopes. The samples for small  $\delta$  values are totally dominated by very few numbers (usually,  $P(\delta|1)$  is not null for small  $\delta$ ) and the fractal behaviour is masked.

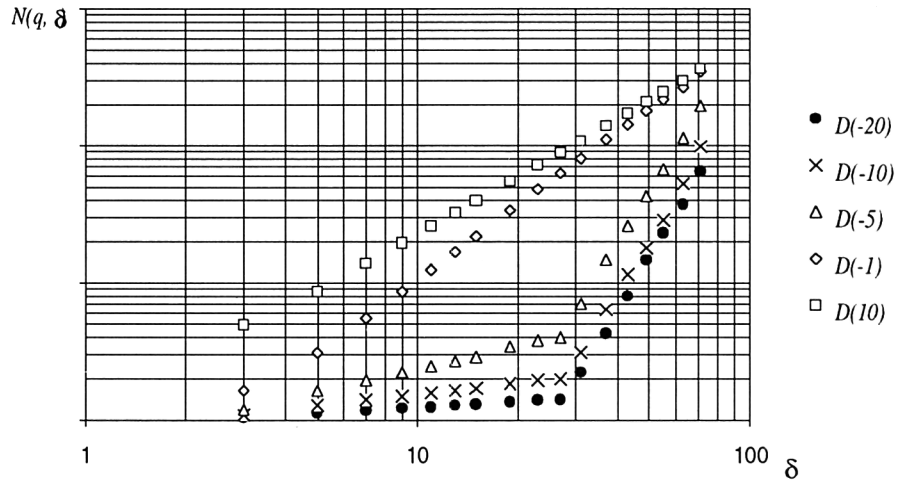


Figure 7: Samples in the bi-logarithmic plane.

In order to evaluate the linearity of the set of measures, we use the



parameter  $I$  proposed in [16] and formally defined as

$$I = \frac{\left[4\mu_{xy}^2 + (\mu_{xx} - \mu_{yy})^2\right]^{1/2}}{\mu_{xx} - \mu_{yy}} \quad (62)$$

where  $\mu_{ij}$  denotes the covariance of the points in the set. The values of the parameter  $I$  are included in the range  $[0, 1]$ , and the maximum value is reached when, and only when, all data lie on a straight line. The scale range  $(\delta_m, \delta_M)$  should be determined for each  $q$  value in order to optimize the linearity, or better, to identify the range in which the multifractal model is verified; with this aim, the parameter  $I$  is estimated over a moving window, with dimension  $(\delta_i, \delta_{i+k})$ , along such a data distribution in the bilogarithmic plane, so producing an estimation of the local linearity  $L(i)$

$$L(i) = I \{[\log \delta_i, \log N_q(\delta_i)], [\log \delta_{i+1}, \log N_q(\delta_{i+1})], \dots, [\log \delta_{i+k}, \log N_q(\delta_{i+k})]\} \quad (63)$$

where  $k$  is experimentally set to  $3 \div 5$  (the behaviour of such  $L(i)$  will be shown in the next paragraph for different multifractal measures). The behaviour of  $L(i)$  shows a plateau bounded by one or two minima, which represent the upper and lower bounds for the linear region, and are assigned to  $\delta_m$  and  $\delta_M$  (see Figure 8).

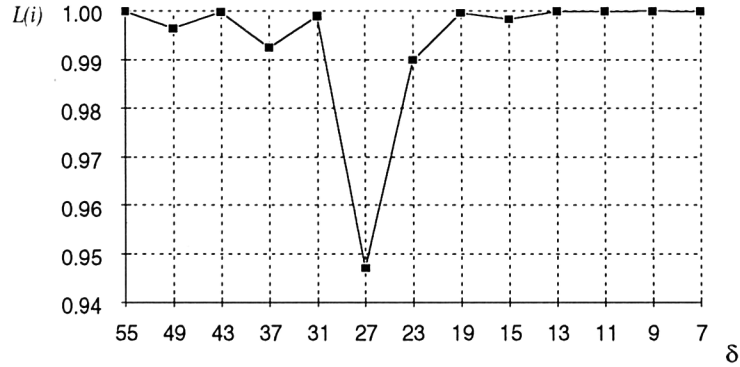


Figure 8: The behaviour of  $L(i)$ .

However, when one deals with small textured areas, there are few scales of measure only and, as for negative  $q$  values the number of scales is reduced, it is not possible to compute a reliable  $\hat{D}(q)$ . Therefore, for negative  $q$  values in  $\hat{D}(q)$ , the resolution should be increased through interpolation in the case of small measuring-scales  $\delta$ . This can be done by choosing between

two possibilities: (i) to use a smoothing interpolant, which produces a minimization of the Mean Square Error (MSE) and a stable measure; (ii) to use an interpolant complying with the multifractal model, as the one described in [3] and based on the Iterated Function Systems (IFS). Both choices were implemented, and some experiments were made in order to find out the best interpolant; in particular, fractal interpolation showed the unwanted property of forcing the set to be a single fractal, as its application results in flattening the  $\hat{D}(q)$  behaviour. On the other hand, the bilinear interpolant also varies this behaviour, but it results only in lowering the fractal dimension  $\hat{D}(-1)$ , without changing the asymptotes and the derivative of  $\hat{D}(q)$ . This is an important aspect, as for texture classification only these features are needed and so the bilinear interpolation is preferred. To sum up, the estimation algorithm includes three steps:

1. the distribution  $P(m|\delta)$  is computed for boxes of size  $\delta = Bs^i$ , where  $i \in \{0, 1, 2, \dots\}$ ;  $s$  is a number between 0 and 1 (and experimentally chosen between 0.8 and 0.9); and  $B$  is the size (in pixels) of the largest box (in this way, a linear series in the bilogarithmic plane is obtained);
2. for each  $q$  value, the scale range and the resolution are computed;
3. an interpolation of multiple  $\delta$  values is performed to estimate the limit of  $\delta \rightarrow 0$  and the correct  $\hat{D}(q)$  value.

## 9.2 Mass distribution

The images are considered as mass distributions generated by a subdivision process  $F(\mathbf{p}, \mathbf{r})$  where  $\mathbf{p} = (p_1, \dots, p_n)$  is the vector of the probabilities of mass distributions, and  $\mathbf{r} = (r_1, \dots, r_n)$  is a space partitioning vector; consequently, each image point has a mass  $f(x, y)$  equal to the grey level of the  $(x, y)$  pixel.

Optical images can be considered samples of a continuous function: the radiance function. It can be easily demonstrated that under these conditions, such a measure is not a multifractal one and leads to a trivial  $D(q)$  function (always uniform). However, images have discontinuities in the first derivatives, thus, the  $D(q)$  function is computed for the image of the gradient. When dealing with non-optical images characterized by high discontinuities, like SAR ones, the multifractal parameters can be estimated directly on original images.

Optical images:  
 $f(x, y) = \|\nabla I(x, y)\|$

SAR images:  
 $f(x, y) = I(x, y)$

As already pointed out, it is necessary to have a set where every point has a unique mass value in order to apply the latter definition of  $D(q)$ . Therefore, each image point  $(x, y)$  with mass  $f(x, y)$  is assumed to be the overlapping of  $n = f(x, y)$  points with unitary mass.

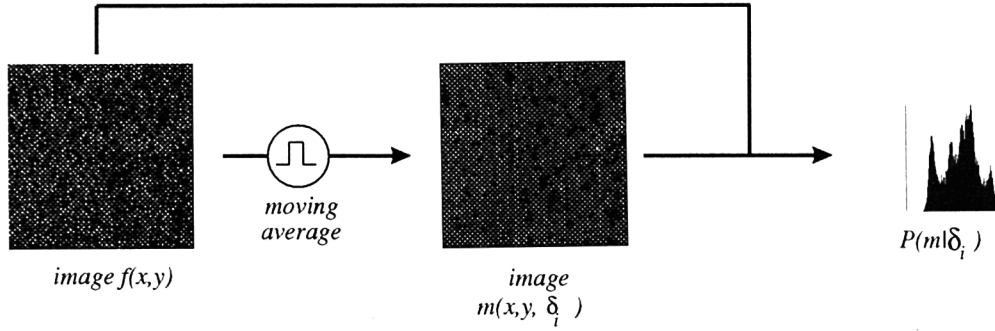


Figure 9:  $P(m|\delta_i)$  estimation algorithm.

If it is compared with the previously described method, the estimation algorithm for  $P(m|\delta_i)$  is very fast: for an optical image, the gradient is computed; afterwards, the image  $m(x, y, \delta_i)$  is obtained by filtering the image  $f(x, y)$  with a moving average (the computational complexity of this filter is independent of its size). Finally, the probability distribution  $P(m|\delta_i)$  is a modified histogram: for each  $m(x, y, \delta_i)$  the correspondig entry  $P\{m(x, y, \delta_i)\}$  of the histogram is increased proportionally to  $f(x, y)$ , that is, the grey value of the pixel in the original image. The estimation of  $D(q)$  is obtained by using the approach described in section 9.1.

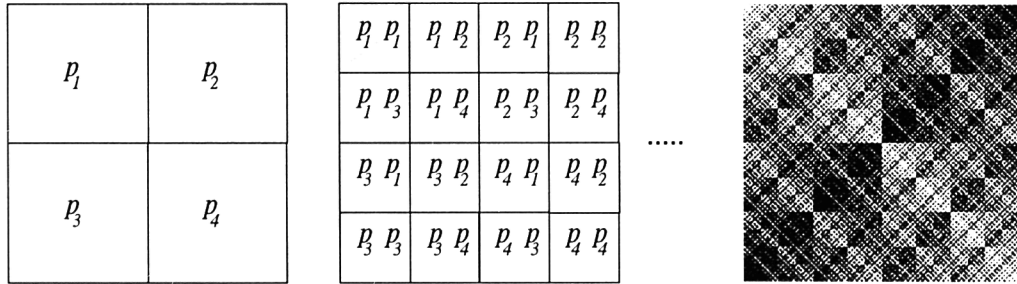


Figure 10: Recursive subdivision algorithm.

Through such definition, it is also possible to generate test images characterized by a  $D(q)$  that is analytically known. By using a recursive mass

subdivision schema, as in Figure 10, one can obtain a fractal distribution denoted by (where  $\sum_i p_i = 1$ )

$$D(q) = \frac{1}{q-1} \frac{\log(\sum_i p_i^q)}{\log 2} \quad (64)$$

that gives estimation results very close to the analytical ones (see Figure 11).

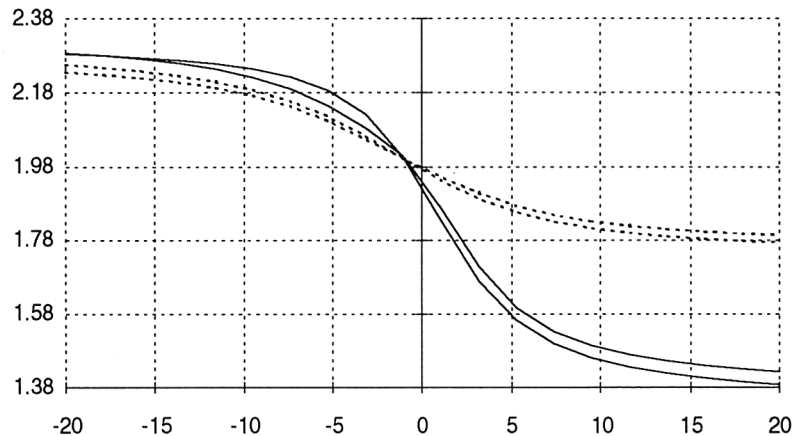


Figure 11: Analytical and estimated  $D(q)$  functions.

## 10 Results on real textures

The effectiveness of the proposed approach is proved by the better results obtained in texture characterization in comparison with the use of the single fractal dimension. Figure 12 gives the functions  $D(q)$  computed on two fractal surfaces (i.e. Takagi's and the Brownian ones, given in Figure 6). Even though such surfaces are characterized by the same fractal dimension, they appear quite different to a human observer. The two functions assume different values, whereas the fractal dimensions, equal to  $D(0)$ , are exactly the same.

The functions  $D(q)$  were estimated also on SAR textures by using the mass distribution algorithm. Windows of  $128 \times 128$  pixels were analyzed, using 15 different measuring scales ( $i = 0, 1, \dots, 14$ , ranging from 3 to 61 pixels, with  $s = 0.87$ ). An extension up to  $256 \times 256$  has confirmed the stability of the result.

The processing results are shown; for each texture, the behaviour of the relevant function  $D(q)$  is shown in terms of mean value and standard

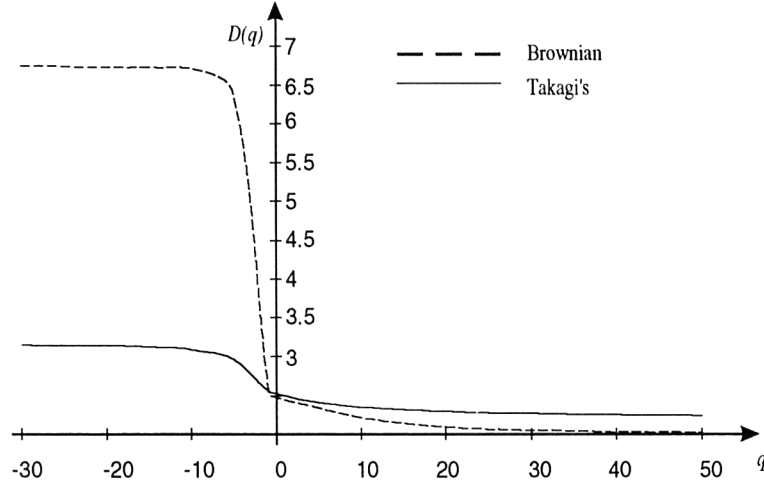


Figure 12:  $D(q)$  for the two surfaces in Figure 6.

deviation. It may be observed that, even though some overlaps occur for certain ranges, significant differences are found for the other ranges, so allowing an easy texture discrimination.

The best results are obtained by using both multifractal measures, that is some  $D(q)$  values of the multifractal mass distribution, and the fractal dimension of the 3D surface. In particular, four features have been used:

- $D(3)$  and  $D(-3)$  values;
- the first derivative computed in  $q = 0$  ;
- the fractal dimension of the 3D surface.

The feature vector obtained has been classified by a k-nn classifier and the results are compared with classical co-occurrence matrix analysis.

Each  $256 \times 256$  image has been partitioned in 64 overlapped  $64 \times 64$  windows (a window every 32 pixels in both  $x$  and  $y$  directions) and the classification results are reported in Table 1 and the following Figures.

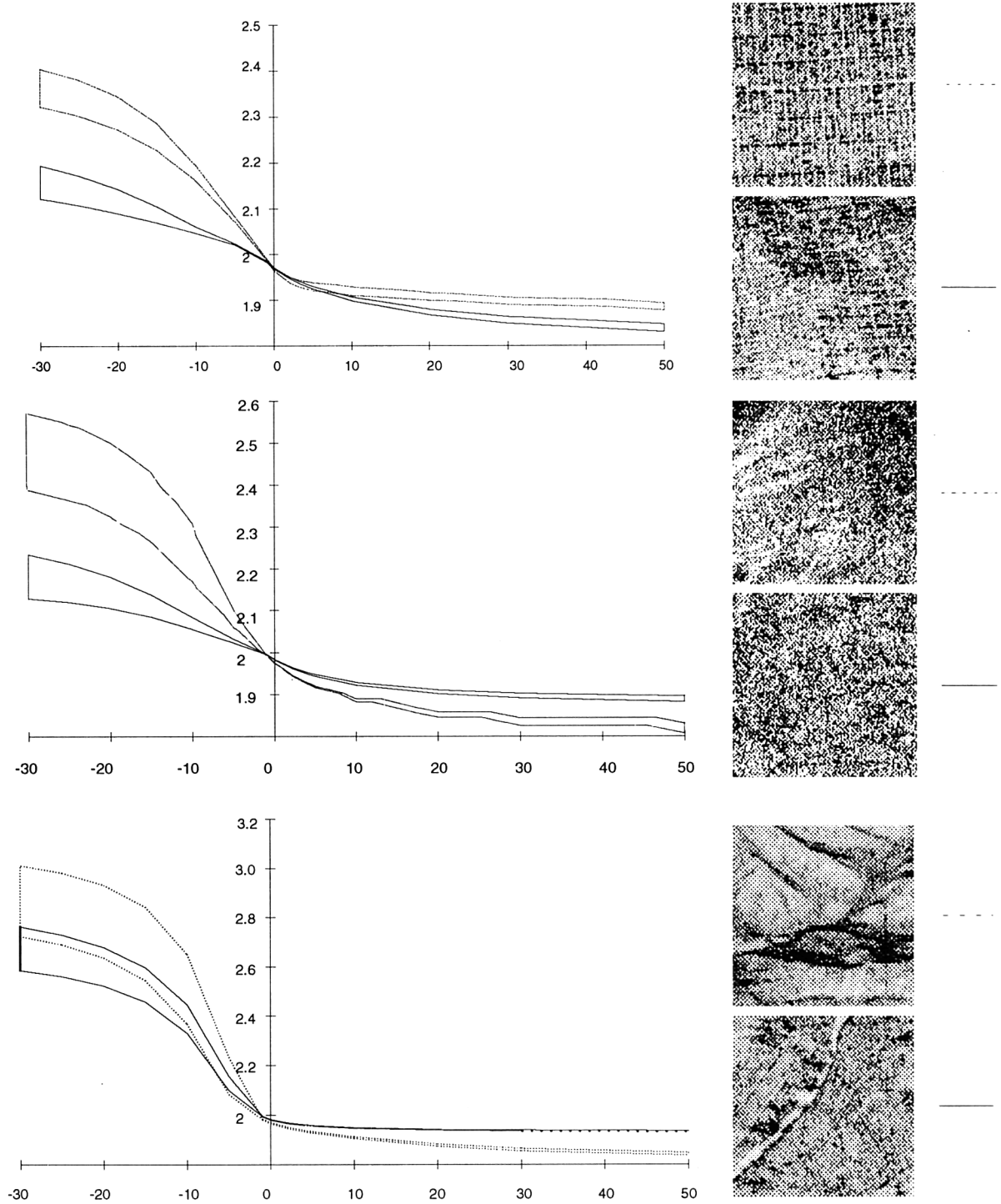


Figure 13:  $D(q)$  behaviour for different SAR textures.

<i>Texture</i>	<i>error with co-occurrences matrices features</i>	<i>error with multifractal analysis</i>
T1	34%	2%
T2	30%	0%
T3	0%	0%
T4	0%	9%
T5	0%	6%
T6	31%	0%
T7	0%	0%
T8	28%	0%
	mean error =15%	mean error=2%

Table 1: Comparison between performance of co-occurrence matrix and fractal classifications.

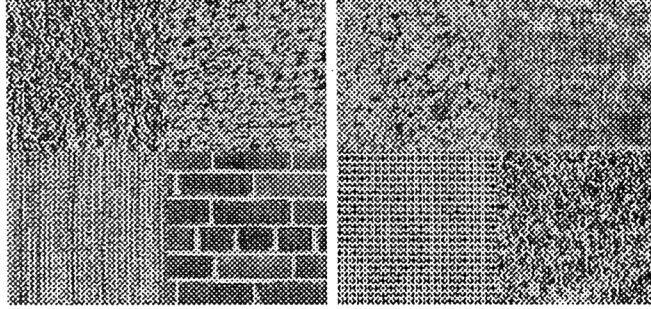


Figure 14: Real (Brodatz[4]) textures, numbered from the upper left corner in a raster way; left: T1-T4; right: T5-T8.

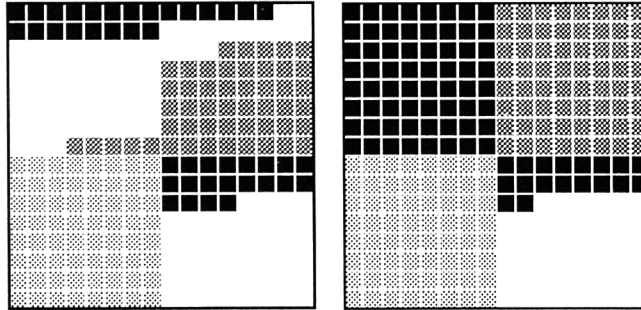


Figure 15: Classification results by using the co-occurrence matrix features.



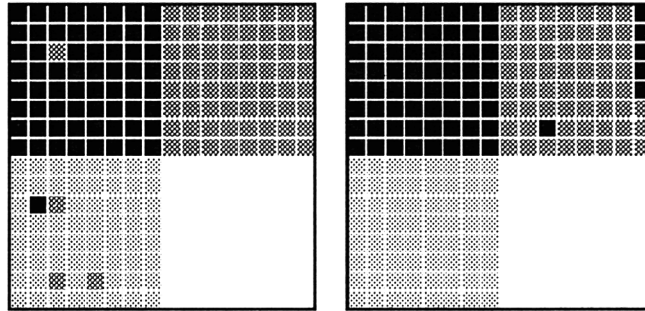


Figure 16: Classification results by using the fractal features.

## References

- [1] F. Arduini, C. Dambra, S. Dellepiane, S. B. Serpico, G. Vernazza, R. Viviani, "Fractal dimension estimation by adaptive mask selection", Proc. IEEE-ICASSP'88, pp. 1116–1119, New York, 1988.
- [2] F. Arduini, S. Fioravanti, D. D. Giusto "On computing multifractality for texture discrimination", Proc. EUSIPCO-92, pp. 1457–1461, Brussels, 1992.
- [3] M. F. Barnsley, *Fractals Everywhere*, Academic Press, 1988.
- [4] P. Brodatz, *A Photographic Album for Artists and Designers*, Dover, New York, 1966.
- [5] B. Dubuc, J. F. Quiniou, C. Roques-Carmes, C. Tricot, S. W. Zucker, "Evaluating the fractal dimension of profiles", *Physical Review A*, vol. 39, no. 3, pp. 1500–1512, February 1989.
- [6] B. Dubuc, S. W. Zucker, C. Tricot, J. F. Quiniou, D. Wehbi, "Evaluating the fractal dimensions of surfaces", *Proc. R. Soc. Lond. A*, vol. 425, pp. 113–127, 1989.
- [7] D. Falconer, *Fractal Geometry*, pp. 254–264, Wiley, 1990.
- [8] J. Feder, *Fractals*, Plenum Press, New York, 1988.
- [9] S. Fioravanti, D. D. Giusto, G. Vernazza, "Estimation of q-order fractal dimensions in textured images", *IEEE Trans. on Signal Processing* (under revision).



- [10] H. Hentschel, I. Procaccia, "The infinite number of generalized dimensions of fractals and strange attractors", *Physica 8D*, pp. 435–444, 1983.
- [11] J. M. Keller, S. Chen, "Texture description and segmentation through fractal geometry", *Computer Vision, Graphics, and Image Processing*, vol. 45, pp. 150–166, 1989.
- [12] M. S. Keshner, "1/f noise", *Proc. IEEE*, vol. 70, no. 3, pp. 212–218, March 1982.
- [13] T. Lundahl, W. J. Ohley, S. M. Kay, R. Siffert, "Fractional Brownian motion: A maximum likelihood estimator and its application to image texture", *IEEE Transactions on Medical Imaging*, vol. MI-5, no. 3, pp. 152–161, 1986.
- [14] B. B. Mandelbrot, *The Fractal Geometry of Nature*, Freeman, San Francisco, 1982.
- [15] U. Mussigman, "Texture analysis using fractal dimensions", in: *Fractal Geometry and Computer Graphics* (J. L. Encarnacao, H. O. Peitgen, G. Sakas, G. Englert, Eds.), pp. 217–230, Springer Verlag, Berlin, 1990.
- [16] N. Otsu, "Karhunen-Loeve line fitting and a linearity measure", *Proc. 7th Int. Conf. on Pattern Recognition*, pp. 486–489, August 1984.
- [17] S. Peleg, J. Naor, R. Hartley, D. Avnir, "Multiple resolution texture analysis and classification", *IEEE Transactions on Pattern Analysis and Machine Intelligence*, vol. PAMI-6, no. 4, pp. 518–523, 1984.
- [18] A. P. Pentland, "Fractal-based description of natural scenes", *IEEE Transactions on Pattern Analysis and Machine Intelligence*, vol. PAMI-6, no. 6, pp. 661–674, 1984.
- [19] N. Sarkar, B. B. Chaudhuri, "An efficient approach to estimate fractal dimension of textural images", *Pattern Recognition*, vol. 25, no. 9, pp. 1035–1041, September 1992.
- [20] R. Voss, "Random fractals: characterization and measurement", in: *Scaling Phenomena in Disordered Systems* (R. Pynn and A. Skjeltorp, Eds.), Plenum Press, New York, 1986.

## Chapter 7

# Mapping Spatial Variability in Landscapes: An Example using Fractal Dimensions

*Steven de Jong\**

## 1 Introduction

Soil survey and vegetation mapping have traditionally been based on hierarchical systems. Depending on the scale of the survey, geomorphology, climate and/or relief are used to distinguish land units and to define uniform mapping units. An example of a hierarchical approach is the system proposed by ITC which considers the following levels [1]: the landscape, the land unit, the land facet and the ecotope or site. Edges of river terraces, cuestas, junctions of major geological or lithological units are used to draw boundaries between mapping units. The selection of diagnostic criteria depends on the objective of the survey: a regional water balance study requires different terrain or mapping units than a wind erosion project or a basic soil survey. Although different disciplines have different information needs, there can be considerable overlap between the interests of different users. An overview of different hierarchical approaches of survey techniques is given in [2].

The interpretation of aerial photographs or satellite images has become an integral part of these types of surveys. The applications of aerial photographs may include [3, 4]: the drawing of provisional boundaries prior to field survey, and the planning of locations for field checks, for post-field interpretation and for presentation. The availability of digital satellite images with channels outside the visible part of the spectrum has provided new

---

\*Department of Physical Geography, University of Utrecht, The Netherlands

opportunities for vegetation and soil survey since 1972. Airborne and spaceborne images play a key role in landscape analysis and advanced methods are needed to analyse and to interpret these images.

The approaches of qualitative descriptions of the variation of the earth's surface discussed previously have treated the world as though it is made up of uniform regions that can be delineated by sharp boundaries. However, the complexity of natural variations, the limitations of field sampling and the uncertainties of cartographic delimitation make it often unsatisfactory to regard sites as crisp sets. Several researchers have shown that land units are mostly not as homogeneous as supposed [5, 6, 7]. Although soil scientists and geographers know from field experience that drawn boundaries on maps are in fact mis-representations of changes that are often gradual or fuzzy, many of them use these mapping units in environmental modelling with GIS [8, 9, 10]. Hence, methods to quantify the spatial and temporal aspects are urgently needed.

Researchers have sought for better representations of the real world. One way is to treat the overlap zones as fuzzy boundaries. Fuzzy set theory is a generalization of Boolean algebra and, in contrast to binary membership functions, fuzzy sets allow a partial membership i.e. mapping units can have a 'partial membership' of multiple units [10]. An example in soil science is soil depth, a soil can be 'deep' or 'shallow' e.g. with a separation boundary defined at 75 cm. In a fuzzy membership function we can now define 75 cm as the ideal centre between deep and shallow soils and express every value between 75 and 150 cm (deep to very deep) on a fuzzy scale for deep soils from 1 to 0 and express every value between 0 and 75 cm on a fuzzy scale between 0 and 1 for shallow soils. Such a fuzzy approach allows us to deal with uncertainties associated with the descriptions of environmental variables [11].

A second approach to tackle the problem of spatial complexity is that of geostatistics [12]. The quantities and spatial distributions of attributes of the Earth's surface are estimated from spatial covariance functions. Geostatistical methods are based on the 'regionalized variable theory' [13], which assumes that the spatial variation of any variable can be expressed as the sum of three components: (1) a structural component: a constant mean value or a constant trend, (2) a random, spatially correlated component and (3) a random noise or residual error term [12]. The variogram (or semivariogram) expresses the spatial relation between distance and variance of the variable. If this relation is known, interpolation techniques such as kriging are useful to compute the value of the variable for any location and to assess the interpolation error. Although the geostatistical approach

has already proven its value, problems arise e.g. when the spatial variation revealed by the variogram differs with direction (anisotropy). Furthermore, variogram estimation and modelling is extremely important for structural analysis and for interpolation and variogram models are only valid when certain mathematical conditions are fulfilled.

The previously discussed methods (the conventional choropleth approach, the geostatistical and fuzzy set approach) treat the variability of environmental variables at the Earth's surface as a set of patterns occurring at specific scales in the landscape. However, the processes that shape the Earth's surface vary from large-scale geological processes affecting the entire Earth to small-scale processes that give only shape to a slope or part of a slope. Hence, there is no reason why any particular scale should dominate and the space era has provided possibilities to study the Earth at many scales. The fractal theory [13] is a first step in the direction of describing how multi-scale complex spatial processes act and how they shape landscapes.

In the last few years a number of researchers [10, 15, 16 17, 18, 19, 20, 21] have assumed that landscapes fulfill the two most important characteristics of fractals: (1) 'self-similarity', the manner in which variations at one scale are repeated at another and, (2) they should have the property of fractional dimension (Hausdorff-Besicovitch dimension). Apart from the methods proposed by [15] to estimate fractal Dimension  $D$  such as the length of a trail, the area-perimeter relation, the variogram, and the Korcak empirical relation for islands, a number of other methods were developed e.g. cell-counting [22], the triangular prism surface area method [23], the isarithm method [16], the robust fractal estimator [24] etc. Based on experiences that objects (surfaces, processes) did not always meet the two previously mentioned conditions, the idea of multi-fractals or non-linear variability was introduced [25]. Research in the application of fractal ideas to landscape studies, cartography, soil and vegetation survey is still in its infancy. Some studies show very promising results while other studies illustrate very well that a number of problems can occur such as non-fractal behaviour and/or noise in the data besides computation difficulties.

The case study that is described next, aims at introducing a method to assess fractal dimensions from remotely sensed images and to discuss some of the problems with computational methods and difficulties encountered during field surveys. The new proposed method is a useful image analysis tool when individual, neighbouring pixels have different spectral signatures, but when the pattern of different signatures is characteristic for a given land cover type. Hence, such a method should capture the local variability of reflectance properties and must be simple and unambiguous to use and be

capable of distinguishing different land cover types.

## **2 Case Study**

Many Mediterranean regions are affected by land degradation resulting from past and present human activities. These have caused the development of highly variable landscapes with vegetation ranging from maquis, garrigue and rangelands to badlands [26, 27]. Mediterranean landscapes are vulnerable to land degradation processes and the natural conditions in many Mediterranean areas are such that disturbed ecosystems do not regenerate easily. Consequently, Mediterranean areas need to be treated with care and methods for sustainable land use need to be developed. In order to develop methods for sustainable land use, information is needed on the present state of these areas and knowledge is required on the functioning of Mediterranean ecosystems. As the Mediterranean regions are extensive and complex, remote sensing techniques may contribute significantly to acquisition of data about complex spatial patterns of vegetation [28, 29]. However, remote sensing techniques that use only pixel-specific spectral signatures to distinguish vegetation types have not been very successful in complex Mediterranean regions so far [30, 31]. Per-pixel classifiers do not recognize adjacent pixels as belonging to the same vegetation class because of the great variety of spatial patterns of vegetation cover and density of Mediterranean landscapes. Classification results may improve if a quantitative measure of spatial heterogeneity is used as additional information in spectral classification procedures [9, 32, 33, 34]. One of the basic assumptions of the current study is that the various Mediterranean land cover types show spatial patterns of differing complexity or texture. This assumption is supported by several other studies [35, 36, 37].

## **3 Characterization of Spatial Variation**

Local variability in a remotely-sensed image can be described by computing statistics of pixel values e.g. coefficient of variance, autocovariance or by fractals. The underlying theory in each of these methods is that the computed parameters express a kind of ‘natural characteristic’ of a spatially contiguous set of pixels for a given type of land cover. Although the individual pixel values may vary, the pattern is distinctive. Open types of natural vegetation such as found in the Mediterranean region often display such patterns.

### 3.1 Coefficient of Variance

The coefficient of variance ( $CV$ ) gives a measure of the total relative variation of pixel values in an area and can be computed quickly and easily, but gives no information about spatial patterns. The same applies for many other neighbourhood operations such as diversity or variation filters: their absolute values are easy to compare but they do not reveal any information on spatial irregularities [5, 10, 18, 20, 38].

### 3.2 Variograms

Spatial patterns can be described quantitatively in terms of the semivariance function, which can be computed from transects of data points measured on the ground or from images. This technique is based on the idea that the statistical variation of data is a function of distance. The variogram relates distances between sample points to the variance of the differences in the data. The parameters of a fitted model may include a range ( $a$ ), a nugget ( $c_0$ ) and a sill ( $c + c_0$ ). The range of the variogram indicates a spatial scale of the pattern; the nugget is an indication of the level of spatially uncorrelated variation in the data; and the sill reveals the total variation. The shape of the variogram is related to the type of variation in the data [5, 12, 14, 39, 40, 41].

Variograms of remotely sensed measurements should be interpreted with care, because some aspects of these variograms may differ from variograms resulting from ordinary samples. In remote sensing, the support size equals the sample spacing i.e. reflection values are averaged over the 'field of view' or pixel size of the measuring device. Furthermore, the sensor's output is always a derivative of the complex composition of radiation from the terrain. Variograms of data collected by remotely sensed devices are influenced by the shape and the distribution of elements in the image (or the transect). Some major points for variogram interpretation are [42, 43, 44, 45]:

- the range is related to sizes of objects in the terrain (e.g. batches of shrubs);
- the shape of the variogram is related to variability in size of objects in the terrain;
- the height of the variogram is influenced by the density of coverage of the objects and the spectral differences between the objects;
- regularization (coarsening the spatial resolution) reduces the overall variance of the data and blurs fine scale variation. Consequently, the sill height will reduce, the range will increase and the nugget will increase;
- anisotropy in the image is expressed by the variation of variogram param-

eters with the direction of the transect.

Variogram parameters could be useful for assessing spatial patterns in remotely sensed images. The nugget reveals information on variability between adjacent pixels, the sill gives information on the total variability of the area considered, the range presents information on spatial dependence of reflectance and the type of variogram model or the shape of the variogram reveals information on the spatial behaviour of the data [46, 47 48, 49]. If one first delineates different land cover types by eye (or by other external criteria), variograms can be computed for each delineation separately. Statistical tests (e.g. *ANOVA* ) could be used to see if areas with apparently similar patterns returned significantly similar or different values of the variogram parameters. This approach is cumbersome and only useful if an external delineation is provided. It is more interesting to see if an analysis of the image patterns could be used to distinguish different vegetation types automatically by using the variogram.

If one were to characterize a part of a remotely-sensed image by using variograms, the conventional approach would be to take a kernel or transect of a limited size, compute the experimental variogram, fit a variogram model, and then write the values of the variogram parameters to the cell location at the centre of the kernel or transect. Such a procedure could yield at least three new data layers per pixel, one for the nugget, one for the range and one for the sill. The kernel/transect would then be moved up one pixel and the computations would be repeated. The result would in principle, be a set of data layers that showed how the patterns in the image varied in terms of estimated variogram parameters, which might reveal the differences in vegetation or land cover pattern that are being sought. Although the variogram seems to be a robust tool, a number of disadvantages of variograms can also be identified:

- many data points are required to compute a reliable variogram (10 lags or more are needed to fit a variogram model). Consequently, an extended transect or a large kernel is required to perform the computation;
- it is difficult to define 'best model criteria' in an automatic procedure for estimating variogram parameters;
- different samples (i.e. sets of observations) from the same landscape units can yield different estimated variograms [14, 46];
- using the transect method, there is no clearly defined central pixel, in which the computed variogram parameters can be stored;
- a local estimator is required to analyze image patterns to distinguish different land cover types, the variogram of a transect is a global estimator

and does not give information on local variation;  
-the computation to derive the variogram and its parameters is considerable.

An easier and more rapid method to assess spatial patterns from remotely-sensed images would be useful. A fractal approach to assess spatial patterns from images meets the needs of such a method. This study examines the use of methods for assessing fractal dimensions of Mediterranean vegetation types using digital images at two different spatial resolutions, tests the usefulness of the fractal approach for distinguishing different types of vegetation and compares it with variogram methods.

### 3.3 Fractals

Fractals are a means of describing complicated, irregular features of variation. Several authors have discussed the use of fractals to quantify 'roughness' of several types of objects [5, 17, 18, 20, 50, 51, 52, 53, 54, 55, 56, 57, 58]. Only a limited number of studies have been carried out so far to assess the usefulness of fractals for image analysis [28, 33, 59, 60, 61, 62, 63, 64]. The fractal dimension ( $D$ ) is a quantitative measure of the irregular features or 'roughness' of phenomena [5,10]. The variability of many natural phenomena is often irregular and sometimes, it can be approximated by a stochastic fractal such as the model of Brownian motion [15]. It is reasonable to suppose that different kinds of terrain might have characteristically different texture or roughness which could be expressed in terms of different fractal dimensions [38, 58, 65, 66, 67]. Therefore, local fractal analysis of remotely-sensed images may reveal information on patterns of vegetation and rock outcrops much better than pixel specific procedures.

A single-band remote sensing image can be considered as a kind of topographical surface: rows and columns of the image matrix represent the spatial location, the pixel value embodies the imaginary elevation. The 'roughness' described by  $D$  is determined by the variation in observed radiance. Values of  $D$  for surfaces range by definition from 2.0 for completely smooth surfaces to just below 3.0 for very irregular surfaces [19]. Overviews of available methods to assess  $D$  are given by [10, 17, 50]. Most methods for determining  $D$  at present only give lumped values for an entire image or an entire catchment. This lumped value is useless for detecting patterns of roughness over the image and local methods to assess  $D$  are required to provide a spatial map of patterns of differing complexity or texture. Although several authors [17, 19, 50, 56, 68, 69, 70] have shown that there is a relation between fractals and landscape development or landscape patterns, the exact relation is not yet fully understood. This study examines



the hypothesis that  $D$  can be used to distinguish different land cover types.

## 4 Two Methods for Estimating Fractal Dimensions

Two methods to determine  $D$  were used in this study: the ‘variogram method’ and a new local method based on the ‘Triangular Prism Surface Area Method’ [23].

### 4.1 The Variogram Method

In the variogram method, the fractal dimension ( $D_V$ ) is estimated from the best fit line of the log-transformed semivariance function computed from one-dimensional transects from field data and from images. Transects are often used to characterize vegetation patterns in the field [71, 72] because the transect method is easy and quick. The slope of the best fitting line relates to  $D_V$  as  $slope = 4 - 2D_V$  [15]. The essence of a log-transformed variogram of a true Brownian fractal is that it has no single, unique range nor a sill. Such a variogram will be a straight line on log-log paper. If the contribution of noise in the data of a true fractal increases, it will shift the variogram upwards along the variance axis. If noise is added to a variogram with a clear range and sill, it will reduce the distinctiveness of the range and sill and the value of  $D_V$  will increase. The value of  $D_V$  for one-dimensional transects can vary by definition between 1.0 (completely smooth) and 2.0 (highly irregular).

The variogram yields several kinds of information on spatial patterns. If a variogram has a well-defined range and sill, then the data do not come from a real fractal. On the contrary, if a clear range and sill is absent then the dataset can be considered as a ‘candidate-fractal’. The linearity and the slope of such a log-log variogram provide information on spatial patterns in the data. Furthermore, the break distance of the log-log variogram (defined by [38] as the maximum distance to which a least-squares line can be fitted with a correlation greater than 0.90) indicates the distance of spatial independence of the data. Unfortunately, the disadvantage mentioned for the common variograms are also true if  $D$  is estimated from variograms: many data points are required to obtain a reliable variogram, the necessary computations are very laborious and the various variograms within one landscape unit do not yield the same results. The objective of

the new proposed local method to estimate  $D$  is to overcome some of these disadvantages.

## 4.2 Triangular Prism Surface Area Method

The ‘Triangular Prism Surface Area Method’ (TPSAM) is a three-dimensional geometric equivalent of the ‘walking dividers’ method proposed by [23]. This method estimates lumped  $D$  values from topographic surfaces or remotely-sensed images. The method takes elevation values ( $DN_s$ ) at the corners of squares, i.e. the centre of a pixel, interpolates a centre value of the square by averaging, divides the square into four triangles and then uses Heron’s formula to compute the surface areas of the imaginary prisms resulting from raising the triangles to their given elevations (figure 1). This calculation is repeated for different square sizes, yielding the relationship between the total area of the surface and the spacing of the squares (resolution). The computed surface area will decrease with increasing square size, because peaks and bottoms will smooth out. The calculations stop if the size of the square is too big to fit on the image. Surface area and spatial resolution are both log transformed and a linear function is fitted through the calculated points. One (lumped) value of  $D$  for the entire image is then estimated by the slope of the regression line. The number of steps (square sizes) to calculate the surface area depends on the size of the image. The required formulae to carry out the computation are given by [23]. The TPSAM provided good estimates of  $D$  for images and small phenomena such as particles and molecules [24].

A local method to assess the fractal dimension ( $D_L$ ) was developed by modifying the original TPSAM. A kernel of 9\*9 pixels is moved over the digital image (figure 2) and at each position of the kernel,  $D_L$  is assessed by calculating 4 times the surface area at different resolutions (squares of 1\*1, 2\*2, 4\*4 and 8\*8 pixels) within the kernel. The surface area is computed in the same way as the lumped TPSAM. Resolution and calculated surface area are both log-transformed and  $D_L$  is estimated from the linear function fitted through these 4 points by  $D_L = 2 - Slope$ .  $D_L$  is written to the centre cell of the kernel in a new image file, the kernel is moved one pixel to the next position over the image and the calculation starts again. A kernel of 9\*9 pixels is chosen as a compromise between computing time and the number of points required to fit the function. The new proposed local method is a type of convolution operation and results in a map of  $D_L$  values for the entire image, which can then be used as an indicator for the spatial variability of land cover categories.

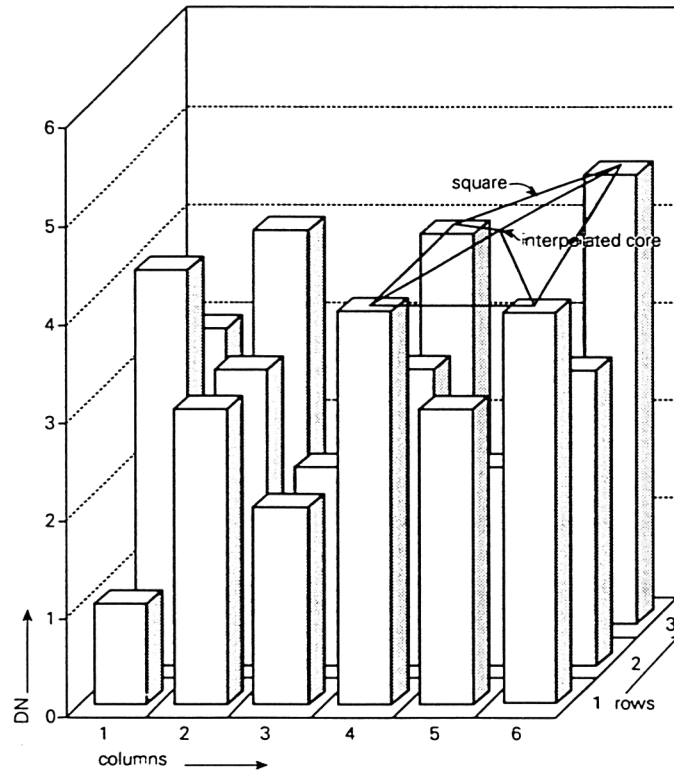


Figure 1: Example of the modified Triangular Prism Surface Area Method to calculate  $D$ . Within a square of increasing size, the ‘surface area’ of the image is assessed. The surface area decreases with increasing square size, because peaks and bottoms are smoothed. The regression line of the log transformed surface area and the log transformed square spacing yield an estimate of the fractal dimension.

## ' Local Triangular Prism Surface Area Method '

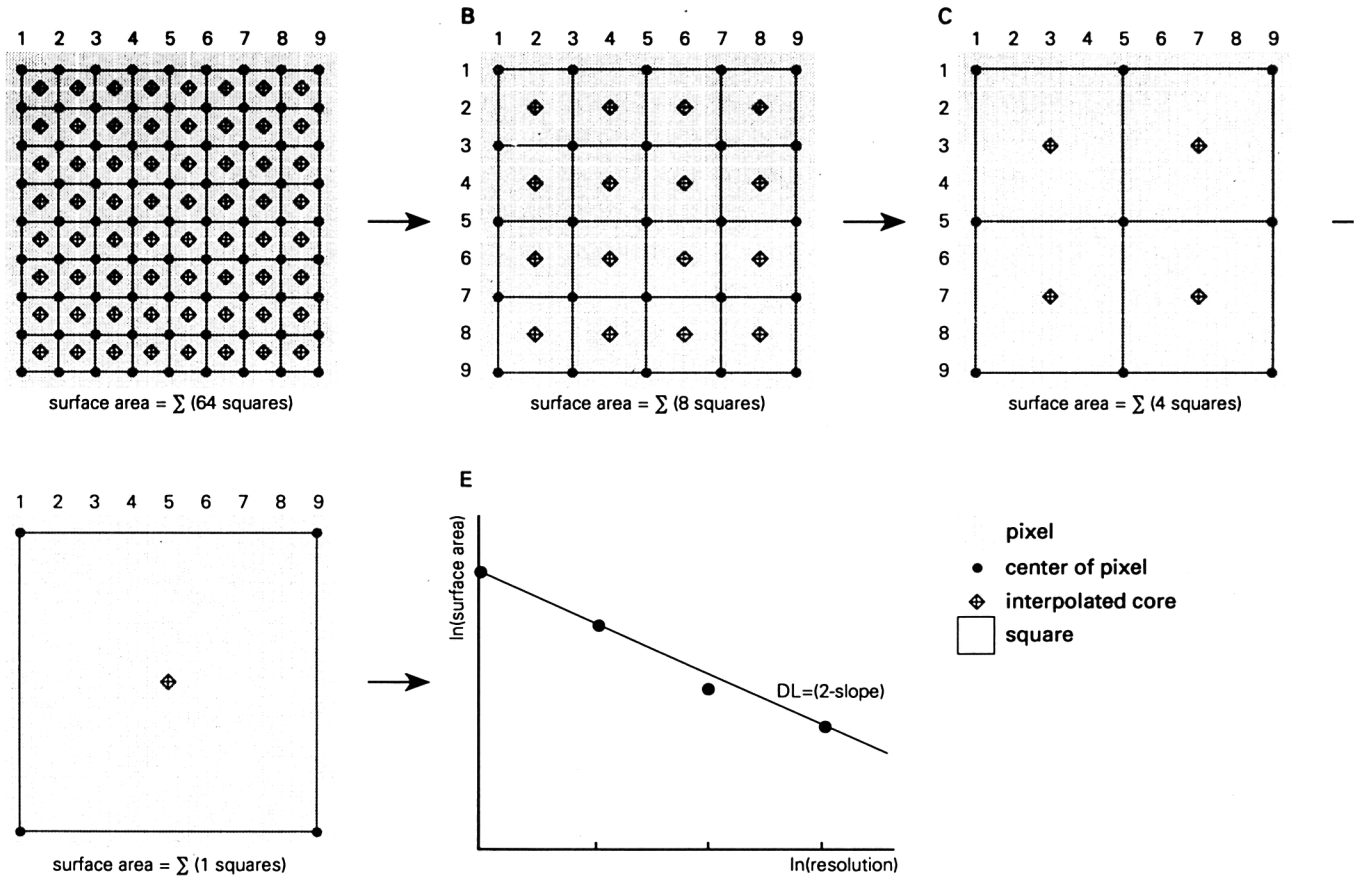


Figure 2: The working method of the new proposed 'local  $D$ -algorithm'. A kernel is moved over the image; for each kernel position the 'surface area' is computed at 4 different resolution (squares).  $D_L$  is assessed from the log-transformed surface areas and resolutions and the kernel is moved to the next position. The method yields a distributed map of  $D_L$ .

The advantages of the new local method are that it is easy to use and quick, it renders information on spatial patterns within the template size, no extended transects are required and it can be used in relatively small areas. A spatially continuous map of  $D_L$  values is produced by writing the computed  $D_L$  value to the centre pixel of the kernel. Due to the size of the kernel (9\*9 pixels), two disadvantages of the new local method can be identified:

- the surface area is calculated within the kernel for four square sizes: 1\*1, 2\*2, 4\*4 and 8\*8 pixels; consequently, only four points are available for the linear regression of the log transformed surface area and resolution; the least square fit might be strongly influenced by extreme values of the computed surface area;
- the relatively large size of the kernel causes blurring or smoothing of the output image, a very common, unfavorable effect of spatial filtering [73] and the size of the kernel causes some boundary effects.

A further limitation of the method is that it is not applicable to multi-band images. Consequently, efficient data reduction methods such as principal component analysis or ratioing should be applied first to the multi-band image.

## 5 The Local Method applied to Artificial Images

Before the proposed 'local  $D$ -algorithm' was used for real digital images, the approach was tested by applying it to artificial images which were not fractals. Some typical examples are presented in figure 3. The images at the left side of figure 3 are artificial input images (two intersecting lines, six flat, homogeneous raised surfaces and a partly random generated image), the images on the right side show the results of the  $D_L$ -algorithm. The size of each artificial image is 40 by 40 pixels and the values of the digital numbers are presented in the legend of the input images. The range of estimated ' $D_L$  values' are by definition between 2.0 and 3.0 and are presented in the legend of the output images. The three examples of figure 3 illustrates the blurring of the algorithm and the boundary effects. A general trend of  $D_L$ -computations is that flat homogeneous areas yield low estimates of  $D_L$  and as the image's heterogeneity increases (intersection of lines, fringes of homogeneous areas),  $D_L$  increases too. Largest  $D_L$  values are found for areas with a very high spatial variability such as the random part of the third example of figure 3.

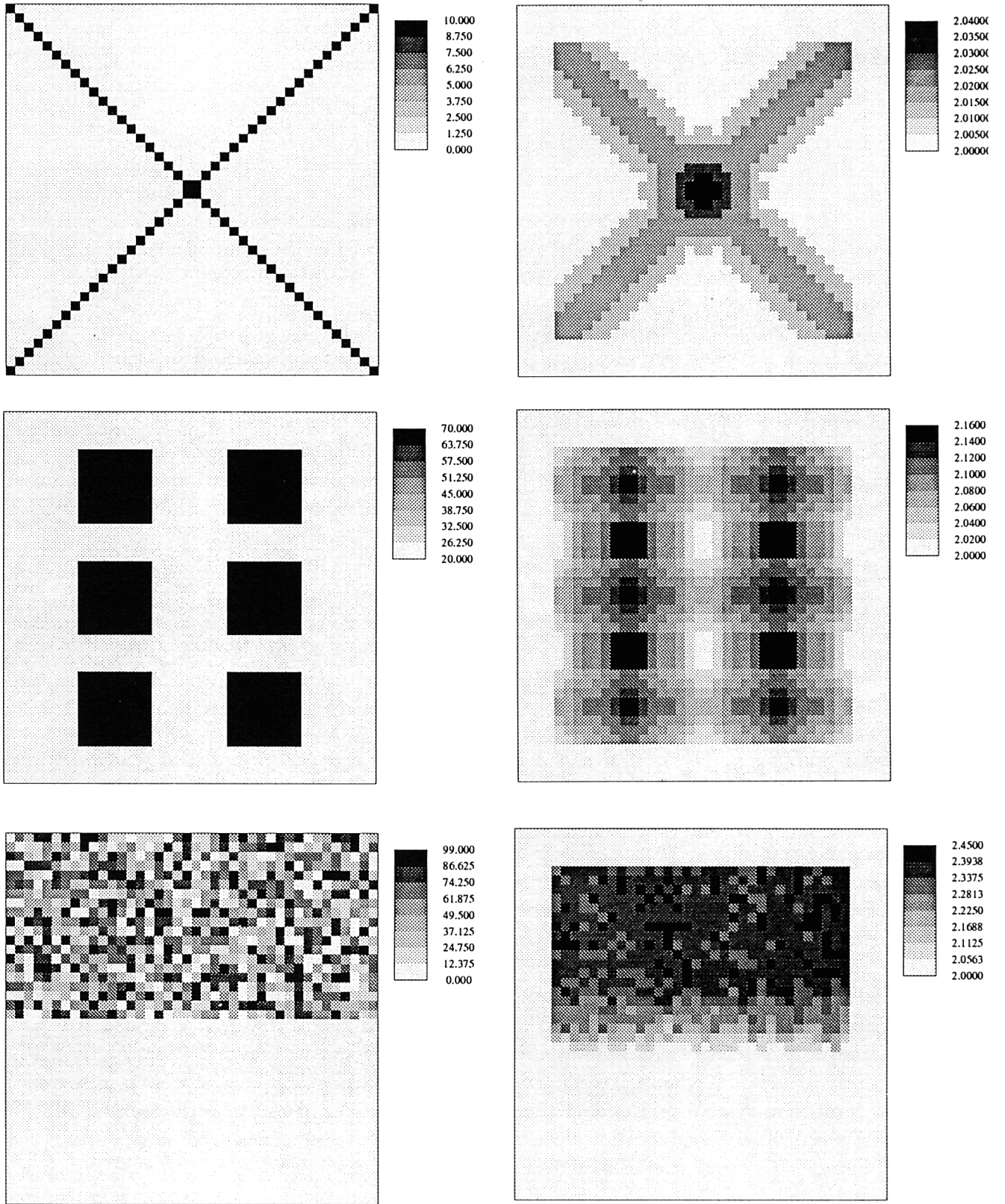


Figure 3: The effect of the ‘local  $D$ -algorithm’ is shown on 3 artificial images. Images on the left show the input images, output images are shown on the right.  $D_L$  values tend to increase with the complexity of the image.

## 6 The Study Area

In the study presented here, two methods are used to estimate  $D$ : the first method (variogram method) is suitable to determine  $D_V$  for one-dimensional field transects; the second method (local  $D$ -algorithm) yields a spatial map of estimated  $D_L$  values, where the new image equals the size of the original image minus half the kernel size due to boundary effects. The case study aimed at finding the answer to two research questions:

-Is the Brownian fractal a useful means of describing the 'roughness' or 'texture' in remotely sensed imagery of Mediterranean land cover types?

-How do the two methods (variogram and local method) perform at distinguishing between different known, types of Mediterranean land cover types?

The suitability of the estimated fractal dimension as a tool for separating different types of Mediterranean vegetation was assessed in a study area in the southern Ardèche province (France). A physiographic survey was carried out resulting in six main land cover classes or mapping units [74]:

- 1. Badlands (strongly incised areas). Bare, high reflectance surfaces varying with densely vegetated areas in gully floors and in between gully systems. Shadows play an important role in badlands with regard to apparent reflectance properties.
- 2. Rangelands - areas dominated by annuals and herbaceous perennials with deep root systems. Shrubs are not present or only scarcely present in the rangelands. Rangelands often form a rather homogeneous cover over extended areas.
- 3. Open garrigue - an area of low scattered bushes, smaller in number than in the previous class. The bushes are rarely more than 2 meters high with bare patches of rock or stony soil between the grasses and herbs.
- 4. Closed garrigue - an open forest type of vegetation with scattered bushes alternating with bare patches, rock outcrops and grasses. Garrigue areas show distinct spatial patterns of shrubs.
- 5. Maquis - forms the local climax vegetation and is a type of evergreen mixed forest dominated by oak species. Maquis has a dense, evergreen vegetative cover.

- 6. The sixth class is dominated by human influences and comprises agricultural areas and built-up areas. The spatial pattern of this class shows spectral variation at regular distances i.e. parcel size.

Two types of digital multi-spectral images were available for this area: a Landsat TM image acquired on 18 July 1991 with a pixel size of 30 x 30m. and an airborne image acquired by the Geophysical Environmental Research (GER) Imaging Spectrometer on 29 June 1989 with a nominal pixel size of 10 x 10m. [75, 76]. Figure 4 shows the TM image of the study area with the 6 land cover types identified. The Landsat TM image was radiometrically corrected using the method proposed by [77] using gain and offset values to convert digital numbers into reflectance. The original GER image contains 63 spectral bands. The radiometric and geometric preprocessing of the airborne image was carried out by the German Aerospace Research Establishment [78] and the Joint Research Centre (JRC) of the European Community in Italy [75]. A selection was made of GER bands corresponding with the TM bands 1 to 5 and 7. The different pixel size of the two images makes it possible to test the new  $D_L$  method on patterns of natural vegetation cover at two levels of space scale. The different dates of data acquisition do not seem to have caused any major differences in the images because the dynamics of the (semi-)natural ecosystems are rather low. In contrast, temporal changes of the agricultural areas can be considerable.

## 7 The Variogram method ( $D_V$ ) to Assess Fractal Dimensions of Transects

The ‘variogram method’ was used to assess  $D$  from transects in the different mapping units which were surveyed in the field. The  $D_V$  values obtained are useful to check whether spatial variation estimated from field data matches that estimated from images. A hand-held radiometer with a field-of view of  $1m^2$  was used to measure reflectance in the visible and near infrared along various transects in the mapping units. Each transect comprised a minimum of 175 sample points. A normalized difference vegetation index was computed from the visible and infrared measurements and for all transects a semivariance function was calculated following the method described by [14]. The variograms were all plotted on log-log paper and for each variogram breaks of slope were located visually [58]. Straight lines were fitted up to the breakpoint using the CSS statistical software package [79] and





Figure 4: Landsat Thematic Mapper image (Bands 4, 5 and 1 as Red, Green and Blue) of the study area showing the six land cover classes: (1) badlands; (2) rangelands; (3) open garrigue; (4) closed garrigue; (5) maquis; (6) agricultural areas. [Image date: 17 July 1992, Original satellite data copyright Eurimage, 1992]

$D_V$  was computed from the regression line. This method was applied to all units except for the agricultural areas. The method is of little use for agricultural regions, because the spatial variation is determined by the human induced boundaries of the parcels. The method also fails in maquis, because maquis is hardly penetrable and the vegetation is too high for hand-held radiation devices. Therefore, variograms for maquis were estimated using data transects taken from the airborne GER image. Table 1 presents  $D_V$  values and break distance for each land cover unit and per transect the  $D$  values and their break distance.

Table 2 shows the average  $D_V$  value, the average variogram model parameters and their  $CV$  values per land cover class.

From the variogram model parameters it can be seen that short variogram 'range distances' are found for open and closed garrigue and badlands, the largest 'range distances' are determined for rangelands and maquis. These results match intuitive expectations that the spatial dimensions of the variability of rangelands and maquis are larger than the variability of badlands and garrigue (i.e. badlands and garrigue have finer patterns). The  $D_V$  values indicate rangelands and maquis as most irregular. The  $D_V$  values are all far in excess of 1.5, indicating that the vegetation index determined from the radiance measured along the transects is highly irregular. Large values of  $D_V$  are also reported by [53, 80]. Discrimination between land cover categories using only  $D_V$  from hand-held radiometer data is poor. Average  $D$  values for the different land cover types are close to each other and the  $CV$  values are relatively high. Maquis is somewhat different than the other land cover types and has the largest  $D_V$ , but it is unclear whether this is a function of the support size of the datasource (GER image) or of the spatial pattern of the maquis. A graph relating  $D_V$  with break distance of the log transformed variograms separates rangelands, open and closed garrigue and maquis (figure 5). Badlands are the most variable and are difficult to group. Furthermore, the question should be answered whether the transects per land cover unit represent real fractals. The linearity of the log-transformed variograms provides information on the self-similarity. Although some log-log variograms are linear over a certain range, most log-log variograms show clear breaks of slope. This non-fractal behaviour might be caused by the limited number of points in the transect (175) or by the fact that the reflectance properties of the studied surfaces are not scale invariant.

Apart from the estimation of  $D_V$ , a conventional statistical procedure was carried out to assess the relative homogeneity of the 6 mapping units. Five test plots of 10 by 10 pixels were located within the core of each

Badlands	$D_V$ variogram	$r^2$	Break- distance (m)
transect1	1.65	0.98	14.8
transect2	1.69	0.99	17.8
transect3	1.78	0.73	11.7
transect4	1.78	0.89	12.0
transect5	1.90	0.86	39.8
Rangelands			
transect1	1.81	0.92	39.8
transect2	1.85	0.91	48.9
transect3	1.79	0.94	48.9
transect4	1.77	0.94	12.0
Open Garrigue			
transect1	1.78	0.92	10.0
transect2	1.70	0.99	48.9
transect3	1.77	0.94	12.0
Closed Garrigue			
transect1	1.81	0.90	7.0
transect2	1.82	0.73	6.1
transect3	1.73	0.96	6.1
transect4	1.82	0.88	7.0
transect5	1.70	0.96	5.8
Maquis			
transect1	1.84	0.91	25.7
transect2	1.96	0.85	39.8
transect3	1.93	0.83	28.1
transect4	1.95	0.82	28.1
transect5	1.89	0.81	32.0

Table 1: Fractal dimension  $D_V$  values and break distances computed for different land cover units using the variogram method based on normalized difference vegetation indices determined along several transects with a hand-held radiometer.

Land Cover Unit Number of transects	Badlands (n=5)	Rangelands (n=4)	Open garrigue (n=3)	Closed garrigue (n=5)	Maquis (n=5)
Avg. D (variogr.): CV (%):	1.76 (5.5)	1.81 (1.9)	1.75 (2.5)	1.78 (3.2)	1.91 (2.4)
Avg. range (m): CV (%):	9.1 (57.1)	36.0 (63.9)	5.6 (41.1)	3.6 (25.6)	27.1 (11.1)
Avg. nugget (c0): CV (%):	5.17 (64.9)	2.82 (55.6)	4.31 (51.5)	3.20 (24.0)	6.11 (26.3)
Avg. Sill-nugget (C): CV (%):	17.7 (66.3)	9.56 (94.0)	6.19 (64.4)	5.56 (14.2)	9.74 (45.4)

Table 2: Average fractal dimension values  $D_V$ , variogram model parameters and coefficient of variance ( $CV$ ) values for different land cover units determined along several transects from hand-held radiometer measurements (variogram method)

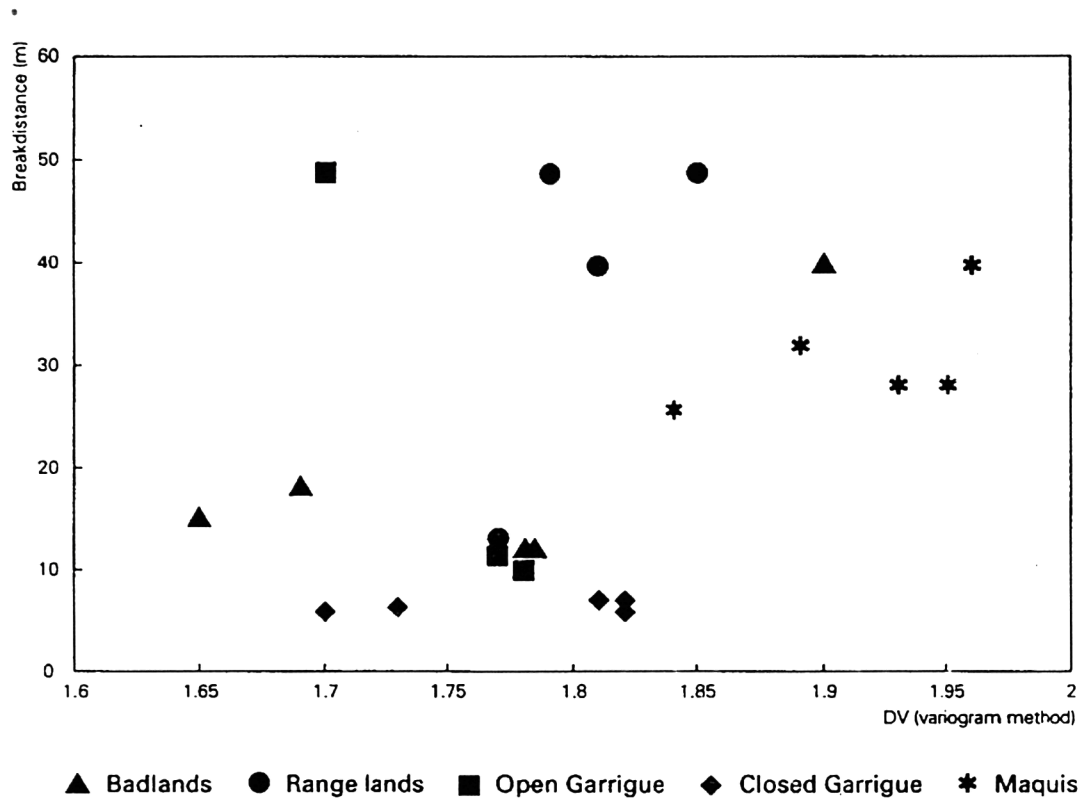


Figure 5: Graph showing the relation between  $D_V$  and break distance from the log transformed variograms for each of the five land cover types.

land cover class in the TM image and in the airborne image. *CV*'s based on a total of 500 pixel values per spectral band per land cover class were computed and are shown in table 3.

Land Cover Unit	TM1	TM2	TM3	TM4	TM5	TM7
Badlands	10.7	14.4	17.5	10.1	11.2	17.5
Rangelands	4.4	6.1	7.5	5.0	6.1	10.3
Open garrigue	6.2	8.6	12.5	6.5	8.9	12.6
Closed garrigue	6.9	9.4	15.1	5.0	11.0	18.8
Maquis	2.6	3.9	6.9	3.9	6.6	11.6
Agricultural	9.7	14.2	22.1	13.3	13.0	22.5

Land Cover Unit	GER1	GER2	GER3	GER4	GER5	GER6
Badlands	23.8	18.8	17.3	9.0	21.0	13.9
Rangelands	28.7	20.2	17.3	8.7	21.3	12.7
Open garrigue	26.2	15.4	15.1	7.7	18.1	12.1
Closed garrigue	32.4	22.7	27.0	7.4	35.7	24.0
Maquis	40.7	20.9	26.0	5.0	33.1	20.1
Agricultural	27.0	22.1	26.4	12.0	45.4	28.3

Table 3: Coefficient of variance (*CV* in experimental plots (n=500 pixels) per land cover class for all spectral bands of the Thematic Mapper (TM) and for the GER-airborne image (GER)

The results of the TM image analysis reinforces intuitive expectations because the largest *CV* values are found for badlands and agricultural areas, smallest *CV* values are computed for rangelands and maquis. It is notable that in the first two visible bands of the TM image badlands have the largest *CV* values of the 6 land cover types whereas agricultural areas show the largest *CV* values in the next 4 TM bands. This can be explained by

the abrupt changes of infrared reflectance between densely covered lots and bare lots. This effect is less pronounced in badlands because vegetation in badlands is often 'water stressed' resulting in smaller contrast between infrared and visible reflection. The *CV* values computed from the GER image show a less distinct pattern. The *CV* values are generally much larger than for the TM image and the land cover types cannot easily be separated. Variability of reflectance within the experimental test plots is apparently much greater. There are two possible explanations: (a) there is a greater variability in the terrain at distances less than 30m., this variability is detected by the GER pixel (10 x 10m.) and is smoothed within the pixel (30 x 30m.) of the TM scanner; (b) there is more noise present in the GER image than in the TM image. A visual interpretation of the GER image showed that the image is of somewhat poor quality and that the contribution of noise to the 'within image variability' might be important. The image was used because the different pixel sizes of the GER and TM image make it possible to study patterns of vegetation cover at two levels of scale. Therefore, image quality was assessed by determining the signal-to-noise ratios.

## 8 Noise in the Digital Images

The quality of the TM image and the GER image was assessed by determining the signal-to-noise ratios (SNR) directly from the images. Nominal SNR for TM measured in the laboratory are between 200 and 500 [81]. Nominal values for the GER image are around 400 [82]. The common procedure to assess SNR from images is by selecting bright, high reflectance, homogeneous surfaces in the image [83]. The quotient of average observed radiance and the standard deviation yields the SNR. Bare bright soils or (empty) parking places are often suitable surfaces. SNR's generally decrease in the shortwave infrared due to lower radiance levels. Furthermore, SNR's determined directly from images tend to be lower than laboratory measurements. The range of SNR for the GER image is between 7 and 15, the values for the TM range from 35 to 85. The values for TM are minimum values because the number of pixels of the selected bright surface was too small for a very accurate estimate. The SNR of the GER image appears to be small but the quality of the TM image is much better and visual interpretation of the image confirms the somewhat poor quality of the GER image. The original GER image looks very speckled in almost all spectral bands due to numerous technical defects during data acquisition

[75]. Consequently, the computations of variability and of  $D$  values using the GER image might be influenced by noise.

## 9 Fractal Dimension of Images by the Local Method ( $D_L$ )

Before the local algorithm for  $D$ -computations was applied to the digital images, the multi-band images were reduced to single band images. Spectral ratioing was preferred for data reduction for two reasons:

- ratioing of one near infrared band and one visible band enhances patterns of vegetation cover;
- ratioing reduces the effect of shadows in the badlands.

The optimal bands for ratioing were determined using the correlation matrix (Pearson correlation) of the experimental test plots described in section 5. The 2 bands with the lowest correlation were selected for ratioing. Band 1 and band 4 have the lowest correlation for both images. A normalized spectral ratio  $(4-1)/(4+1)$  was calculated for both images and after scaling used as input for the  $D_L$  algorithm. The  $D_L$  algorithm, applied to the TM and GER ratio images, yielded two new images with  $D_L$  values. In contrast to the variogram method, the  $D_L$  algorithm yields rather small  $D$  values. The next step in this study was to determine the accuracy with which the two images reflect the 6 land cover classes. Objective assessment of accuracy of the new map is very difficult because:

- the spatial transition of the units, e.g. rangelands to open garrigue is fuzzy;
- the distinguished land cover classes are not exactly defined in terms of cover percentage or species;
- only a map based on aerial photo interpretation and fieldwork of the land cover types was available and the accuracy of this map is unknown.

The usefulness of the  $D_L$  images was estimated by digitizing polygons (minimum of 800 pixels) within the centre of each land cover class. For each polygon the average  $D_L$  value and the standard deviation was computed and is presented in table 4.



GER Image	Badlands	Range-lands	Open garrigue	Closed garrigue	Maquis	Agric. area
Average $D_L$	2.19	2.25	2.24	2.28	2.22	2.21
S.D.	0.03	0.03	0.02	0.03	0.02	0.04
n pixels	1148	793	2698	1108	829	1615

TM Image	Badlands	Range-lands	Open garrigue	Closed garrigue	Maquis	Agric. area
Average $D_L$	2.23	2.10	2.22	2.18	2.14	2.27
S.D.	0.05	0.02	0.04	0.03	0.03	0.06
n pixels	1595	1763	1164	2992	2218	10527

Table 4: Average  $D_L$  values and their standard deviations ( $SD$ ) for polygons centralized in each mapping unit

Normalized curves of the average  $D_L$  values for all 6 polygons are plotted in figures 6 and for the GER and TM image, respectively. The degree of separability between the land cover types using  $D_L$  is indicated by the amount of overlap between the curves. A  $t$ -test for independent samples was carried out for all 6 polygons and for either image. Although all units are significantly different at the 0.05 level, the results should be interpreted with care because the number of cases is very large. Figures 6 and 7 show that  $D_L$  values in the TM image separate the six land cover types much better than the GER image. Five peaks are distinguished in the TM curves of figure 7. Rangelands give a nice distinct peak, maquis and closed garrigue are less pronounced. Agricultural areas result in very broad-shaped curves, this might be expected because estimating  $D_L$  within one agricultural lot will yield low values, estimating  $D_L$  for fringes of lots will yield high values. The curves for badlands and open garrigue coincide, indicating that they cannot be separated using  $D_L$ . The curves resulting from the GER image (figure 6) coincide to a large extent. No single unit can be recognized easily.

Visual interpretation of the 'level-sliced' TM image of  $D_L$  and the 'level-sliced' GER image of  $D_L$  confirms that the TM image shows the general

pattern of maquis, garrigue, rangelands and badlands much better. This is in contrast with expectations because the smaller pixel size of the GER image matches the variogram ‘range distance of spatial dependence’ (table 2) much better than the TM pixel size. However, as described previously, GER image results may be distorted by noise present in the image.

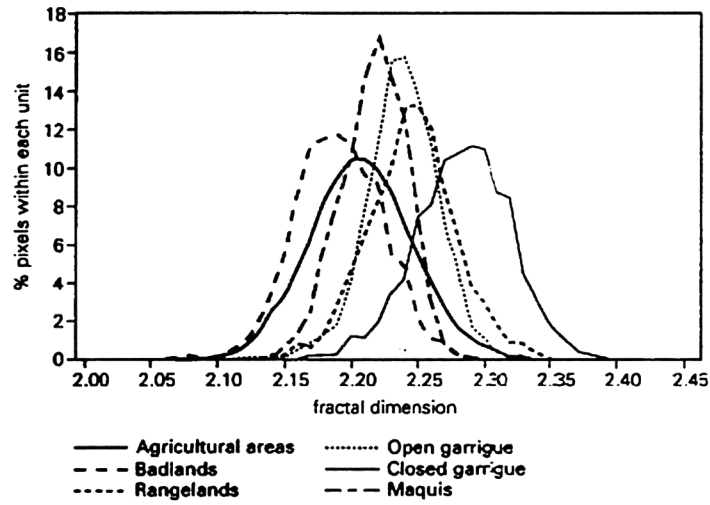


Figure 6: Curves of the estimated fractal dimensions ( $D_L$  method) of the polygons centralized in the mapping units in the GER image. The  $x$ -axis represents the fractal dimension, the  $y$ -axis shows the percentage of pixels per land cover class. An individual peak for a unit indicates that it is feasible to discriminate the unit in the image based on  $D_L$ .

## 10 Discussion and Conclusions

The research presented here has attempted to answer two questions: (1) Is the Brownian fractal a useful means of describing the ‘roughness’ or texture of remotely sensed imagery of different kinds of Mediterranean vegetation, and (2) which of the two methods of estimating fractal dimensions of these vegetation patterns is most appropriate? Before answering the first question it was necessary to estimate fractal dimensions by both methods.

The results show that though both methods of estimating  $D$  are feasible, they require much data and care. The variogram method requires

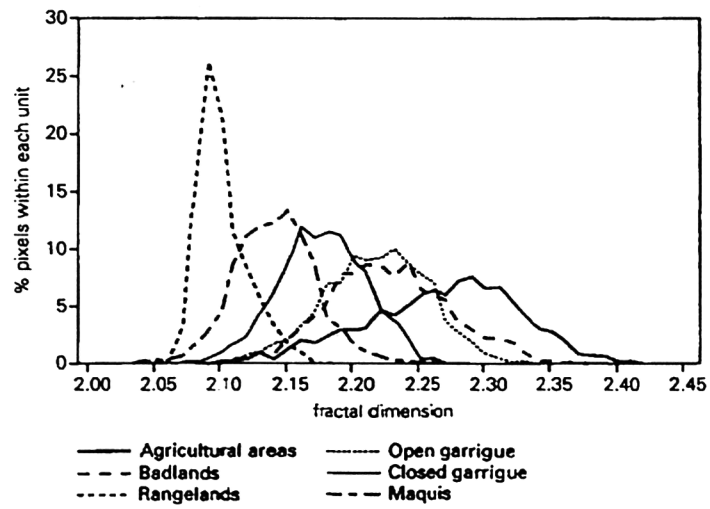


Figure 7: Curves of the estimated fractal dimensions ( $D_L$  method) of the polygons centralized in the mapping units in the TM image. The  $x$ -axis represents the fractal dimension, the  $y$ -axis shows the percentage of pixels per land cover class. An individual peak for a unit indicates that it is feasible to discriminate the unit in the image based on  $D_L$ .

large numbers of data points in order to get information over sufficient lags/spatial scales, and if only a few linear transects are used they may return widely differing values of  $D_V$ . Other problems concern anisotropy of the pattern in the image and the fact that it is difficult to assign the parameters of a variogram that have been estimated over a large sample uniquely to a given pixel location for image enhancement. The local method avoids the latter constraint of the variogram method but uses few data (a kernel of 9 x 9 pixels) and suffers from image blurring and boundary effects, and  $D_L$  is estimated from only 4 lags.

The two methods yield results that suggest that both  $D_V$  and  $D_L$  may be useful in the classification of the land cover types in the study area, though there are many instances where the two methods strongly differ. The variogram method yields large values of  $D_V$  (all > 1.7) for all land cover types, whereas the local estimator produces smaller values (all < 2.3).  $D$  values where the decimal component is large (> 0.5) imply a weak pattern of noisy, random variation, whereas  $D$  values where the decimal component is small (< 0.3) imply smooth variation with little local noise. The ability of  $D_L$  to separate land cover type clearly depends on the imagery used. The estimates of  $D$  depend on spatial resolution (which varied from 1 x 1m. along the transects to 30 x 30m. for the TM imagery) and it is not clear whether the differences in estimated  $D$  values can be wholly ascribed to the differences in methodology or whether they can be explained by the variations in the imagery of the vegetation patterns not being self-similar and therefore not truly fractal. The only situation where data from the same source and resolution were used by both methods is the GER data for the maquis:  $D_V$  was estimated at 1.91 and  $D_L$  at 2.22. This result suggests that the methods do indeed differ considerably, a conclusion that is further borne out both by the negative Pearson correlation between  $D_V$  and  $D_L$  (i.e. -0.65) but also by examining the rank order of estimated  $D$  values for all vegetation types as estimated by both methods from all data sources (table 5).

These results suggest strongly that the images used are not true fractals. Significant differences in the estimates of  $D$  obtained from one-dimensional and two-dimensional methods applied to the same area have also been found by [17] and [24]. Clarke and Schweizer [24], without giving an answer, have asked whether a fractal dimension estimated by a variogram method necessarily bears any relation to that estimated by the walking dividers method, and clearly this dependence of estimated  $D$  on method is an important area that needs to be investigated, as does their other question as to whether the fractal dimension of a profile (transect) across a fractal surface necessarily

Land cover type	$D_V$	$D_L$ (GER)	$D_L$ (TM)
Badlands	4	1	5
Rangelands	2	4	1
Open Garrigue	1	3	4
Closed Garrigue	3	5	3
Maquis	5	2	2

Table 5: Rank order of estimated fractal dimensions. [Note: rank 1 is the smoothest (smallest  $D$ ) and 5 is the roughest]

has a fractal dimension of that of the surface minus one.

The difference in estimated fractal dimension between  $D_V$  and  $D_L$ (TM) in this study may also be due to smoothing of local variation within the 30 x 30m. pixels - in other words the variation is scale dependent. This information, together with the appearance of strong breaks of slope in the variograms of the transect data, reinforce our conclusions that the remotely sensed images of the land cover units are not true fractals, though they undoubtedly differ in roughness. This finding is consistent with the conclusions of [5, 17, 50, 54, 58] and others that land surfaces and/or landscapes are only rarely self-similar, and then only within limited scales. The disappointing results for the airborne GER image are most probably due to the low signal to noise ratio and poor image quality which caused the severe overlap between the land cover classes (figure 6).

Although  $D_L$  for TM imagery does seem to reflect the different vegetation types in the study area, it is clear that  $D_L$  by itself is insufficient for the automatic classification of TM images into land cover categories. The relations between  $D_V$  and break distance (the range of the variogram) in figure 5, suggest that information about the texture of patterns may be used to separate important vegetation classes, though more research is needed to determine how this information can be unambiguously acquired and used.

## 11 Acknowledgements

The author would like to thank Dr. K. C. Clarke and Dr. Z. Xia for provision of literature and Mr. C. Wesseling for his contributions in preparing the software for the fractal analysis. The Institute for Remote Sensing Applications of the Joint Research Centre (Ispra, Italy) of the European Community is thanked for providing the GER images.

## 12 References

- [1] I. S. Zonneveld (1972): ITC Textbook of Photo-Interpretation (Enschede: ITC).
- [2] C. Mitchell (1991): Terrain Evaluation (Harlow, UK: Longman).
- [3] D. Dent and A. Young (1981): Soil Survey and Land Evaluation, (London: G. Allen and Unwin).
- [4] FAO (1967): Aerial Photo Interpretation in Soil Survey, Soils Bulletin 6, Food and Agricultural Organisation, Rome.
- [5] P. A. Burrough (1993): Soil Variability: a Late 20th Century View, Soils and Fertilizers vol.56, No.5, pp.529-562.
- [6] R. Webster (1985): Quantitative Spatial Analysis of Soil in the Field, Advances in Soil Science Vol.3 (New York: Springer-Verlag).
- [7] P. H. T. Beckett and R. Webster (1971): Soil Variability: a Review, Soils and Fertilizer 34, pp.1-15.
- [8] A. P. J. De Roo (1993): Modelling Surface Runoff and Soil Erosion in Catchments, Netherlands Geographical Studies 157, Thesis (Utrecht: KNAG).
- [9] S. M. De Jong (1994): Applications of Reflective Remote Sensing for Land Degradation Studies in a Mediterranean Environment, Netherlands Geographical Studies 177, Thesis (Utrecht: KNAG).
- [10] P. A. Burrough (1986): Principles of Geographical Information Systems for Land Resources Assessment. (Oxford: Clarendon press).
- [11] G. B. M. Heuvelink and P. A. Burrough (1993): Error Propagation in Cartographic Modelling using Boolean Logic and Continuous Classification. Int. Journal of Geographical Information Systems, 7.
- [12] A. J. Journel and C. J. Huijbegts (1978): Mining Geostatistics (London: Academic Press).
- [13] G. Matheron (1971): The Theory of Regionalized Variables and its Applications (Paris: Les Cahiers du centre de Morphologie Mathematique de Fontainebleau. Ecole Nationale Supérieure des Mines de Paris).

- [14] E. H. Isaaks and R. M. Srivastava (1989): An Introduction to Applied Geostatistics, (New York: Oxford University Press).
- [15] B. B. Mandelbrot (1982): The Fractal Geometry of Nature. (San Francisco: W. H. Freeman).
- [16] N. S. Lam and L. De Cola (1993): Fractals in Geography. (Englewood Cliffs NJ: Prentice-Hall).
- [17] B. Klinkenberg and M. F. Goodchild (1992): The Fractal Properties of Topography: A Comparison of Methods. *Earth Surface Processes and Landforms*, Vol.17, pp. 217-234.
- [18] R. S. Snow and L. Mayer, Eds. (1992): Fractals in Geomorphology, *Geomorphology*, Vol. 5, No.1/2, pp. 194.
- [19] D. L. Turcotte (1992): Fractals and Chaos in Geology and Geophysics, (Cambridge: Cambridge University Press).
- [20] D. Unwin (1989): Fractals and the Geosciences, *Computers and Geosciences* (Special Issue on Fractals and the Geosciences), Vol.15, No.2, pp.163-165.
- [21] P. A. Burrough (1981): 'The Fractal Dimensions of Landscapes and other Environmental Data, *Nature* 294, pp. 240-242.
- [22] M. F. Goodchild (1980): Fractals and the Accuracy of Geographical Measures *Mathematical Geology* 12, pp.85-98.
- [23] K. C. Clarke (1986): Computation of the Fractal Dimension of Topographic Surfaces using the Triangular Prism Surface Area Method, *Computers and Geosciences* Vol.12, No.5, pp. 713-722.
- [24] K. C. Clarke and D. M. Schweizer (1991): Measuring the Fractal Dimension of Natural Surfaces Using a Robust Fractal Estimator, *Cartography and Geographic Information Systems* Vol.18, No.1, pp. 37-47.
- [25] D. Lavalle, S. Lovejoy, D. Schertzer and P. Ladoy (1993): Non-linear Variability of Landscape Topography: Multifractal Analysis and Simulation. In [16].
- [26] M. Grenon and M. Batisse (1989): Futures for the Mediterranean Basin: The Blue Plan (London: Oxford University Press).
- [27] H. N. Le Hourou (1981): Impact of Man and His Animals on Mediterranean Vegetation, In: F. di Castri, D. W. Goodall and R. L. Specht (Eds.), *Ecosystems of the World 11: Mediterranean-type Shrublands*, pp.479-517 (Amsterdam :Elsevier).
- [28] J. LaGro Jr. (1991): Assessing Patch Shape in Landscape Mosaics, *Photogrammetric Engineering and Remote Sensing*, Vol.57, No.3, pp. 285-293.
- [29] J. M. Briggs and M. D. Nellis (1991): Seasonal Variation of Heterogeneity in the Tallgrass Prairie: A Quantitative Measure Using Remote

Sensing, Photogrammetric Engineering and Remote Sensing, Vol.57, No.4, pp. 407-411.

[30] J. Hill and J. Mégier (1986): Rural Land Use Inventory and Mapping in the Ardèche Area: Improvement of Automatic Classification by Multi-temporal Analysis of TM Data, Proc. ESA Symp. on Europe from Space, Lyngby, Denmark, 25-28 June, pp.75-85.

[31] B. Lacaze, G. Debussche and J. Jardel (1983): Spatial Variability of Mediterranean Woodlands as Deduced from Landsat and Ground Measurements, Proc. Int. Geoscience and Remote Sensing Symp., San Francisco CA, Aug.31 - Sept.2.

[32] A. H. Strahler (1980): The Use of Prior Probabilities in Maximum Likelihood Classification of Remotely Sensed Data, Remote Sensing of Environment 10: 135-163.

[33] S. M. de Jong (1993): An Application of Spatial Filtering Techniques for Land Cover Mapping using TM Images, Geocarto International, Vol. 8, No.1, pp.43-49.

[34] S. M. de Jong and H.Th. Riezebos (1991): Use of a GIS-database to Improve Multi-spectral Image Classification Accuracy. Proc. of the 2nd European Conf. on GIS (EGIS'91), 2-5 Apr. Brussels, pp. 503-508.

[35] B. Lacaze, G. Debussche and J. Jardel (1984): Analyse de l'Hétérogénéité Spatial d'un Taillis de Chêne Vert (*Quercus ilex* L.) à l'Aide de Techniques Visuelles, Photographiques et Radiométriques. Ile Coll. Int. Signatures Spectrales d'Objects en Télédétection, Bordeaux, 12-16 Sept., pp.265-275.

[36] A. G. Brown (1990): Soil Erosion and Fire in Areas of Mediterranean Type Vegetation: Results from Chaparral in Southern California, USA and Matorral in Andalucia, Southern Spain, In: J. B. Thornes (Ed.), Vegetation and Erosion: Processes and Environments, pp.269-287 (Chichester: Wiley and Sons).

[37] P. Quézel (1981): Floristic Composition and Phytosociological Structure of Sclerophyllous Matorral around the Mediterranean, In: F. di Castri, D. W. Goodall and R. L. Specht (Eds.) Ecosystems of the World 11: Mediterranean-type Shrublands, pp.107-122 (Amsterdam: Elsevier).

[38] B. Klinkenberg (1992): Fractals and Morphometric Measures: is there a Relationship? Geomorphology 5, pp. 5-20.

[39] P. A. Burrough (1987): Spatial Aspects of Ecological Data, In: R. H. G. Jongman, C. J. F. ter Braak and O. F. R. van Tongeren (Eds.), Data Analysis in Community and Landscape Ecology, pp. 213-251, (Wageningen, Pudoc).

[40] A. B. McBratney and R. Webster (1983): Optimal Interpolation and Isarithmic Mapping of Soil Properties: V. Co-regionalisation and Multiple



- Sampling Strategy, *Journal of Soil Science* 34, pp. 137-162.
- [41] R. Webster (1985): Quantitative Spatial Analysis of Soil in the Field. *Advances in Soil Science*, Vol. 3, pp. 1-70.
- [42] C. E. Woodcock, A. H. Strahler and D. L. B. Jupp (1988): The Use of Variograms in Remote Sensing: I. Scene Models and Simulated Images, *Remote Sensing of Environment* 25, pp. 323-348.
- [43] C. E. Woodcock, A. H. Strahler and D. L. B. Jupp (1988): The Use of Variograms in Remote Sensing: II. Real Digital Images, *Remote Sensing of Environment* 25, pp.349-379
- [44] R. Webster R., P. J. Curran and J. W. Munden (1989): Spatial Correlation in Reflected Radiation from the Ground and Its Implication for Sampling and Mapping by Ground-Based Radionetry. *Remote Sensing of Environment* 29, pp. 67-78.
- [45] P.J. Curran (1988): The Semivariogram in Remote Sensing: An Introduction, *Remote Sensing of Environment* 24, pp. 493-507.
- [46] R. Webster and M. A. Oliver (1992): Sample Adequately to Estimate Variograms of Soil Properties, *J. Soil Science* 43: 177-192.
- [47] P. J. Curran and J. L. Dungan (1989): Estimation of Signal-to-Noise: A New procedure Applied to AVIRIS Data, *IEEE Transactions on Geoscience and Remote Sensing*, Vol.27, No.5, pp.620-628.
- [48] H. F. M. Ten Berge, L. Stroosnijder, P. A. Burrough, A. K. Bregt and M. J. de Heus (1983): Spatial Variability of Soil Properties Influencing the Temperature of the Soil Surface *Agricultural Water management* 6: 213-226.
- [49] A. B. McBratney and R. Webster (1981): Spatial Dependence and Classification of the Soil along a Transect in northeast Scotland. *Geoderma* 26: 63-82.
- [50] Z. Xia (1993): The Uses and Limitations of Fractal Geometry in Digital Terrain Modelling. PhD-thesis, City University of New York, 252 pp.
- [51] R. Moussa (1991): Variabilité Spatio-Temporelle et Modelisation Hydrologique. Application au Bassin du Gardon d'Anzude, PhD-thesis, University of Montpellier, France, 314 pp.
- [52] J. B. Thornes (1990): Big Rills have Little Rills, *Nature*, Vol.345, pp.764-765.
- [53] P. A. Burrough (1981): The Fractal Dimensions of Landscapes and other Environmental Data, *Nature* 294, pp. 240-242.
- [54] P. A. Burrough (1989): Fractals and Geochemistry, In: D. Avnir (Ed.), *The Fractal Approach to Heterogeneous Chemistry*. Wiley and Sons Ltd., pp. 383-405.
- [55] M. G. Turner, R. Costanza and F. H. Sklar (1989): Methods to Eval-

uate the Performance of Spatial Simulation Methods, *Ecological Modelling* 48, pp. 1-18.

[56] W. E. H. Culling and M. Datko (1987): The Fractal Geometry of the Soil-Covered Landscape. *Earth Surface Processes and Landforms*, Vol. 12, pp. 369-385.

[57] M. Dicke and P. A. Burrough (1988): Using Fractal Dimensions for Characterizing Tortuosity of Animal Trails, *Physiological Entomology* 13, 393-398.

[58] D. M. Mark and P. B. Aronson (1984): Scale-Dependent Fractal Dimensions of Topographic Surfaces: An Empirical Investigation, with Applications in Geomorphology and Computer Mapping, *Mathematical Geology*, Vol.16, No.7, pp. 671-683.

[59] L. N. Vasilyev and A. S. Tyufin (1992): Fractal Characteristics of Geosystem Spatial Structure from Space Imagery, *Mapping Sciences and Remote Sensing* 29, pp.93-102.

[60] F. Ardini, S. Fioravanti and D. D. Giusto (1991): Multifractals towards Remote Sensing Surface Texture Characterization, *Proc. Int. Geoscience and Remote Sensing Symp. (IGARSS'91)*, June 3-6, Espoo, Finland, pp. 317-320.

[61] S. J. Walsh, L. Bian and D. G. Brown (1991): Issues of Spatial Dependency for Surface Representation through Remote Sensing and GIS, In: J. L. Star (Ed.), *The Integration of Remote Sensing and Geographic Information System*. ASPRS, Bethesda, Maryland.

[62] L. De Cola (1989): Fractal Analysis of a Classified Landsat Scene, *Photogrammetric Engineering and Remote Sensing* Vol.55, pp. 601-610.

[63] J. G. Jones, R.W. Thomas and P. G. Earwicker (1989): Fractal Properties of Computer-Generated and Natural Geophysical Data. *Computers and Geosciences*, Vol.15, No.2, pp. 227-235.

[64] S. Lovejoy (1982): Area-Perimeter Relation for Rain and Cloud Areas, *Science* vol. 216, pp. 185-187.

[65] C. G. Fox and D. E. Hayes (1985): Quantitative Methods for Analyzing the Roughness of the Seafloor. *Rev. Geophys.* 23, pp. 1-48.

[66] G. I. Barenblatt, A. V. Zhivago, Y. P. Neprochnov and A. A. Ostrovskiy (1984): The Fractal Dimension: A Quantitative Characteristic of Ocean-Bottom Relief. *Oceanology* 24, pp. 695-697.

[67] R. H. Bradbury and R. E. Reichelt (1983): Fractal Dimension of a Coral Reef at Ecological Scales, *Marine Ecology Progress Series* 10, pp. 169-171.

[68] N. A. Lifton and C. G. Chase (1992): Tectonic, Climatic and Lithologic Influences on Landscape Fractal Dimension and Hypsometry: Implications for Landscape Evolution in the San Gabriel Mountains, California, *Geo-*

morphology 5, pp. 77-114.

[69] C. G. Chase (1992): Fluvial Landsculpting and the Fractal Dimension of Topography, *Geomorphology* 5, pp. 39-57.

[70] J. K. Elliot (1989): An Investigation of the Change in Surface Roughness through Time on the Foreland of Austre Okstindbreen, North Norway, *Computers and Geosciences*, Vol.15, No.2, pp. 209-217.

[71] D. Mueller-Dombois and H. Ellenberg (1974): *Aims and Methods of Vegetation Ecology*. (London, Wiley and Sons).

[72] M. Kent and P. Coker (1992): *Vegetation Description and Analysis, A Practical Approach*. (London, Belhaven Press).

[73] R. C. Gonzalez and P. Wintz (1987): *Digital Image Processing*, Addison-Wesley Pub., Reading, Massachusetts.

[74] S. M. de Jong, J. C. van Hees, P. B. M. Haemers and H. Th. Riezebos (1990): Physiographic and Pedological Mapping for Erosion Hazard Assessment (Ardèche test site). JRC-Ispira, Italy, Contract Report No. 3787-89-08ED.ISP.NL.

[75] J. Hill (1990): Analysis of GER Imaging Spectrometer Data Acquired During the European Imaging Spectrometry Aircraft Campaign (EISAC'89), *Proc. of 10th EARSeL Symp.*, Toulouse, France, 17-20 May.

[76] S. M. de Jong (1992): The Analysis of Spectroscopical Data to Map Soil Type and Soil Crusts of Mediterranean Eroded Soils, *Soil Technology* Vol.5, pp. 199-211.

[77] B. L. Markham and J. L. Barker (1986): *EOSAT Landsat Technical Notes*, No.1. EOSAT, Lanham, Maryland, pp. 1-8.

[78] F. Lehmann, S. Mackin, R. Richter, H. Rotfuss and A. Walbrodt (1989): The European Imaging Spectroscopy Campaign 1989 (EISAC), Preprocessing, Processing and Data Evaluation of the GER Airborne Imaging Spectrometer, *Techn. Report*, Joint Research Center, Ispira, Italy.

[79] Statsoft (1991): *User's Manual- Complete Statistical Software Package (CSS)*, (Tulsa, Oklahoma. Statsoft Inc.).

[80] P. A. Burrough (1993): Fractals and Geostatistical Methods in Landscape Studies. In: N. S. N. Lam and L. De Cola (Eds.), *Fractals in Geography*. Prentice Hall.

[81] USGS (1982): *Landsat Data Users Notes* 23, United States Geological Survey, Sioux Falls, South Dakota.

[82] W. E. Collins and S. H. Chang (1990): The Geophysical Environmental Research Corp. 63 Channel Airborne Imaging Spectrometer and 12 Band Thermal Scanner, In G. Vane (Ed.), *Imaging Spectroscopy of the Terrestrial Environment*. *Proc. SPIE* 1298, pp. 62-71.

[83] Bo-Cai Gao (1993): An Operational Method for Estimating Signal

to Noise Ratios from Data Acquired with Imaging Spectrometers, Remote Sensing of Environment 43: 23-33.

## Chapter 8

# Applications of the L-systems to Canopy Reflectance Modelling in a Monte Carlo Ray Tracing Technique

*Yves Govaerts\* and Michel M. Verstraete*

### 1 Introduction

In various fields of geophysics, the acquisition of satellite remote sensing data supports an increasing number of scientific investigations and thereby contributes directly to our knowledge and understanding of the Earth as a global and integrated system. Satellite instruments can only measure one or a few radiation characteristics, such as light intensity, in a limited number of spectral intervals, even though the radiation itself has been affected by many processes on its way to the instrument. The nature and behaviour of electromagnetic waves (or the associated photons) is described by Maxwell's equations, and the interactions of radiation with atoms and molecules can be studied with the methods of quantum physics. At the most fundamental level, the transfer of radiation through macroscopic natural media, however, cannot be described explicitly in terms of quantum interactions because of the number of photons involved and the diversity and complexity of the materials in the environment. Specific models must therefore be designed to represent this macroscopic interaction between fields of radiation and finite-size materials, and to account for the anisotropy of natural surface [1].

Solar radiation interacts with the vegetation in a way that depends, among other factors, on the canopy architecture characteristics. There is

---

\*Institute for Remote Sensing Applications, Joint Research Centre, European Commission, 21020 Ispra, Varese, Italy

thus a need to understand the relations between the plant structure complexity and the interaction of radiation with that medium. In this paper, we emphasize how we can achieve this goal with the joint use of both the L-systems to describe the structural diversity of the vegetation and a Monte Carlo ray tracing radiation transfer model to study the scattering properties of light in different types of modelled canopies. In the next Section, we address the main problems resulting from the canopy reflectance modelling. In Section 3, we describe our model of radiation transfer in plant canopies of arbitrary complexity. The principles of L-systems are explained in Section 4. Section 5, is dedicated to an application of radiation transfer modelling in a forest of varying density to illustrate the opportunities offered by our approach.

## 2 Modelling the radiation transfer in the canopy

The complexity of the representation of the transfer of radiation in natural media such as vegetation results in part from the fact that natural surfaces reflect light differently in different directions. Such surfaces are called anisotropic. This anisotropy results from the optical and the structural properties of the medium. Models that represent the reflectance of these surfaces as a function of the positions of both the source of illumination and the observer are called bidirectional reflectance models. Ideally, a general purpose bidirectional reflectance model should take into account the optical and the structural properties over a variety of spatial scales. In the solar spectral region, according to the approach of Westin *et al.* [2], we may assume that the overall canopy reflectance results from a combination of effects at three different scales; the *milliscale*, the *mesoscale* and the *macroscale* effects.

### The milliscale

With regard to the bulk structure of the canopy, the milliscale is defined as the basic scattering object *i.e.*, a leaf or any other phytoelements. The main effect of a single leaf on the light transfer is to reflect, transmit or absorb the radiation differently as a function of the wavelength and the type of surface (see Figure 1). This statement implies that the leaves are considered as “black boxes” when part of a canopy reflectance model. In fact, this scale conceals another scale, the *microscale* which deals with the cell structure of a leaf. The inter-

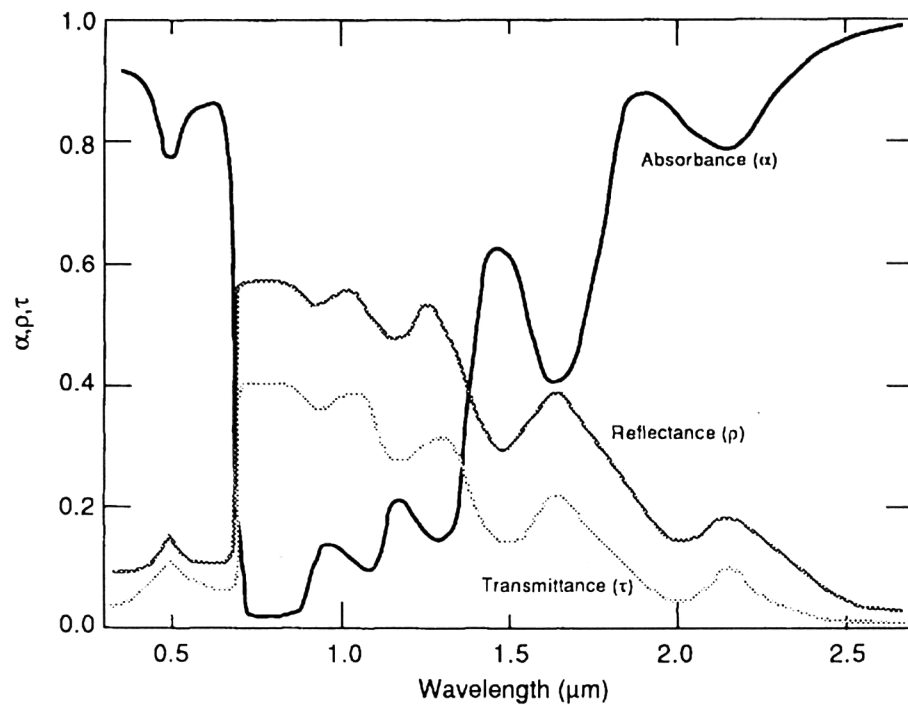


Figure 1: Qualitative reflectance, transmittance and absorbance spectra for a 'typical' green leaf.

action of light with these cells is extremely complex due to the similar size between the objects and the wavelength, and can only be properly described by considering the wave nature of the light. However, as mentioned in the introduction, it is not possible to express the radiation transfer in the vegetation in terms of quantum interactions. In practice, all these effects are statistically embodied at the milliscale through statistical distribution functions such as the scattering phase function. This scale is thus mainly characterised by spectral effects resulting from the cellular structure and chemical composition of the scatterers.

### **The mesoscale**

The mesoscale deals with the spatial organization of the single scatterers or phytoelements in space, typically a single plant or a homogeneous set of plants. The mutual shadowing effect due to the finite

size of the scatterers causes the so-called hot-spot phenomenon. Its intensity depends principally on the scatterer's size, density and orientation. The canopy architecture at this scale is most often described in terms of leaf area index (LAI), leaf area density (LAD), or leaf angular distribution. This scale is thus governed by directional effects resulting from the leaf arrangement.

### **The macroscale**

The range of the macroscale runs from the plant local heterogeneous arrangements to the broad landscape patterns. The effects of this scale on the reflectance result mainly from heterogeneities due to the fragmentation of the landscape and the topography.

Obviously, in the case of laboratory reflectance measurements from a single leaf, only the milliscale effects have to be considered. On the contrary, to model or to extract information from low resolution measurements such as those provided by the AVHRR instrument on the NOAA platform, the full range of effects should be taken into account. Canopy reflectance models have always attempted (more or less successfully) to introduce the effects of these three scales in their models (*e.g.*[3]). In the rest of this section, we briefly review the existing physically-based approaches with their range of validity. Geometrical models describe the bidirectional reflectance on the basis of classical optics, they represent particularly well the illumination, and therefore the shadowing of scattering elements of finite dimension by direct solar radiation. These models often represent the scatterers as geometrical volumes whose optical properties are more representative of the bulk properties of the canopy than of the individual scatterers. The method thus permits the description of the macroscale effects. The classical theory of radiation transfer in turbid media allows the description of the radiation transfer in homogeneous media where the inter-particle distance is large enough and the media density is low enough to satisfy the far field approximation. This approach thus represents the milliscale effects but cannot represent the meso- and macroscale effects. Hybrid models combine the approach of radiation transfer in turbid media with the geometrical description of the size and orientation of the scatterers. This approach emphasizes the mesoscale effects but is also able to represent the milliscale effects. Finally, computer models have been developed to describe explicitly the transfer of photons in canopies. They are mainly based on Monte Carlo methods or computer graphics techniques such as the ray tracing and the radiosity method. Hence, they are able to represent the effects resulting from all three scales. In a previous paper [4], the authors have reviewed



existing computer graphics technique and justified their preference for the ray tracing approach to design a general purpose model.

Each approach has its own advantages and drawbacks and the choice of one type of model rather than another depends mainly on the aim of the study. For instance, the hybrid models are invertible but fail to represent the spatial heterogeneities. The general framework of this approach is to study the scattering of light in a medium as complex as the vegetation with a very high level of realism. In that context, models based on computer graphics techniques offer a definite advantage, although they cannot be inverted against reflectance measurement.

### 3 Computation of the radiation transfer with Raytran

We developed a new radiation transfer model, called Raytran, which as been designed to investigate radiation transfer problems in terrestrial environments over a variety of spatial scales. The canopy reflectance is solved on a photon-by-photon basis using the Monte Carlo ray tracing technique. Monte Carlo procedures are used to generate incident photons, to define the type of interaction when collisions occur, and to compute the scattering angles while the propagation of light is described in terms of geometric optics. The Monte Carlo method itself involves three main steps: (1) generation of random numbers  $\alpha$  uniformly distributed in the interval  $[0,1]$ ; (2) computation of the random variables characterized by more complicated distribution functions of  $\alpha$ ; (3) estimation of the statistical properties of the simulated process by the realization of random variables obtained in step 2 [5]. The program is composed of 7 main parts. The first two perform the initialization of the model while the five remaining ones are iterative processes.

1. *Construction of the target.* The target is described with a set of geometrical solid objects (*e.g.* polygons, discs, spheres, cylinders, cones, boxes) characterized by their location, orientation, and dimension. The optical properties of the objects are defined by their reflectance ( $\rho$ ) and transmittance ( $\tau$ ) coefficients and by scattering distribution functions which characterize their directional behaviour.
2. *Choice of an illumination model.* The incident rays, initiated at the top of the scene, represent the incident radiation. If all rays are ini-

tially parallel, the model represents direct solar radiation. Other distribution can be selected to describe diffuse illumination.

3. *Generation of the photons (rays).* Photons are generated in forward mode, *i.e.*, from the source to the target. The origin of the rays is uniformly distributed in the area located at the top of the scene. The model allows the specification of the wavelength of the incident radiation, and later interactions with objects can be made dependent on this wavelength.
4. *Determination of the localization of the photon-surface interaction.* The closest intersection point between a ray and a surface element is searched with an optimized geometrical sorting algorithm based on bounding individual objects in axis-aligned bounding boxes and on a uniform subdivision of the scene in smaller volumes called “voxels” [6]. In the latter method, each voxel contains the list of all totally or partially included objects.
5. *Determination of the type of interaction.* When an interaction occurs, the simulation of the type of scattering (absorption, reflection, transmission) is performed by generating a random variable  $u$  uniformly distributed in  $[0, 1]$  such that
  - a reflection occurs if  $u \leq \rho$
  - an transmission occurs if  $\rho < u \leq \rho + \tau$
  - a absorption occurs if  $\rho + \tau < u$
6. *Determination of the new direction.* In the case of scattering, the new direction  $(\theta_r, \phi_r)$  is defined with a Monte Carlo procedure applied to the scattering distribution function. In the case of a lambertian surface, the following distribution is used [7]:

$$\theta_r = \arcsin(\sqrt{u_1}) \quad (1)$$

$$\phi_r = 2\pi u_2 \quad (2)$$

where  $u_1$  and  $u_2$  are uniformly distributed in  $[0, 1]$ .

7. *Extraction of relevant information from the ray path.* Two types of physical values are extracted from each ray path: the radiation regime in the target and the bidirectional reflectance function (BRDF). For the former type, the target is divided into  $m$  horizontal layers and one simply counts the number of absorbed or escaped rays in each layer.

To compute the BRDF, the hemisphere above the scene is divided into  $n$  equal area elementary surfaces  $S_l$ . The BRDF  $f_l$  of the elementary surface  $S_l$  is calculated according to [8]

$$f_l = \frac{E_l}{N\Delta\Omega_l}, \quad l = 1, \dots, n \quad (3)$$

where  $E_l$  is the number of photons which crosses the surface  $S_l$ ,  $N$  is the total number of generated photons and  $\Delta\Omega_l$  is the projected solid angle corresponding to the elementary surface  $S_l$ . Note that different measurements may be defined simultaneously.

Steps 4 to 7 are executed for all generated photons, while steps 5 and 6 are repeated until the photon either is absorbed or leaves the outer boundary of the modelled scene.

Two strategies can be followed to represent the geometrical structure of a vegetation canopy as required by step 1. In the first case, each plant is directly constructed from measurements with a set of simple geometrical surfaces and volumes. Quantitative descriptions of the architecture of plants do exist in the literature (*e.g.*[9] or [10]), but remain scarce and often limited to plants under stress. Alternatively, iterative mathematical formulations such as L-systems and fractals have been used to describe biological structures (*e.g.*[11] or [12]). The shapes of plants produced with these advanced concepts are quite realistic, and allow flexibility to change the morphologies. This approach requires information on the actual structure of canopies, and in particular on the frequency and angles of branching, the average length of stems, etc.

## 4 Plant architecture modelling with the L-systems

Recent advances in computer graphics have made possible the generation of images of plants that are extremely realistic. The concepts behind this ‘artificial botany’ are based mostly on two mathematical theories: fractals and L-systems. L-systems were introduced by Lindenmayer in 1968 as a mathematical theory of plant development. The principle is based on the central concept of parallel rewriting by successively replacing parts of simple objects, called the *alphabet*, using a set of *production rules*, starting from an initial condition or string of characters called the *axiom*. In the course of the algorithm, a long string of characters is generated. For example, the

rule  $p_1 : a \rightarrow ab$  means that the letter  $a$  is to be replaced by the string  $ab$  and the rule  $p_2 : b \rightarrow a$  means that the letter  $b$  is to be replaced by  $a$ . If we assume that the axiom is the letter  $b$ , in the first step of rewriting,  $b$  is replaced by  $a$  using rule  $p_2$ . In the second step,  $a$  is replaced by  $ab$  using production  $p_1$ . In the next rewriting step, both  $a$  and  $b$  are simultaneously replaced with  $p_1$  and  $p_2$ , and the resulting string is  $aba$ . The next derivation generates the string  $abaab$  which in turn yields  $abaababa$  and so on (see Table 1). The correspondence between the produced strings and the geometric

Axiom	$\omega$	$:$	$b$
Production rules	$p_1$	$:$	$a \rightarrow ab$
	$p_2$	$:$	$b \rightarrow a$
Derivation	0		$b$
	1		$a$
	2		$ab$
	3		$aba$
	4		$abaab$
	5		$abaababa$
	...		...

Table 1: Example of definition and derivation of an L-system.

interpretation is established via a ‘LOGO-like turtle’ [13] which interprets the characters sequentially as basic commands such as “move forward”, “turn left”, and so on. In a tridimensional space, the state of the turtle is defined by its position and three vectors which define its current orientation [14].

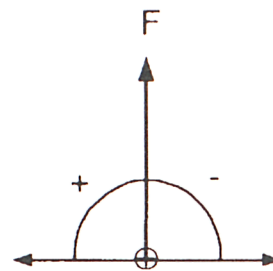
There are many kinds of L-systems. The simplest one, the 0L-system may be formally defined as an ordered triplet  $(V, \omega, P)$ , where  $V$  is the alphabet,  $\omega$  is the axiom which is a non-empty word out of the alphabet and  $p$  is a finite set of productions rules. A pair  $(a, x)$  composed of a letter  $a$  and the word  $x$  is called the production, and is written as  $a \rightarrow x$ . The letter  $a$  and the word  $x$  are called predecessor and the successor of this production, respectively. A 0L-system is deterministic (D0L-system) if and only if for each letter  $a$  of the alphabet  $V$  there is exactly one word  $x$  such that  $a \rightarrow x$ . Thus, in such L-systems, the number of productions can not exceed the number of symbols in the alphabet of the L-system. A simple example of 0L-system is given in Figure 2 with the interpretation of the turtle movements.

Various extensions of the 0L-systems have been proposed and studied

alphabet : 'F' '-' '+'  
 axiom : F - F - F - F  
 production:  $F \rightarrow F - F + F + FF - F - F + F$

Turtle interpretation of strings:

F : move forward a step of length  $d$   
 + : turn left by an angle  $\delta$  ( $90^\circ$ )  
 - : turn right by an angle  $\delta$  ( $90^\circ$ )



$n = 0$



$n = 1$

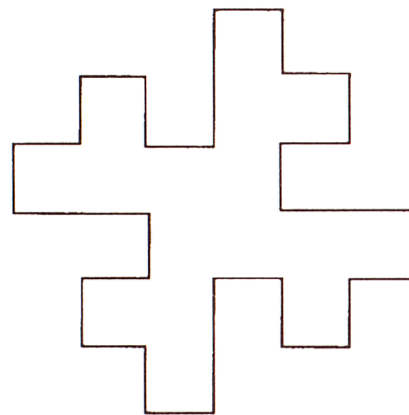


Figure 2: Von Koch quadratic island. Top: Definition of the corresponding DOL-system with the geometric interpretation rules. Bottom: The first 2 stages in the generation of the system.

to achieve flexibility and variety in the sequences of symbols that can be generated by an L-system. We list here the main features we used in the present study. In a stochastic L-system, for one or more symbols, there is a set of rules such as  $a \xrightarrow{l} x$ ,  $a \xrightarrow{m} y$ , which are applied with specific probabilities  $l$  and  $m$  with  $l + m = 1$ . So far, L-systems are only able to represent discretized values and fail to capture properly continuous phenomena. To solve this problem, numerical parameters can be associated with production rules to give parametric L-systems. A formal definition is given in [14]. A T0L-system (T is for table) is an ordered quadruplet  $(V, \omega, P, T)$  where  $V, \omega, P$  have the same definition as for the 0L-system and  $T$  is a finite non-empty collection of subsets of  $p$ , called tables. It is assumed that for each table  $t$  belonging to the collection  $T$ , and for each letter  $a$ , there is at least one production  $p$  in table  $t$  with the predecessor  $a$  [15]. Such systems are used to describe two or more successive phases of growth by means of a change in the production rules. These changes in production rules can be used to alter the growth of the structure after a certain number of stages. T0L-systems can be combined with parametric one as illustrated in Table 2.

Axiom	$\omega$	:	$A(4, 4), B(2)$
Production rules	$p_1$	:	$A(x, y) : y \leq 3 \rightarrow A(x \times 2, x + y)$
	$p_2$	:	$A(x, y) : y > 3 \rightarrow B(x)A(x/y, 0)$
	$p_3$	:	$B(x) : x < 1 \rightarrow C$
	$p_4$	:	$B(x) : x \geq 1 \rightarrow B(x - 1)$

Table 2: Example of production rules for a parametric T0L-system.

Another useful implementation of the L-systems can be used to simulate branching mechanisms by saving the position and orientation of the turtle before generating a new axis and then restoring the original position of the turtle. Moreover, it is also possible to introduce a “tropism vector” to represent phenomena which influence physiological processes. This vector allows to adjust the orientation of the turtle in response to a stimulus such as light or gravity.

Finally, we close this section with a brief comparison between L-systems and fractals. Although the L-systems are very similar to fractals as evident from Figure 2, they present the advantage of being more versatile and convenient to manipulate simultaneously different types of objects. They also lend themselves rather easily to the mathematical description of physiological processes in the form of production rules. In the framework of canopy

reflectance modeling, L-systems offer a unique opportunity to describe plant architecture with a very high level of complexity and realism, using a set of geometrical objects of given shape, size and position. In the next section, we give an illustrative example of radiative transfer in various types of forest constructed with trees generated by a L-system.

## 5 Application to forests

The potential of L-systems to generate realistic-looking plants has been shown by many authors (*e.g.*[12]). More recently, Goel and Rozehnal [16] have also explored some non-biological applications of the L-systems. However, in the case where the L-systems are used to generate plants for canopy reflectance modeling purpose, the requirement is not so much to represent realistic-looking plants than to produce plant architectures with realistic morphological properties. For example, a given L-system may produce a very realistic-looking tree but with a completely unrealistic LAI value. In the seventies, Hallé *et al.* [17] have suggested that each individual species has a precisely determined structure or *architectural model*. They found that by using a set of simple growth characteristics it was possible to categorize all trees into 23 architectural models which encompass the total diversity of tree forms. Each of these models is identified by the name of a Botanist. Our concern here is not to reproduce explicitly a specific existing tree species but rather to create a *generic* tree obeying classification criteria corresponding to one of the 23 standard architectural models, *i.e.*, the Rauh's model, which includes, among others, poplar trees, birch trees, pine trees and fruit trees of temperate regions [18]. This model considers rhythmic orthotropic monopodial growth. Rhythmic growth results from seasonal climatic changes and produces shoots with an articulated branching process as shown in Figure 3A. The angular behaviour of a branch or axis with regard to the bearing axis is an important parameter. It is *plagiotropic* if the development is rather horizontal and *orthotropic* is the development is rather vertical. A *monopod* is a ramified system which includes a unique main axis, the trunk.

To take full advantage of parametric table oriented L-systems in our growth model, we divided our generic tree into three parts (Figure 3B). The lower one is composed of the bare trunk. The medium one is composed of sparse rather horizontal mother branches and the upper one is composed of dense mother branches which become more vertical as we reach the top of the tree. Each part has its own growth unit which defines the frequency

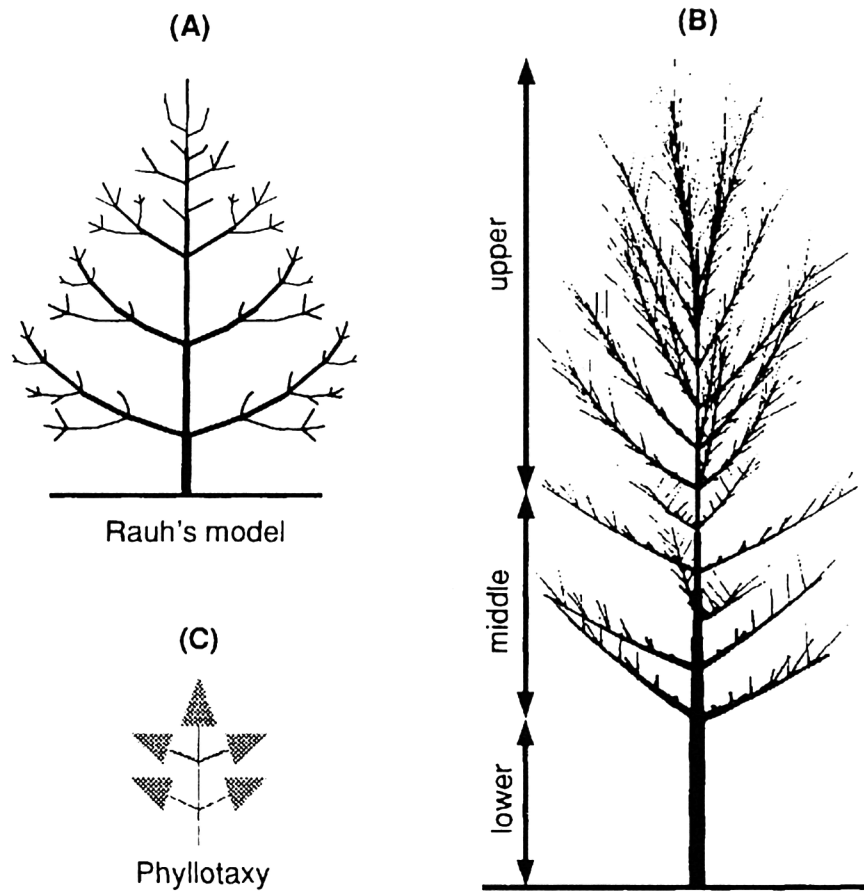


Figure 3: (A) Rauh architectural model with rhythmic orthotropic monopodial growth. (B) Silhouette of our 'generic tree' derived from production rules based on the Rauh's model. (C) Adopted plagiotrop phyllotaxy.



of the branching processes. The rhythmic growth of the tree is determined by the number of iterations used to derive the trunk (first order axis), the middle and upper part mother branches (second order axis), the daughter branches (third order axis) and the twigs (fourth order axis). The twigs produce the stems (fifth order axis) which bear the leaves with a plagiotrop phyllotaxy (Figure 3C). The production rules used to define the L-system are summarized in Table 3. Moreover, growth functions delimit the max-

⇒	the trunk produces two (in the middle part) or three (in the upper part) mother branches at each branching process
⇒	the mother branches produce two (in the middle part) or three (in the upper part) daughter branches at each branching process
⇒	the length of the trunk segments are shortened by a constant ratio with respect to the first segment
⇒	the sum of the mother branch diameter at every branching points is equal to the diameter of the trunk at this point
⇒	the growth of the trunk stops when the height defined by the growth function is reached
⇒	the growth of the mother branches stops when the length defined by the growth function is reached
⇒	the angle between the trunk and the mother branches decreases with respect to the height
⇒	the length of the daughter branches increases with regard to the distance from the trunk
⇒	the daughter branches produce a twig at each branching process
⇒	the twig produce a clumping of 5 leaves at each branching process

Table 3: List of production rules used to define the L-system of the generic Rauh tree.

imum horizontal and vertical development of the tree. The simplest, but quite arbitrary, way to represent plant growth is to use sigmoidal function. The term *sigmoidal* refers to a function with a plot in the shape of the letter S. Such functions are commonly found in biological processes [19]. However, since we are more interested in producing adult plants than in modelling their actual growth mechanism, we have used logarithmic functions. These

functions control the height of the three parts of trunk (Figure 4A, solid line), the bottom radius of the trunk (Figure 4B), the vertically projected area of the tree (Figure 4C, solid line) and the area of the leaves (Figure 4D). The resulting number of leaves and LAI of our generic Rauh tree are given in Figure 4E and F, solid lines.

So far, the morphological properties apply to trees whose development may proceed with a minimum of disturbance. By contrast, in natural environments such as forests, tree growth may be modified due to stress conditions such as storms, climatic events, fires or crown density [20]. We introduced a new parameter to take into account the effects of surrounding trees; the smaller the parameter, the denser the forest. The main effects of this parameter is to reduce the vertical development of the tree and the total number of leaves (Figure 4C and E, dashed lines), as well as to increase the growth unit in the middle part. We are thus able to control the effects of an homogeneous tree density on the development of the individuals.

We have simulated three different types of forest density: an “open” forest with a fractional cover of 40%, a “normal” forest with a fractional cover of 80% and a “dense” forest with a fractional cover of 100%. The fractional cover is simply the ratio of the projected area of the plant on the soil to the area of the soil. Each forest is represented with a sample of  $3 \times 3$  trees whose age ranges from 17 to 22 years. To simulate an infinite forest, we assume that each sampling area is surrounded by similar areas such that rays which escape the scene from one lateral side are translated to the opposite side while the direction remains unchanged. In the “open” configuration, the sampling area is a square of 30m on the side, and where the mean distance between the trees is 10m (Figure 5A). In the “normal” configuration, the mean distance between the trees is 6.5m such that the side length of the sampling area is 20m (Figure 5 B). The “dense” configuration is characterized by a mean distance between the trees of 4m and the sampling area is 7m on the side (Figure 5C). The ground is supposed to be a “green soil” for the open and normal forest and a bare soil for the dense forest. The values of the spectral parameters of the soil, branches and leaves are given in Table 4. All surfaces are supposed to be lambertian. For each configuration, we compute the radiation regime in the visible (VIS at  $0.6\mu\text{m}$ ) and the near-infrared (NIR at  $0.9\mu\text{m}$ ) regions.

To generate the trees, we use Graphtal<sup>1</sup> which allows the definition of context-free, table oriented L-systems with stochastic production rules.

---

<sup>1</sup>Grphtal is a public domain software developed by C. Streit in 1992, it is available on the anonymous ftp server [iamsun.unibe.ch](http://iamsun.unibe.ch).

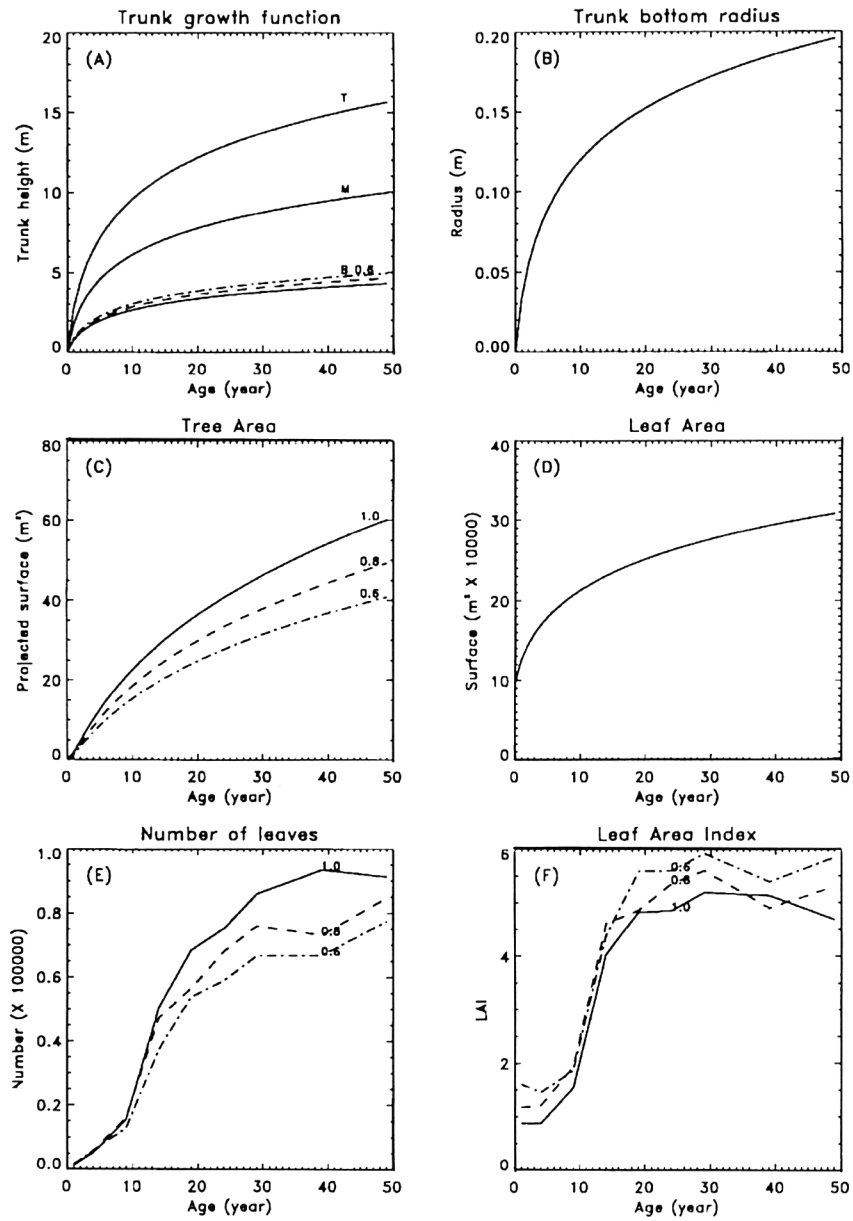


Figure 4: Growth functions (see text for details).

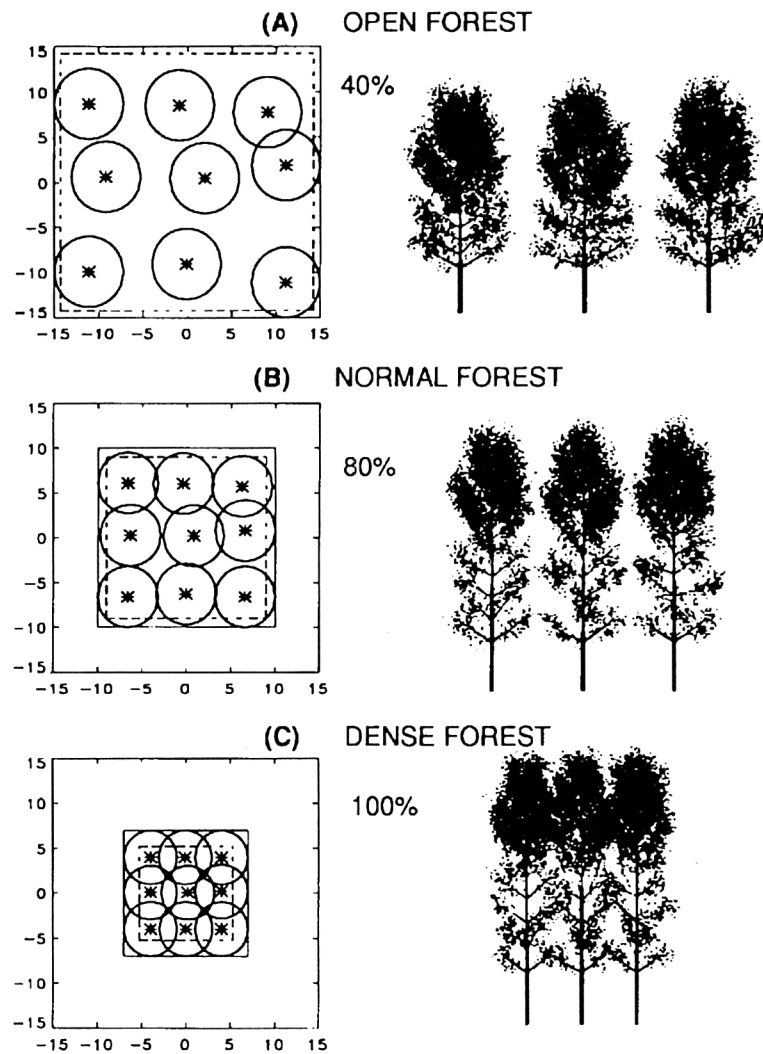


Figure 5: Types of forest. Left column: Top view of the tree arrangement. Circles represent the projected areas of the trees and dashed squares the lighted areas. Right: Silhouettes of the trees corresponding to each density.

	VIS ( $0.6\mu\text{m}$ )		NIR ( $0.9\mu\text{m}$ )	
Element	$\rho$	$\tau$	$\rho$	$\tau$
Ground under open forest	0.08	0.	0.35	0.
Ground under normal forest	0.08	0.	0.3	0.
Ground under forest	0.08	0.	0.2	0.
Trunk and branches	0.09	0.	0.3	0.
Leaves	0.06	0.06	0.6	0.3

Table 4: Spectral values for the various elements of the scene ( $\rho$  = reflectance;  $\tau$  = transmittance).

This software is able to produce an output compatible with Raytran geometric primitives. The branches are defined with cylinders and cones and the leaves with triangles. For example, a 20 year old tree described following the rules of Table 3 is represented with 289,280 different geometric primitives. To save computer time, we reduced the number of objects used to describe each tree: Daughter branches, twigs and stems were not included in the scene and the clumping of 5 leaves has been replaced by a single leaf of equivalent area. Sensitivity tests have shown that the difference between the hemispherical reflectance of the original tree and the simplified one is less than 1%. These simplifications allow each forest scene of  $3 \times 3$  trees to be composed of  $\pm 100,000$  different geometric objects. A scene is lit with 50 million parallel photons which originate from a square located at the top of the canopy. To avoid illuminating the soil near the sides of the scene in the case of an infinite canopy, the size of the energy source is slightly smaller than actual size of the target. This area is indicated by the dashed squares on the left column of Figure 5.

First, we have explored the radiation regime in various forest density types. The scene has been divided into 20 horizontal layers and the numbers of rays escaping the scene from each layer and absorbed in each layer were evaluated. The number of escaped rays is divided by the total number of escaped photons to provide an estimate of the contribution of each layer to the observed reflectance, while the number of absorbed rays is divided by the total number of generated photons to assess how each layer contributes to the total absorption of the canopy. Figure 6 gives the profiles of escaped and absorbed rays for a sun zenith angle of  $45^\circ$ . It appears quite clearly that, in the dense forest case, all the reflected radiation comes from the very top layer of the canopy. This kind of configuration may thus be easily modelled as a dense monolayer canopy. One can also observe the large

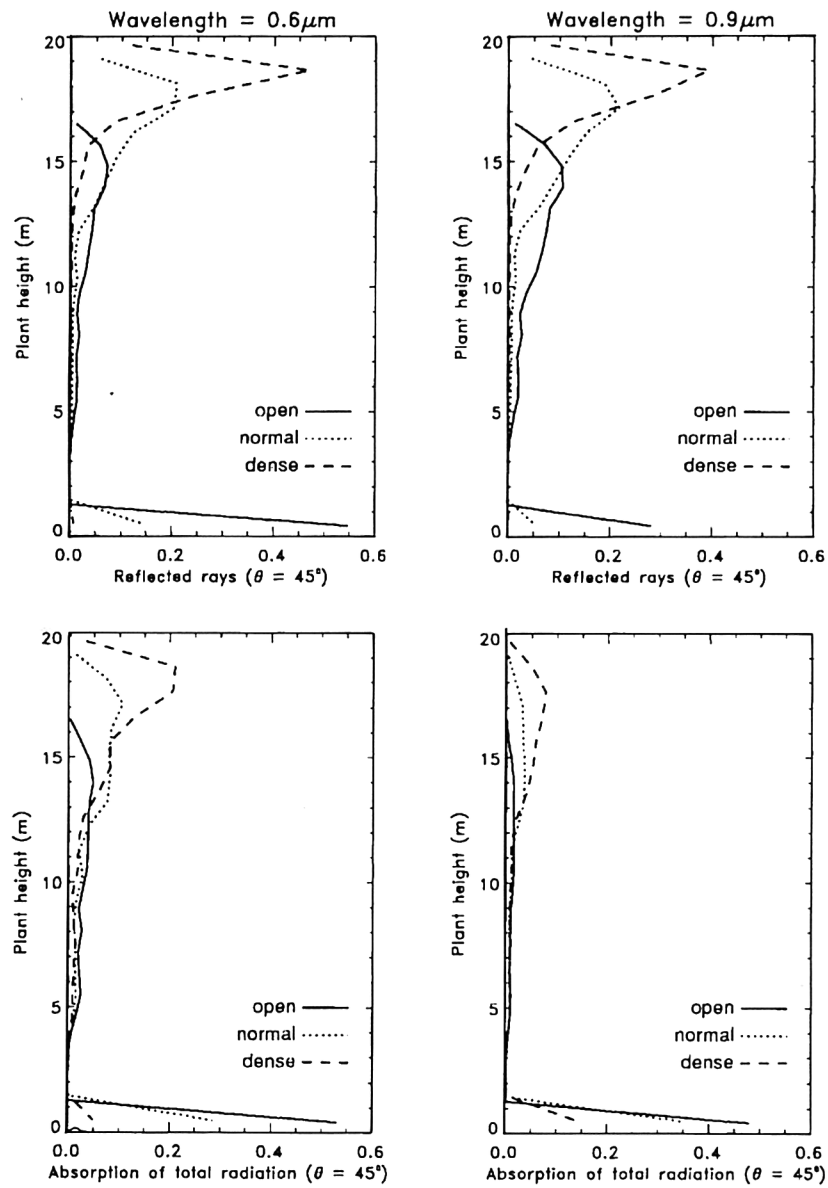


Figure 6: Radiation regime in the three types of forest for a sun zenith angle of  $45^\circ$ .

differences between the origin of the reflected radiation in the case of the open! forest for the two simulated wavelengths. In the visible region, more or less half of the signal comes from the trees and half from the ground. In the near-infrared region, most of the total reflected radiation exiting the scene ( $\pm 70\%$ ) comes from the trees. This phenomenon is due to the multiple scattering effect which is much stronger in the latter case and nearly absent in the former case. Indeed, in the visible region, a ray which is first reflected by the ground and next intercepted by a leaf has a very high probability to be absorbed while this probability is quite weak in the near-infrared region.

Next, we have computed the BRDF. Figure 7, represents tridimensional

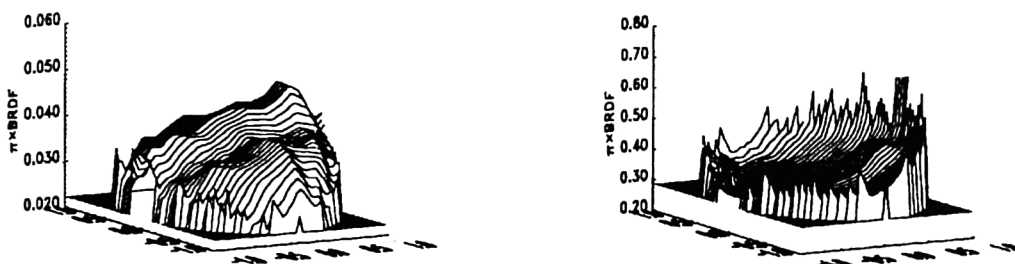


Figure 7: BRDF of an open forest for a sun zenith angle of  $45^\circ$ . Left: The visible region. Right: The near infrared region.

polar plots of the BRDF of an open forest lighted with a sun zenith angle of  $45^\circ$ . This example illustrates very well the influence of the multiple scattering and ground effects on the angular distribution of reflectance. In the visible region (left), the presence of the hot-spot peak is obvious while its shape is much smoother in the near-infrared. For the sake of clarity, we have plotted the BRDF in the principal plane which is the defined by the incoming solar direction and the local vertical (Figure 8). We may deduce the following points for the different wavelengths and tree density from these graphs:

1. There is relatively more directional variability between the forest density configurations in the VIS region than in the NIR.

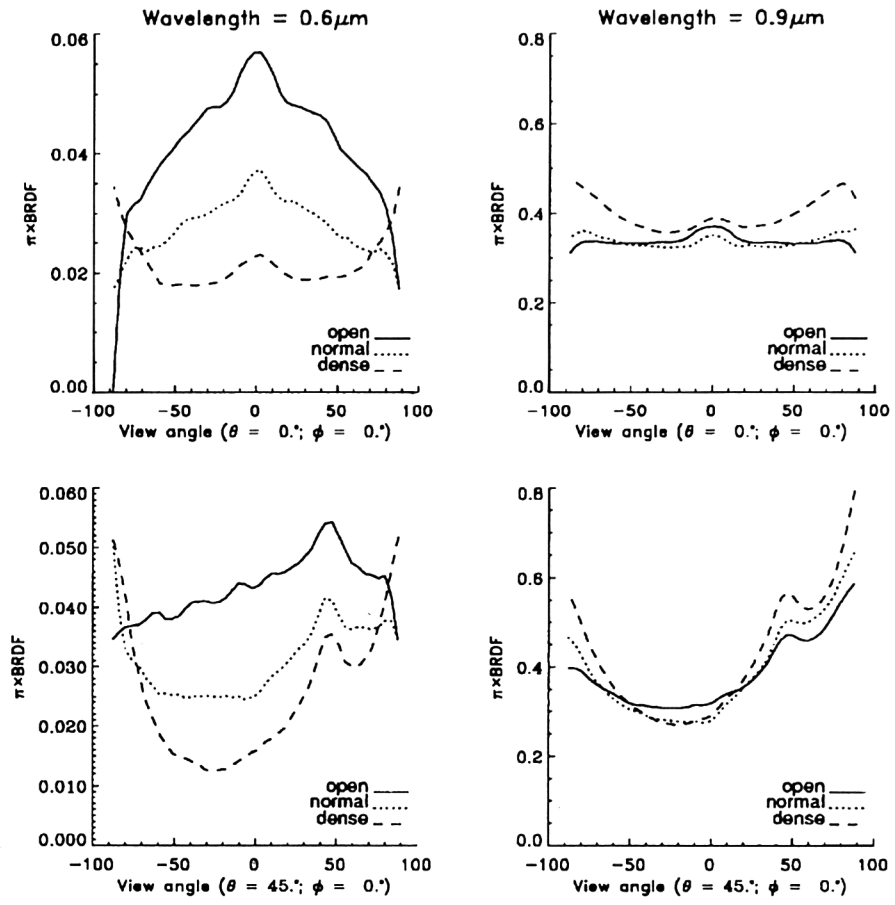


Figure 8: BRDF in the principal plane for a sun zenith angle of  $0^\circ$  (top row) and  $45^\circ$  (bottom row) in the VIS (left column) and the NIR (right column).



2. As already mentioned, the hot-spot phenomenon is stronger in the VIS than in the NIR.
3. For a sun angle of  $45^\circ$  in the NIR, the reflectance of open forest is higher than the dense one at the nadir but lower for low observation angles, due to the contribution of the background surface (soil) between the tree crowns.

Finally, we plotted the directional hemispherical reflectance or spectral albedo (Figure 9). We observe the following:

1. As the forest becomes denser, the hemispherical reflectance decreases in the VIS and increases in the NIR. This is due to the contrast between the optical properties of the leaves and the ground which are opposed in the two spectral regions.
2. In the VIS, the effect of large sun zenith angles is to decrease the hemispherical reflectance of the dense configuration and to increase it for the two other configurations.
3. In the NIR, it is possible to discriminate the open and normal configuration only at low sun zenith angles.

What can we conclude, from a practical point of view, from these results? Global environmental monitoring from remotely sensed data such as NOAA-AVHRR are most often based on linear combinations of radiometric values (vegetation indices) and supervised classification procedures [21]. As part of this approach, land-cover discrimination results from empirical trial and error methods based on locally adjusted threshold values. Our study has shown that since we are able to predict the origin of the received signal for the various wavelengths and tree density, one can define *a priori* threshold values from which it becomes possible to discriminate land-cover categories for a given observation geometry. As an illustrative example, we have computed the Normalized Difference Vegetation Index (NDVI) and the Global Environmental Monitoring Index (GEMI) [22] for these forest types on the basis of the directional hemispherical reflectances computed above. The result is also shown Figure 9. NDVI does not really differentiate between the normal and the dense configuration especially at low sun zenith angles. On the contrary, GEMI does not significantly discriminate the open and normal cases except at low sun zenith angles. Many more cases should be investigated before drawing firm conclusions, involving a variety of plant canopies and a representative sample of illumination and

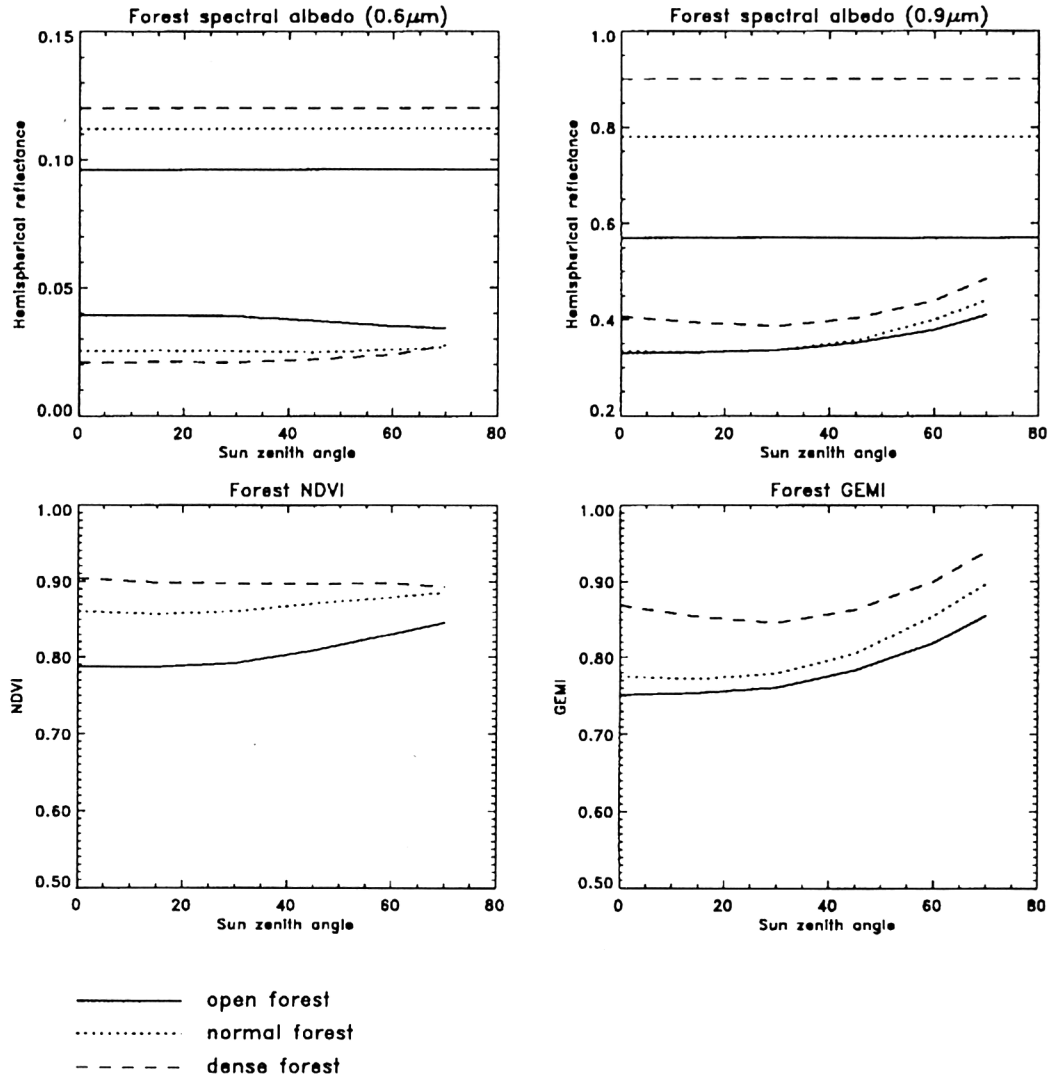


Figure 9: Top plots: Hemispherical reflectance for various sun zenith angles in the VIS and NIR. The straight lines represent theoretical values calculated as  $(\sigma_{f_{ground}}\alpha_{ground} + \sigma_{f_{trees}}\alpha_{trees})$  where  $\sigma_f$  is the fractional cover and  $\alpha$  is the single scattering albedo. Bottom plots: Vegetation indices; NDVI (left) and GEMI (right).

viewing conditions. Nevertheless, a few interesting points should be studied further. First, there is a great sensitivity of the GEMI to solar zenith angle. This is a side effect (and a confirmation) of its sensitivity to the amount of vegetation as already shown in a previous study [23]. Second, the NDVI appears to differentiate better between the open forest on the one hand and the normal and closed forest on the other hand. The GEMI, for its part, is able to maintain a significant sensitivity to forest density as it distinguishes between the dense forest and the two other types.

## 6 Conclusion and perspectives

As we have shown, L-systems are very easy to use to model the growth and structural complexity of the vegetation. Monte Carlo ray tracing methods constitute a very powerful tool to study the transport of light into these simulated media. However, due to the large number of different variables, strategies have to be designed to ensure the efficient utilization of the model. In that sense, L-systems appear to be more appropriate to produce single plants while a fractal approach may be very helpful to describe the large scale landscape patterns. In such a way, one can study the relation between the actual geometric fractal dimension of a scene with the fractal dimension resulting from radiometric measurements. This kind of results will improve the methods used to compare high and low resolution remote sensing data. Moreover, coupling this radiation transfer model with bio-physical models which describe the leaf light use efficiency or the carbon cycle in the vegetation would allow to highlight the relation between the spectral signature of a plant and its physiological properties.

This model provides a state of the art representation of the transport of light in plant canopies (and other natural surface environments) and complements the more classical models developed so far. It is expected that model intercomparisons will lead to significant model improvements. The flexibility afforded by L-systems opens new perspectives and opportunities with respect to radiation transfer modeling and its application to remote sensing data interpretation.

## Acknowledgments

The authors would like to thank Philippe Martin, Nadine Laporte and Daniele Ehrlich for their help in assembling information on plant architecture.

## References

- [1] B. Pinty and M. M. Verstraete, (1992), "On the design and validation of bidirectional reflectance and albedo models", *Remote Sensing of Environment*, Vol. 41, pp. 155–167.
- [2] S. H. Westin, J. R. Arvo and K. E. Torrance, (1992), "Predicting reflectance functions from complex surfaces", *Computer Graphics*, Vol. 26, pp. 255–265.
- [3] G. H. Suits, (1972), "The calculation of the directional reflectance of a vegetative canopy", *Remote Sensing of Environment*, Vol. 2, pp. 117–125.
- [4] M. M. Verstraete and Y. Govaerts, (1994), "Modelling the scattering of light in arbitrarily complex media: motivation for a ray tracing approach", Tech. Rep. In Press, Institute for Remote Sensing Applications, CEC Join Research Centre, Ispra, Italy.
- [5] J. Ross and A. Marshak, (1991), "Monte Carlo methods", in *Photon - Vegetation Interactions* (R. Myneni and J. Ross, ed.), pp. 441–467, New York: Springer-Verlag.
- [6] J. Arvo and D. Kirk, (1989), "A survey of ray tracing acceleration techniques", in *An Introduction to Ray Tracing* (A. Glassner, ed.), pp. 201–262, New York: Academic Press.
- [7] V. S. Antyufeev and A. L. Marshak, (1990), "Monte Carlo Method and Transport Equation in Plant Canopies", *Remote Sensing of Environment*, Vol. 31, pp. 183–191.
- [8] J. Ross and A. Marshak, (1989), "The influence of leaf orientation and the specular component of leaf reflectance on the canopy bidirectional reflectance", *Remote Sensing of Environment*, Vol. 27, pp. 251–260.
- [9] H. Sinoquet, B. Moulia and R. Bonhomme, (1991), "Estimating the three-dimensional geometry of a maize crop as an input of radiation models: comparaison between three-dimensional digitizing and plant profiles", *Agricultural and Forest Meteorology*, Vol. 55, pp. 233–249.
- [10] S. N. Martens, S. L. Ustin and J. M. Norman, (1991), "Measurement of tree canopy architecture", *International Journal of Remote Sensing*, Vol. 12, pp. 1525–1545.

- [11] P. de Reffye, E. Elguero and E. Costes, (1991), "Growth units construction in trees: a stochastic approach", *Acta Biotheoretica*, Vol. 39, pp. 325–342.
- [12] N. S. Goel, L. B. Knox and J. M. Norman, (1991), "From artificial life to real life: computer simulation of plant growth", *International Journal of General Systems*, Vol. 18, pp. 291–319.
- [13] S. Papert, (1980), *Mind-Storms: Children, Computers, and Powerful Ideas*. New York: Basic Book.
- [14] P. Prusinkiewicz and A. Lindenmayer, (1990), *The Algorithmic Beauty of Plants*. New York: Springer-Verlag.
- [15] N. S. Goel, I. Rozehnal and R. L. Thompson, (1991), "A computer graphics based model for scattering from objects of arbitrary shapes in the optical region", *Remote Sensing of Environment*, Vol. 36, pp. 73–104.
- [16] N. S. Goel and I. Rozehnal, (1991), "Some non-biological applications of L-systems", *International Journal of General Systems*, Vol. 18, pp. 321–405.
- [17] F. Hallé, R. A. A. Olderman and P. B. Tomlinson, (1978), *Tropical Trees and Forests. An Architectural Analysis*. Berlin: Springer-Verlag.
- [18] P. de Reffye, C. Edelin, J. Francon, M. Jaeger and C. Puech, (1988), "Plant models faithful to botanical structure and development", *Computer Graphics*, Vol. 22, pp. 151–158.
- [19] D. A. Charles-Edwards, D. Doley and G. Rimmington, (1986), *Modelling plant growth and development*. Sydney: Academic Press.
- [20] P. B. Tomlinson, (1983), "Structural elements of the rain forest", in *Tropical Rain Forest Ecosystems. Structure and Function* (F. B. Golley, ed.), pp. 9–28, Amsterdam: Elsevier.
- [21] D. Ehrlich, J. E. Estes and A. Singh, (1994), "Applications of NOAA-AVHRR 1km data for environmental monitoring", *International Journal of Remote Sensing*, Vol. 15, pp. 145–161.
- [22] B. Pinty and M. M. Verstraete, (1992), "GEMI: a non-linear index to monitor global vegetation from satellites", *Vegetatio*, Vol. 101, pp. 15–20.

- [23] M. M. Verstraete, C. Leprieur, S. De Brisis and B. Pinty, (1993), "GEMI: A new index to estimate the continental fractional vegetation cover", in *6th European AVHRR Data Users' Meeting*, (Belgirate, Italy), pp. 143–150, EUMETSAT.

## Chapter 9

# Fractal Modelling of Chernobyl's Radioactive Fallout over Europe

*G. Salvadori<sup>\*</sup>, S. P. Ratti, G. Belli and E. Quinto  
G. Graziani<sup>†</sup> and M. de Cort*

### 1 Introduction

The Joint Research Centre of the European Commission at Ispra (Italy) started in 1987 to store measurements collected by several European Laboratories beginning April 26<sup>th</sup>, 1986, when the Chernobyl nuclear accident occurred. The R.E.M. (Radioactivity Environmental Monitoring) data bank contains not only official documents provided by E.C. Member States, but also many other measurements collected in unofficial reports and private communications from Research Institutes and Universities. The investigation [1] of the R.E.M. data bank, carried out within the Radiation Protection Programme of the European Commission turned out to be a difficult task, due to its heterogeneity and complexity. The post-Chernobyl *air/air dust* pollution measurements (for the nuclides  $^{137}\text{Cs}$ ,  $^{134}\text{Cs}$ ,  $^{131}\text{I}$  and  $^{132}\text{I}$ ) were analysed in several Italian (and French) provinces. The following parametric function, returning the temporal trend of the radioactivity for all the investigated counties and nuclides (roughly speaking, it shows some features of “universality”), was provided [1]:

$$RA(t) = k + e^{(-\frac{A}{\tau}t+B)}(1-\exp(\frac{C}{t}-t)) \quad (1)$$

where  $RA$  means “Radioactivity”,  $\tau$  is the life-time of the nuclide;  $A$  is the effective rate of the exponential decay law (characteristic of a given nuclide

---

<sup>\*</sup>Dipartimento di Fisica Nucleare e Teorica, Università degli Studi, Pavia, Italy

<sup>†</sup>Environment Institute, Joint Research Centre, European Commission, Ispra, Italy

but independent of geographical variables);  $B$  accounts for the pollution strength (depending upon geographical variables);  $C$  is related to the arrival time of the polluting cloud at a given location;  $K$  is the radioactive background (usually negligible), taken from the literature when available; the time origin is the date of the accident. In Fig. 1 we show the  $^{137}\text{Cs}$  data (black squares) collected in the province of Milano and the corresponding fit (solid line) using formula 1.

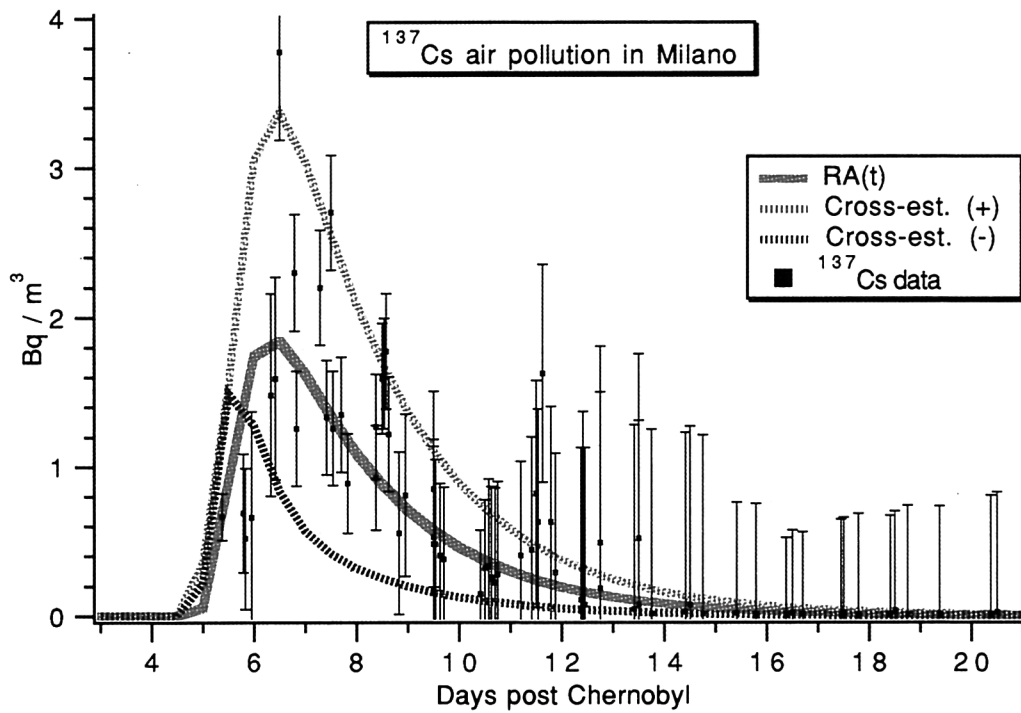


Figure 1:  $^{137}\text{Cs}$  air data (black squares) collected in the province of Milano and the corresponding fit (solid line) of formula (1); the two dashed lines represent function (1) as calculated using the cross-estimated parameters (varied by plus (upper) and minus (lower) one standard deviation)

## 2 Cross-estimate of the $^{137}\text{Cs}$ parameters

We are interested here in describing the  $^{137}\text{Cs}$  air pollution in Northern Italy, a relatively “homogeneous” area; the choice of this nuclide is due to



the fact that it is quite “stable” (its mean life time is  $\approx 30$  years), and hence possible side effects (e.g. those due to a fast decay rate) can be disregarded in further modelling (see later). Originally, reliable  $^{137}\text{Cs}$  measurements (and hence the corresponding temporal behaviour as given by formula 1) were available [1] only for 6 provinces in Northern Italy (i.e., Alessandria, Milano, Piacenza, Pavia, Vercelli and Bologna); in order to improve the overall knowledge of the radioactivity distribution we show here an original algorithm [2] to calculate the parameters of the interpolating function 1 when no data are provided in a given location, based on empirical relationships between its coefficients estimated for different nuclides. The fractal approaches outlined in the next sections will take benefit of this procedure, since (as for any empirical model) the “quality” of the results depends on the amount of input data.

It has been shown [1] that the parameter  $A$  does not depend on the geographical location but is a function only of the given nuclide; hence, the common value  $A = -0.433 \pm 0.004$  is assumed here for the  $^{137}\text{Cs}$ . Furthermore, since the background  $K$  is always negligible [1] and does not effect the behaviour of function 1, we set it equal to the (weighted) average of the values calculated for the provinces where  $^{137}\text{Cs}$  data are available. Also, given the facts that the nuclides arrived at the same time and that the value  $\sqrt{C}$  is a reliable approximation [1] of their (common) arrival time, it is natural to assume that the parameter  $C$  for  $^{137}\text{Cs}$  in a given location can be calculated by using the (weighted) average of the arrival times of the available nuclides in the same place. More involved is the estimate of the parameter  $B$ , based on the following empirical observation [1]: the (average) ratio  $R_x^{^{137}\text{Cs}}$  between the value of  $B$  of  $^{137}\text{Cs}$  and of another nuclide  $X$  (in our case  $^{131}\text{I}$ ,  $^{103}\text{Ru}$ ,  $^{132}\text{Te}$  or a combination of such elements) is fairly well defined. Therefore, we estimate  $B(^{137}\text{Cs})$  in those locations where  $^{137}\text{Cs}$  is missing simply by multiplying  $R_x^{^{137}\text{Cs}}$  times  $B(X)$ , where  $X$  denotes a nuclide (or a combination of nuclides) locally present.

In Table 1 we list the values of the parameters  $B$  and  $C$  (for  $^{137}\text{Cs}$ ) for the ten provinces in Northern Italy of interest here; in Genova, Padova, Pisa and Trieste they are calculated by using the cross-estimate algorithm. In order to test of this procedure, function 1 fitted on the available data is compared to the one obtained using the cross-estimated parameters (clearly, only in those provinces where  $^{137}\text{Cs}$  is measured). As an example, in Fig. 1 we show the  $^{137}\text{Cs}$  data set (black squares) of the Milano province and the corresponding fit (solid line) of formula 1; the two dashed lines represent function 1 using the cross-estimated parameters within the corresponding “error band” of one standard deviation (obviously, the data set of Milan is

<i>Province</i>	<i>Parameter B</i>	<i>Parameter C</i>
<b>Alessandria</b>	$3.58 \pm 0.13$	$47.06 \pm 0.97$
<b>Milano</b>	$3.55 \pm 0.79$	$30.74 \pm 0.44$
<b>Piacenza</b>	$3.50 \pm 0.74$	$81.03 \pm 2.12$
<b>Pavia</b>	$3.40 \pm 0.32$	$36.92 \pm 0.31$
<b>Vercelli</b>	$3.22 \pm 0.12$	$29.35 \pm 0.58$
<b>Bologna</b>	$2.64 \pm 0.75$	$46.35 \pm 1.66$
<b>Genova</b>	$2.25 \pm 0.04$	$32.23 \pm 0.34$
<b>Padova</b>	$3.97 \pm 0.09$	$40.54 \pm 0.13$
<b>Pisa</b>	$2.40 \pm 0.02$	$82.21 \pm 0.59$
<b>Trieste</b>	$4.40 \pm 0.18$	$100.00 \pm 74.01$

Table 1: estimates of the parameters  $B$  and  $C$  of function 1 for the nuclide  $^{137}\text{Cs}$  in Northern Italy; in the first six provinces the values are calculated fitting function 1 on the available data, while in the remaining four we use the cross-estimate procedure explained in the text.

not used to calculate them).

### 3 The monofractal model

Many natural phenomena, from the molecular to the planetary scale and more, show an extremely complex behaviour. This is the phenomenological background that has stimulated the research on fractals [3a-d] and multifractals [3c,d]. The fractal model presented here is based on the *Fractal Sum of Pulses (F.S.P.)* theory [3e]. According to it, the intensity of a phenomenon (e.g. radioactive pollution in a region at a given time) is considered as the sum of *primary pulses*, whose intensities, time duration and geometrical spreads are random variables properly distributed and generated according to a precise strategy. In this way, it is possible reproduce some features of the phenomenon itself such as *scaling* properties and strong fluctuations (see below).

In our model the primary pulses mentioned above have the shape of “bubbles” [3e] and are distributed in a three-dimensional space, where two coordinates are spatial (i.e. longitude and latitude of the site being considered) and the third one is time. For a pulse volume  $V$  we use the following

*hyperbolic* probabilistic distribution law [3e]:

$$Pr(V > V^*) \propto \frac{1}{V^*} \quad (2)$$

where  $Pr$  means “probability” Such choice automatically preserves the scaling property and allows for the presence of *strong fluctuations* [3]. The intensity  $Z(\vec{r})$  of a pulse (at position  $\vec{r}$  from the pulse centre) is assumed to be:

$$Z(\vec{r}) = \pm s(\vec{r})V^{\frac{1}{D}} \quad (3)$$

where  $D$  is the fractal dimension of the phenomenon,  $V$  is the pulse volume and  $s(\vec{r})$  is a smoothing function (usually having a Gaussian shape) tuning the “fading” of the pulse intensity as moving away from its centre. Thus,  $Z$  represents the (additive) contribution (e.g. radiation dose) of each pulse to the global phenomenon. Since the fractal dimension is kept constant, the model is *monofractal* in character; we assume here  $D \approx 1.67$ , as calculated for some meteorological phenomena [3e]: in fact, we are convinced that the presence of radionuclides in the atmosphere is low enough not to affect neither rainfall nor cloud formation and transport of pollutant.

Having chosen a proper value for  $D$ , we need now a reasonable criterion to introduce the primary pulses in the Euclidean space  $E = E(x, y, t)$ . In our case [2], aiming to recover a distribution  $R(x, y, t)$  of “real” data, it is natural to “guide the growth” of the fractal structure exploiting the information provided by the experimental data. A simple way of doing this consists in assigning to every point of  $E$  a probability  $P(x, y, t)$  proportional to the local value of  $R$ ; in other words, the greater the value of  $R$  in a region  $A$  of  $E$ , the more the fractal algorithm “works” in  $A$ . In our case,  $R$  is simply given by function 1 - see, e.g., Fig. 1. However, since its parameters are known only in a few counties (see Table 1), we overcome the problem by considering “basins of attraction” of each province (instead of the proper geopolitical boundaries) and assuming that  $RA(t)$  be the same in all the area of interest; roughly speaking, the model generates spatial-temporal “fractal fluctuations” starting from a homogenous “background” value given by  $RA(t)$ . In Fig. 2 we show the basins of the ten provinces in Northern Italy. Finally, the contributions given by each pulse are added; the numerical output is then properly normalised so that the total amount of pollutant estimated in some area at a given time  $t^*$  equals the value obtained by (spatially) integrating  $R(x, y, t^*)$  over the same region.

The fractal model allows the estimation [2] of the  $^{137}\text{Cs}$  air concentration in large unsampled areas: in fact, it “covers” all Northern Italy (i.e. 49 provinces, from 7.0 to 14.0 West in longitude and from 43.5° to 46.5° North

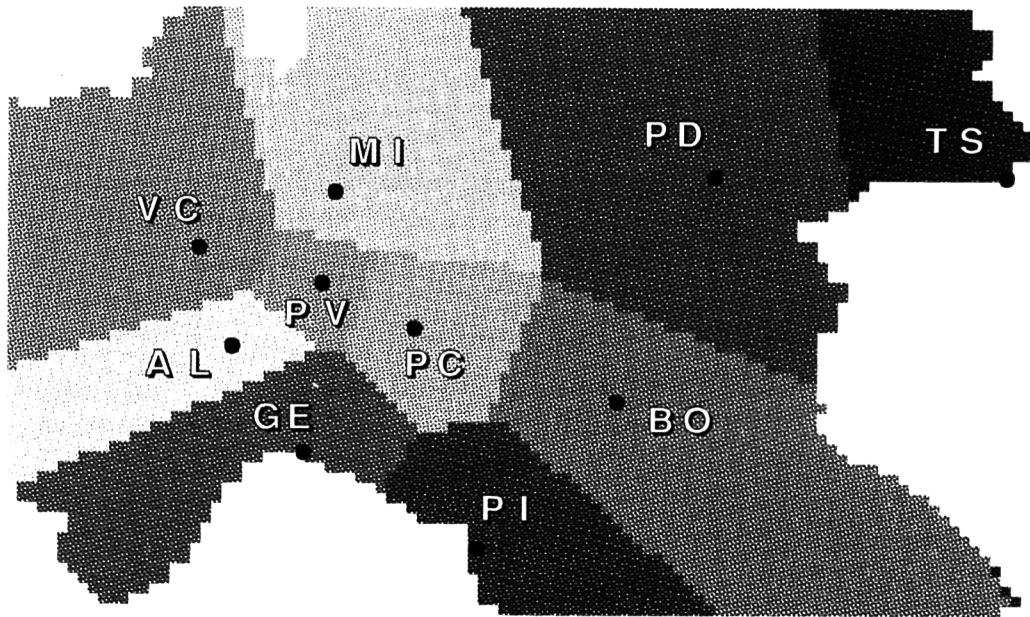
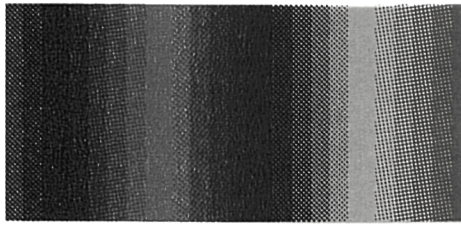


Figure 2: “Basins of attraction” of the ten provinces considered in Northern Italy; i.e. Alessandria (AL), Milano (MI), Piacenza (PC), Pavia (PV), Vercelli (VC), Bologna (BO), Genova (GE), Padova (PD), Pisa (PI) and Trieste (TS)

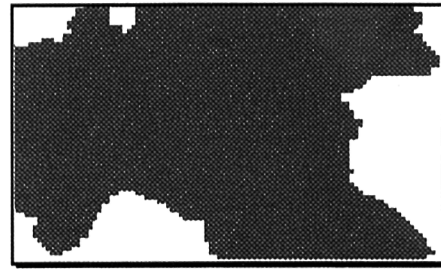
in latitude) while a description based upon function 1 works only for 10 provinces (see Table 1). It is important to stress that both the spatial and the temporal resolution are input parameters (in Figs. 3 and 4 we use  $\approx 0.1^\circ$  in longitude,  $\approx 0.05^\circ$  in latitude and 1 day in time) and hence they can be refined as needed. In Figs. 3 we show a two-dimensional display of the output of the monofractal model in Northern Italy, from 4 till 12 days after the Chernobyl accident (i.e., from April 30<sup>th</sup> till May 8<sup>th</sup>, 1986) with a regular one day step.

In order to check [2,4] quantitatively how bad or how good the recovery might be, we systematically neglect, one at time, any of the 10 provinces providing input information, re-run the simulation and compare the results to the experimental data. In all cases the disagreement does not exceed a

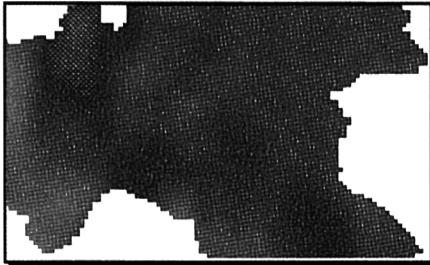




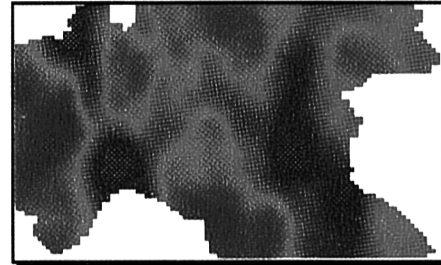
**Intensity Spectrum**



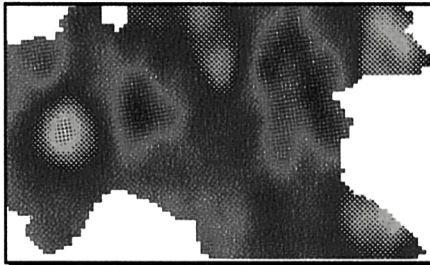
**4 Days Post-Chernobyl**



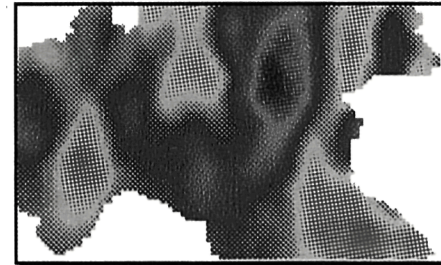
**5 Days Post-Chernobyl**



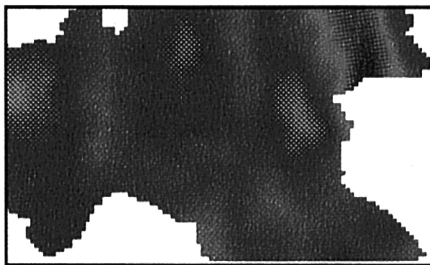
**6 Days Post-Chernobyl**



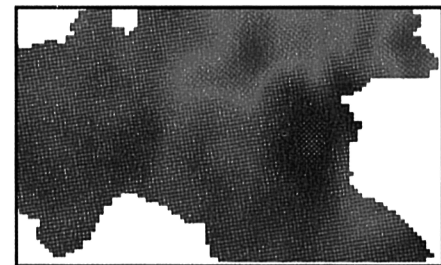
**7 Days Post-Chernobyl**



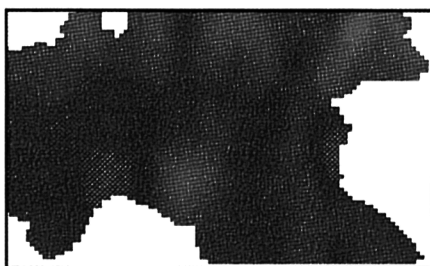
**8 Days Post-Chernobyl**



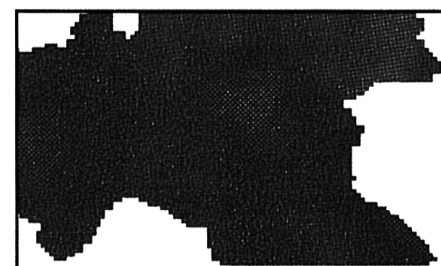
**9 Days Post-Chernobyl**



**10 Days Post-Chernobyl**



**11 Days Post-Chernobyl**



**12 Days Post-Chernobyl**

Figure 3: Qualitative two-dimensional display of the output of the monofractal model in Northern Italy, from 4 till 12 days after the Chernobyl accident. The spectrum indicates increasing values of radioactivity from left to right

factor of two; furthermore, in some provinces the model returns estimates of the amount of pollution in days when no measurements were made. As a further test, the comparison is also performed neglecting, respectively, the province with most data (i.e. Milano), the extreme eastern one (i.e. Trieste) and the extreme western one (i.e. Vercelli). The same considerations as before apply; also, the results seem to be reasonably “stable” independently of which province is disregarded. Overall, we are able to estimate the  $^{137}\text{Cs}$  concentration in about 50 provinces where no measurements were available starting from the data of only 10 provinces. A more accurate quantitative analysis of the results is in progress [4].

## 4 The multifractal model

The experience gained analysing the Chernobyl’s pollution in Northern Italy and devising a fractal model is now exploited in order to provide a more complex multifractal approach. The basic idea is to take advantage of the possibilities offered by *multifractals* [3c,d] to take into account the different “degrees of fractality” of increasing levels of pollution. At present, we only show preliminary results, since several refinements and improvements of the model presented here are still needed; however, given the encouraging results obtained (see below), we feel confident that important progresses will be made in the next future.

The data used here, extracted from the R.E.M. data bank, consists of measurements of cumulative deposition of  $^{137}\text{Cs}$  on soil over several European Countries (see Table 2 and, as an example, fig. 6 -top right). During the quality assurance process [2,4], several data were rejected and some Countries were disregarded (due to an insufficient number of samples). Also, in order to obtain a homogeneous set of measurements useful for further modelling, we “renormalised” all the available data as if they had been collected on July 1<sup>st</sup>, 1987; this operation was accomplished by using the well known exponential law of radioactive decay:

$$R(t) = R_0 e^{-\frac{t}{\tau}} \quad (4)$$

where  $R, (R_0)$  is the amount of radio at time  $t$  (at time zero) and  $\tau$  is the  $^{137}\text{Cs}$  decay life-time. Furthermore, wherever measurements of  $^{134}\text{Cs}$  were available, we calculated the corresponding intensity of  $^{137}\text{Cs}$  using the known ratio between the two nuclides ( $\approx 1/2$ ): this, in turn, allowed us to slightly increase the total number of available data.

<i>Country</i>	<i># data</i>	<i>Min.</i>	<i>Max.</i>	<i>Hyp. exp.</i>
<b>Austria</b>	97	0.740	581.130	-1.19
<b>Ex-Czechosl.</b>	105	0.220	19.000	-2.36
<b>FRG</b>	293	0.451	44.090	-1.15
<b>Greece</b>	1108	0.100	149.240	-1.50
<b>Italy</b>	383	0.001	490.720	-1.20
<b>Ireland</b>	98	0.301	14.260	-5.44
<b>Norway</b>	447	0.401	103.700	-2.52
<b>The Netherl.</b>	85	0.270	6.070	-2.46
<b>Poland</b>	349	0.790	82.880	-2.05
<b>Rumania</b>	200	0.429	54.640	-2.45
<b>Ex-USSR</b>	109	19.000	261.000	-1.09
<i>Average</i>	298	2.06	164.25	-2.13
<i>Std. Deviation</i>	286	5.36	189.57	1.19

Table 2: Features of the data sets of  $^{137}\text{Cs}$  cumulative soil deposition for all the European Countries investigated here; we show the number of data used, the pollution range (in  $\text{Bq/m}^2$ ) and the value of the hyperbolic exponent (see text). Also shown are the corresponding Averages and Standard Deviations.

The measurements are surveyed on a country-by-country basis (see Table 2; however, it is worth pointing out that neither theoretical nor practical limitations exist to do it on a wider geographical basis and we foresee such extension in the next future. The analysis of the data involves two different operations [2,4]: on the one hand we investigate the (geographical) sparseness of the measurements, on the other hand we study the statistical distribution of the radioactivity. The former operation can be accomplished by calculating the fractal dimension  $D_F$  of the set of stations showing a value larger than a given threshold  $T$ , obtaining in turn a function  $D_F(T)$  representing the “spectrum” of the fractal dimensions of different levels of pollution. Thus, the multifractal approach is more sensitive than the rigid monofractal one, as it accounts for the fact that lowly contaminated regions are expected to be more uniformly spatially distributed than possible “hot spots”. The second operation requires to check whether the following probabilistic relation holds at least for radioactivity intensity  $R$  large enough (i.e., we investigate whether, asymptotically,  $R$  is hyperbolically

distributed):

$$Pr\{R > r\} \propto r^{-h} \quad (5)$$

where  $h > 0$  is called *hyperbolic exponent*. In fig. 4 we show the multifractal spectrum  $D_F(T)$  as calculated using the data collected in ex-Czechoslovakia.

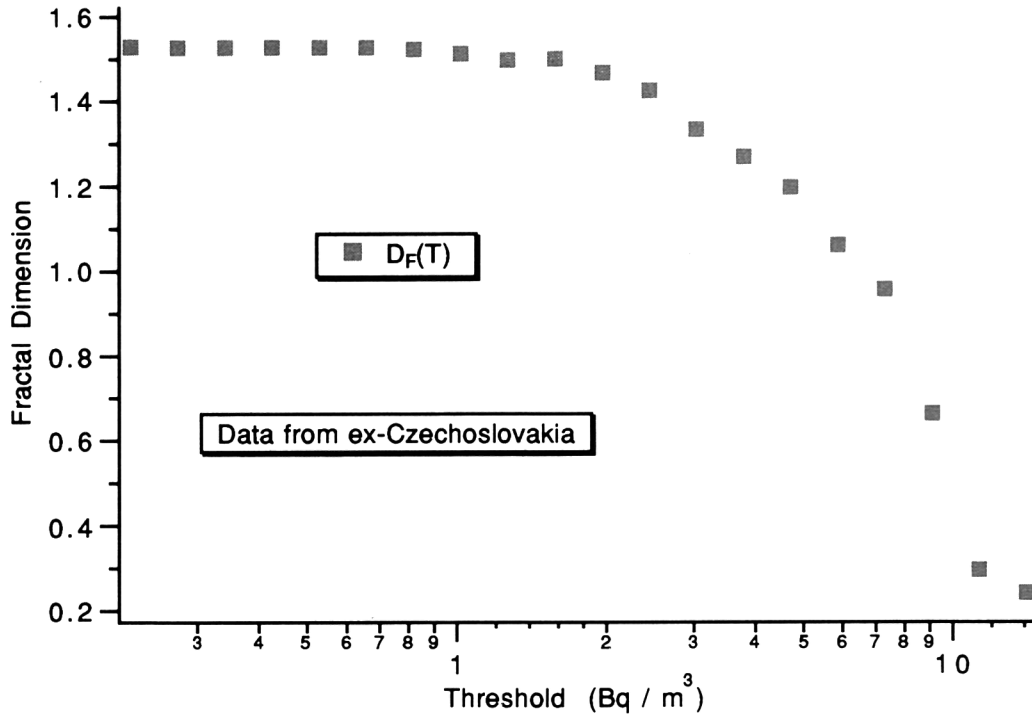


Figure 4: The multifractal spectrum  $D_F(T)$  using the data collected in ex-Czechoslovakia on a semi-logarithmic scale (see text). As expected, the fractal dimension  $D_F$  of the set of stations measuring values greater than an arbitrary threshold  $T$  is a decreasing function of  $T$ .

Fig. 5 shows, on a bilogarithmic scale, the (asymptotic) hyperbolic distribution of the same data; thus, the parameter  $h$  in equation 5 can be estimated by the slope of the interpolating line. The last column of Table 2 contains the values of the hyperbolic exponents for all the countries investigated here.

Briefly, the multifractal algorithm works as follows [2,4]. First we generate a set of pulses (as for the monofractal model) having intensities distributed according to formula 5, where  $h$  is estimated from real data (see



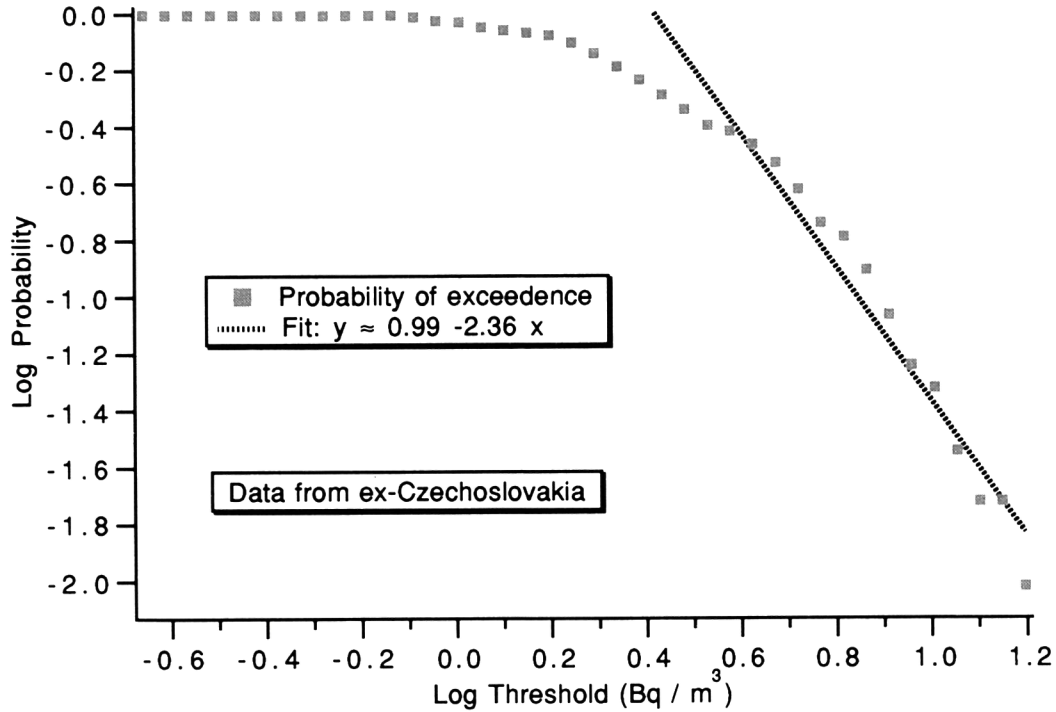


Figure 5: The (asymptotic) hyperbolic distribution of the data collected in ex-Czechoslovakia (on a bilogarithmic scale). The hyperbolic exponent  $h$  [see equation (5) and table 2] can be estimated by the slope of the interpolating line.

Table 2); then we arrange such pulses on an arbitrary grid taking into account the information given by the function  $D_F(T)$ : pulses having intensities larger than  $T$  are distributed over a “network” having fractal dimension  $D_F(T)$ , where such networks are generated by means of “pseudo Lévy Flights” [2,3a,4]. The link between the actual geographical distribution of pollution and its usage in our model represents an original innovation; in fact, we provide a consistent way to take into account, simultaneously, both the position and the “strength” of each station. The basic idea is that each measurement has an “influence” on the simulation proportional to its intensity; moreover, such effect is not concentrated onto a single point in space, but spreads over a whole “basin” whose width (depending on the sparseness of the original data) can be adjusted as a free parameter. A simple way to

model such behaviour is to use “spatial potentials”  $V$  defined as:

$$\begin{cases} V(\vec{x}) = V_0 \left(1 - \frac{|\vec{x}|}{L}\right) & \text{for } |\vec{x}| \leq L \\ V(\vec{x}) = 0 & \text{for } |\vec{x}| > L \end{cases} \quad (6)$$

where  $V(\vec{x})$  is the value of the potential at position  $\vec{x}$  from the location of the station;  $V_0$  is the value of radioactivity measured by the station and  $L$  is a (constant) free parameter tuning the influence of the station over the neighbouring space. The overall potential is simply given by the (spatial) integral (over the chosen grid) of all the single potentials; then, the global potential is exploited to “drift” any purely random network (generated by means of “pseudo Lévy Flights” toward a spatial configuration closer to the actual distribution of pollution [2,4]. Fig. 6 -bottom left shows the global potential as calculated using the data collected in Austria.

Finally, each numerical realisation of the process is added to the previous ones and the resulting field (properly normalised [2,4] is compared to the actual intensity of pollution: if some (arbitrary) criterion of convergence is satisfied [2,4] the simulation stops, otherwise it produces more and more fields. Fig. 7-bottom-right shows an example of multifractal simulation over Austria. Similar results [4] have been obtained for all the other investigated Countries. Further tests [4], performed neglecting some fraction of the input data, have shown that the quality of the outputs is not too much affected, indicating a fairly good “stability” of the multifractal model. As a general comment, we see that the model is able estimate the pollution intensity in locations not sampled by the network; moreover, the original “hot spots” are almost always correctly reproduced and further constraints in the model would probably lead to a more accurate simulation.

## 5 Conclusions

This study represents the very first attempt to apply monofractals and multifractals to environmental radiation protection. The models presented show that it is possible to simulate radioactive pollution using fractal techniques. Indeed, this mathematical framework is more powerful than classical statistical ones, which are not able to account for possible anomalous and/or violent fluctuations of natural phenomena. Not only the algorithms proposed provide estimates (both in space and in time) that agree reasonably well with the available data, but they are also able to “predict” the concentration of pollutant in unsampled regions and when no input data are locally available.

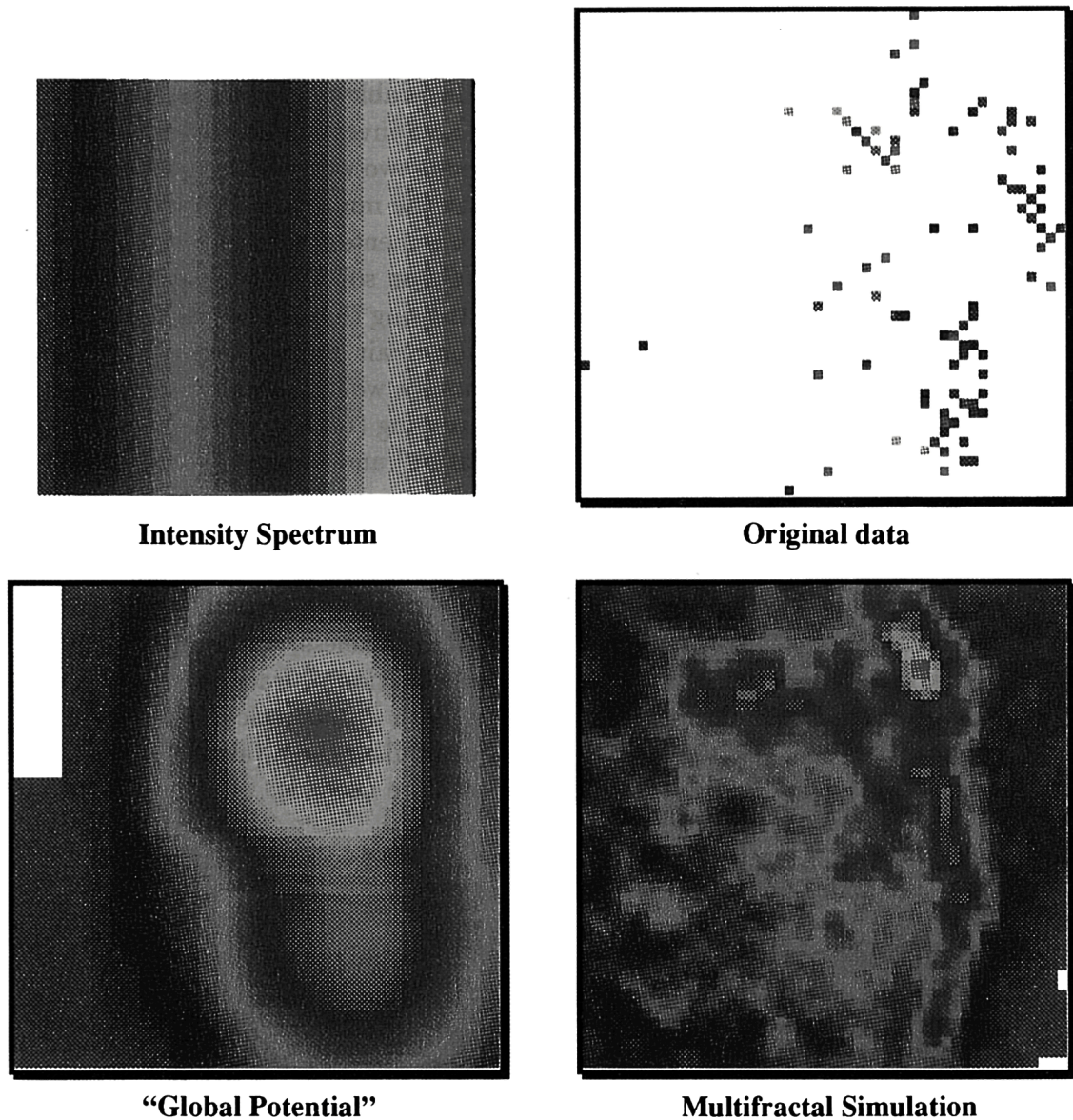


Figure 6: Qualitative two-dimensional display of the relevant input-output “information” involved in the multifractal modelling (see text); the horizontal and vertical axes are, respectively, longitude and latitude; the spectrum indicates increasing values of radioactivity from left to right. Top-Right: The  $^{137}\text{Cs}$  cumulative soil deposition data collected in Austria arranged on a 50x50 grid; Bottom-Left: The “global potential”; Bottom-Right: The multifractal simulation

On the one hand, we find that the monofractal approach, exploiting an input data set very “sparse” in space (about 10 locations) but dense in time (even continuous, by using function 1), is able to provide an estimate of  $^{137}\text{Cs}$  air pollution over the geographical area investigated (Northern Italy) for the whole time interval considered (about two weeks after the Chernobyl accident). On the other hand, we see that the multifractal model, starting from data sets of only a few hundred measurements at a fixed time, is able to estimate the cumulative deposition of  $^{137}\text{Cs}$  on soil over geographical areas as large as a whole Country. It is worth stressing that the physical nature of the two investigated phenomena (pollution in air and soil deposition) does not affect the (multi)fractal approach. Finally, we feel essential to point out that these models are not CPU-time consuming (taking only a few minutes on a Macintosh to generate a full simulation) and hence they can provide real-time approximations in case of a nuclear accident; clearly the goodness of the estimates may depend upon the quantity and the quality of the input data. This aspect will be investigated in the future.

Indeed, we are far from exploiting all of the opportunities offered by the mathematical framework of fractals; nevertheless, we believe that this work may represent the first concrete introduction of fractals into radioactivity environmental sciences, providing both a theoretical framework to handle real data and an operative tool to simulate them (also in emergency conditions, when crude real-time estimates are needed).

## 6 References

- [1] S. P. Ratti, G. Belli, G. Bressi, M. Cambiaghi, A. Lanza, G. Salvadori, and D. Scannicchio: (a) Report EUR 12549 EN, Vol. 1, Part A (1990); (b) Proceedings of “Seminar on Methods Codes for Assessing the Off-Site Consequences of Nuclear Accidents” Report EUR 13013, Vol. 2, 1183 (1990).
- [2] S. P. Ratti, G. Belli, E. Quinto, G. Salvadori, M. Cambiaghi, A. Lanza, and D. Scannicchio: Commission of the European Communities, Contract BI7\*-CT90-0062-MNLA, Final Report (1993).
- [3] (a) B. Mandelbrot, *The Fractal Geometry of Nature*, Freeman, S. Francisco (1983). (b) K. J. Falconer, *The Geometry of Fractal Sets*, Cambridge University Press, Cambridge (UK), 1988. (c) J. Feder, *Fractals*, Plenum Press, New York, 1989. (d) K. J. Falconer, *Fractal Geometry*, J. Wiley & Sons, Chichester (UK), 1990. (e) S. Lovejoy and B. Mandelbrot, *Tellus*, 37A, 209 (1985).

- [4] S. P. Ratti, D. Schertzer, F. Schmitt, G. Salvadori, G. Belli, D. Scannicchio, M. Cambiaghi, A. Lanza, A. Ravera and E. Quinto: Commission of the European Communities, Contract FI3P-CT93-0077, Intermediate Report (1994).

# Chapter 10

## Fractals in Geosystems and Implications for Remote Sensing

*Leonid Vasiliev\**

### 1 Introduction

The number of branches of science that have not yet appreciated the potential of fractal geometry is becoming steadily less and less. As a rule, the results of pilot studies have become the subject of symposiums dedicated to applications of fractals such as “Fractals in Physics” [1], “Fractals in Fundamental and Applied Sciences” [2] or have been accompanied by special issues of journals of geophysics [3], geomorphology [4], computer and geosciences [5], optics [6]. This is evidence of the fact that most investigators are intuitively realizing the attractiveness of fractal geometry -though initial experiments are not always convincing or yielding new knowledge in certain disciplines, which has given birth to a somewhat sceptical attitude to possible practical uses of fractals. Nevertheless it should be recognized that for quantitative description of irregular chaotic structures over the Earth's surface the potential of fractal geometry seems attractive and encourages the development of new concepts.

The fractal approach seems most adequate in view of the fact that many phenomena observed in nature have one common characteristic associated with the idea that microscopic behaviour is the foundation of macroscopic effects manifesting themselves as scaling.

On the other hand, remote sensing of the Earth creates a problem of interrelating the characteristics of geophysical fields with those of spatial features observed at different spatial resolutions. A sampling of irregular 3D geophysical fields may strongly change their pattern, depending on the

---

\*Institute of Geography, Moscow, Russia

pixel size. It is far from being an easy task to try and find some universal distribution the characteristics of which, within certain limits, would be independent of the spatial resolution cell. Therefore, the description of geophysical fields is closely associated with remote sensing as a data source.

Attempts are now being made to use fractal geometry to quantitatively describe multidimensional fields estimated from remote sensing data and the estimates seem to be interpretable in terms of geophysical and geographical parameters. To my knowledge this volume results from the first scientific seminar entirely dedicated to “Fractals in Geosciences and Remote Sensing” which could help formulate a certain opinion about this problem.

In this chapter I will try to present the results of an investigation of the fractal properties of spatial structures of geosystems with various components. Each type of structure is the result of its origin and evolution. Hence, the definition of the fractal dimension of structures relies upon several models most adequately describing the process of their formation. The diversity of natural and man-made structures requires a large number of models, thus making the problem very complex. The goal of the investigation I have made was to reveal and understand scaling properties of fractal spatial structures of geosystems and the pattern of their manifestation. It will be shown that in self-similar 2D structures and 3D self-affine multifractal geophysical fields the scaling range of self-similarity and self-affinity radically differs.

Scaling properties of fractal structures are also used as a basis for the problem of extrapolation of measurement data to a minimal size already beyond the spatial resolution of the available remote sensing data.

## **2 Self-similar fractal structures of geosystems**

Among the multitude of fractal spatial structures formed on the Earth's surface the following should be singled out:

- 2D land use/land cover structures with a wide range of components
- river and erosion networks
- transport networks
- spatial urban structures
- geological lineaments

Of course, we are not going to summarize all possible fractal structures. No doubt, the list of examples could and should be made longer. The above group of examples was given to show the diversity of *models* of fractal structures. Two-dimensional land use/land cover structures classified from multiband imagery form fractal sets [7]. The distribution of each class of crops or cover type is fairly well described by grid  $D_G$  or mass  $D_M$  dimensions:

$$N(r) \propto r^{-D_G} \quad (1)$$

or

$$M(L) \propto L^{D_M} \quad (2)$$

where  $D_G = D_M$ .

There is evidence for the scaling relation

$$M(L/b) = b^{-D} M(L) \quad (3)$$

However the scaling range  $[L_{min}, L_{max}]$  specifying the length scales of self-similarity is wider than  $[r_{min}, r_{max}]$  if Eq. 2 is being used. Basically, studies of the spatial distribution of land use/land cover in various physical/geographical zones and management conditions demonstrate only scaling dependence, but in no case do they imply fractality in terms of the Hausdorff - Besicovitch dimension. As will be shown, however, it does not prevent several useful conclusions. In fact this is the way to describe spatial structures representing only one type of land use/land cover classes.

In a more general statement of the problem, when a combination of several classes is simulated, a set is a fractal with unequal parts:

$$\sum_m r_m^D = 1 \quad (4)$$

Such structures made of 2 or 3 components drastically reduce the scaling range as compared with structures formed by single components.

A river and erosion network structure within a catchment area may be considered as a model of irreversible growth of a branching process [7].

If a number of concentric circles is drawn around the point assumed as the beginning of growth, they would intersect the branches of a river and erosion network (Fig. 1).

We denote those intersections as  $\rho(R)$  then their number  $Nr\rho(R)$  is related to the radius  $R$  of a circle by



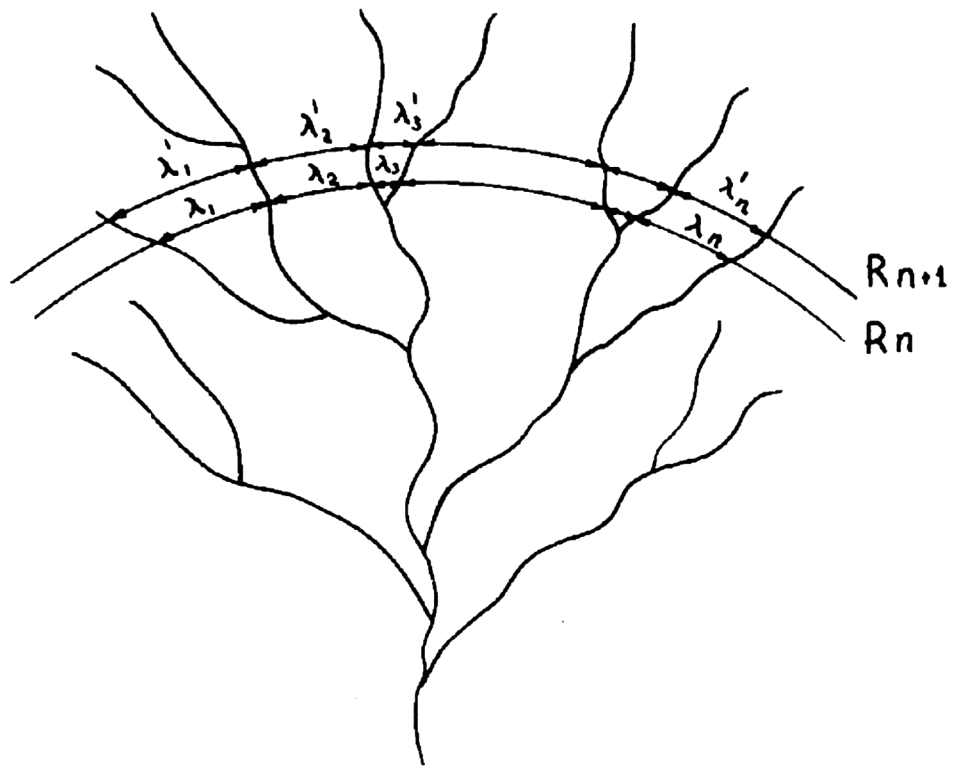


Figure 1: Determination of distances  $\lambda(R)$  between branches of a river/erosion network around the circle

$$Nr\rho(R) \propto R^{D-2} \quad (5)$$

The main theoretical problem is to seek a realistic model of growth for various types of river and erosion networks and to confirm their fractal properties. One of the methods to determine a fractal dimension in a growth model employs the dependence:

$$\langle \lambda(R) \rangle \propto R^N \quad (6)$$

where  $\langle \lambda(R) \rangle$  is the mean distance between the intersections along the arcs of a circumference with an  $R$  radius. Experimental studies made at several catchments show that a Laplacian fractal-type model may be sometimes adequate for describing a river or erosion network. In this case Eq. 5 is written as:

$$\langle \lambda(R) \rangle \propto R^{\frac{d-D}{d-1}} \quad (7)$$

where  $d$  is the Euclidean dimension.

For studied catchments covered with such networks fractal dimensions have been found to be in the range 2.22 to 2.66. In any case at a qualitative level of interpretation Eqs. 4 and 6 describe two kinds of dependences for networks similar to that on the Seym river catchment image (Fig. 2): non-linear increase of network element density with increasing distance to the origin point where growth begins and, therefore, decreasing distance between those components.

Eq. 4 was used to describe the railway network of Paris [8]. However, contrary to the river and erosion network pattern, the density of stations  $\langle \lambda(R) \rangle$  decreases with distance to the origin point of growth which is in the centre of the city and at  $D < 2$ .

Networks of geological lineaments interpreted on images at different scales may be regarded as ordered chaotic structures formed by a great number of faults, fractures, tectonic or lithologic contacts of different though finite length. Above all the analysis of lineaments puts forward the problem of assessing the homogeneity of a geological environment. Also there is the problem of deciding whether the criteria of lineament combinations are common for the entire area and what characteristics of individual groups are critical for separating or combining them. Hence it follows that the main task is to divide lineaments into portions which - on a certain scale and according to a signature chosen - may be considered quasi-homogeneous.

One of the approaches which can be used is based on the partitioning of a lineament network into percolation clusters [9]. The remaining

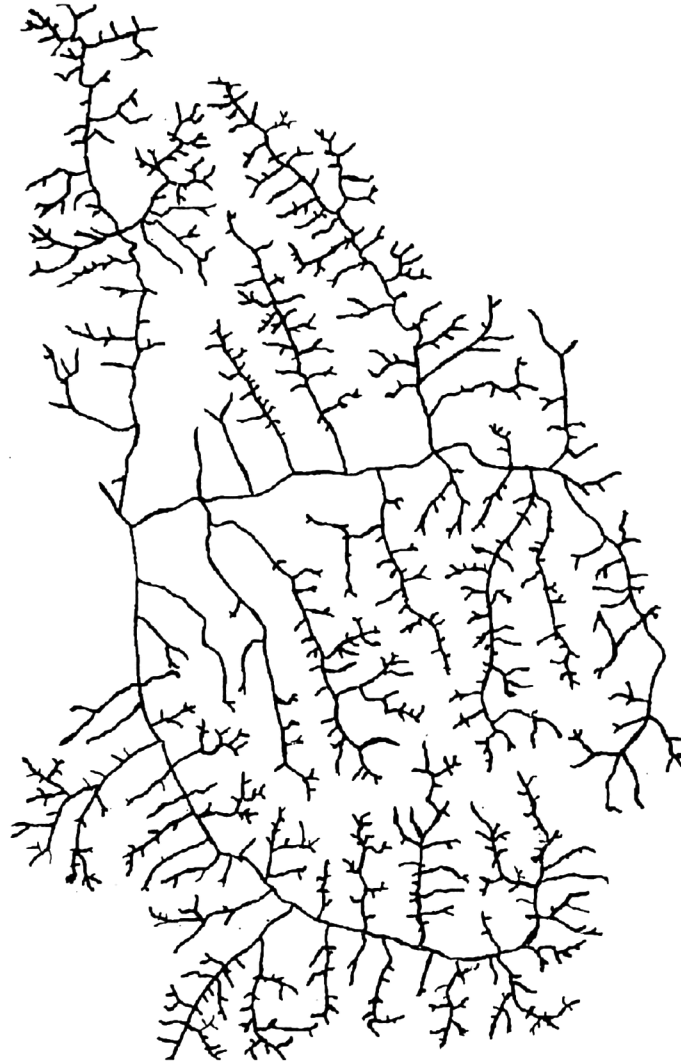


Figure 2: Erosional pattern of the Seym River Basin in the central Russian uplands (derived from COSMOS imagery)

non-bound lineaments fill vacancies (holes) in individual clusters or spaces among percolation clusters (Fig. 3,4).

The clusters thus identified are restricted to squares with an  $L$ - side so that percolation can spread out in meridional or latitudinal directions, then within each cluster the dependence is observed between the “mass” (length) of lineaments  $M(L)$  and the side  $L$  of a given square

$$M(L) \propto L^D \quad (8)$$

where  $D$  is the mass dimension.

In fact, a percolation cluster is one of the most popular models of a fractal. The model adequate for analysis would be fractal percolation clusters of Mandelbrot-Given [10] with the following dimensions:

$D = \ln 8 / \ln 3 = 1.8928$  for loops and free ends,

$D = \ln 6 / \ln 3 = 1.6309$  for the backbone,

$D = \ln 5 / \ln 3 = 1.4649$  for its rings' hull boundary.

Studies of the lineament network of the eastern part of the Baltic shield have shown that it forms structures with various fractal dimensions (Table 1). The log-log plot in Fig.5 demonstrates an example of mass dimensions determination. The comparison of identified clusters with tectonic and geological maps reveals similarity with large-scale subdivisions (domains) of structural or tectonic zoning. Ten percolation clusters are combined into four groups with  $D = 1.80, 1.60-1.66, 1.51-1.56$ , and  $1.45$ , which are close to theoretical values of Mandelbrot - Given's fractal curve. The comparison of clusters identified with geological maps shows that they are most similar to major tectonic units and the correlation of values of fractal dimensions with the intensity of deformations and a degree of linearization of fold and fault structures.

As Fig. 5 and Table 1 show, upper limits of self-similarity depend on the size of a cluster whereas its lower limits are restricted by the spatial resolution of the imagery used and, therefore, do not determine the genuine scaling range.

It is best seen in those cases when within the limits of one cluster several tectonic structures are combined. This points to their common foundation but, because of insufficiently detailed data available, does not permit identifying the boundaries of specific and not so deep-seated structures. Interpretation of fractal dimensionalities of percolation clusters has demonstrated their relationship with the characteristics of various tectonic structures. They map both the intensity of general dislocation and the degree of linear regularity of folds and faults.



Figure 3: Lineaments in the eastern Baltic Shield (derived from Landsat TM imagery)

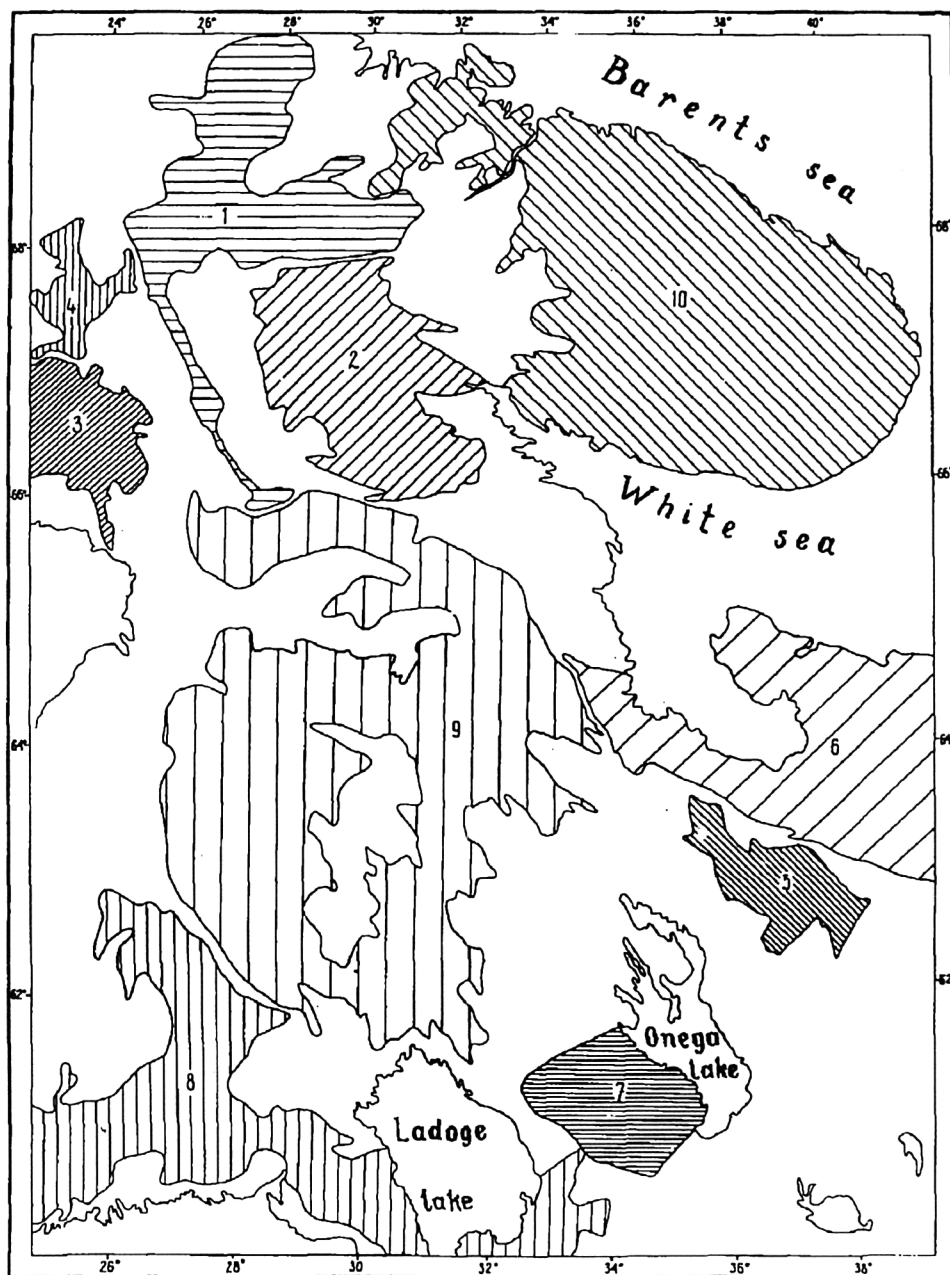


Figure 4: Map showing locations of selected fractal percolation clusters

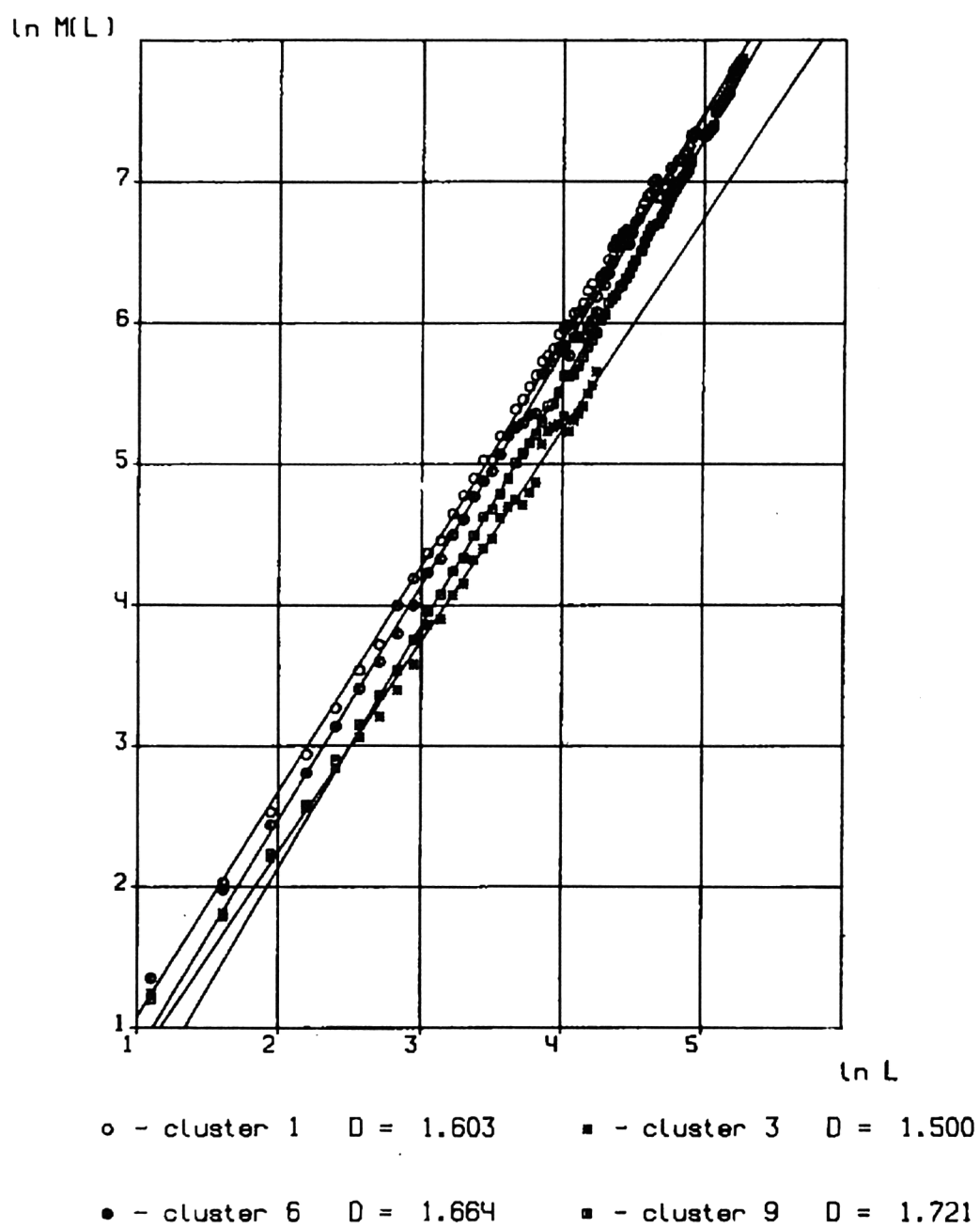


Figure 5: Eastern Baltic Shield: log-log plot of average length of lineaments versus scale coefficient for percolating clusters

No.	Fractal dimension $D$	Square side $L_0, km$	Scaling range $[L_{min}, L_{max}], km$	Lineaments length in a square with side $L_0, \sum_{L_0} L, km$	Lineaments length in a percolation cluster $\sum_{cl} L, km$
1	$1.60 \pm 0.01$	446	[2.1, 58.5]	77186	16787
2	$1.80 \pm 0.02$	226	[2.1, 36.6]	26422	14098
3	$1.46 \pm 0.02$	193	[2.1, 29.0]	14504	3245
4	$1.56 \pm 0.02$	128	[1.3, 29.0]	8764	2405
5	$1.51 \pm 0.02$	168	[1.3, 30.7]	11932	3484
6	$1.66 \pm 0.02$	337	[2.1, 35.8]	33997	10591
7	$1.46 \pm 0.02$	133	[1.3, 29.9]	5781	2117
8	$1.56 \pm 0.01$	628	[3.0, 71.1]	80637	19295
9	$1.74 \pm 0.02$	521	[2.5, 74.5]	79446	30718
10	$1.74 \pm 0.02$	382	[3.0, 71.1]	52590	15778

Table 1: Fractal dimensions, sizes and scaling ranges of percolation clusters of the Eastern Baltic Shield.

### 3 Extrapolation to small scales

The examples given above of spatial self-similar fractal structures within geosystems, however strongly the models of their generation and growth might differ, deserve attention, as they are associated to the main problem: the relationship between structures at microscopic and macroscopic scales. Let us emphasize again that the computed  $D_G$  and  $D_M$  fractal dimensions and parameters of the irreversible growth model only determine scaling properties and the self-similarity interval  $[L_{min}, L_{max}]$  or  $[r_{min}, r_{max}]$ . It is absolutely obvious that in cases where imagery is used, the lower limit of the self-similarity interval, i.e.  $\inf r_{min}$  depends on the pixel size whereas  $\sup r_{max}$  is governed by the area of fractal homogeneity. Theoretically self-similar fractal sets, however, allow infinite extrapolation and seem attractive since extrapolation of the asymptotic behaviour of Eqs. 1 or 2 toward smaller values of  $r$  or  $L$  becomes possible as well as curve straightening in the log-log plot and calculations of the limit  $D = \lim_{r \rightarrow 0} \ln N(r) / \ln r$ . The arguments rely on the fact that the power law relationship for a self-similar fractal set is valid at all scales. Self-similar fractal structures are most closely related with the hyperbolic distribution:



$$P(a) = P(A > a) = Fa^{-D} \quad (9)$$

where the exponent is equal to the fractal dimension  $D$ , and  $a$  is the area of elements making a fractal set [11]. If we are going to be careful in setting  $a_{min}$ , then  $Nr(A > a)$  will be finite whereas the integral of  $P(a) = Fa^{-D}$  determines the area covered.

Relying upon this idea, measurement data acquired from imagery may be extrapolated beyond the spatial resolution specified by the pixel size. An experiment was conducted to determine the pattern of vegetation in Moscow from multiband photos made with the COSMOS-1939 MSU-E system whose spatial resolution was 40m. (Fig. 6).

In the technogenic urban geosystem, vegetation strongly influences the climate and improves sanitary and hygienic conditions in the city. The urban microclimate does not depend much on large territorial units, of greater importance are small housing developments, with various types of surface. Within surrounding streets and buildings vegetation may be one of the main climate - generating factors comparable in its role to urban park areas. As the role of vegetation in the horizontal heat exchange is not so essential, special attention is given to vegetation structures surrounded by buildings and in the streets - from the viewpoint of microclimatic differentiation.

Vegetation is also an important factor in the formation of a thermal field structure from the viewpoint of spatial distribution of gaseous and dust substances in the atmosphere. Numerous investigations made in large cities have proved that there indeed exists a relationship between the thermal field and atmospheric pollution.

The estimation of the spatial structure of trees and shrub vegetation in a city implies the assessment of the area they cover, of their areal distribution and of the relationship between the biomass and population. Topoclimatologic simulation demands information about the species composition of trees and shrubs and the bulk of their biomass. Of course, it is extremely difficult to make estimates of the interaction of numerous factors - as to how they affect population in a city which is a heat island. And it is for this reason that the problems of architecture and planning of the urban development should rely on genuine ecological conditions rather than on norms and standards.

Hence the assessment of the pattern of vegetation covering about half the territory of any city is the attribute *sine-qua-non* in the urban geoinformation system.

Fundamentally, however, this problem appears to be non-trivial. In-

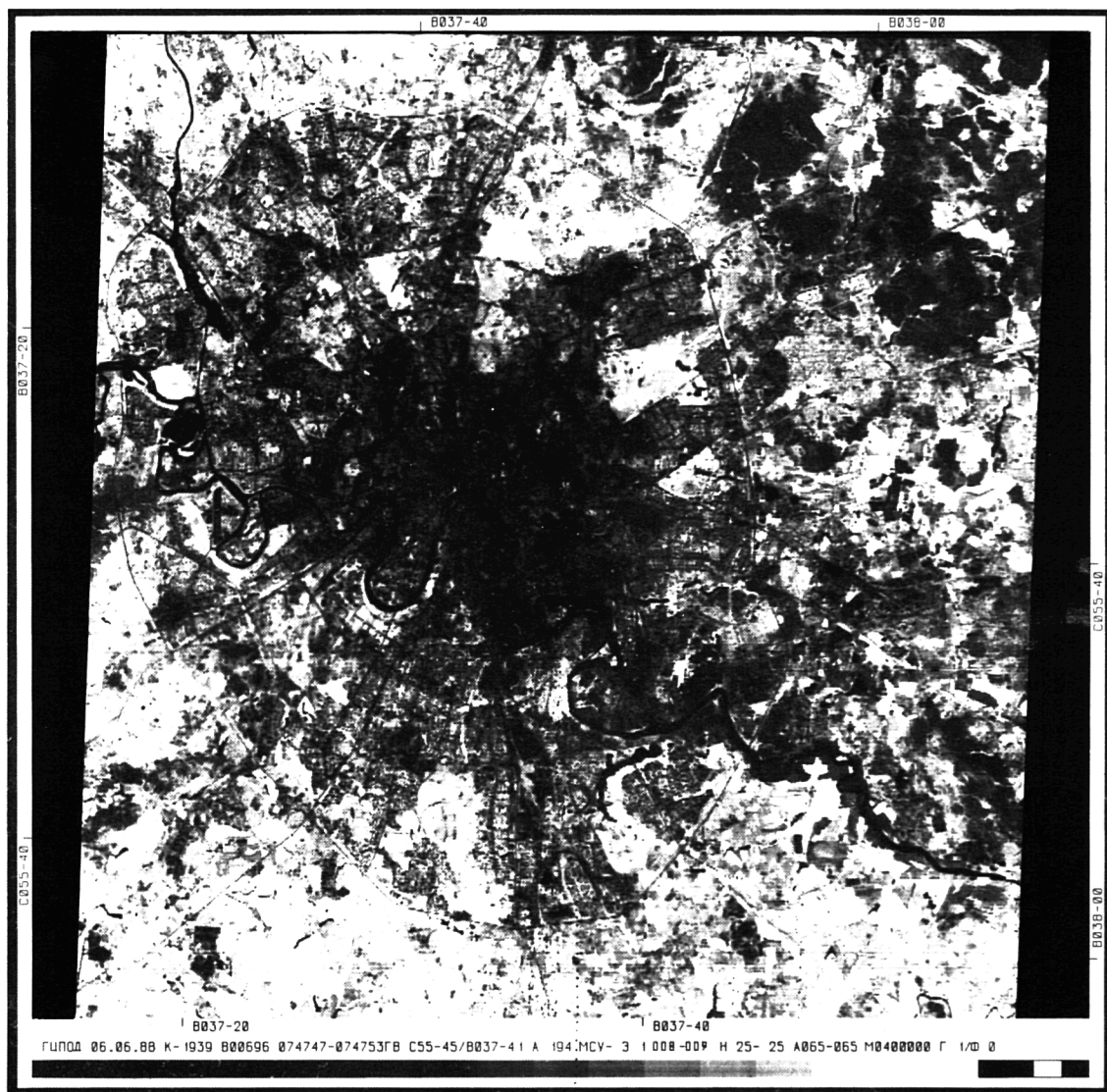


Figure 6: COSMOS 1939 MSU-E (800-900nm. wavelength) image of Moscow taken on 6th. June 1988

deed, what should be considered? -the boundary and the area of a space covered with trees among buildings or around a single house? The area and boundaries could be related with the percentage cover of vegetation and the smaller the measurement unit the more detailed 'indentations' would be mapped on images. This difficulty with mapping, bringing some uncertainty, distinctly manifests itself on 1:2000 topographic plans of Moscow, where the boundaries of vegetated areas are somewhat conventional whereas in a number of cases plantings along the streets, individual trees, alleys are shown by symbols without observing the scale. That is why even large-scale maps could not help measure exactly the overall area under vegetation in the city. Thus green areas in the city form a spatial structure of "islands" with very different areas and with wriggling boundaries that suggest the possibility of fractality [12].

The log-log plot (Fig. 7) shows the determination of the fractal behaviour of urban green areas in Moscow leading to the fractal dimension  $D = 1.86 \pm 0.02$ .

Note that the grid and mass dimensions do not differ by more than 0.02 whereas the self-similarity range derived from the Equation  $M(L) \propto L^D$  is 5 to 127 pixels or 210 to 5000 sq.m. The  $M(L)$  values for  $L < 5$  pixels, drop from the line since they are strongly affected by mixed pixels which cause errors in pixel classification. Extrapolation of green islands to small scale is based on the hyperbolic distribution  $P(a) = P(A > a) = Fa^{-D}$ , where the  $F$  coefficient is derived from the  $a$  - distribution over the interpreted image:

$$F = \frac{\sum_{i=1}^n a_i^{-D} N_i(a_i)}{\sum_{i=1}^n (a_i^{-D})^2} \quad (10)$$

The result of extrapolation to  $a = 1/16$  of a pixel size, which corresponds to the physical interpretation of one tree crown, with the size of the square  $2.5 \times 2.5m$  is shown in Fig. 8.

The Equation  $Nr(A > a) = 15000a^{-1.86}$  yields the following estimates of vegetation areas distribution in Moscow within the city boundaries:

Total area, percent	45.5
Number of green areas	2, 829, 200
Tree plantation area and parks, percent	11.2
Vegetation among buildings, squares, alleys, percent	34.3

It is interesting that among vegetation within blocks of houses areas up to  $40 \times 40m$  amount to 91%. The use of extrapolation down to 1/16th of

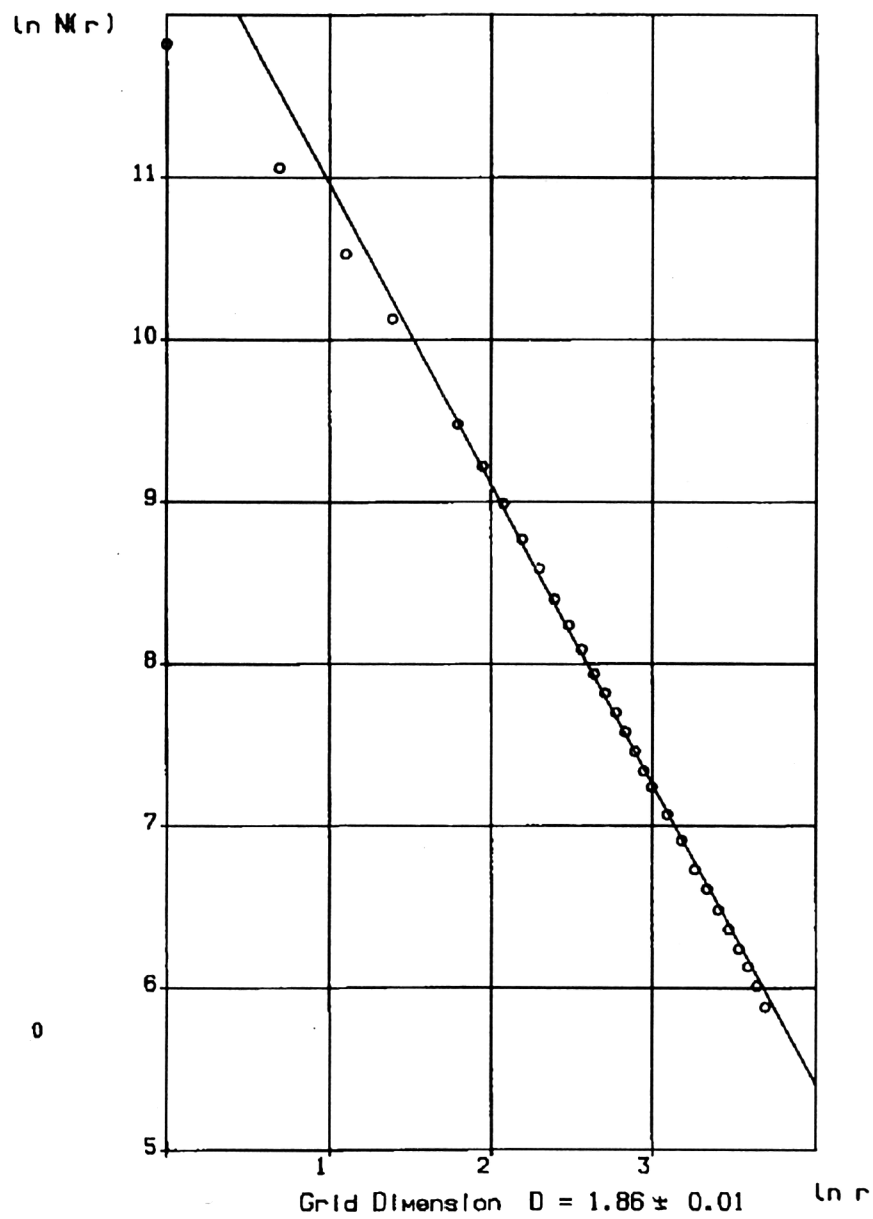


Figure 7: The 'Greening of Moscow' -log-log plot of number of boxes  $\ln N(r)$  versus side length of square boxes  $\ln(r)$  [From COSMOS-1939, MSU-E]

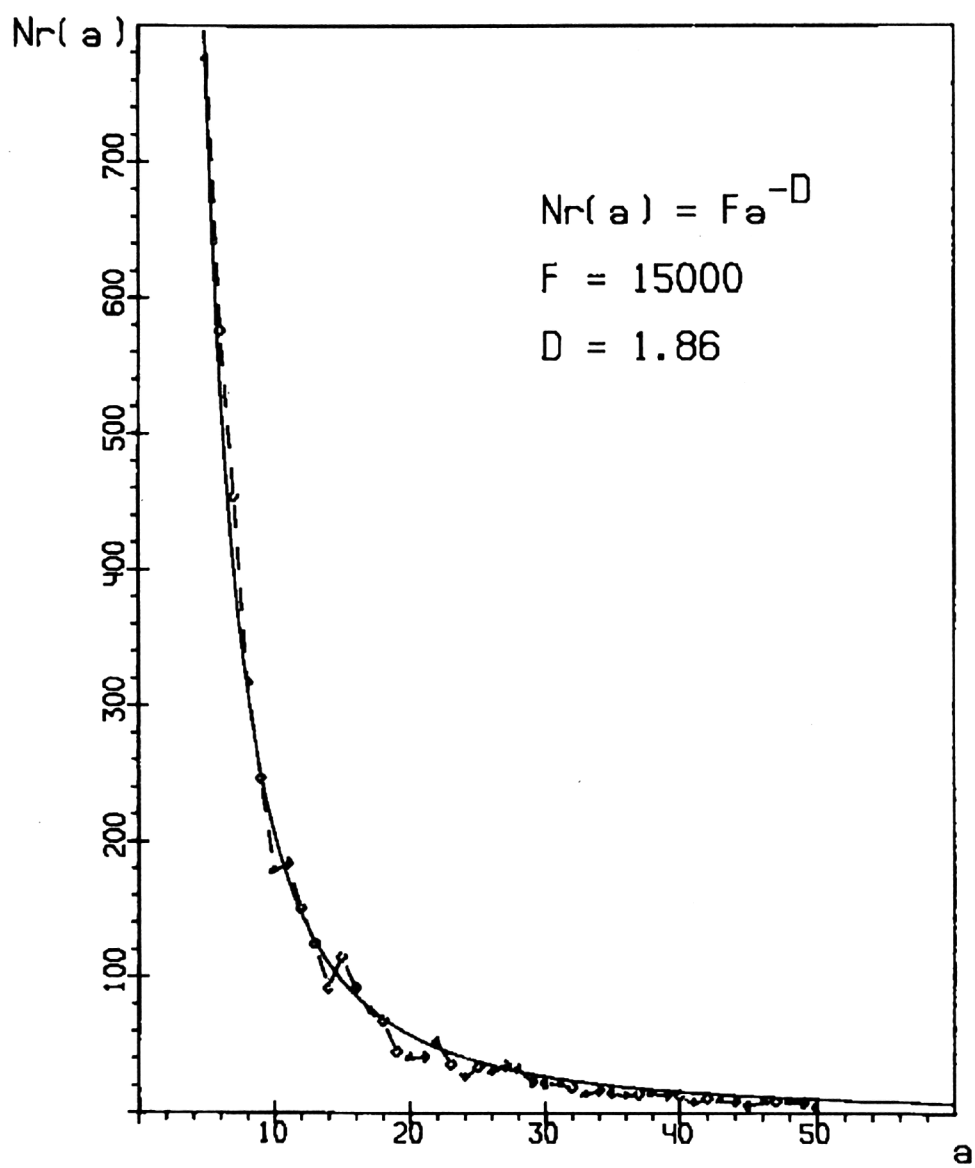


Figure 8: Comparison between theoretical and experimental results of the hyperbolic distribution of the greening of Moscow

a pixel reduced the relative error in the determination of vegetation area from 7 to 1%. Thus the pattern of vegetation in Moscow is characterized by fractal properties with a scaling, defined by Equation 3. The latter shows that the arrangement of the spatial pattern of vegetation in some parts of a whole city are statistically similar, after rescaling to the whole city. It implies scale invariance of vegetation distribution for territorial units of any size. Implications of the result shown in the experiment described above, are not restricted to one individual example. The rule of extrapolation of self-similar fractal structures of geosystems to small scale is substantiated both theoretically and experimentally. When measurements are made on imagery there always arises a necessity to move beyond the spatial resolution cell so as to reach the preset accuracy and to estimate the real self-similarity range as an inherent property of geosystems, manifesting itself both at micro- and macroscopic scales.

Fractality of a self-similar structure unequivocally governs the hyperbolic distribution of areas, thus justifying the rule of extrapolation to minimal sizes of structural elements within the boundaries of the self-similarity interval beyond the spatial resolution of images. The method developed is especially instrumental in the cases when the objects are considered inaccessible, the spatial resolution of an image is restricted by technical conditions and when high resolution images can be made in limited areas. Such conditions occur when sea ice or planets are to be observed by remote sensing. As our first experiments show, sea ice and Martian or Lunar craters obey the hyperbolic distribution whereas a considerable fraction of “small-size” elements are not resolved. The necessary limit of the extrapolation to small dimensions is determined from a single high resolution image.

## 4 Self-affine multifractal geophysical fields

Many 3D geophysical fields whose parameters are remotely sensed, are self-affine fractal sets [13]:

- spectral albedo;
- radiation and heat fields;
- back-scattering fields;
- topography and its roughness.

Self-affine fractal set properties are explained using different measurement units in the  $xy$ -plane and along the  $z$ -axis [14]. Apparently it is not only this that matters: topography is measured in the same units along all axes, but still the surface may be a self-affine fractal. In contrast to the case of self-similar fractals, self-affine fractals are characterized by two dimensions:  $D_L$  - local and  $D_G$  - global. As a result, interpolation and extrapolation of self-affine fractals lead to a restriction which determines crossover, scaling range and general behaviour.

One of the procedures for estimating fractal dimensions of a 3D geophysical field or its transect profile, relies upon the dependence of variance along coordinate axes from the section length [15]. The curve of a transect profile is divided by the yardstick method taking the length of a unit line  $a_0$  as constant and the coordinates of the resulting points  $P_i(x_i, z_i)$  are measured. Then the entire curve is divided into sections  $Na_0$  - long. In each of them  $x$  -, and  $z$  - variances  $\sigma_x^2, \sigma_z^2$ , of all of the measured points of a section are calculated. The equations:

$$\sigma_x \propto N^{v_x}, \sigma_z \propto N^{v_z} \quad (11)$$

are valid for fractal curves. Exponents  $v_x, v_z$  are not equal in a general case and are related via

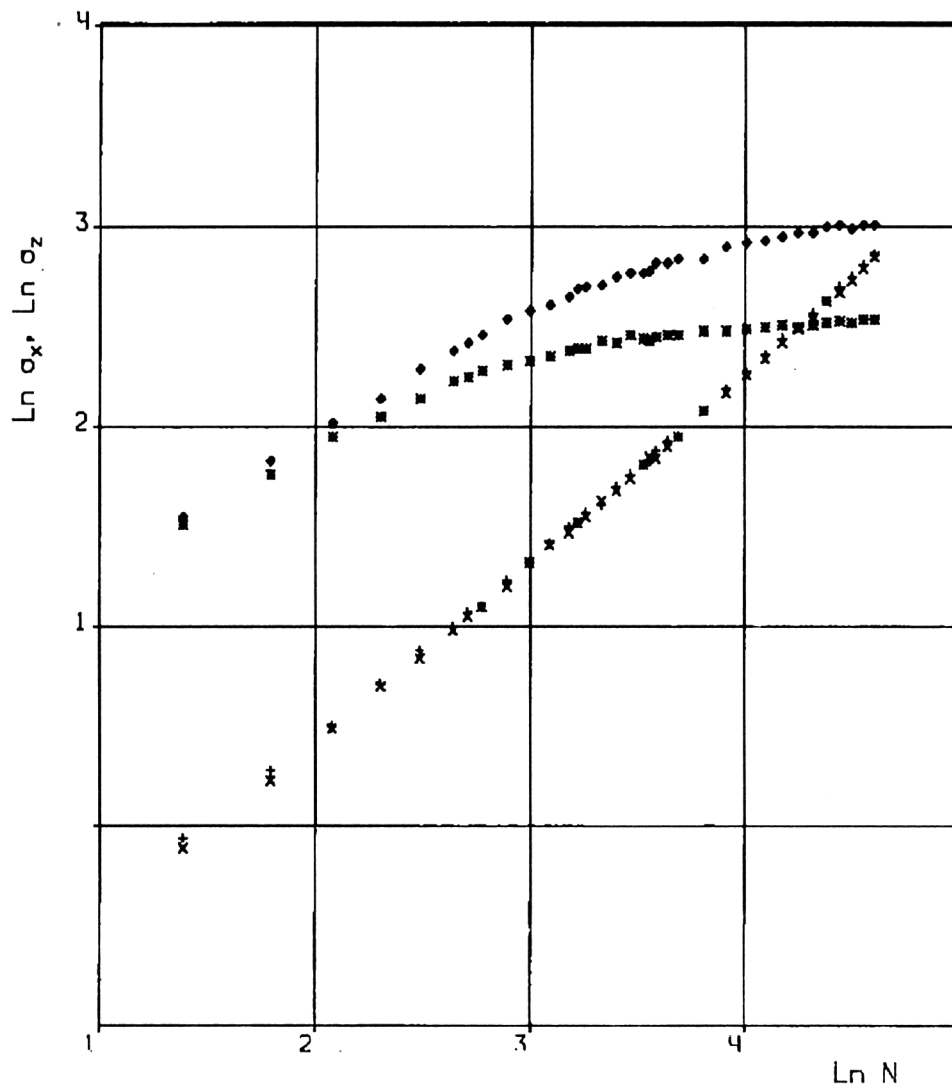
$$\sigma_z = \sigma_x^H \quad (12)$$

where  $H = v_z/v_x$  and  $0 < H < 1$ . For self-affine fractals  $v_x = 1$  and  $0 < v_z < 1$ . In the case of self-similarity  $v_x = v_z$  and  $D = 1/v_x$ .

The method is simple but it does not give an unambiguous solution. First, the measurement units are indeed different and the relationships of scales along  $x$ - and  $z$ -axes are uncertain. Second, Eqs. 9 are sensitive to the selection of unit length  $a_0$ . Therefore, with  $a_0$  changing the calculations lead to different  $H$ . However most essential for 3D geophysical self-affine fractal fields is that when they are measured with different spatial resolution the Hurst coefficient  $H$  changes, and, therefore, so does the fractal dimension.

The above phenomenon is demonstrated by two examples. Fig. 9 illustrates the results of fractal dimension determination for a spectral radiance field measured simultaneously by two COSMOS-1939 scanners, MSU-E and MSU-SK with resolutions of 40 and 200 m. In both cases the section length  $N$  is given in pixel units,  $H_1 = 0.65$  and  $H_2 = 0.59$  but, with the spatial resolution value taken into account, the crossover is at 2.9 and 12km.

The second example (Fig. 10) shows the estimate of the fractal dimension of the topography transect profile, measuring it simultaneously from an



MSU-E :  $\times \sigma_z$ ,  $+\sigma_x$ ,  $\gamma_x = 0.94$ ,  $\gamma_{zL} = 0.65$ ,  $\gamma_{zG} = 0.29$

MSU-SK:  $o \sigma_z$ ,  $\times \sigma_x$ ,  $\gamma_x = 0.94$ ,  $\gamma_{zL} = 0.58$ ,  $\gamma_{zG} = 0.09$

Figure 9: Transect profile of Kursk, for fractal dimension determination from the 3-D spectral radiance pattern



aircraft from a height of 200m. with a laser altimeter and a radar-altimeter with an accuracy of 0.3 to 1m., respectively. The antenna 'fields of view' covered areas of 1.7 and 12m. at the surface, respectively.

For those data  $H_1 = 0.63$  and  $H_1 = 0.52$ , whereas the crossover was at 80 and 300m., respectively.

Both experiments prove the dependence of the fractal dimensionality of the self-affine fractal 3D geophysical field on spatial resolution. The tendency is obvious: with growing pixel size the exponent  $H$  decreases and the crossover shifts. Hence, the determination of the fractal dimensionality of 3D geophysical fields from remotely sensed data is fraught with ambiguity.

Let us try to explain how fractal signatures differ for self-affine fractal 3D fields when remotely-sensed with different spatial resolutions.

Distribution smoothing leads to drastic violations of additivity in fractal sets. By sampling the growth of such functions their shape strongly changes depending on the scale of quantization. Hence a question arises whether some universal characteristic of the distributions could be mentioned that, within certain limits, would be independent of the quantization value. Of course, the answer to this question is in no way unequivocal. We now consider one of the possible versions. Let a certain portion be obtained of a histogram plotted with an interval  $\delta$  (Fig. 11).

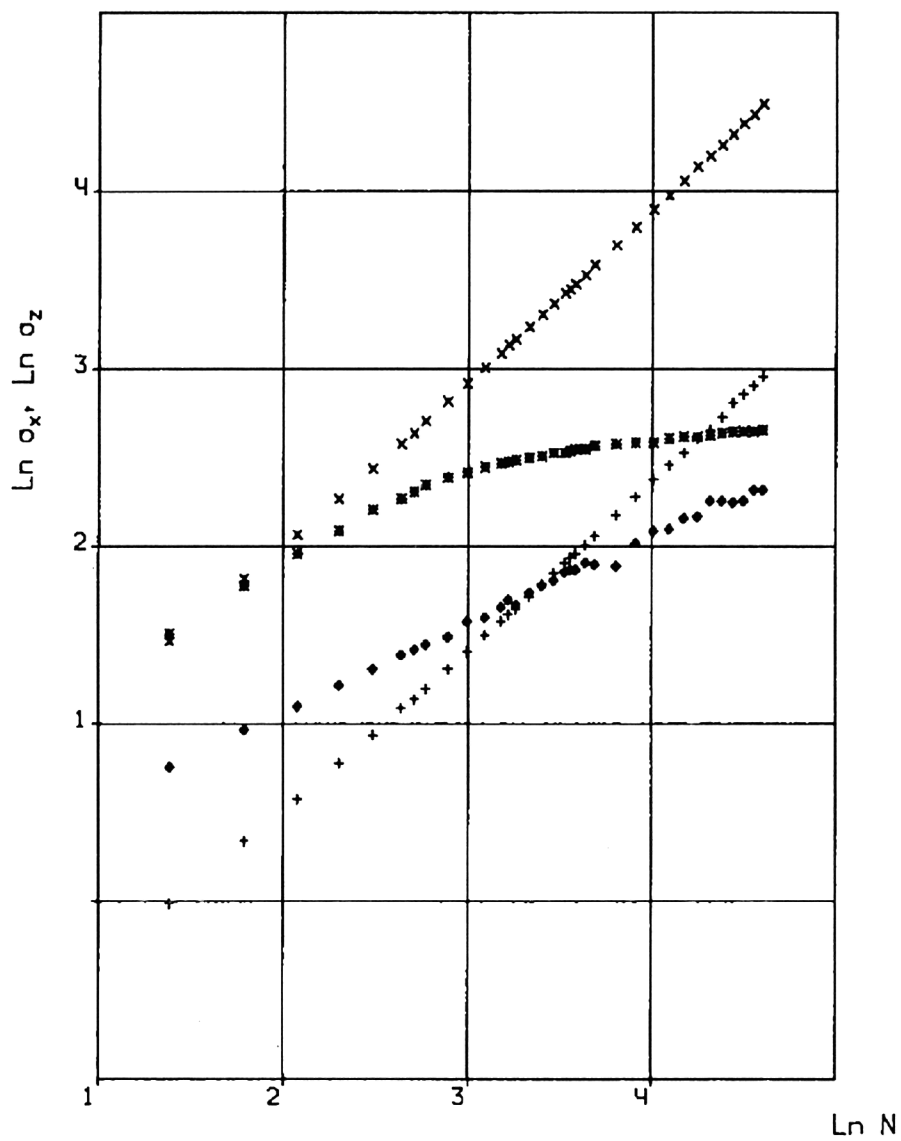
The ordinate of the function is  $y_0$ , its area is  $S_0$  respectively,  $S_0 = y_0\delta$ . If the histogram is compiled from the measurements where the interval was  $\delta/2$ , their respective coordinates would be  $y_1$  and  $y_2$  and the overall area would be  $S_{1+2} = S_1 + S_2 = \frac{1}{2}\delta(y_1 + y_2)$ . The condition  $S_{1+2} = S_1 + S_2$  implies - when the distribution is normalized - that  $y_0 = \frac{1}{2}(y_1 + y_2)$ . This is valid, however only for smooth curves. As to fractal curves they do not possess such a property. Instead, the following relationship may be considered:

$$(2y_0)^D = y_1^D + y_2^D \quad (13)$$

with the branching index  $D$ , and an attempt could be made to equalize histograms at different spatial resolution or quantization.

The appearance of local  $D_L$  and global  $D_G$  dimensions in a fractal 3D-geophysical field affects the interpolation and extrapolation rule. Basically, it differs from the one used for extrapolation of self-similar sets. Experiments show that transect profiles of optical, microwave and radar measurements made with different dividing length units  $a_0$ , at least are controlled by three separate fractal dimensions  $D = 1/H$ ,  $D_L = 2 - H$  or  $D_L = 1 + H$ ,  $D_G = 1$ .

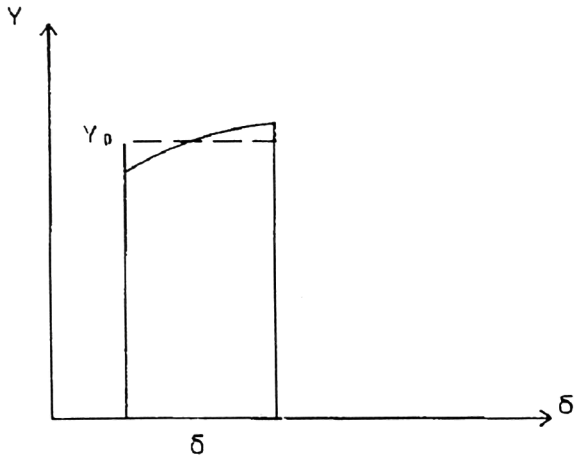
If intervals for the scaling ratio relationship:



Lidar:  $\times \sigma_z$ ,  $+\sigma_x$ ,  $\nu_x = 1.02$ ,  $\nu_{z_L} = 0.63$ ,  $\nu_{z_G} = 0.11$

Radioaltimeter:  $o \sigma_z$ ,  $\times \sigma_x$ ,  $\nu_x = 1.02$ ,  $\nu_{z_L} = 0.52$ .

Figure 10: Transect profile of Kursk, for fractal dimension determination from the landform measured by LIDAR and radar altimetry

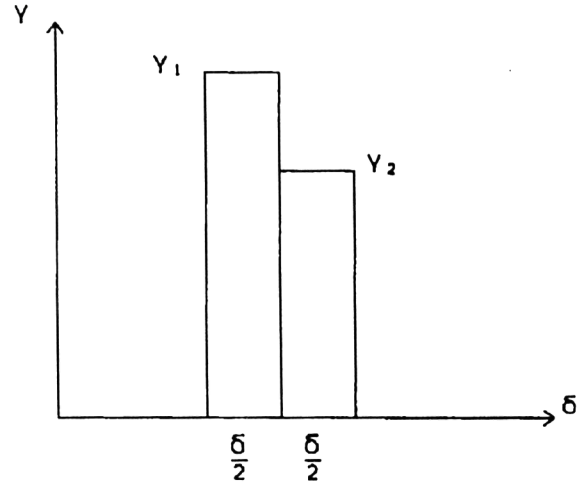


For smooth function

$$S_0 = Y_0 \delta$$

$$S_{1,2} = S_1 + S_2 = \frac{1}{2} \delta (Y_1 + Y_2)$$

$$Y_0 = \frac{1}{2} (Y_1 + Y_2)$$



For fractal function

$$(2Y_0)^D = Y_1^D + Y_2^D$$

Figure 11: Detailing of histogram by changing resolution

$$z(\lambda x) = \lambda^H z(x) \quad (14)$$

are determined by the crossover length and boundaries between three regions, then the main problem remains outstanding: how multifractal self-affine structures should be interrelated at micro- and macroscopic scales. In particular, there exists such a necessity in the context of the International Satellite Land Surface Climatology Project (ISLSCP) when heat fluxes are modelled at various climatological space scales, and high-resolution ground-based or sub-satellite measurements are used for satellite data calibration and validation. Thus, the unequivocal description of a climatological cell at various levels of spatial resolution, using remotely sensed data, appears to be not a trivial task at all.

## 5 Conclusions

This chapter has dealt with only a small part of the problem associated with the use of “fractals in geosciences and remote sensing” which reflect only the trends of my studies and the results obtained. Nevertheless they point to the priority tasks, which may help derive new understanding in geography and related disciplines using fractal analysis. No doubt, the fundamental problem is that of the relationship among structures within geosystems at micro- and macrolevels; it is obvious that remote sensing could be very instrumental here. Practical problems have been outlined which may be solved with the help of fractals, such as the determination of self-similar microstructures beyond normal spatial resolution limits. Fractal geometry encourages the development of models of spatial formations and of the growth of natural and man-made chaotic structures. New methods are still to be found for evaluating fractal dimensions of self-affine 3D geophysical fields so as to prevent ambiguities. One of the approaches could be a two-stage evaluation: first, a “crude” tool is used, and, next, attempts are made to refine it. I do not think, however, that the conclusions would be radically changed. Perhaps we could expect only better, more stringent confirmation. The general tendency in the development of fractals allows us to be optimistic and believe that they may provide new knowledge in Earth sciences.

## 6 References

- [1] L. Pietronero and E. Tosatti, Eds. (1986): "Fractals in Physics", (North-Holland, Amsterdam).
- [2] H.-O. Peitgen, J. M. Henriques, L. F. Penedo, Eds. (1991): "Fractals in the Fundamental and Applied Sciences", (North-Holland, Amsterdam).
- [3] H. Christopher, H. Scholz, B. B. Mandelbrot, Eds. (1989): "Fractals in Geophysics", Pure and Applied Geophysics, Special issue, Vol. 131, No. 1/2.
- [4] R. S. Snow, L. Moger, Eds. (1992): "Fractals in Geomorphology", Geomorphology, VII, Vol. 5, No. 1/2.
- [5] D. Unwin, Ed. (1989): "Fractals and the Geosciences", Computers and Geosciences, Vol. 15, No. 2.
- [6] D. L. Turcotte, Ed. (1990): "Optics and Image Science", J. Optical Society of America A, Vol. 7, No. 6.
- [7] L. N. Vasiliev, A. S. Tyufin (1992): "The fractal nature of the spatial structure of geosystem", Sov. J. Remote Sensing, Vol. 9, No. 4, pp. 630–642.
- [8] L. Benguigui, M. Daoud (1991): "Is the suburban railway system a fractal?", Geographycal Analysis, Vol. 23, No. 4, pp. 362–268.
- [9] L. N. Vasiliev, A.B. Kachalin, V. M. Moralev, E. N. Terekhov (1994): "Tectonical zoning and fractal percolation clusters in the lineament network of the Eastern Baltic Shield", Doklady Russian Academy of Sciences, Vol. 334, No. 6, pp. 718–722.
- [10] B. B. Mandelbrot, J. Given (1984): "Physical properties of a new fractal model of percolation clusters", Physical Review Letters, Vol. 52, No. 2, pp. 1853–1856.
- [11] B. B. Mandelbrot (1982): "The Fractal Geometry of Nature", (San Francisco: W. H. Freeman).
- [12] L. N. Vasiliev, A. B. Kachalin, A. S. Tyufin (1994): "The spatial structure of greening in Moscow and estimation by using satellite imagery", Earth Research from Space, No. 1, pp. 86–92.
- [13] L. N. Vasiliev (1993): "Multifractal nature of geophysical fields measured by remote sensing techniques", Proceedings of the 12th Symposium of the European Association of Remote Sensing Laboratories entitled 'Remote Sensing for Monitoring the Changing Environment of Europe', held in Eger/Hungary, 8–11 September 1992. (Ed. P. Winkler, A. A. Balkema, Rotterdam), pp. 279–287.
- [14] B. B. Mandelbrot (1986): "Self-affine fractal sets", in Fractals in Physics, L. Pietronero and E. Tosatti, Eds., North-Holland, Amsterdam, pp. 3–

28.

- [15] M. Matsushita, S. Ouchi (1989): “On the self-affinity of various curves”,  
Physica D, Vol. 38, pp. 246–251.

# Chapter 11

## Fractal-Based Evaluation of Relief Mapping Techniques

*Laurent Polidori\**

### 1 Introduction

Relief mapping became an operational application of remote sensing after the launch of SPOT in 1986. Digital photogrammetry, which was already feasible with scanned aerial photographs, gave rise to numerous digital terrain model (DTM) extraction facilities in public and private companies. More recently, ERS-1 has provided a new source of data which allows the improvement of 3D mapping techniques by use of stereoradargrammetry or interferometry. Particular methods such as altimetry or shape-from-shading can be considered to compute altitudes although they are not used for operational relief mapping. In future years, the need for topographic information could justify the development of new techniques such as along-track stereoscopy in the field of optical remote sensing or multiple incidence angle observation in the field of radar.

Such a variety of relief mapping techniques brings up the problem of their validation. Indeed, their robustness has seldom been quantitatively evaluated due to the lack of accurate references for comparison, and because their results are often related to a set of sensor parameters, viewing geometry and terrain shapes.

Evaluating the quality of a DTM is not a simple task, especially if the needs of different applications are to be taken into account. For instance, the classical and straightforward RMS error estimation does not evaluate the accuracy of altitude derivatives (slope, curvature, aspect...) which are very useful for many geoscience applications.

---

\*Aerospatiale, Cannes La Bocca, France

A rigorous DTM evaluation should consist of a comparison between the satellite-derived DTM and a very dense and accurate reference data set. In most cases, such a reference is not available, but two other approaches may then be considered. The first approach is an internal validation, i.e. a check of *a priori* assumptions concerning texture or hydrography, in complement to a rough external validation. The second approach consists of testing a 3D mapping tool on synthetic images which have been simulated over a perfectly known landscape.

The aim of this chapter is to show that fractal terrain modelling can usefully contribute to these two approaches. In section 2, the aptitude of fractal surfaces to model relief is discussed, and some techniques for 3D texture analysis and DTM resampling using fractals are described. Section 3 proposes fractal-based quality criteria which can be used to reveal artifacts in a DTM. Finally, the aim of the fourth section is to show that fractal synthesis can improve the validation of a relief mapping technique using image simulation.

## 2 Fractal modelling of topography

### 2.1 Is relief a fractal surface?

The self-similarity of relief had been noticed very long before the rise of fractal concepts, and it was even one of the first sources of inspiration for fractal geometry [15]. Stochastic self-similarity is a property of surfaces which conserve the same statistical characteristics over a wide range of scales. Different mathematical formulations can be used to describe self-similar behaviour, such as a power spectrum or semivariogram. In the case of a vertical terrain profile  $z(x)$ , the semivariogram represents the variations of the semivariance as a function of the horizontal distance  $\Delta x$ :

$$\gamma(\Delta x) = \frac{1}{2}E[(z(x + \Delta x) - z(x))^2] \quad (1)$$

where  $E$  refers to the expected value. In other words, the larger  $\gamma(\Delta x)$ , the steeper the average slope over  $\Delta x$ .

The semivariogram characterizes the degree of spatial dependence between the heights of adjacent terrain points. It is the basic concept in the theory of regionalized variables, which is extensively used in mining and petroleum geology [18]. A clear interpretation of the semivariogram is given in [7]. One of the most classical models for a statistical self-similar surface is 2D fractional Brownian motion, a bi-variate random process such



that for any displacement  $\Delta x$ , the height increment over  $\Delta x$  has a Gaussian distribution with mean 0 and variance:

$$\sigma^2 = \Delta x^{2(3-D)} \quad (2)$$

It follows that a fractional Brownian surface has a linear log-log semivariogram which can be written :

$$\log \gamma(\Delta x) = C + 2(3 - D) \log(\Delta x) \quad (3)$$

where  $D$  is the fractal dimension of the surface and  $C$  is a constant. A fractional Brownian surface is characterized by  $C$  and  $D$  only, and the slope of its semivariogram is given by  $2(3 - D)$  in the log-log space. Several authors have commented on the physical meaning of  $D$  (see [16], [20], [10]). The smaller the value of  $D$ , the steeper the variogram and the smoother the surface. This concept can be illustrated by considering displacements along a profile in any direction but over the same horizontal distance:

- if  $D < 2.5$ , then the two slopes are likely to have the same sign
- if  $D = 2.5$ , then they are independent (pure Brownian motion)
- if  $D > 2.5$ , then the two slopes are likely to have opposite signs

A rigorously analogous interpretation of self-similar surfaces can be done in terms of a power density spectrum, which is supposed to be an unbounded straight line in the case of a fractal surface.

Is relief a fractal surface ?

As noted above, the log-log semivariogram of a rigorously fractal surface, such as a fractional Brownian surface, would be an unbounded straight line. The semivariogram of the topographic surface is always bounded, since altitude is, but it often displays a linear trend over a large scale interval. Relief can then be considered as a nearly fractal surface, and its lack of ‘fractalness’ is often due to local breaks in the self-similarity behaviour.

Indeed, most landscapes have slope breaks in their semivariogram at horizontal distances which generally coincide with typical morphological features in topography [17]. In other words, the self-similarity of a surface may have different behaviour according to the scale at which it is observed. Similarly, the power spectrum of different sea-floor and terrain profiles reveals strong curvatures for some particular wavelengths in spite of general linear trends [8]. Goodchild noted that the fact that an observer can estimate the scale of a physical landscape implies that pure self-similarity is generally not a property of real landscape [9]. Consequently, despite a high degree of self-similarity in the topographic surface, fractal modelling has to be handled with care.

## 2.2 Fractal-based 3D texture analysis

Digital terrain models are often used as ancillary data for image rectification. In this case they only need to provide accurate elevation values with no need for slope or any other derivative. However, many DTM applications need more than terrain elevation. For instance, numerous studies in civil engineering or environmental geology need to characterize the structure or texture of relief by analysing altitude derivatives. Different tools can be implemented to characterize the terrain surface, such as Fourier transforms, wavelet transforms, co-occurrence matrices or variograms. Specific indicators are then derived to quantify a particular property (isotropy, roughness...).

In the case of texture analysis, one of the most suitable tools is the variogram, already defined in the previous subsection. It is of interest in many remote sensing applications, whenever textures are to be described or compared. A comparison of variograms of different land use areas can be useful to perform classifications or to select a sampling rate for remote sensing images. Curran derived several texture indices from a generic variogram, referring to different aspects of the radiometric content of a remote sensing image (see [7]). A comparison of the concepts of variogram and fractal dimension for remotely-sensed image texture classification can be found in [24].

Similarly, 3D texture analysis can usefully be studied through the relief variogram. In particular, interpreting the variogram of a nearly fractal surface allows the definition of specific textural indices [26]. The fractal-based indices are very sensitive to the 3D texture of relief, and they present some degree of correlation with the lithological and hydrological properties of the surface, which make them a valuable analysis tool for geologists.

The fractal properties of relief can be derived from the semivariogram through a least squares linear estimation of the fractional Brownian surface which best fits the real surface. Obviously, it is recommended to check the linearity of the variogram (i.e. the ‘fractalness’ of the surface to be analysed) before giving a physical meaning to such surface descriptors as fractal dimension (derived from the variogram slope) or the abscissa of a slope break. Despite its great interest for geosciences, fractal-based 3D textural analysis presents two major limitations. First, if the relief variogram is not linear, the computation of textural parameters can be carried out by least squares adjustment, but they cannot be interpreted as if the surface were fractal. Secondly, the meaningful computation of a variance or any other statistical parameter requires a large number of samples, which

is in contradiction to the need for a local textural index. Although fractal analysis offers an attractive tool for 3D texture characterization, it must be interpreted carefully.

### 2.3 Fractal-based DTM resampling

Most digital terrain models used in geoscience and remote sensing are obtained by automated stereomatching or by interpolating digitized contour-lines. In both cases, the highest frequencies of relief do not appear in the computed surface, which is generally excessively smooth. In order to avoid this artifact, specific interpolation techniques can be considered, based on the continuity of the variogram.

A specific resampling method called ‘kriging’ has been developed for mine evaluation. Non-observed points are interpolated between neighbours using optimal weights in order to preserve the spatial correlation predicted by the semivariogram. The practical implementation of kriging as well as its advantages and limitations are discussed in detail in [4].

Another technique, call ‘random midpoint displacement’(RMD), also based on the statistical properties predicted by the semivariogram, consists of using a random function to preserve self-similarity. RMD interpolation can be used either for the resampling of a DTM using its variogram or for the generation of a synthetic DTM fitting an ideal variogram. The methods for RMD implementation and the applications of this algorithm in geoscience and computer vision have been widely published (see [2], [16], [25], [19], [10], [26], [23]). A particular application to spaceborne data simulation will be presented in the last section of this chapter.

RMD is used for dichotomic interpolation by extending the supposedly linear variogram of a sampled surface towards shorter distances as illustrated in fig. 1. Since the DTM variogram is likely to slightly depart from linearity, it has to be approximated by a least squares straight line, which is the basis for the computation of  $D$  and  $\sigma$ . The interpolation is then performed by extending it to a half-pixel scale. It can be shown that fitting this straight line at a half-pixel distance is obtained by adding to the initial surface a random Gaussian term defined by the standard deviation:

$$\sigma' = \frac{\sigma}{2^{3-D}} \sqrt{1 - 2^{4-2D}} \quad (4)$$

It can occur that the RMD interpolation does not yield very realistic results, mainly if the landscape to be resampled is not fractal or if the variogram obtained from the DTM is biased by some artifacts. In such cases, the

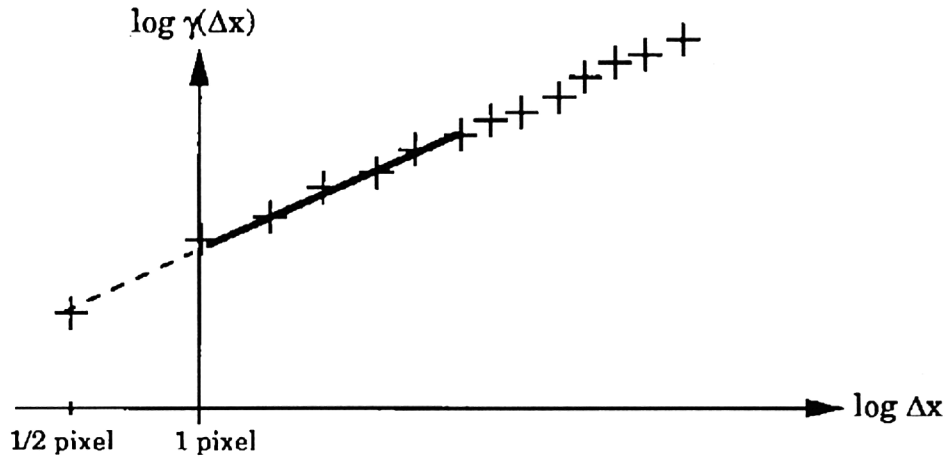


Figure 1: Extension of log-log semivariogram to half-pixel scale

RMD interpolation can be adapted in order to fit to a higher degree of realism. For instance, a weighted RMD interpolation can reduce the impact of the random term in areas where the input DTM departs from the fractal hypothesis [23].

It should be noticed that both kriging and RMD are designed to preserve the statistical properties of the sampled surface, but disregard the local hydrographic and structural aspects of relief.

## 2.4 Fractal-based landscape synthesis

RMD interpolation can be used not only to resample a DTM at sub-pixel scale, but also to synthesise a whole landscape with a given fractal dimension and vertical scaling factor - in other words, to synthesise a particular fractional Brownian surface. Fig. 2 shows two fractional Brownian surfaces with different fractal dimensions.

Once again, the procedure can be adapted in order to yield a more realistic landscape. For instance, the synthetic landscape can be chosen to be multifractal, with a given fractal dimension for each interval of horizontal distances. Another adaptation can be to consider a spatially variable fractal dimension, e.g. as a function of altitude. Indeed, comparing the fractal dimensions of digitized contour-lines at different altitudes often re-

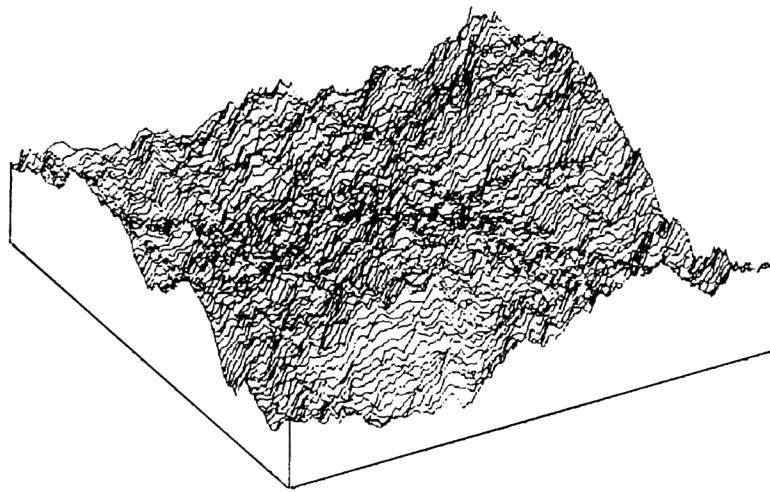
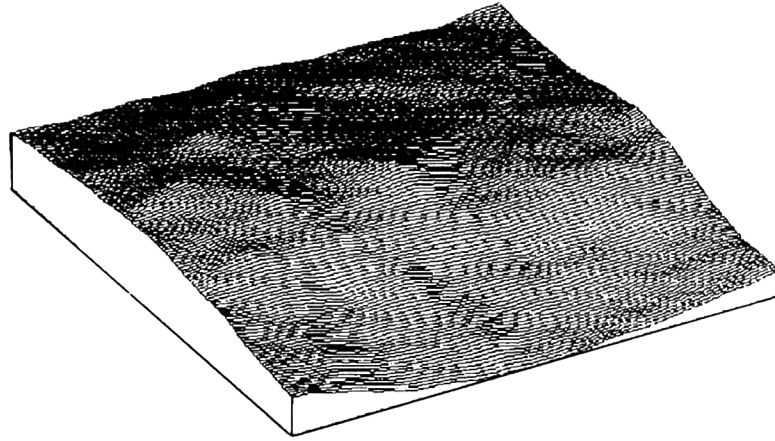


Figure 2: Two fractional Brownian surfaces with different fractal dimensions [ $D = 2.05$  (upper);  $D = 2.25$  (lower)]

veals a positive correlation between altitude and fractal dimension [9]. Such a correlation can be observed in alpine relief with rocky peaks and smooth valleys. It can be synthesized by multiplying the semivariance by a monotonic function of height.

The basic concepts presented in this section concerning the fractal modelling of relief will be used in the following sections in the context of DTM assessment.

### 3 Internal validation of DTM's

#### 3.1 On the quality of digital terrain models

The aim of digital terrain model quality assessment is to quantitatively evaluate the discrepancies between the DTM and the real topographic surface. This can be done in two different ways, which can be called internal and external validation.

Internal validation consists in checking the consistency of the DTM with some *a priori* knowledge of the surface. For instance, it can be assumed that all rivers go downhill, so that an artifact may be seen wherever a river goes uphill over some distance. On the contrary, external validation is an objective comparison with a reference data set.

Since a DTM is seldom generated when another DTM of higher accuracy already exists over the same area, external validation is generally performed using a restricted set of ground control points (GCP's). Very accurate GCP's can be employed, for instance GPS stations [1] but this is quite an expensive method. Most often, ground control points are plotted on medium scale maps.

In fact, the comparison of a DTM with a set of GCP's has two major limitations. First, statistical quality indicators such as RMS height error become meaningless when the number of GCP's is too low. More seriously, a reduced number of GCP's does not permit the evaluation of the derivatives of height, such as slope, orientation or curvature. Since the derivatives of height are the indicators of terrain shapes, they have to be carefully controlled. Indeed, the topographic surface is so familiar for us, it has so many intuitive properties, that we have far more requirements for its cartographic representation than for the representation of any other physical surface [5]. For instance, the geoid has a clear physical meaning, but its local shapes have no intuitive significance.

Due to the severe requirements just mentioned, the local shapes have to

be controlled with care. Several authors have observed that the extraction of geomorphological information in DTM's is limited by the lack of accuracy in the derivatives of height [11]. Since the comparison with a set of GCP's does not allow one to draw conclusions concerning the derivatives, they generally have to be evaluated by internal validation. This is commonly done in most stereomapping facilities, where the output DTM is manually controlled.

The aim of this section is to show that fractal dimension measurements can contribute to the external validation of digital terrain models, by comparing the fractal properties of the DTM to the properties of the mapping and sampling algorithms. Two properties are considered, namely, self-similarity and isotropy.

### 3.2 The self-similarity criterion

Plotting the log-log variogram of a DTM generally reveals that the DTM is not a fractional Brownian surface. Fig. 3 is a typical variogram over a

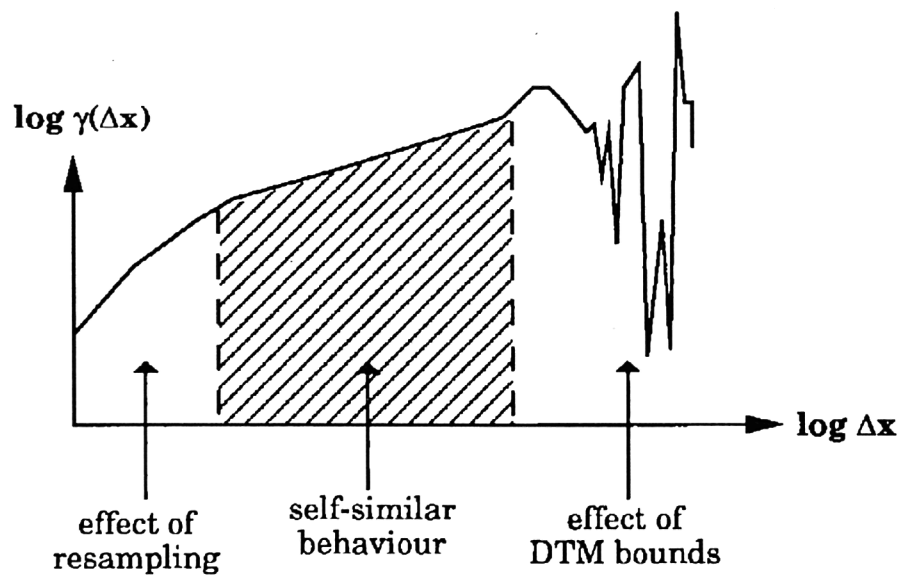


Figure 3: Typical log-log semivariogram over a resampled DTM

nearly fractal terrain (e.g. alpine relief) with a linear trend at most scales, and a peculiar behaviour at the limit scales, which can be interpreted as follows:

- at the DTM scale, the number of samples decreases so the variance becomes meaningless
- at the pixel scale, the variogram slope is expected to be maximum when smooth interpolators (e.g. splines) are used

However, this departure from a self-similar behaviour cannot be viewed as an interpolation effect without some assumptions. These assumptions can be based on the knowledge of the method which is used to generate the DTM (initial height computation technique, spatial distribution of the observed terrain points, resampling algorithm...).

In order to control the quality of a DTM obtained by interpolating digitized contour-lines with a classical spline interpolator, it may be useful to compare the variogram slope for short distances and for long ones, i.e. shorter and longer than the average horizontal distance between the contour-lines in the input map (see [22]). The DTM is controlled by comparing fractal dimensions between 10 and 30 pixels ( $D=2.25$ ) and between 1 and 5 pixels ( $D=2.07$ ). The fact that  $D$  becomes close to 2.0 means that the resampled surface is locally planar, and this may be interpreted as the effect of a smooth interpolator.

The limit between the two distance intervals was chosen in order to discriminate the short distances, over which the interpolation is relevant, and the longest ones, over which it is not. Obviously, the limit between these two scales is known only if the original map is available, but this is not a critical point. A more critical point is the need for an *a priori* knowledge of the real surface. Indeed, the slope break in the DTM variogram cannot be interpreted as an effect of the smoothing interpolator without the guarantee that the real surface has no similar slope break at this particular scale in its variogram.

### 3.3 The isotropy criterion

Another classical effect of grid resampling is a directional tendency in the output DTM. The same method as mentioned above is proposed in [22] for detecting directional artifacts. A DTM obtained by interpolating contour-lines in two directions (N-S and W-E) is analysed by measuring fractal dimensions in the exploring directions and in the complementary ones. Of



course, the scale interval is a crucial parameter for such an analysis. For large distances, for which interpolation has no incidence, fractal dimension measurements do not show any anisotropic behaviour. On the contrary, an important discrepancy is observed over short distances. Indeed, fractal dimension is much lower in the exploring directions (close to 2.0).

Once again, the anisotropic texture of the DTM cannot be interpreted as an effect of the anisotropic interpolator without the guarantee that the real surface has no intrinsic anisotropy in these particular directions and at this particular scale.

The same approach is used in [3] for the control of USGS DTM's. They compare fractal measurements in different directions in order to detect systematic directional artifacts which may result from the aerial photograph scanning procedures.

### 3.4 Limitation of fractal-based evaluation

Internal validation is not possible without some assumptions about the real surface. These assumptions can be difficult to justify, for instance the fact that the fractal dimension of the real surface does not change from observed surfaces to resampled ones. This assumption, as well as isotropy, can be partially confirmed by a geomorphological analysis of local relief using the DTM. However, their best justification is the correlation between the phenomena detected through fractal measurements and the characteristics of the mapping and sampling algorithms. Provided that these algorithms are known, fractal measurements can contribute to the internal validation of digital terrain models.

The quality assessment of a DTM using fractal assumptions has several limitations. For instance, the need for a local fractal measurement implies that fractal dimensions have to be estimated over small windows (e.g. 5 by 5 pixels). Variances are then computed from a limited number of samples, and this does not allow very meaningful statistics.

The limitations related to the need for an *a priori* knowledge of the real surface have already been discussed. However, these limitations partially disappear if the control is carried out for a large number of DTM's over a large variety of landscapes, but obtained with the same techniques. In this case, a slope break or an anisotropy in the average variogram can be related to DTM artifacts with more and more confidence since it becomes less and less probable to observe the same multifractal or anisotropic behaviour in all landscapes. For this reason, fractal-based internal validation is more suitable for the quality assessment of a relief mapping technique than for

the control of individual DTM's. Fractal-based and other internal validation techniques are often limited to the evaluation of terrain shapes. In other words, they are not sensitive to absolute location errors. For this reason, they are complementary to standard height error estimations, and they have no use if the DTM is only required to provide elevations with a minimum RMS error. On the contrary, RMS height error is not a suitable quality criterion for a DTM which is supposed to provide information about the relief shapes for hydrological or geomorphological studies.

Since DTM's play an increasing role in geographic information systems, they have to be evaluated according to quality requirements corresponding to different applications and different users. This quality criteria combination is crucial for the design of multiple user geographic data bases. As observed by Burrough, a good GIS should include a range of interpolation techniques that allow the user to choose the most appropriate method for the job in hand [4].

## **4 Parametric evaluation of relief mapping techniques using image simulation**

### **4.1 Interest of image simulation in remote sensing**

Spaceborne image simulation can be performed using a parametric description of both the observed landscape (DTM, land use) and the satellite (orbit, instrument...), provided that suitable models are available for the geometric and radiometric computations. Image simulation has useful applications in remote sensing.

Due to cost considerations, sophisticated simulation tools are generally designed during the specification phase of a spaceborne mission for the following tasks:

- adjustment of the technical specifications
- prediction of the image quality
- validation of the ground-segment
- training of future users

Image simulators can also be used for the design or validation of image exploitation techniques such as topographic mapping, by testing these techniques on the simulated data sets. In the case of relief mapping, the validation is carried out by comparing the resulting DTM with the reference

DTM used for the simulation, as illustrated in fig. 4. The simulation-based approach has several basic advantages:

First, a wide variety of image data over different landscapes and with different viewing configurations can be analysed, so that more general conclusions may be drawn.

Second, the variety mentioned above can be handled with relevant parameters, namely:

- system parameters (platform, instrument, processor)
- topographic parameters (height, slope, orientation, roughness)
- environment parameters (atmosphere, surface change between two data takes).

The control of each of these parameters allows the evaluation of its impact on the performances of a mapping technique.

Finally, the simulation approach enables comparison with a reference datum.

Indeed, even if the input DTM differs from the real surface, it is supposed to represent a reference landscape with an infinite accuracy. The DTM derived from the simulated images is required to be as similar as possible to the reference DTM. This allows an objective comparison. The comparison with the input DTM is preferable to the mere comparison with a set of GCP's for two reasons: (a) the reference data set is dense so that the derivatives of elevations can be evaluated as well; (b) the reference data set has no error, while the GCP's plotted on a map can have an error comparable with the accuracy of the evaluated technique.

Testing a relief mapping technique on simulated image data has two main limitations. On the one hand, the approximations made in the geometric and radiometric models limit the representativity of the simulated images. On the other hand, the conclusions about the performances of the mapping technique are limited to the shapes and frequencies contained in the input DTM.

The aim of this section is to show how fractals can increase the interest in the simulation-based evaluation of relief mapping techniques by increasing the variety of shapes. Indeed, because of the conventional requirement to minimise standard error, most DTM's are smoothed to reduce altimetric noise, but at the expense of micro-relief, as discussed in [21]. Consequently, such a smooth DTM does not allow the evaluation of the aptitude of a relief mapping technique for the restitution of microrelief.

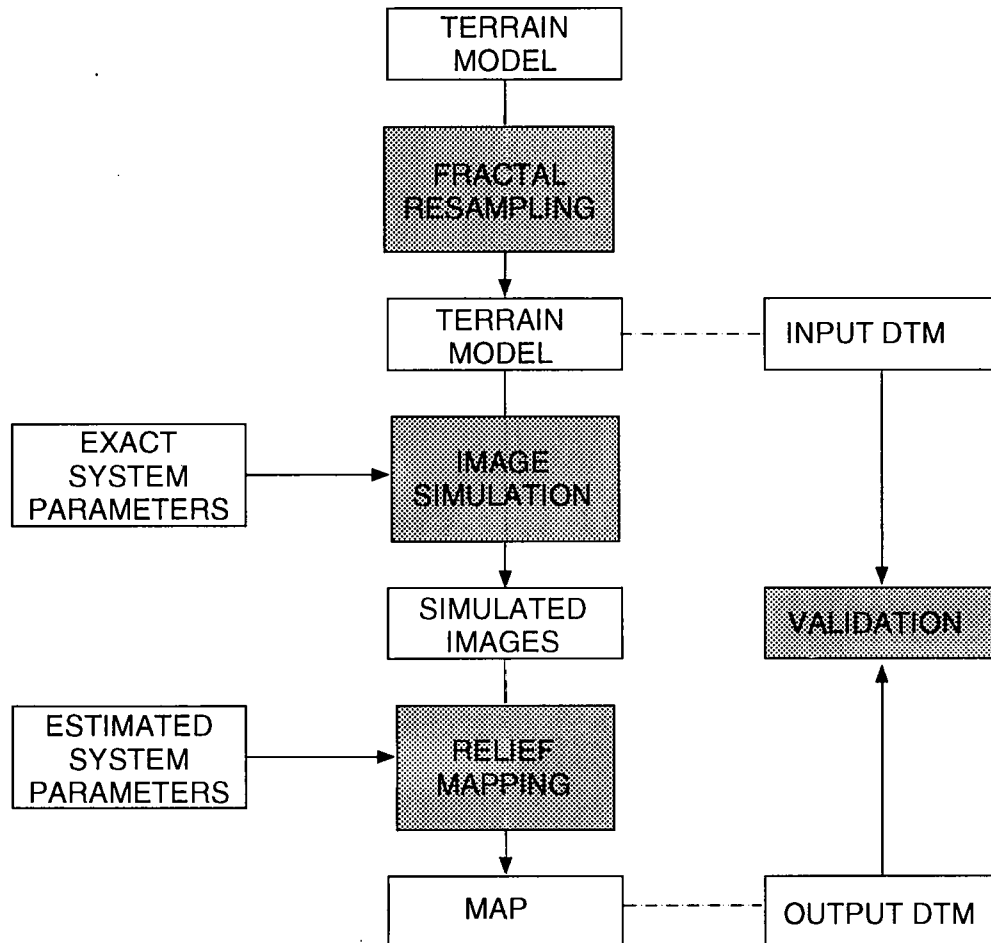


Figure 4: Procedure for simulation based evaluation of relief mapping techniques

The interest in fractal resampling is precisely to generate the microrelief in the DTM before simulating the satellite images.

## 4.2 Fractal landscape synthesis for image simulation

A simple method for fractal resampling has been described in sections 2.3 and 2.4. It is obviously preferable to generate a realistic landscape, but this is not the most critical requirement. The first aim is to ensure that the DTM spectrum be as wide as possible. Indeed, if the performances of the mapping technique are expressed in terms of a transfer function, the behaviour of this transfer function cannot be evaluated for frequencies that do not appear in the input DTM.

It would be possible to simulate the effects of micro-relief directly in the output image, by synthesizing a random radiometric texture in coherence with an assumed terrain roughness. However, this method is excluded if image simulation is used to test a mapping technique, and the high frequencies of relief have to be simulated in the DTM, so that the correspondence between terrain texture and image texture is deterministic and not stochastic. This is the only way of ensuring that two images of a stereo pair represent the same landscape.

It would also be possible to resample the DTM while computing the image, in particular in the case of radar image simulation which is generally based on object-space algorithms [13]. However, the on-line resampling of the DTM has several drawbacks:

- the DTM used for simulation has to be stored, so that it is available for the control of the output DTM
- the best way of ensuring that two images of a stereo pair represent the same landscape is to use the same physical DTM

The RMD algorithm presented in the section 2 is based on a dichotomic interpolation, so that each iteration divides the mesh size by 2 and multiplies the DTM size by 2 in both directions. If the sampling rate must be conserved, the input DTM has to be previously subsampled before oversampling. Fig. 5 shows an input DTM with a 40m. mesh, and the same DTM after two RMD iteration on a 160m. mesh subsampled DTM.

For a fully parametric evaluation, it can be useful to use a synthetic fractional Brownian surface, described by two parameters ( $\sigma$  and  $D$ ) as explained in 2.4. On the contrary, resampling the DTM of a natural surface leads to a more realistic landscape model but it cannot be described by a simple parameter.

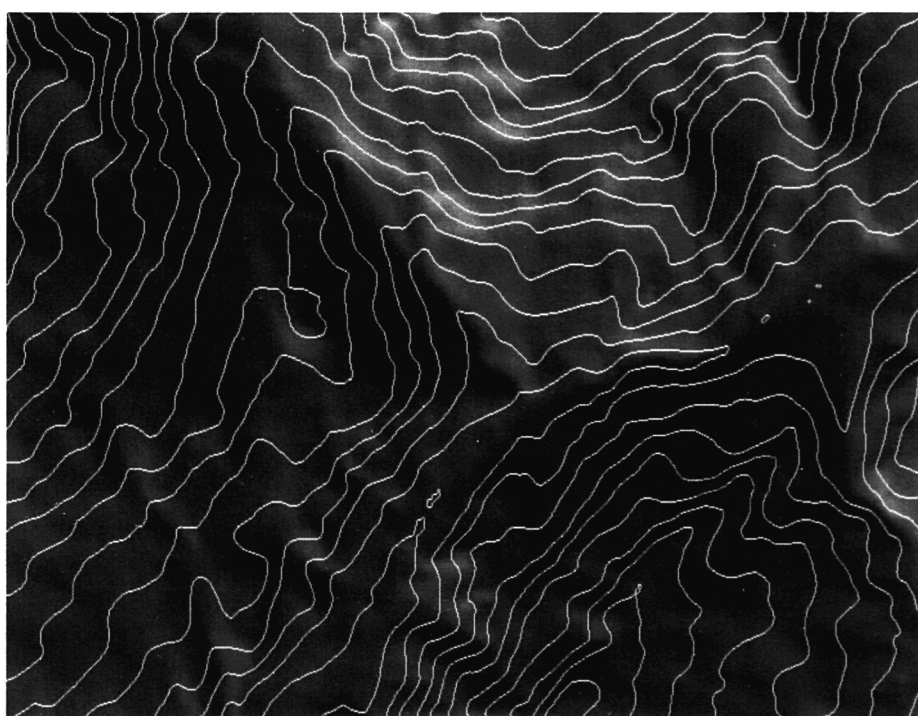
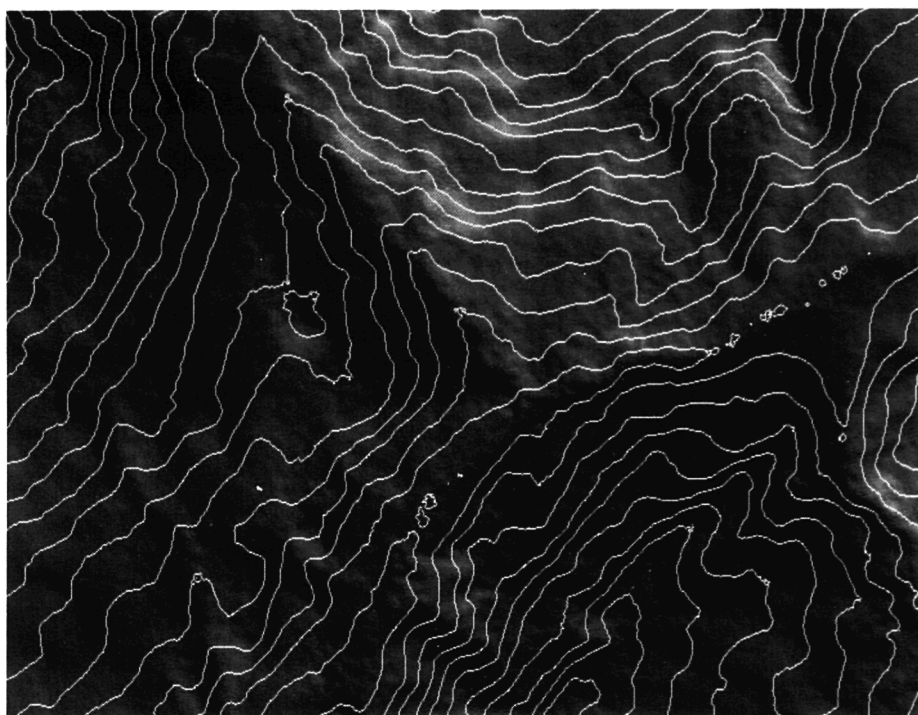


Figure 5: Input DTM (upper) and RMD sampled DTM (lower)

### 4.3 Contribution of fractal synthesis to the validation of a relief mapping technique

Microrelief is a very important factor in the performance of a mapping technique. It acts as both a noise and a signal. On the one hand, it acts as a noise with an impact on the robustness of mapping algorithms, e.g. stereo matching. On the other, it acts as a signal and the efficiency of the algorithm depends on its capacity to restore this signal. The second aspect is important if the DTM is required to faithfully describe relief shapes, the first one is important whatever the application.

Once a DTM has been derived from the simulated data by photogrammetry, interferometry or any other technique, it has to be compared with the input DTM. The comparison has to be carried out with care. First, it is necessary to generate a DTM directly comparable with the reference in terms of co-ordinate system and mesh size. Indeed, an intermediate resampling might add discrepancies independent from the evaluation technique, so that they would contaminate the evaluation. Second, the comparison of the two DTM's has to be done according to selected criteria, which depend on the scheduled application of the data. The main quality criteria are based on:

- the histogram of height discrepancies
- the histogram of slope discrepancies
- the geometry of the hydrographic network
- the topology of the hydrographic network etc.

One can use specific criteria for the detection of high frequency artifacts such as those due to the resampling process, already mentioned. For instance, those proposed in the previous section are based on two fractal assumptions, namely, self-similarity and isotropy. An important advantage of these criteria in the context of simulation-based DTM validation has to be pointed out. Indeed, the fractal assumptions based on an *a priori* knowledge of the real surface and previously discussed, are no longer questionable with the simulation approach, since a perfectly accurate reference DTM is available. In other words, the possibility to check that smoothness and anisotropy do not appear in the reference make it an objective quality assessment method.

The simulation-based validation described in this section is of great interest for validating a whole relief mapping technique, thanks to the fact

that many experiments can be run with different landscapes and different system parameters, so that the intrinsic performances and limitations of this technique can be isolated. Moreover, the control of all parameters makes it easier to optimise the algorithms, and this is the final aim of the quality assessment.

## 5 Conclusion

The interest in fractal modelling for the validation of relief mapping techniques has been analysed in this article. The fractal properties of natural terrain shapes have been discussed, and two separate methods for DTM quality assessment using fractals have been proposed. The first method aims at detecting high frequency artifacts through fractal measurements and some *a priori* assumptions about the fractal properties of the real surface. The second method consists of testing a mapping algorithm on a synthetic image (or set of images) simulated from a DTM, and the role of fractals is to broaden the spectrum of the input DTM for a more complete evaluation. Both methods are not designed for the validation of an individual DTM, but for the validation of a relief mapping technique. Given the increasing amount of satellite data and the increasing number of relief mapping tools, the overall quality of generated cartographic value-added products is about to become a crucial problem, and fractals could play an important role in dealing with it.

## 6 References

- [1] K. F. Adkins and C. J. Merry (1994): Accuracy assessment of elevation data using the Global Positioning System, *Photogrammetric Engineering and Remote Sensing*, Vol. 60, No 2, pp. 195-202.
- [2] P. A. Brivio, M. Righetti and D. Marini (1992): Fractal based technique for mountain relief reconstruction, *EARSeL Advances in Remote Sensing*, Vol. 1, No 3, pp. 136-141.
- [3] D. G. Brown and T. J. Bara (1994): Recognition and reduction of systematic error in elevation and derivative surfaces from 7 1/2 minute DEMs, *Photogrammetric Engineering and Remote Sensing*, Vol. 60, No 2, pp. 189-194.



- [4] P. A. Burrough (1986): Principles of geographic information systems for land resources assessment, (New York: Oxford University Press).
- [5] J. Carter (1988): Digital representations of topographic surfaces, Photogrammetric Engineering and Remote Sensing, Vol. 54, No 11, pp. 1577-1580.
- [6] J. Chorowicz, J. Kim, S. Manoussis, J. P. Rudant, P. Foin and I. Veillet (1989): A new technique for recognition of geological and geomorphologic patterns in digital terrain models, Remote Sensing of Environment, Vol. 29, No 3, pp. 229-239.
- [7] P. J. Curran (1988): The semi-variogram in remote sensing: an introduction, Remote sensing of environment, 24:493-507.
- [8] L. E. Gilbert (1989): Are topographic data sets fractal?, Pure and Applied Geophysics, 143(1-2):241-254.
- [9] M. Goodchild (1982): The fractional Brownian process as a terrain simulation model, Modelling and Simulation, 13:1133-1137.
- [10] M. Goodchild (1988): Lakes on fractal surfaces: a null hypothesis for lake-rich landscapes, Mathematical Geology, Vol. 20, No 6, pp. 615-630.
- [11] L. H. Graff and E. L. Usery (1993): Automated classification of generic terrain features in digital elevation models, Photogrammetric Engineering and Remote Sensing, Vol. 59, No 9, pp. 1409-1417.
- [12] S. K. Jenson and J. O. Domingue (1988): Extracting topographic structure from digital elevation data for geographic information system analysis, Photogrammetric Engineering and Remote Sensing, Vol. 54, No 11, pp. 1593-1600.
- [13] F. W. Leberl (1990): Radargrammetric image processing (New York: Artech House).
- [14] J. Lee, P. K. Snyder and P. F. Fisher (1992): Modeling the effect of data errors on feature extraction from digital elevation models, Photogrammetric Engineering and Remote Sensing, Vol. 58, No 10, pp. 1461-1467.

- [15] B. Mandelbrot (1967): How long is the coast of Britain? Statiscal self-similarity and fractional dimension, *Science* 156, pp. 636-638.
- [16] B. Mandelbrot (1982): *The fractal geometry of nature*, (San Francisco: Freeman).
- [17] D. Mark and P. Aronson (1984): Scale-dependent fractal dimensions of topographic surfaces : an empirical investigation, with applications in geomorphology and computer mapping, *Mathematical Geology*, Vol. 16, No 7, pp. 671-683.
- [18] G. Matheron (1971): The theory of regionalized variables and its applications, *Les Cahiers du Centre de Morphologie Mathématique de Fontainebleau*, Ecole Nationale des Mines de Paris.
- [19] G. Miller (1986): The definition and rendering of terrain maps, *Computer Graphics*, Vol. 20, No 4, pp. 39-48.
- [20] A. P. Pentland (1984): Fractal-based description of natural scenes, *IEEE Transaction Pattern Analysis and Machine Intelligence*, Vol. 6, No 6, pp. 661-674.
- [21] L. Polidori (1991): Validation de modèles numériques de terrain; application à la cartographie des risques gologiques, PhD thesis, University of Paris-7.
- [22] L. Polidori, J. Chorowicz and R. Guillge (1991): Description of terrain as a fractal surface and application to digital elevation model quality assessment, *Photogrammetric Engineering and Remote Sensing*, Vol. 57, No 10, pp. 1329-1332.
- [23] L. Polidori and J. Chorowicz (1993): Comparison of bilinear and Brownian interpolation for digital elevation models, *ISPRS Journal of Photogrammetry and Remote Sensing*, 48 (2), pp. 18-23.
- [24] G. Ramstein and M. Raffy (1989): Analysis of the structure of radiometric remotely-sensed images, *International Journal of Remote Sensing*, Vol. 10, No 6, 1049-1073.
- [25] R. Voss (1985): Random fractal forgeries, in *Fundamental Algorithms*

for Computer Graphics (Ed. R. Earnshaw), (New York: Springer Verlag), pp. 805-835.

- [26] N. Yokoya, K. Yamamoto and N. Funakubo (1989): Fractal-based analysis and interpolation of 3D natural surface shapes and their application to terrain modelling, *Computer Vision Graphics and Image Processing*, 46, pp. 284-302.

# Chapter 12

## Characterisation and Imaging of Fractal Topography

*W. G. Rees\**

### 1 Introduction: the relationship between surface topography and image brightness

Let us consider a plane surface illuminated from the direction  $(\theta_0, \phi_0)$  and viewed from the direction  $(\theta_1, \phi_1)$  where the angles  $\theta$  are measured from the surface normal and  $\phi$  are azimuthal angles measured from some reference direction (see figure 1). The manner in which the surface reflects radiation is specified by its BRDF (bidirectional reflectance distribution function), which is denoted by  $R$  and is in general a function of all four angles  $\theta_0, \phi_0, \theta_1$  and  $\phi_1$ . For most naturally-occurring materials, however, the azimuthal dependence may be neglected. The BRDF is defined (e.g. [1]) such that if the incident flux density is  $F$ , the radiance  $L$  observed in the direction  $\theta_1$  is given by:

$$L = FR \cos \theta_0 \quad (1)$$

For a pseudo-Lambertian surface, the BRDF is constant with a value of  $r/\pi$ , where  $r$  is the hemispherical albedo.

We can use these simple ideas (although see e.g. [2] for a more detailed discussion of the effect of topographic effects on images) to understand the basis of the relationship between surface topography and the spatial structure of an image of the surface, assuming that the dominant source of illumination is direct sunlight (e.g. [3]). Let the surface normal be described

---

\*Scott Polar Research Institute, University of Cambridge, UK

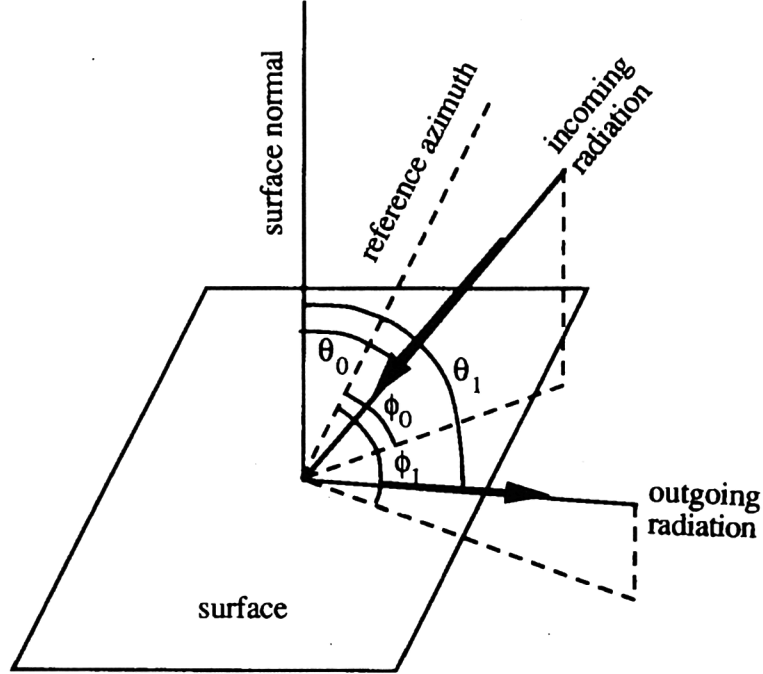


Figure 1: Geometry to describe the bidirectional reflectance distribution function (BRDF)

by a unit vector  $\mathbf{N}$ , and the unit vector from the surface towards the sun be  $\mathbf{S}$ . The direction of the incident radiation is clearly given by:

$$\cos \theta_0 = \mathbf{N} \cdot \mathbf{S} \quad (2)$$

If the sun's altitude above the horizon is  $\alpha$ , we can set:

$$\mathbf{S} = (\cos \alpha, 0, \sin \alpha) \quad (3)$$

where the  $x$ -axis has been chosen to be horizontal to the sun's azimuth, and the  $z$ -axis is vertical (see figure 2). If we write  $n_x$  and  $n_y$  for the  $x$ - and  $y$ -components of the unit surface normal in the same coordinate system, we have:

$$\mathbf{N} = (n_x, n_y, [1 - n_x^2 - n_y^2]^{\frac{1}{2}}) \quad (4)$$

so that application of equation (2) gives:

$$\cos \theta_0 = n_x \cos \alpha + (1 - n_x^2 - n_y^2)^{\frac{1}{2}} \sin \alpha \quad (5)$$

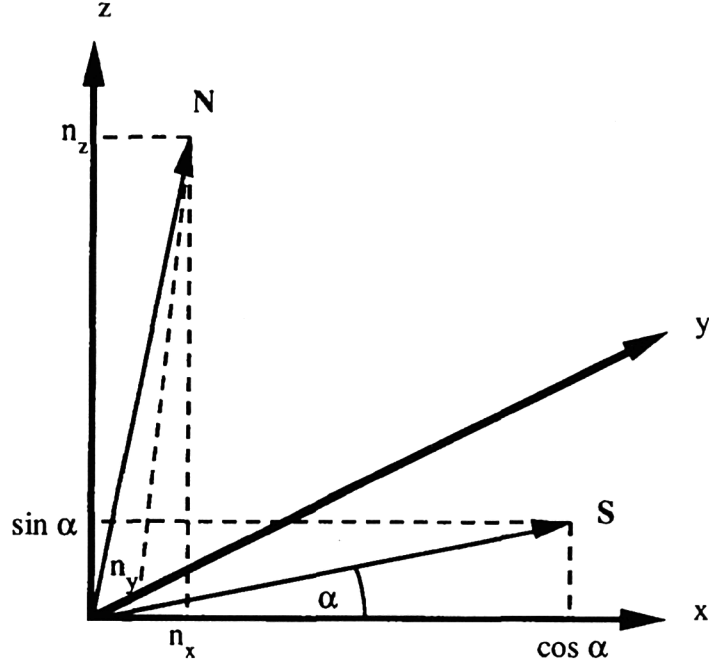


Figure 2: Relative geometry of the unit vector  $\mathbf{S}$  from the surface to the sun and of the unit surface normal vector  $\mathbf{N}$  described in a Cartesian coordinate system

If the surface is pseudo-Lambertian, the reflected radiance  $L$  is (by equation 1) just proportional to  $\cos \theta_0$ . Even if it is not, so that  $R$  is a function of  $\theta_0$  and  $\theta_1$  (and possibly also  $\phi_0$  and  $\phi_1$ ), we can perform a Taylor expansion of equation (1) to linearise  $L$  with  $\theta_0$ . However, we will continue to assume that  $L$  is proportional to  $\cos \theta_0$ .

Equation (5) implies that  $\cos \theta_0$ , and hence  $L$ , is almost independent of  $n_y$  but linear in  $n_x$ , as long as the solar elevation  $\alpha$  is low enough and  $n_x > -\sin \alpha$  (if this condition is not satisfied, the surface is in shadow and the radiance falls to zero). This is illustrated by figure 3, which shows contours of equal values of  $\theta_0$  in the  $(n_x, n_y)$  plane for  $\alpha = 10$  deg. The implication of this result is that, for direct solar illumination at a fairly glancing angle, the outgoing radiance  $L$  (to which the image brightness is proportional) can be written as:

$$L \approx An_x + B \quad (6)$$

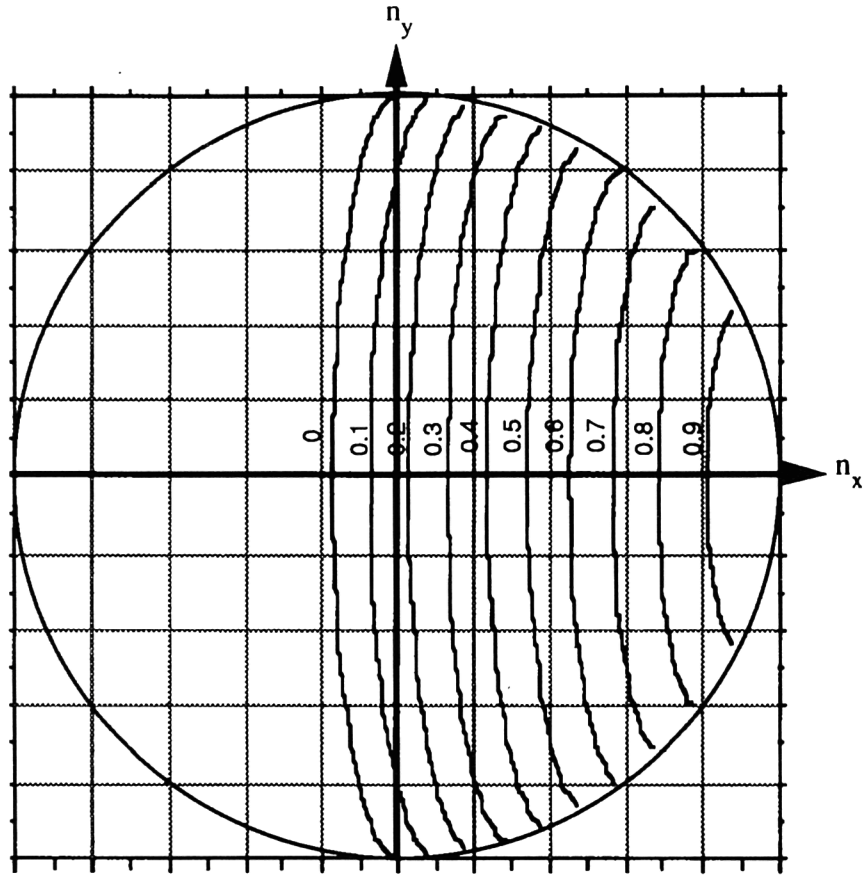


Figure 3: Contours of equal values of  $\theta_0$  in the  $(n_x, n_y)$  plane, for solar illumination 10 degrees above the horizon.  $n_x$  and  $n_y$  are shown ranging between  $-1$  and  $+1$ : only values within the circular area are possible

where  $n_x$  is the component of the surface slope in the direction parallel to the solar azimuth, and  $A$  and  $B$  are constants for a surface of constant BRDF. This result forms the basis of many so-called ‘shape-from-shading’ algorithms.

## 2 Shape from shading

If the conditions discussed in section 1 are met, so that the validity of equation (6) may be assumed, we can use the image brightness to determine the corresponding surface topography. Assuming equally spaced pixels along the direction parallel to the solar azimuth, we can in effect integrate equation (6) to obtain (e.g. [3], [4]):

$$h_i = a \sum_{j=1}^i L_j + b_i + c \quad (7)$$

where  $h_i$  is the height of the  $i$ th pixel,  $L_i$  is its brightness, and  $a$ ,  $b$  and  $c$  are constants. The pixel  $j=1$  from which the integration begins is clearly arbitrary. Although the constants  $a$  and  $b$  can, in principle, be deduced from knowledge of the BRDF and the solar illumination angle, the constant  $c$  is necessarily derived from a known height  $h_i$  at a known position  $i$ , and it is probably safest to obtain all three constants in this way, using a minimum of three control points. The advantage of the technique is that it yields topographic data at the single-pixel scale to ‘fill in’ the heights between the control points.

This method has been applied [3] to the topography of the Nordaustlandet ice cap in the Svalbard archipelago, using a Landsat MSS image acquired in March 1973 and topographic height data acquired about 10 years later by radio echo-sounding methods. Dry snow, such as would be expected in this area in Spring, has a very uniform BRDF, so that equation (6) should hold fairly accurately. Rees and Dowdeswell [3] found that with three height control points distributed fairly evenly over a 110km. transect, the algorithm generated height errors with an RMS value of about 80m., roughly 10% of the total range of height encountered in the transect. While this RMS error is large, it seems probable that most of the power in the error spectrum is concentrated at low spatial frequencies and that more height control points would effectively solve this problem. This suggests the possibility of a powerful synergy between radar altimeter data, which sample topography at a scale of the order of 10km., and visible-wavelength



satellite imagery, which has a sampling scale of 10m. to 1km. It also suggests the usefulness of the shape-from-shading approach in characterising surface roughness.

### 3 Fractal dimension as a measure of surface roughness

The roughness of a one-dimensional transect  $h(x)$  could obviously be defined as the standard deviation  $\sigma$  of the height:

$$\sigma = \sqrt{\langle h^2 \rangle - \langle h \rangle^2} \quad (8)$$

where  $\langle \rangle$  denotes spatial averaging over all  $x$ . However, such a definition immediately presents a problem in the case of a transect which is linear but which has a non-zero slope  $k$ . If the transect is defined over a finite range  $\xi$  of  $x$ ,  $\sigma = \xi|k|/\sqrt{12}$ . This clearly tends to infinity as the length  $\xi$  of the transect tends to infinity, but it is unsatisfactory at a more basic level in that one's intuitive description of such a transect is that it is perfectly smooth. While one might attempt to avoid this problem by defining the roughness as the RMS deviation from the mean straight line fitted through the transect, measured perpendicular to the line, even this definition would fail to register the intuitive smoothness of, for example, a pure sine curve. What is required here is a 'scale-free' measure of surface roughness.

A powerful new approach to the problem of characterising the roughness of surfaces, especially naturally occurring surfaces, was introduced by Mandelbrot who developed the concept of fractals and fractional dimensionality (e.g. [5]). Various workers have demonstrated that natural surfaces often exhibit fractal behaviour over certain ranges of spatial scale (e.g. [5] - [8]), and Pentland [6] has shown that the fractal dimension corresponds very well to an intuitive idea of roughness.

A fractal transect or surface is characterised by its fractal dimension  $D$ , which is larger than the topological dimension normally associated with the geometry under consideration. For example, a transect can be represented as a line on a plane, and topologically speaking the line has one dimension. However, if the line is irregular, it partakes to some extent of the character of the plane (which has two topological dimensions), and the transect has a fractal dimension between 1 and 2. If the line is so irregular that it passes through every point in the plane (e.g. the Peano curve [9]), its fractal dimension is equal to 2. Similarly, a connected surface defined in

three dimensions has a topological dimension of 2, and a fractal dimension between 2 and 3. A plane surface has  $D=2$ , and a very rough surface (a sheet of heavily crumpled paper is an approximation) has  $D=3$ .

### 3.1 Geometric self-affinity

Fractals exhibit self-affinity, in either the strictly geometric sense or in the statistical sense. A well-known example of the geometrically self-affine type of fractal is the Koch curve [10]. Figure 4 shows a finite approximation to the Koch curve. The Koch curve has the property that it can be broken

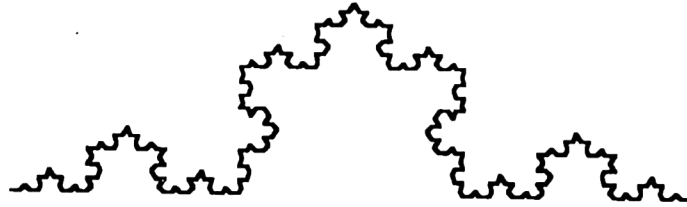


Figure 4: Approximation to the Koch curve at the fourth level of iteration. The true Koch curve, which is nowhere differentiable, is generated by an infinite number of iterations

into four identical parts, each of which is an exact one-third scale copy of the original curve. This illustrates one definition of the fractal dimension  $D$ : If an object can be broken into  $N$  identical parts, each of which is an exact  $1/S$ -(linear) scale replica of the original, the dimensionality of the object is:

$$D = \frac{\log N}{\log S} \quad (9)$$

The fractal dimension of the Koch curve is thus  $(\log 4)/(\log 3) = 1.262$ . A straight line, on the other hand, clearly obeys the relationship  $N = S$ , giving it a dimension of 1, a square obeys  $N = S^2$  ( $D=2$ ) and a cube  $N = S^3$  ( $D=3$ ).

### 3.2 Statistical self-affinity

This definition cannot be applied in its strict sense to statistically self-affine objects, and of course real natural objects are highly unlikely to possess the strict geometric self-affinity of the Koch curve. The fractional dimensionality of such objects can be defined by box-counting or by measuring the compass dimension. These will be discussed with reference to curves drawn in a plane, but can readily be extended to surfaces defined in space having three topological dimensions.

The box-counting dimension is defined by superimposing a square grid of size  $s$  on the curve, and counting the number  $n$  of grid squares which contain some of the curve. A fractal curve of dimension  $D$  is characterised by the following dependency of  $n$  on  $s$ :

$$n \propto s^{-D} \quad (10)$$

Consequently, a graph of  $\log n$  against  $\log s$  will be a straight line of slope  $-D$ .

The compass dimension is defined by measuring the length of the curve using a compass set to describe arcs of length  $s$ . The curve is thus represented as a set of connected straight-line segments, each of length  $s$ , joined at points lying on the curve. If there are  $n$  of these segments, the length of the curve measured at the precision defined by  $s$  is  $L = ns$ , and a fractal curve is characterised by:

$$L = ns \propto s^{1-D} \quad \text{or} \quad n \propto s^{-D} \quad (11)$$

Again, a graph of  $\log n$  against  $\log s$  will be a straight line for a fractal curve.

This approach has been applied to Mandelbrot's question [11]: 'How long is the coastline of Britain?' Estimates of this quantity vary typically between 7400km. and 8000km. Mandelbrot showed, using the compass dimension, that, for  $10 \text{ km.} < s < 1000 \text{ km.}$ , the coastline is well described by equation (11), with a value of  $D \approx 1.25$ , so that no unique length can be assigned to it. Indeed, if equation (11) were valid down to  $s=0$ , the length would be infinite. Box-counting gives an almost identical result of  $D = 1.26$  for  $s$  between 10km. and 100km. (see figure 5).

Many other naturally occurring curves, surfaces and other phenomena have been shown to display fractal characteristics over some range of length scales  $s$ , and the concept is now generally accepted as a valid and useful one in characterising the geometry of natural constructs. Table 1 gives a few

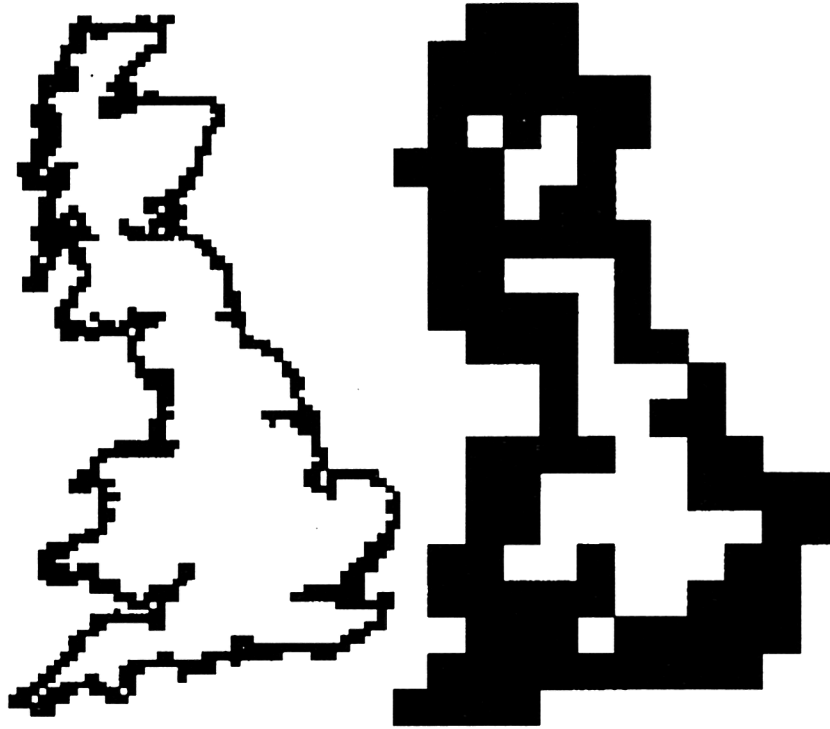


Figure 5: Estimation of the fractal dimension of the coastline of mainland Britain using the box-counting dimension. In the figure on the left, a 10km grid has been overlaid on the coastline, and those grid cells in which some of the coastline appears have been coloured black. There are 740 such cells. In the figure on the right, the grid size is 50km and the coastline occupies 99 cells. The fractal dimension is thus  $\log(740/99) / \log 5 \approx 1.25$

Phenomenon	D	Range	Source
Norwegian coastline	1.52	0.6km - 80km	[12]
Cloud outline	1.35	1km - 1000km	[13]
Steel fracture surface (1D)	1.28	2 $\mu$ m - 300 $\mu$ m	[14]

Table 1: Examples of natural phenomena showing fractal behaviour, together with the fractal dimension D and the range of scales over which this behaviour persists

examples to illustrate the range of phenomena for which the concept has been found useful. However, it must be emphasised (as equations 9, 10 and 11 make clear) that no natural construct can be a true fractal in the sense of obeying equation (9), (10) or (11) over all scales from zero to infinity. There will be a small-scale limit imposed by atomicity or by the breakdown of the physical process responsible for the fractal characteristic, and there will be a large-scale limit imposed by the physical size of the object itself or by an upper bound to the scale of the process.

## 4 Fractional Brownian motion

A particular type of fractal behaviour, called fractional Brownian motion (FBM - see e.g. [15], [16]), can be displayed by functions such as time series or surface profiles. As the name suggests, FBM is a generalisation of classical Brownian motion.

In a one-dimensional random walk, a particle makes steps of length  $x$  along the  $x$ -axis, at regular intervals  $\tau$  and with equal probability forwards and backwards. The direction of any step is uncorrelated with that of any other. Under these conditions, it can easily be shown that:

$$\langle x(t + t') - x(t) \rangle = 0$$

and

$$\langle [x(t + t') - x(t)]^2 \rangle = \frac{\xi^2 t'}{\tau}$$

where the angle brackets  $\langle \rangle$  denote the expectation value. The Brownian motion thus has the statistically self-affine property that if the time-coordinate is scaled by a factor  $k$ , the  $x$ -coordinate must be scaled by a factor of  $\sqrt{k}$  to preserve its statistical properties.

A more general statement of the fundamental property of the classical random walk is that the variance of the increment  $x(t + t') - x(t)$  is proportional to  $t'$ . In the fractional Brownian motion, this power-law index is allowed to take any value from 0 to 2. This is equivalent to abandoning the requirement that increments are uncorrelated. If the index is less than 1, the time-variance shows antipersistence, in the sense that an increasing trend in the past is likely to be followed by a decreasing trend in future (and conversely), whereas if the index is greater than 1, the time dependence shows persistence, with trends tending to remain of the same sign.

A function  $P$  of a single variable  $x$  (which can denote either space or time coordinates) exhibits fractional Brownian motion if:

$$Pr \left[ \frac{P(x + d) - P(x)}{d^H} < y \right] = F(y) \quad (12)$$

i.e. the cumulative probability distributions of  $P(x + d) - P(x)$  are identical for different values of  $d$  apart from scaling by a factor of  $d^H$ , where  $H$  is a constant known as the Hurst exponent. If we set

$$F'(y) = \frac{dF}{dy}$$

it follows that the probability distribution function of

$$A = \frac{P(x + d) - P(x)}{d^H}$$

is  $F'(A)$ , and hence that

$$\langle [P(x + d) - P(x)]^n \rangle = d^{nH} \int_{-\infty}^{\infty} F'(y) \cdot y^n dy \quad (13)$$

If we consider a statistically stationary variable  $P(x)$ , it is clear that the first-order moment ( $n=1$ ) will be zero so the first non-zero moment will correspond to  $n=2$ . Whether  $P(x)$  is stationary or not, we define the semivariance  $\gamma_P(d)$ :

$$\gamma_P(d) = \frac{1}{2} \langle [P(x + d) - P(x)]^2 \rangle \quad (14)$$

The use of the semivariogram (a plot of  $\gamma$  against  $d$ ) in image analysis is already well established (e.g. [17], [18]). In other branches of physics, the

semivariance is known as the structure function. It is a necessary condition for a FBM that the semivariance obeys the power-law relationship:

$$\gamma_P(d) \propto d^{2H} \quad (15)$$

where  $H$  is a constant. The fractal dimension  $D$  of the transect represented by the variable  $P(x)$  is then:

$$D = 2 - H \quad (16)$$

where  $0 \leq H \leq 1$  so that  $1 \leq D \leq 2$ . For classical Brownian motion,  $H = 1/2$  so  $D = 1.5$ . Examples of fractal brownian motion with different values of  $D$  are shown in figure 6. Many natural phenomena show fractal Brownian

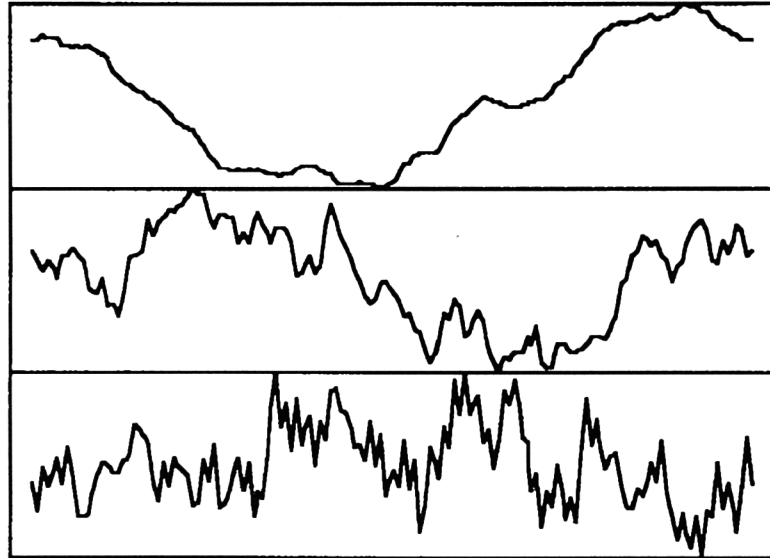


Figure 6: Examples of fractal Brownian motion with values of  $D = 1.2$ ,  $1.5$  and  $1.8$ . The respective values of the Hurst exponent  $H$  are  $0.8$ ,  $0.5$  and  $0.2$ , corresponding to persistent, classical Brownian and antipersistent behaviour respectively

motion, either directly or in their time-integrated forms. In the latter case, the fractal behaviour can be demonstrated using either the semivariogram analysis or Hurst's R/S analysis [19], which is described below.

#### 4.1 R/S analysis (see e.g. [12])

Given a variable  $q(x)$ , where  $x$  is an integer argument, we define the mean value  $\langle q \rangle_L$  over  $L$  values of  $x$  as:

$$\langle q \rangle_L = \frac{1}{L} \sum_{x=1}^L q(x) \quad (17)$$

The variable  $Q(x, L)$  is then defined as the cumulative departure of  $q$  from this mean value:

$$Q(x, L) = \sum_{y=1}^x [q(y) - \langle q \rangle_L] \quad (18)$$

the range  $R(L)$  is defined as the interval between the maximum and minimum values of  $Q(x, L)$ , as  $x$  ranges from 1 to  $L$ , and  $S$  is the standard deviation of the  $L$  values of  $q(x)$ . Hurst [19] found empirically that for many naturally-occurring time series of data,

$$\frac{R}{S} = \left[ \frac{L}{2} \right]^H \quad (19)$$

where  $H$  is the same Hurst exponent as was defined in equation (12). A value of  $H = 1/2$  implies that the data  $q$  are uncorrelated:  $H > 1/2$  implies persistence, and  $H < 1/2$  implies antipersistence. Hurst showed that many natural phenomena are characterised by a value of  $H \approx 0.73$ , implying that the cumulative sum of  $q$  (after subtraction of the mean) is a fractional Brownian motion with  $D \approx 1.27$ . Examples of this phenomenon are given in table 2 (all the data are from [19] except the temperature data which are new to this work):

### 5 Fractal dimension of natural topography

The semivariogram method (equations 14 to 16) has been used to estimate the fractal dimension of linear transects through natural topography.

First we consider a 10km. transect through Ben Nevis, at 1343m. above sea level the highest mountain in the UK. The transect, which was derived by digitising a 1:63360 scale map at intervals of 0.16km., is shown in figure 7. The transect clearly shows the smooth U-shaped valley profiles characteristic of heavily glaciated terrain.

In figure 8 we plot the semivariogram, on logarithmic axes. It can be seen that the power-law relationship of equation (15) is obeyed for scales



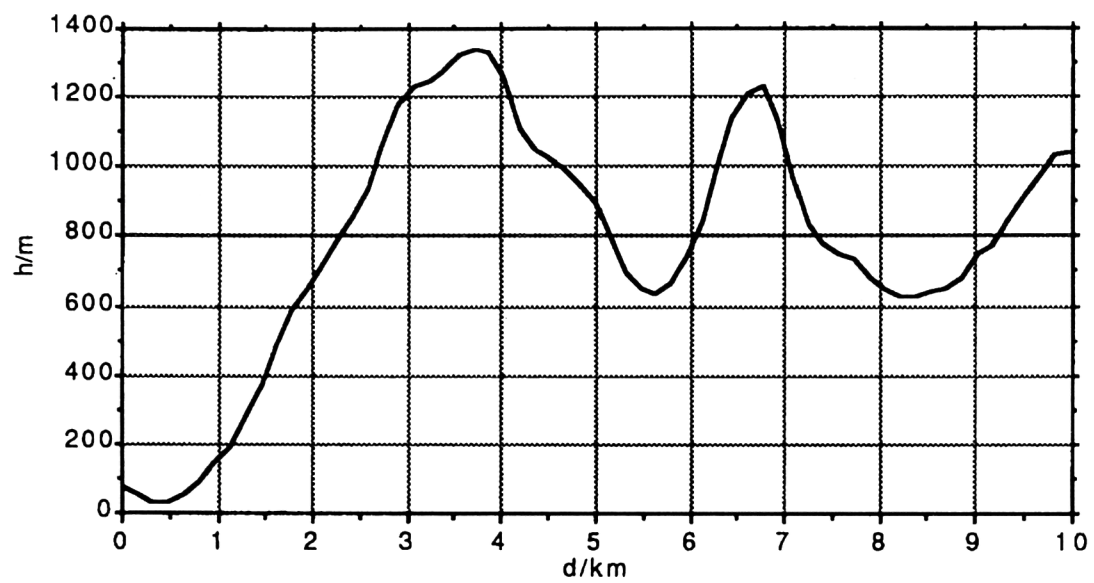


Figure 7: Transect through Ben Nevis (Scotland). The vertical exaggeration is about 3.5

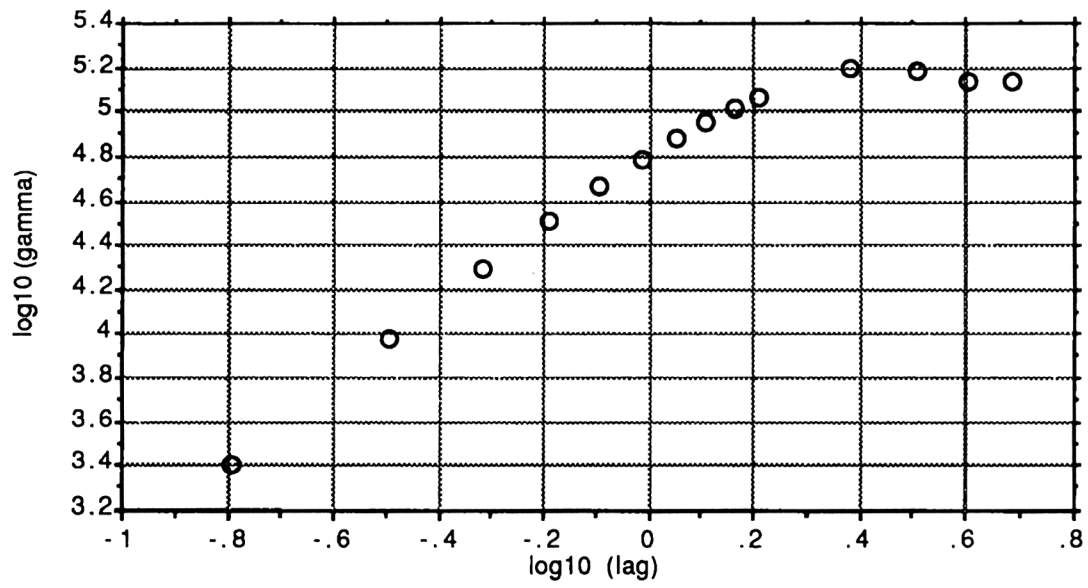


Figure 8: Logarithmic semivariogram of the transect shown in figure 7. The  $x$ -axis shows  $\log_{10}(d/\text{km})$  and the  $y$ -axis  $\log_{10}(\gamma/m^2)$

Phenomenon	Range	H
River discharge	10yr - 100yr	$0.72 \pm 0.09$
Rainfall	24yr - 211yr	$0.70 \pm 0.09$
Air temperature (Central England dataset)	11yr - 292yr	$0.73 \pm 0.08$
Air pressure	29yr - 96yr	$0.63 \pm 0.07$
Sunspot number	38yr - 190yr	$0.75 \pm 0.06$

Table 2: Examples of time series exhibiting Hurst's R/S scaling law. The table shows the lengths of datasets examined, and the value of the Hurst exponent  $H$ .

of 0.16km to 1.6km. A least-squares fit to the data gives  $2H = 1.66 \pm 0.04$ , so that the fractal dimension  $D$  of the transect is  $1.17 \pm 0.02$ . At larger scales, the effective value of  $H$  is  $\approx 0$ , suggesting that a different process is responsible for the topography.

A similar analysis has been performed for another area of glaciated mountain topography in the UK: the Rhinog mountains in Wales. The transect (obtained from a 4km. section of a 1:25000 scale map) is shown in figure 9, and the semivariogram in figure 10. The behaviour is qualitatively very similar to that for Ben Nevis. The fractal behaviour persists over the range of scales from 0.05km. to 0.75km, with a value of  $D$  of  $1.14 \pm 0.02$ . A comparison of the results for the two mountains suggests that  $D \approx 1.15$  is characteristic for heavily glaciated mountain topography, with a maximum scale size of the order of 1km.

A similar analysis for the bedrock topography beneath the Nordaustlandet ice cap [8] gives a fractal dimension of  $1.38 \pm 0.04$ . This rock is very much younger than the two examples just discussed, and the greater fractal dimension (roughness) is not surprising.

A third example is shown in figure 11. This is a 20km. E-W transect of the surface topography just north of Cambridge, where the terrain is very flat. However, the large vertical exaggeration in figure 11 shows that the 'gentle' relief has in fact a very jagged appearance, and this manifests itself in a higher fractal dimension. The logarithmic semivariogram of this transect is shown in figure 12. Fractal behaviour persists over scales from 0.25km. to 1.75km., with a corresponding value of  $D = 1.27 \pm 0.02$ . There is some evidence for another fractal regime at longer scales, with an even higher fractal dimension.

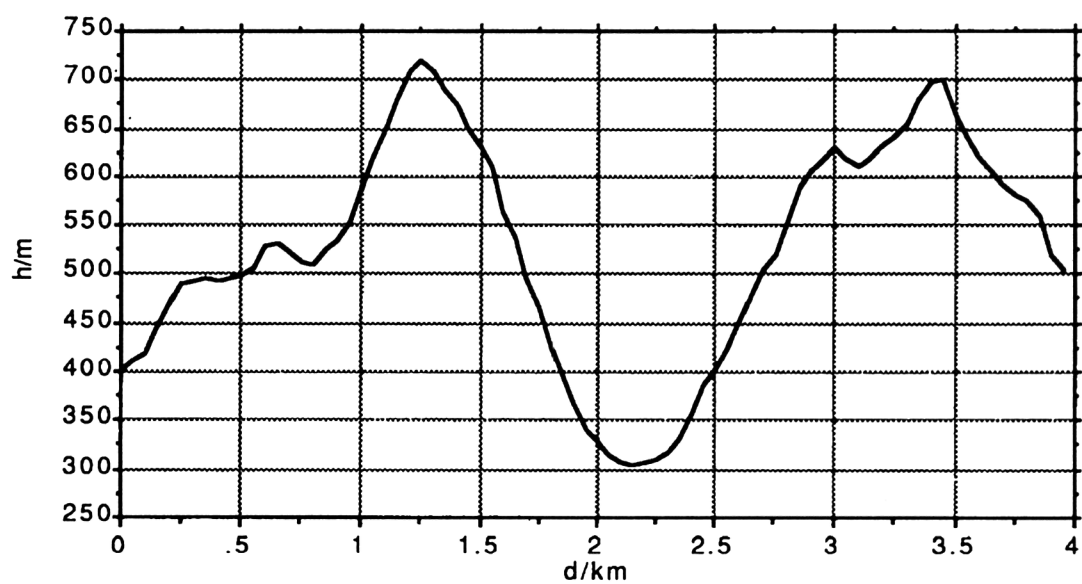


Figure 9: Transect through Rhinog Fawr and Rhinog Fach, Wales. The vertical exaggeration is about 4.0

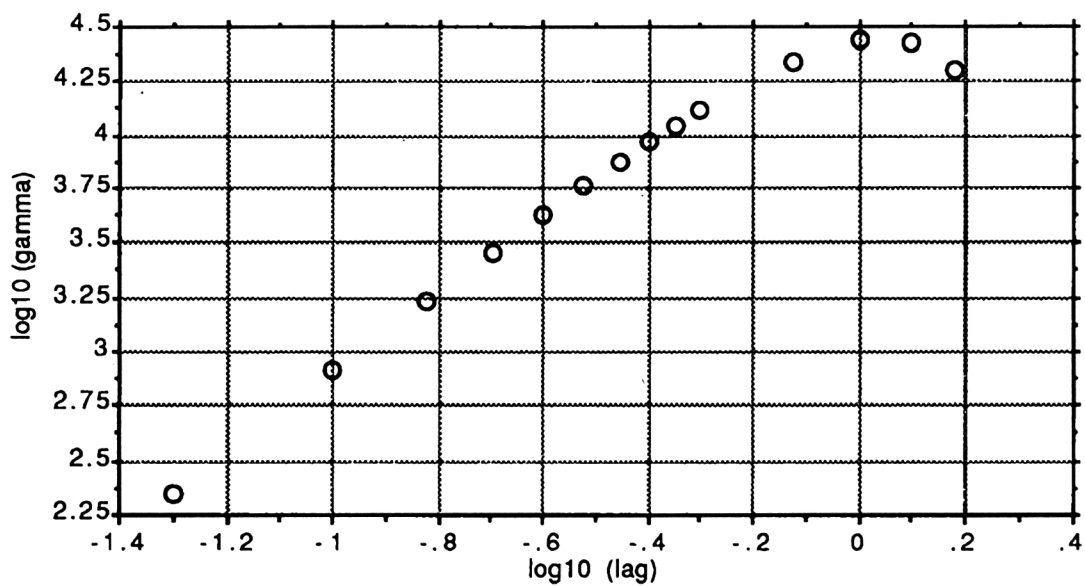


Figure 10: Logarithmic semivariogram for the transect of figure 9

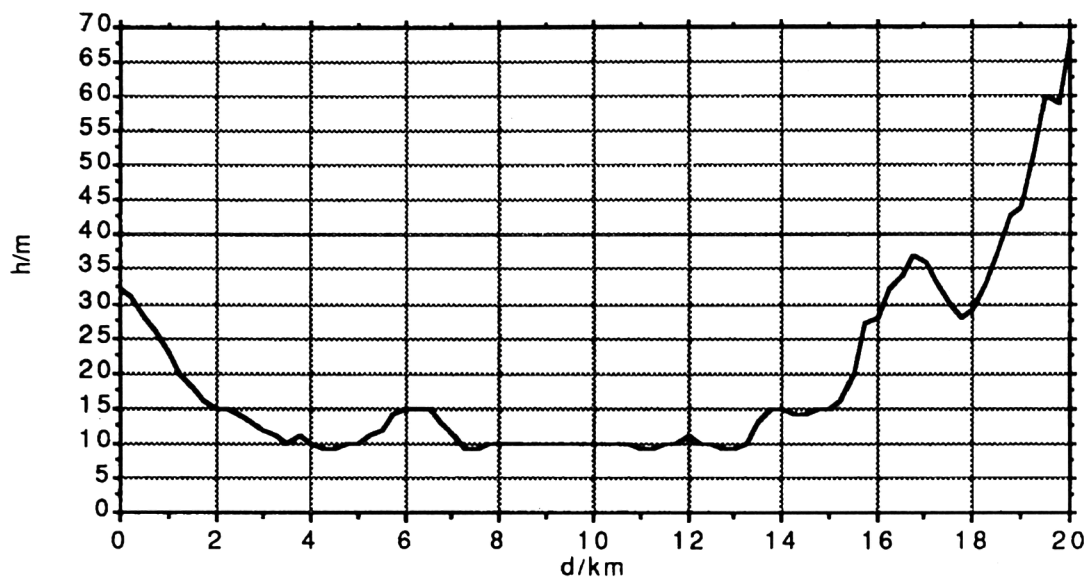


Figure 11: E-W transect of the topography just north of Cambridge, England. The vertical exaggeration is about 150

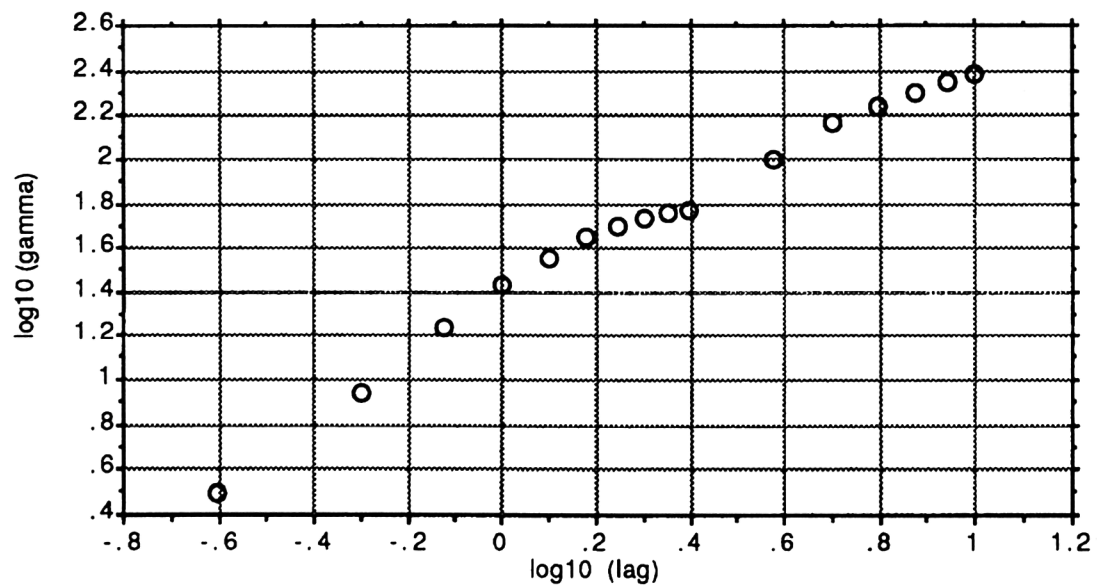


Figure 12: Logarithmic semivariogram for the transect of figure 11

Figure 13 summarises semivariance data from a large number of sources, for ice sheets, ice caps and glaciers in the Arctic. The data are from the Greenland ice sheet, the Nordaustlandet ice cap (Svalbard) and Ayerbreen glacier (Svalbard), and cover a range of scales from 0.2m. to 800km. The datasets corresponding to scales below 100m. are unpublished and have been derived from in situ measurements in Svalbard and Greenland, [20] - [22]. The three datasets corresponding to scales greater than 10km. have been derived from the Seasat radar altimeter map of Greenland [23]. The dataset corresponding to scales between about 300m. and 30km. was derived [8] from Landsat imagery of the Nordaustlandet ice cap, Svalbard, using the 'shape from shading' algorithm described above.

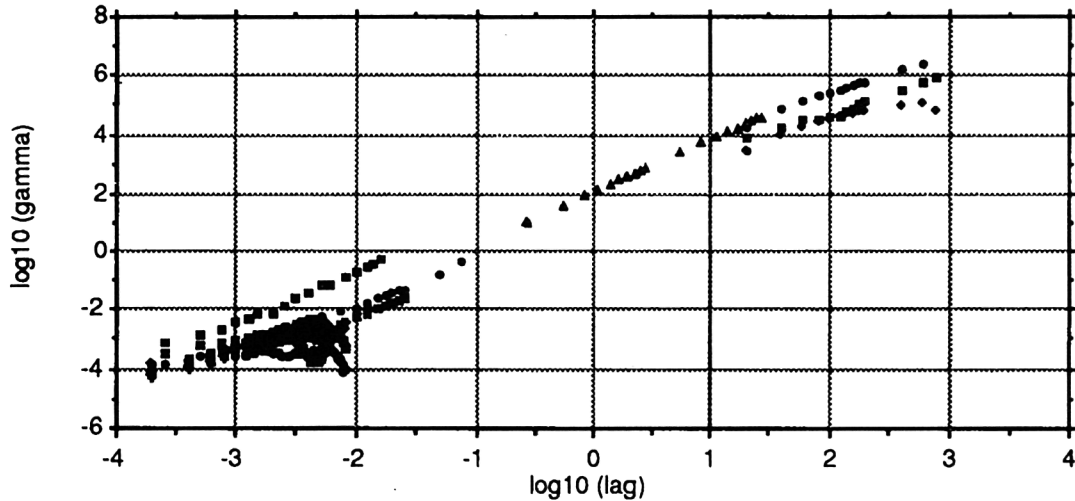


Figure 13: Logarithmic semivariogram for ice sheet, ice cap and glacier surfaces, for scales from 0.2m. to 800km. The  $x$ -axis shows  $\log_{10}(\text{lag}/\text{km})$  and the  $y$ -axis  $\log_{10}(\gamma/\text{m}^2)$

Several features are apparent from figure 13, but the most obvious feature is the general conformity of all the datasets to a single curve. There are small vertical departures from this curve, corresponding to variations of a factor of about 10 in the semivariance of different transects at a particular scale, and most of the semivariograms begin to diverge from the base curve at some maximum scale which is presumably a reflection of the scale at which the topography is no longer dominated by the behaviour of the ice itself. However, the consistency of the slope (and hence the fractal

dimension) of different datasets at the same scale is remarkable.

The semivariograms have been analysed in decades of scale. For scales between about 10m. and 100km.,  $D$  lies fairly consistently in the range 1.1 to 1.2. It is suggested that this value, over this range of scales, is characteristic of large ice masses. For scales between 100km. and 1000km.,  $D$  increases somewhat to about 1.4. For scales between 0.1m. and 10m.,  $D$  is also increased, to between 1.4 and 1.5.

Other topographic datasets have been analysed using this technique, or a close approximation to it. For example, Bishop and Chellis [24] have analysed sonar profiles of the undersides of sea-ice floes using a FBM formalism to derive the fractal dimension of ice keels and 'non-keel' structures. They found that, on spatial scales from approximately 1m. to a few tens of metres, the fractal dimensions of one (topological) dimension transects of keels lay in the range 1.2 to 1.7, whereas for 'non-keel' structures the range was somewhat lower at 1.2 to 1.6.

The data that have been presented in this section are shown in table 3 for comparison.

Topography	D	Scale range/km
Glaciated mountain terrain, UK	1.1-1.2	0.1 - 1
Sea-ice keels	1.2-1.7	0.001 - 0.01
Lowland terrain, UK	1.3	0.3 - 2
Ice cap bedrock, Svalbard	1.4	1 - 10
Large ice masses	1.4-1.5	0.0001 - 0.01
Large ice masses	1.1-1.2	0.01 - 100
Large ice masses	1.4	100 - 1000

Table 3: Examples of fractal topography determined by the semivariogram method, showing the fractal dimension  $D$  of a one-dimensional transect, and the range of scales for which this value is valid

## 6 Do fractal surfaces have fractal images?

It has been shown above that, under suitable conditions (direct illumination at oblique incidence, no shadowing) the radiance  $L$  detected from a surface should be given approximately by equation (6) i.e.:

$$L = An_x + B$$

where  $n_x$  is the horizontal component of the surface normal vector in the direction parallel to the solar azimuth, and  $A$  and  $B$  are constants. The spatial properties of  $L$  are thus determined by those of  $n_x$ . Whether or not  $n_x$  obeys FBM statistics, we can define its semivariogram from equation (14) as:

$$\gamma_{n_x}(d) = \frac{1}{2} \langle [n_x(x+d) - n_x(x)]^2 \rangle \quad (20)$$

Using equation (6), this can be expressed as:

$$\gamma_{n_x}(d) = A^2 \gamma_L(d) \quad (21)$$

i.e. the statistical properties of  $L$  differ from those of  $n_x$  only by a simple change of scale. In particular, if  $n_x$  is a FBM,  $L$  will be a FBM with the same fractal dimension. Strictly speaking, it is impossible for  $n_x$  to show true FBM characteristics, for a number of reasons. Firstly, as has been pointed out before, no real surface can be a true FBM since it cannot describe all spatial scales from zero to infinity. Secondly, even if a surface were to display FBM characteristics over some range of scales, the value of  $n_x$  could not formally be defined since a FBM is not differentiable. Thirdly, the power-law form of the semivariogram (structure function) of a FBM requires that the appropriate variable (in this case  $n_x$ ) can take any value, whereas  $n_x$  is limited to the range from -1 to +1.

None of these need impose fundamental limitations, however. It is always necessary to recognise that a real surface can be only approximately represented as a fractal, and that its description in fractal terms is valid only over some range of scales. The impossibility of differentiating a FBM surface can similarly be avoided by ‘rolling off’ the fractal behaviour below some minimum scale in order to smooth the surface. (However, Efford [25] has considered in some detail the effect of fractal geometry at sub-pixel scales on the image radiance.) The limitation imposed by the finite range of  $n_x$  is less real than apparent, since the assumptions implicit in equation (6) require that  $n_x$  varies over only a small part of the possible range.

A more fruitful approach is found by following Kube and Pentland [7]. If we write  $h(x, y)$  for the height of the surface, and set

$$p(x, y) = \frac{\partial h(x, y)}{\partial x} \quad (22)$$

and

$$q(x, y) = \frac{\partial h(x, y)}{\partial y} \quad (23)$$



we can write the surface normal vector  $\mathbf{N}$  as:

$$\mathbf{N} = \left[ \frac{-p}{\sqrt{p^2 + q^2 + 1}}, \frac{-q}{\sqrt{p^2 + q^2 + 1}}, \frac{1}{\sqrt{p^2 + q^2 + 1}} \right] \quad (24)$$

Substituting this into equations (2) and (3), we obtain:

$$\cos \theta_0 = \frac{\sin \alpha - p \cos \alpha}{\sqrt{p^2 + q^2 + 1}} \quad (25)$$

Provided that both  $p$  and  $q$  are much less than 1, the quadratic terms can be neglected and we can deduce that  $\cos \theta_0$ , and hence  $L$ , is linearly dependent on  $p$ .

Firstly we consider the case of a surface with one topological dimension, so that the height  $h$  is a function of a single variable  $x$ . We assume that this profile is a FBM with fractal dimension  $D$ , so that:

$$\gamma_h(d) \equiv \frac{1}{2} \langle [h(x+d) - h(x)]^2 \rangle \propto d^{4-2D} \quad (26)$$

This clearly implies that the power spectrum  $\mathbf{F}_h(k)$  of  $h$  is proportional to  $k^{2D-4}$ , so the amplitude spectrum  $F_h(k)$  must be given by:

$$|F_h(k)| \propto k^{D-2} \quad (27)$$

The amplitude spectrum  $F_p(k)$  of the differential  $p = dh/dx$  is thus given by:

$$|F_p(k)| \propto k^{D-1} \quad (28)$$

Equation 28 This can be squared to find the power spectrum  $\mathbf{F}_p(k)$ , but since (from equation 25) the image radiance  $L$  is linearly dependent on the differential  $p$ , the power spectrum  $\mathbf{F}_L(k)$  is proportional to  $\mathbf{F}_p(k)$  apart from a delta-function term at  $k=0$ . We can therefore put

$$\mathbf{F}_L(k) \propto k^{2D-2} \quad (29)$$

and hence

$$\gamma_L(d) \propto d^{2-2D} \quad (30)$$

Now we can proceed along similar lines to consider the image of a statistically isotropic surface  $h(x, y)$  having two topological dimensions. We assume that any linear transect through the surface will show FBM properties such that:

$$\gamma_h(d, \phi) \equiv \frac{1}{2} \langle [h(x + d \cos \phi, y + d \sin \phi) - h(x, y)]^2 \rangle \quad (31)$$

is proportional to  $d^{4-2D}$  and independent of  $\phi$ . The fractal dimension of a transect is again  $D$ , with  $D$  lying in the range  $1 \leq D \leq 2$ , and the fractal dimension of the surface is  $D + 1$ . We can define a pair of two-dimensional Fourier transforms to convert between a function  $a(x, y)$  and its two-dimensional amplitude spectrum  $F_a(k, \phi)$  as shown in equations (32) and (33):

$$F_a(k, \phi) = \int_{-\infty}^{\infty} \int_{-\infty}^{\infty} a(x, y) \exp(ikx \cos \phi) \exp(iky \sin \phi) dx dy \quad (32)$$

$$a(x, y) = \int_0^{\infty} \int_0^{2\pi} F_a(k, \phi) \exp(-ikx \cos \phi) \exp(-iky \sin \phi) k dx d\phi \quad (33)$$

Relating (32) to the assumed form of  $\gamma_h(d, \phi)$ , we must have:

$$|F_h(k, \phi)| \propto k^{D-3} \quad (34)$$

and hence

$$|F_p(k, \phi)| \propto \cos \phi k^{D-2} \quad (35)$$

where  $p = \partial h / \partial x$ . From equation (25), this implies that the power spectrum  $\mathbf{F}_L(k, \phi) \equiv (F_L(k, \phi))^2$  of the image radiance is given by:

$$\mathbf{F}_L(k, \phi) \propto \cos^2 \phi k^{2D-4} \quad (36)$$

so that the two-dimensional semivariogram  $\gamma_L(d, \phi)$  of the radiance  $L$  will be given by:

$$\gamma_L(d, \phi) \propto \cos^2 \phi d^{2-2D} \quad (37)$$

This shows that the image radiance of an isotropic FBM surface will have a power-law frequency spectrum, with a power-law index that is independent of orientation. The absolute value of the frequency spectrum (or the semivariance) is, however, dependent on the orientation  $\phi$  of the transect, as implied by equation (37), and will (subject to the assumptions implicit in equation (25)) fall to zero at  $\phi = \pm\pi/2$ . This angle corresponds to horizontal transects perpendicular to the solar azimuth.

We can see that the image radiance cannot itself be fractal for the following reason. Since the value of  $D$  must lie in the range 1 to 2, the power-law index  $2 - 2D$  in equation (32) or (37) must lie in the range 0 to -2. The power-law index of the semivariogram of a FBM, on the other hand, must lie between 0 and +2. However, provided that (a) the moduli of the surface slope components  $p \equiv \partial h / \partial x$  and  $q \equiv \partial h / \partial y$  remain much less than unity, (b) the illumination is oblique, and (c) shadowing is insignificant, we can

deduce that a FBM surface will give an image of which the semivariance is a power-law function of the separation  $d$ . A very smooth surface ( $D \approx 1$ ) will give  $\gamma_L(d) \propto d^0$ , i.e. a flat spectrum, and a very rough surface ( $D \approx 2$ ) will give  $\gamma_L(d) \propto d^{-2}$ , i.e. a spectrum with most of the power at high spatial frequencies.

We may ask whether, in investigating the topographical properties of a surface through its image, it is better to calculate the frequency spectrum of the image or first to apply the ‘shape from shading’ algorithm discussed above. Although there are advantages on both sides, it is useful to recognise that the image represents a differentiated version of the topography, and is therefore more likely to be adversely affected by noise. This is particularly so in the case of digitisation noise, since the low solar elevation angles necessary to this technique will imply generally low image radiances. It thus appears likely that more reliable conclusions will be drawn from an image by first generating a topographic surface from it using ‘shape from shading’, and then calculating its statistical (fractal or otherwise) properties.

## 7 Discussion and conclusions

The work described in this paper addresses two principal, linked, themes: the well-known correlation between image brightness and surface topography under suitable imaging conditions, and the statistical properties of the surface topography itself. Variations in the image brightness across a scene are caused by (i) the physical properties, and (ii) the orientation, of the surface, and where it is reasonable to assume that the appropriate physical properties remain constant (e.g. over a homogeneous region of soil or snow), the properties of the image can be used to make deductions about the surface topography.

To estimate the fractal (or otherwise) properties of a surface from optical imagery, it is necessary to use imagery obtained under conditions of low sun-angle. In principle, the statistical properties of the surface can be determined either by first measuring the spatial frequency spectrum of variations in image brightness, or by first using a shape-from-shading algorithm to determine the topography. Although the latter approach requires some geometric control, it is probably preferable since the image noise is effectively smoothed by integration.

Using this method, or using surface topography data directly, it has been shown that (i) the topography of naturally occurring surfaces is often best described by a type of fractal geometry known as fractal Brownian

motion, and that (ii) the fractal dimension so determined appears to be reasonably characteristic of the surface type, at least for the limited range of surfaces so far investigated. This is not unreasonable, since the fractal dimension provides a 'scale-free' measure of roughness that corresponds well with intuitive perceptions, so that, for example, heavily glaciated terrain is smoother (has a lower fractal dimension) than younger rock that has not yet been subjected to extensive glacial action. The scope of this approach for characterising and discriminating between eroded and uneroded soil surfaces, although not yet thoroughly investigated, appears promising.

## 8 Acknowledgments

I am greatly indebted to Miss I.-I. Lin for many illuminating discussions on fractal geometry and the imaging process.

## 9 References

- [1] Rees, W. G. (1990): 'Physical Principles of Remote Sensing', (Cambridge: Cambridge University Press).
- [2] Proy, C., Tanr, D. and Deschamps, P. Y. (1989): 'Evaluation of topographic effects in remotely sensed data', Remote Sensing of Environment, vol. 30, pp. 21-32.
- [3] Rees, W. G. and Dowdeswell, J. A. (1988): 'Topographic effects on light scattering from snow', Proceedings of the 1988 International Geoscience and Remote Sensing Symposium entitled "Remote Sensing - Moving towards the 21st century", held at Edinburgh, 12-16 September 1988. (ESTEC, Noordwijk: ESA Publications Division). ESA SP-284 (1988) pp. 161-164.
- [4] Lodwick, G. D. and Paine, G. H. (1985): 'A digital elevation model of the Barnes Ice-Cap derived from Landsat MSS data', Photogrammetric Engineering and Remote Sensing, volume 51, pp. 1937-1944.
- [5] Mandelbrot, B. B. (1982): 'The Fractal Geometry of Nature', (San Francisco: W. H. Freeman).

- [6] Pentland, A. P. (1984): 'Fractal-based description of natural scenes', IEEE Transactions on Pattern Analysis and Machine Intelligence vol. PAMI-6, pp. 661-674.
- [7] Kube, P. and Pentland, A. (1988): 'On the imaging of fractal surfaces', IEEE Transactions on Pattern Analysis and Machine Intelligence, vol. PAMI-10, pp. 704-707.
- [8] Rees, W. G. (1992): 'Measurement of the fractal dimension of ice-sheet surfaces using Landsat data', International Journal of Remote Sensing, vol. 13, pp. 663-671.
- [9] Peano, G. (1890): 'Sur une courbe, qui remplit toute une aire plane', Mathematische Annalen, vol. 36, pp. 157-160.
- [10] von Koch, H. (1904): 'Sur une courbe continue sans tangente, obtenue par une construction géométrique élémentaire', Arkiv für Matematik, vol. 1, pp. 681-704.
- [11] Mandelbrot, B. B. (1967): 'How long is the coastline of Britain?', Science, vol. 155, pp. 636-638.
- [12] Feder, J. (1988): 'Fractals', (New York: Plenum).
- [13] Lovejoy, S. (1982): 'Area-perimeter relation for rain and cloud areas', Science, vol. 216, pp. 185-187.
- [14] Mandelbrot, B. B., Passoja, D. E. and Paullay, A. J. (1984): 'Fractal character of fracture surfaces of metals', Nature, vol. 308, pp. 721-722.
- [15] Mandelbrot, B. B. and van Ness, J. W. (1968): 'Fractional Brownian motions, fractional noises and applications', SIAM review, vol. 10, pp. 422-437.
- [16] Voss, R. F. (1986): 'Characterization and measurement of random fractals', Physica Scripta, vol. T13, pp. 27-32.
- [17] Woodcock, C. E., Strahler, A. H. and Jupp, D. L. (1988): 'The use of semivariograms in remote sensing. I. Scene models and simulated images', Remote Sensing of Environment, vol. 25, pp. 323-348.

- [18] Woodcock, C. E., Strahler, A. H. and Jupp, D. L. (1988): 'The use of semivariograms in remote sensing. I. Real digital images', *Remote Sensing of Environment*, vol. 25, pp. 349-379.
- [19] Hurst, H. E., Black, R. P. and Simaika, Y. M. (1965): 'Long-Term Storage: An Experimental Study', (London: Constable).
- [20] Gorman, M. R. (1990), Personal communication: unpublished topographic data from the Greenland ice sheet.
- [21] Diamant, A. D. (1991), Personal communication: unpublished topographic data from Nordaustlandet, Svalbard.
- [22] Marshall, G. J. (1992), Personal communication: unpublished topographic data from Ayerbreen (glacier), Svalbard.
- [23] Bindschadler, R. A., Zwally, H. J., Major, J. A. and Brenner, A. C. (1989): 'Surface topography of the Greenland Ice Sheet from Satellite Radar Altimetry', (Washington DC: National Aeronautics and Space Administration Office of Management - Scientific and Technical Information Division), NASA SP-503.
- [24] Bishop, G. C. and Chellis, S. E. (1989): 'Fractal dimension: A descriptor of ice keel surface roughness', *Geophysical Research Letters*, vol. 16, pp. 1007-1010.
- [25] Efford, N. D. (1993): 'Scattering laws for reflected solar radiation and the characterisation of terrain roughness', *International Journal of Remote Sensing*, vol. 14, pp. 1055-1080.

# Chapter 13

## The Fractal Structure of Materials and Surfaces

*Giovanni Dietler\**

### 1 Introduction

In this chapter, I have changed my original plan to present fractals only as they are applied to topographic data and have decided also to include an example of the fractal structure of materials, since the structure of disordered materials plays an important role in geosciences and because it is a good example of how fractal geometry [1] can be used to decipher the problem posed by such materials. The comparison between the results obtained on the disordered materials and the results of a study of the Swiss landscape is very instructive.

### 2 Disordered Materials

Let us begin with the presentations of a few results about the aggregation of colloidal silica in water. The interest in the aggregation phenomena, which includes the microscopic step of the aggregation of single particles up to the formation of a macroscopic disordered material, was awakened by the now famous diffusion limited aggregation (DLA) model by Witten & Sanders [2]. This model was born just a few years after Mandelbrot had introduced the concept of fractal geometry to a broad scientific community [1]. The DLA model is one of the first examples of a microscopic model with simple rules showing the formation of complex structures, which was directly applicable to some *real* phenomena.

---

\*Institute of Physics, University of Fribourg, CH-1700 Fribourg, Switzerland

Much earlier, exactly the same phenomena were observed in cellular automata and in critical phenomena. In the first case, a simple rule applied to the evolution of a cellular automata, produced a complex non-trivial pattern, while in critical phenomena it was shown, that short range interactions were enough to produce long range ordering with power law-like correlation functions.

Let us describe the DLA model as it was originally proposed by Witten and Sanders [2]. There are two irreversible processes here, namely the diffusion of a particle and secondly its sticking to the aggregate. In Fig. 1 the details about the DLA model are given. After many particles are released, a tree like aggregate is formed, which is statistically fractal (see Fig. 2). The fractal dimension  $d_f$  is defined by the usual power law dependence of the average mass  $m(r)$  upon the size  $r$  of the aggregate:

$$m(r) \sim r^{d_f} . \quad (1)$$

Witten and Sanders measured, in order to determine the fractal dimension, the density-density correlation function of the aggregate in Fig. 2. The form of the density-density correlation function  $c(r)$  is a power law, which clearly indicates the scale invariance of the aggregates:

$$c(r) \sim \langle \rho(r)\rho(0) \rangle \sim r^{-(d-d_f)} . \quad (2)$$

Experiments confirmed the results of the DLA model with a modification, namely that in real systems there is more than one particle diffusing at one time and that there are many aggregates forming, which can also undergo aggregation. This modification leads to the cluster-cluster aggregation (CCA) model by Kolb, Botet and Jullien [3]. Table 1 compares the experimentally determined fractal dimension of aggregates with the theoretical predictions by the DLA and CCA models.

The fractal dimension was determined by light scattering from aggregates in dilute solutions and from gels produced from concentrated solution of silica colloids [4]. The scattered intensity as a function of the transfer moment  $q$  is given by the following expression:

$$I(q) = \frac{I_o}{\left(1 + \frac{q^2 \xi^2}{d_f/2}\right)^{d_f/2}} . \quad (3)$$

It is evident, that from light scattering experiments, it is possible to determine the fractal dimension and also the length scale  $\xi$  on which the sample is



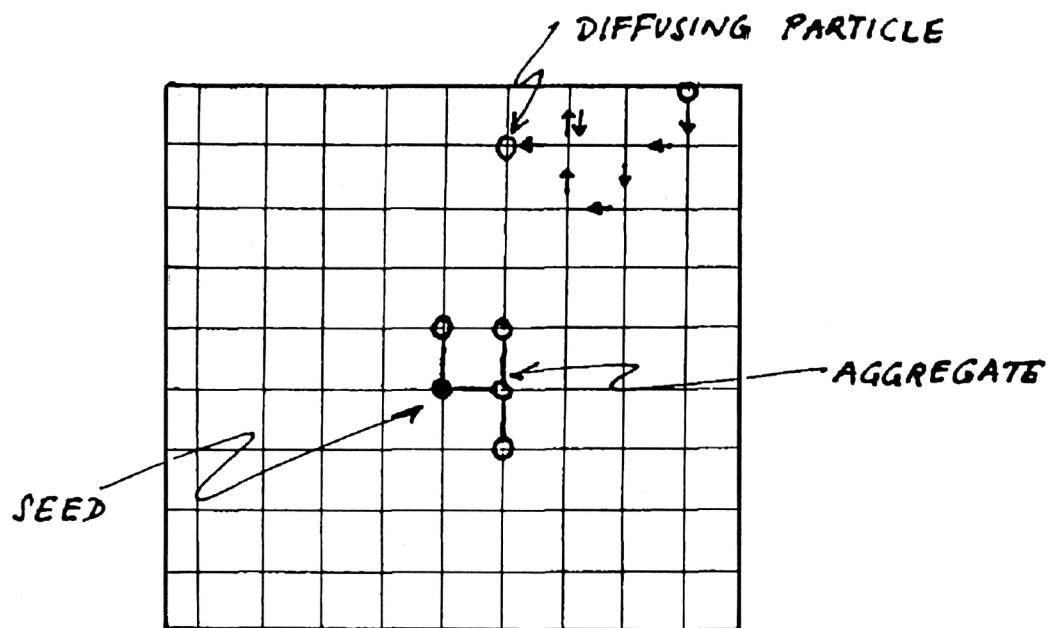


Figure 1: The diffusion limited aggregation (DLA) model by Witten and Sanders [2]. A seed is placed on the lattice centre at the beginning of the simulation and then one particle at a time is released at the lattice edges and is allowed to diffuse by Brownian motion until it reaches a site near an occupied site. At this moment the particle irreversibly binds to the existing aggregate. The process continues by releasing a new particle.

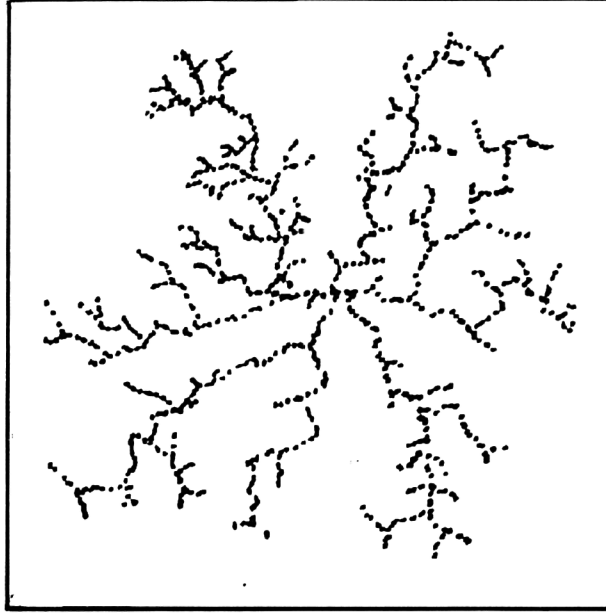


Figure 2: Result of the simulation using the DLA rules of Fig. 1. Physically the tenuous structure stems from the fact that incoming diffusing particles stick with high probability to the outer branches of the aggregate. That is the tips grow faster than the inner parts of the aggregate, preventing that the structure becomes compact.

Fractal Dimension $d_f$				
Simulations			Experiments <sup>c</sup>	
	DLA <sup>a</sup>	CCA <sup>b</sup>	Dilute	Concentrated
d=2	1.7	1.38		
d=3	2.4	1.75	(1.75 ± 0.10)	(2.16 ± 0.10)

Table 1: Fractal Dimension for Aggregates <sup>a</sup> Ref. [2], <sup>b</sup> Ref. [3], <sup>c</sup> Ref. [4].

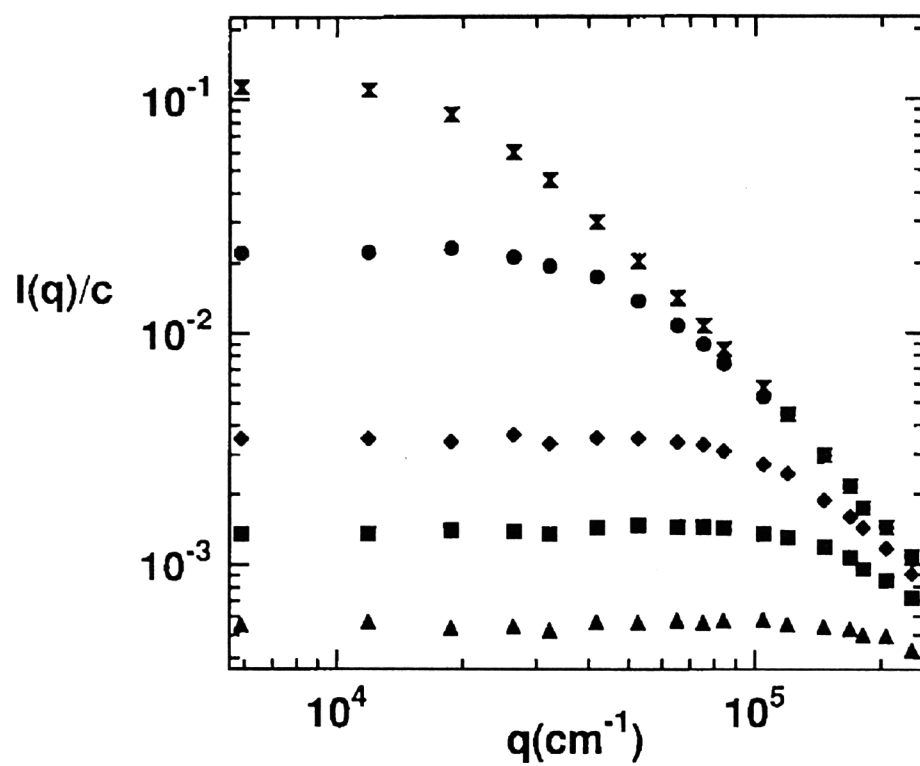


Figure 3: Intensity  $I(q)$  of the light scattered by the silica gels as a function of the transfer moment  $q$ .

fractal. The experimental measured light intensities are displayed in Fig. 3 for a set of gels with different total concentrations. Fits to the experimental data with equation (3) yield the fractal dimension and the cross-over length  $\xi$ . The fractal dimension is independent of the concentration as one would reasonably expect, while the cross-over length  $\xi$  is concentration dependent. Since the transfer moment  $q$  has the dimension of an inverse length, the plots of Fig. 3 show that the cross-over length  $\xi$  diminishes with an increasing concentration. The fitted value of  $\xi$  can be plotted versus  $c$  on a double logarithmic graph in Fig. 4, which indicates a power law of  $\xi$  on the concentration  $c$ . We have proposed a model [4] in order to explain the

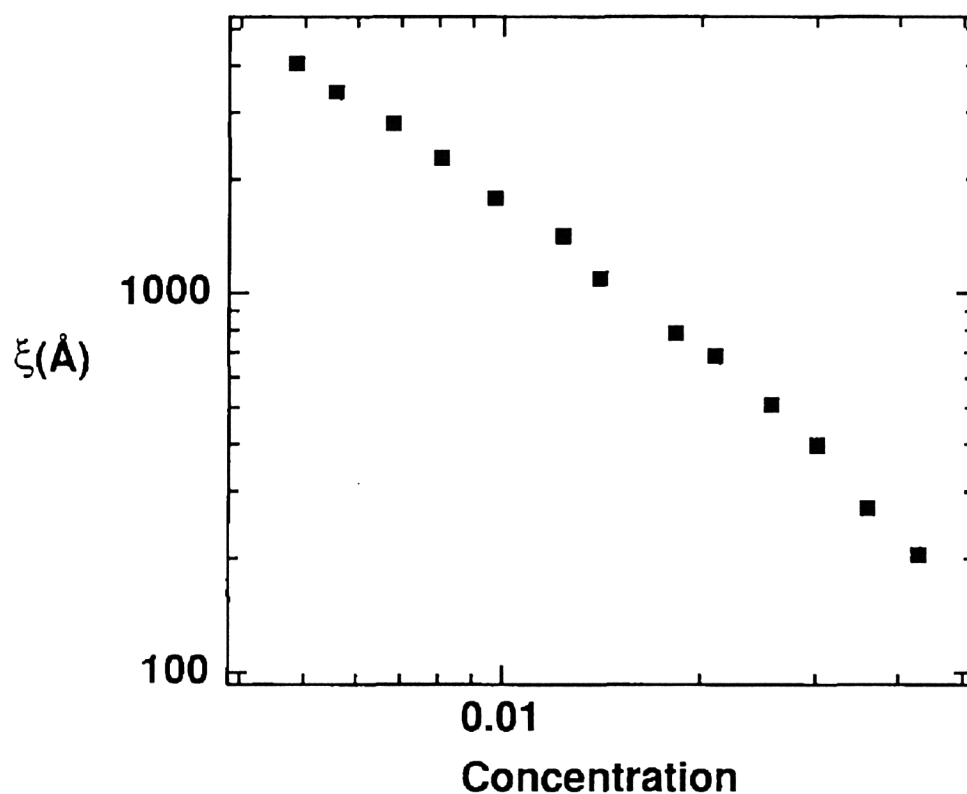


Figure 4: Cross-over length  $\xi$  versus the concentration  $c$ . The value of  $\xi$  were obtained by fitting the curves of Fig. 3 with equation (3).

structure of these gels by assuming that the sample is built, on average, of fractals of size  $\xi$ . Given  $\xi$  and the fractal dimension  $d_f$  using equation (1), one can express the concentration of one of these fractals as:

$$c(\xi) \sim \frac{m(\xi)}{V(\xi)} \sim \frac{\xi^{d_f}}{\xi^d} \quad (4)$$

and thus

$$\xi(c) \sim c^{-\frac{1}{d-d_f}}. \quad (5)$$

Fits to the data of Fig. 4 have given a slope of  $1.17 \pm 0.10$ , which nicely agrees with equation (5) and a fractal dimension of  $d_f = 2.15$ . If the gels are self-similar objects, it is enough to perform on them a scale transformation and they will statistically overlap. The way we are doing this here, is loaned from critical phenomena. The  $q$ -axis of Fig. 3 can be made dimensionless by a multiplication with a length, its natural value being  $\xi$ , which is for each sample different. The intensity data are replotted in a scale independent graph in Fig. 5, resulting in a universal curve for all the data.

This procedure is called, in critical phenomena, static scaling. Needless to repeat, that the gels are all identical up to a concentration dependent scale factor. A by-product of the scale invariance is, that the gels are uniquely determined by two numbers, the fractal dimension  $d_f$  and the length scale  $\xi$  or the concentration  $c$ . This is a very economic way of telling the position of each colloidal particle in a gel.

### 3 Surfaces

Now we turn our attention to landscapes and in general to surfaces. My interest into surfaces was spurred by the now well-known Kardar-Parisi-Zhang (KPZ) equation [5], which is a non-linear Langevin equation:

$$\frac{\partial h(x,t)}{\partial t} = \nu \nabla^2 h(x,t) + \frac{\lambda}{2} (\nabla h(x,t))^2 + \eta(x,t). \quad (6)$$

This equation describes the spatial and temporal evolution of the height  $h(x,t)$  of an interface under the action of the surface tension  $\nu$ , a growing term proportional to  $(\nabla h(x,t))^2$  and a Gaussian noise term  $\eta(x,t)$ . It has solutions for the interface width  $w(L,t)$  in the form:

$$w(L,t) \sim L^\chi f(t/L^z), \quad (7)$$

where  $\chi$  is the roughening exponent,  $z$  the dynamical critical exponent and  $f(t/L^z)$  is an appropriate scaling function. The scaling function  $f(x)$  goes

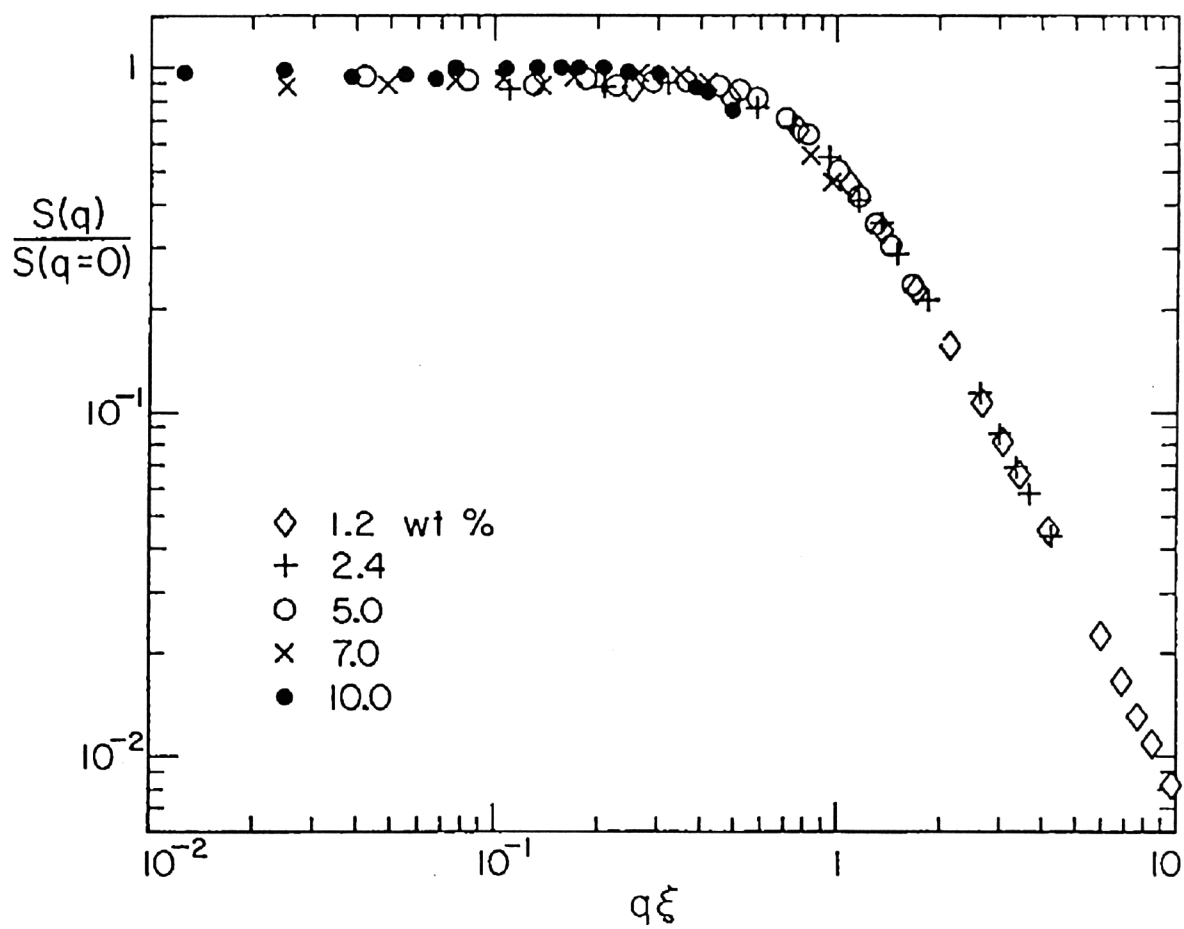


Figure 5: Data as in Fig. 3 but plotted in a scale independent way. The  $q$  axis is substituted by a  $q\xi$  axis.

to a constant for  $x \gg 1$  (long times) and  $f(x) \sim x^{x/z}$  for  $x \ll 1$  (short times), indicating that  $\Delta h \sim L^x$  at large time scales. The dynamic of any topographic feature of size  $L$  has an average lifetime of the order  $t \sim L^z$ . For time  $t \ll L^z$  the surface roughness evolves as  $\Delta h(L) \sim t^{x/z}$ . The approximated value for the exponents are:

$$\chi \approx \frac{2}{d+3} \quad \text{and} \quad z \approx \frac{2(d+2)}{d+3}$$

where  $d$  is the dimension of the system.

Sornette and Zhang [6] modified equation (6) and applied it to erosion processes. The detailed prediction of the KPZ equation are given in Table 2. The exponent  $z$  is for us of little interest, since it describes the

Dimension $d$	$\chi$	$z$	$d_f = d - \chi$
$d = 2$	$2/5 = 0.4$	$8/5$	$8/5 = 1.6$
$d = 3$	$1/3 \approx 0.33$	$5/3$	$8/3 \approx 2.67$

Table 2: Exponents from the KPZ equation.

temporal evolution of the surface over geological time scales, which falls very well outside of our life span. Only for some fast erosion process, it will be possible and useful to know  $z$ . The exponent  $\chi$  stimulates our interest, because it is involved in the spatial dependence of the surface width, hence it is connected to the fractal dimension  $d_f$ . An additional advantage to study  $\chi$  is that static data are more readily available than the dynamical information. Topographic data usually extend from the meter scale up to hundreds of kilometers, offering a unique test of the KPZ equation. Beside the test of the KPZ equation, one would also like to learn something particular about the object under study, and not just prove its universal behavior. In the case of silica gels, we could determine the microscopic process being responsible for the aggregation (DLA model versus CCA model), for the topography it would be of great interest to know more about the erosion processes.

To this end the height data of the Swiss topography, available in numeric format on computer disk [7], were analyzed in detail. First, let us define

the static width  $w(L)$  of the interface by:

$$w(L) = \sqrt{\left\langle \frac{1}{N^2} \sum_{i,j=1}^N (h_{ij} - \bar{h})^2 \right\rangle} \quad (8)$$

where  $N = L/\ell_o$  is the number of raster points in a length  $L$  and  $\ell_o$  the raster,  $h_{ij}$  the height in meters at the coordinate  $ij$  and  $\bar{h} = 1/N^2 \sum_{i,j=1}^N h_{ij}$  the average height. Expression (8) is essentially the *rms* deviation of the surface height.

Secondly, the width  $w(L)$  has to be calculated [8]. For this purpose the whole Swiss surface was divided in squares of size  $L \times L$  and  $w(L)$  was averaged over all the squares, as it is defined in equation (8). Then to check for scaling behavior,  $w(L)$  was plotted on a double-logarithmic graph versus  $L$ . There are two scaling regions, one for small  $L < 5$  km and one for large  $L > 5$  km. The small  $L$  region has a scaling exponent  $\chi \approx 0.57$  whereas the large  $L$  region possesses a scaling exponent  $\chi \approx 0.27$ . The cross-over from one scaling regime to the other is at  $\xi \approx 5$  km. The second scaling regime is not true scaling, but is due to the linear slope in the data. If a plane is subtracted from the data,  $w(L)$  becomes constant for  $L > 5$  km as it is shown by the dotted line in Fig. 6. How can we interpret our result and what can we learn from  $w(L)$ ? Two points are worth mentioning: (a) a scaling regime for  $L < 5$  km and (b) a cross-over to a regime where  $w(L)$  is constant. This behavior is similar to the one found for gels, which are self-similar on length scales smaller than a cross-over length  $\xi$  and behave like homogeneous materials for length scales larger than  $\xi$ .

We therefore conclude, that the Swiss surface can be assimilated to a random collection of self-affine squares of size 5 km x 5 km, which have identical statistical properties.

Previous studies have never demonstrated the cross-over, probably because they were done on a limited set of data. Nevertheless, it is interesting to compare the fractal dimension found from different data sets. In Table 3 an incomplete set of values is listed, together with theoretical predictions and an experimental value. The studies are mostly on 2-dimensional (transect data) data sets and all have a fractal dimension  $d_f \approx 1.5$ , which is in good agreement with the KPZ predictions. One very interesting case, is the experiment of Czirk et al. [16], where a sand pile was eroded away by water poured on top of it and the fractal dimension has the lowest of all the 2-dimensional data sets. In general the theoretical predictions for  $d_f$  are higher than the measured values independently of the space dimension. Results from 3-dimensional data sets are listed in Table 3. For topographic



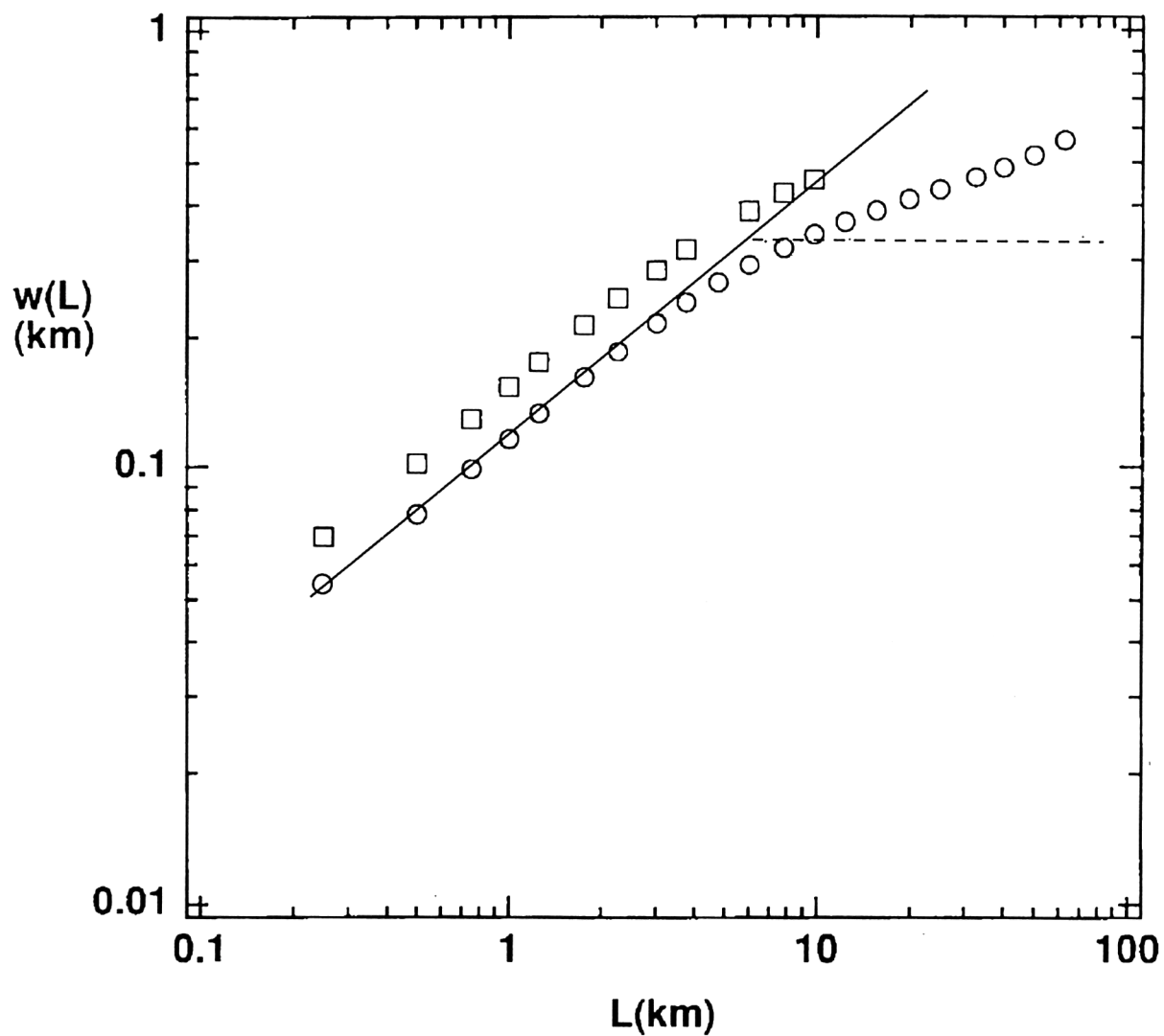


Figure 6: The interface width  $w(L)$  versus the horizontal scale  $L$ . For small  $L < 5$  km the data follow a power law with exponent  $\chi \approx 0.57$ . For  $L > 5$  km the width  $w(L)$  seems to obey a power law with another exponent  $\chi \approx 0.27$ .

Author	Description	$d$	Size of Data Set	$d_f$
Bell <sup>a</sup>	Seafloor	2	700 km	1.5
Barenblatt et al. <sup>b</sup>	Seafloor	2	2500 km	1.285
Fox & Hayes <sup>c</sup>	Seafloor	2		1.5
Gibert & Courtillot <sup>d</sup>	South Atlantic	2	25 km	1.5
Huang & Turcotte <sup>e</sup>	Earth Surface	3	4.5 km x 4.5 km	2.1
		2		1.5
Newman & Turcotte <sup>f</sup>	Earth Surface	2	75 km	1.5
Dietler & Zhang <sup>g</sup>	Swiss Topography	3	350 km x 250 km	2.43
Dietler <sup>h</sup>	Hard Material	3	10 $\mu\text{m}$ x 10 $\mu\text{m}$	2.05
KPZ Equation <sup>i</sup>	Theory	2		1.6
		3		2.67
Czirók et al. <sup>j</sup>	Experiments	2	18 cm x 60 cm	1.21

Table 3: Fractal dimension from topographic data.

<sup>a</sup>Ref. [9], <sup>b</sup>Ref. [10], <sup>c</sup>Ref. [11], <sup>d</sup>Ref. [12], <sup>e</sup>Ref. [13], <sup>f</sup>Ref. [14], <sup>g</sup>Ref. [8],  
<sup>i</sup>Ref. [15], <sup>i</sup>Ref. [5], <sup>j</sup>Ref. [16].

data  $d_f$  is in the range 2.1 to 2.43, well below the theoretical predictions. A further example of 3-dimensional data is inserted in Table 3 and concerns the surface of a polished steel. The surface was imaged with an atomic force microscope and the height data were analyzed according to equation (8). The resulting  $w(L)$  curve is depicted in Fig. 7. If we assume, as we have concluded for the Swiss topography, that the surfaces are a collection of self-affine squares of the size  $\xi \times \xi$ , the width  $w(L)$  can be expressed by a simple formula:

$$w(L) = \frac{w_o}{1 + \left(\frac{\xi}{L}\right)^\chi} \quad (9)$$

From fits of the curve in Fig. 7 the fractal dimension  $d_f = d - \chi = 2.05$  and the cross-over length  $\xi = 570$  nm were determined.

## 4 Comparison between Disordered Materials and Surfaces

Let us compare the colloidal silica gels and the topography of surfaces. One important result of the colloidal aggregation is the differentiation between the DLA model and the CCA model, made possible by the fractal dimension. The small difference between the two models is reflected in a marked difference in fractal dimension. Thus, from the measured fractal dimension, one can draw conclusions about the microscopic processes undergoing during aggregation, demonstrating the power of fractal geometry.

The surfaces behave in this respect rather differently, it is enough to look at the last column in Table 3 to perceive the message. In 2-dimensions the fractal dimension is  $d_f \approx 1.5$ , regardless of the very different geological objects that were considered, from the seafloor to the mountain ranges. This is in some respects a deceiving conclusion, since one would like to gain more knowledge out of the fractal dimension as it was the case for aggregation.

One point I would like to stress here, namely that we need more reliable methods to determine  $d_f$ . Spectral methods have usually a larger uncertainty and require larger data sets, whereas our method is more precise. However, the measurement of the interface width  $w(L)$  is not without flaws. During the analysis of the Swiss topography we took a limited set of data (17.5 km  $\times$  12.5 km) with a 25 meter raster [7] and analyzed it according to equation (8). The results were confusing, since the scaling exponent  $\chi$ , and consequently  $d_f$ , are dependent upon the raster length  $\ell_0$ .

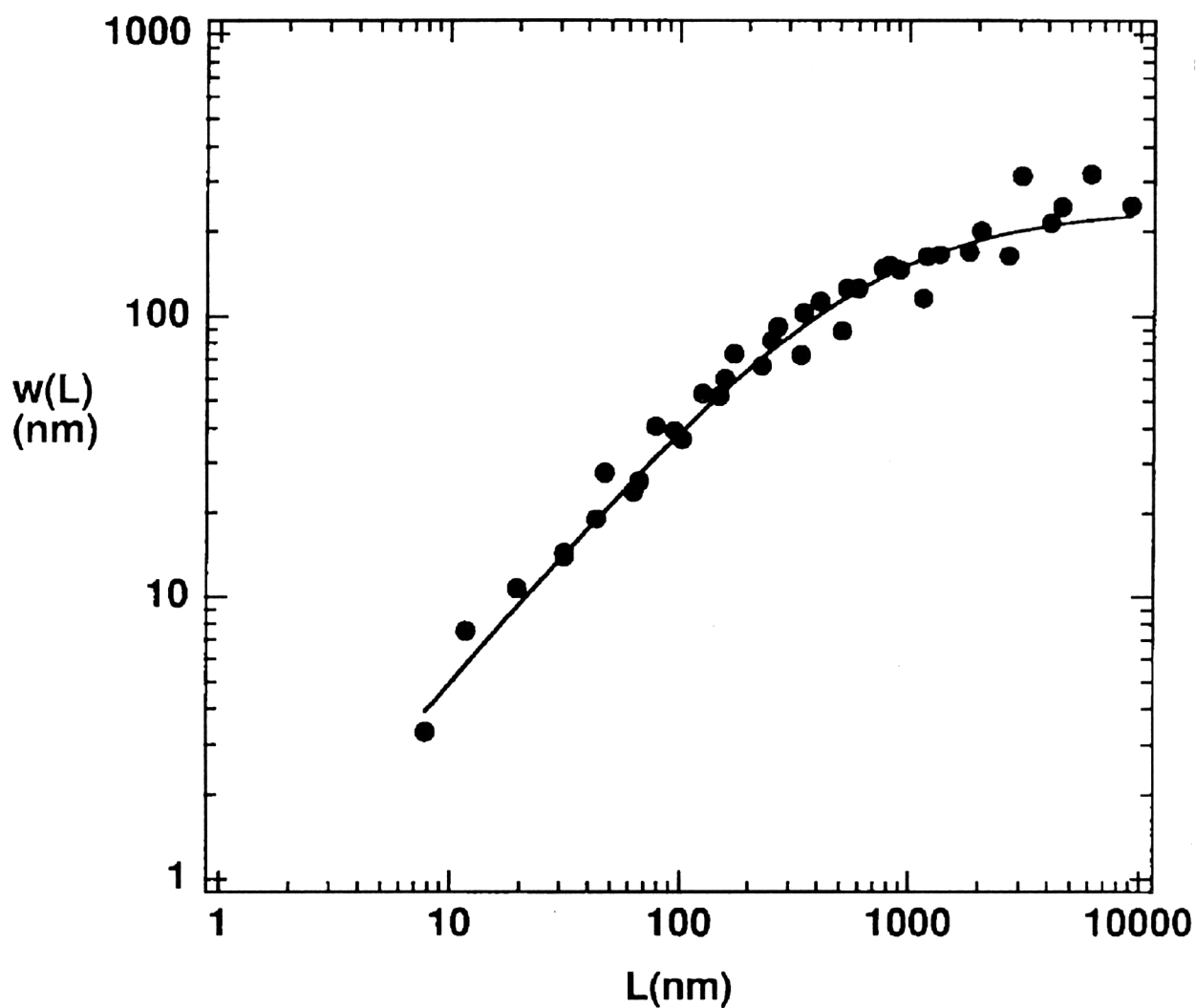


Figure 7: The interface width  $w(L)$  versus the horizontal scale  $L$  for a polished steel surface. There are about 8 orders of magnitude difference between this plot and the one in Fig. 6. The topography of this surface was measured on a square of size  $10\text{ }\mu\text{m} \times 10\text{ }\mu\text{m}$ .

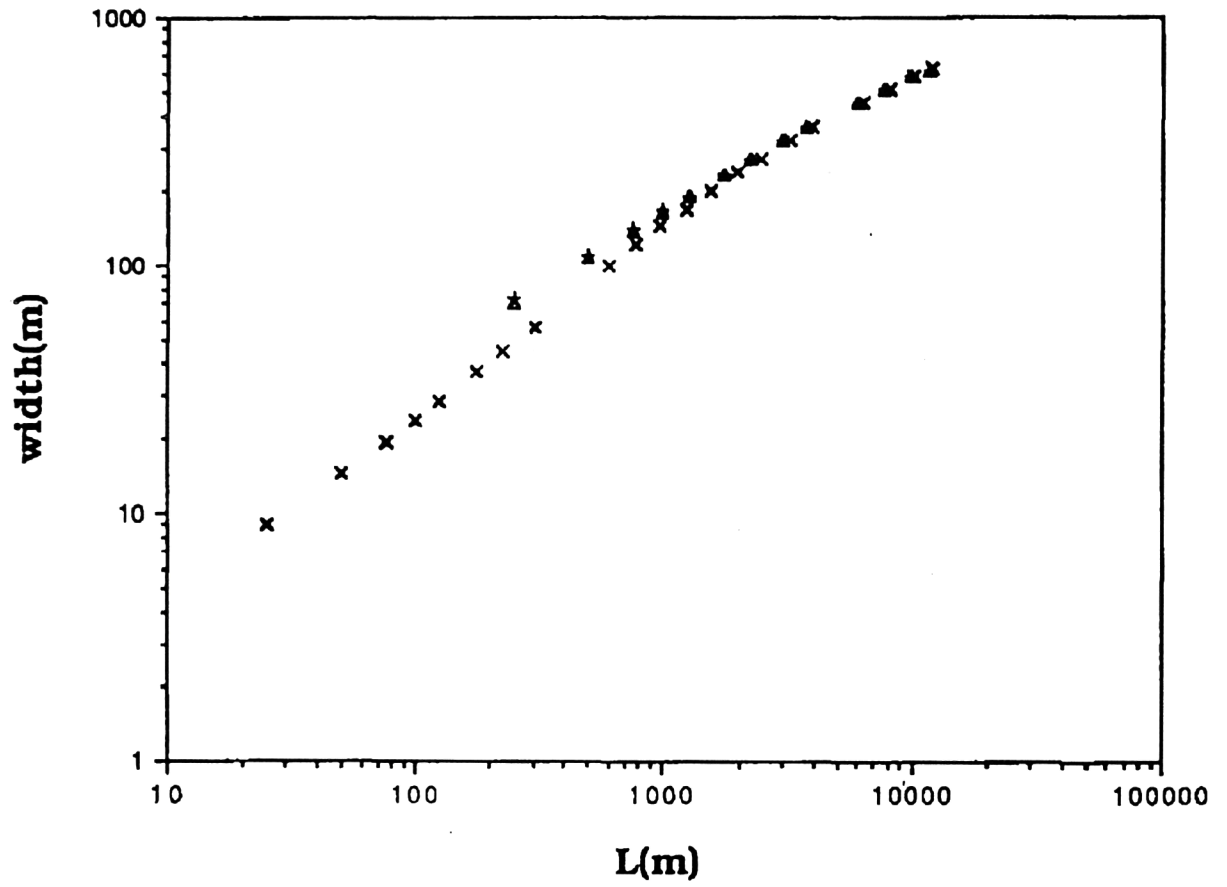


Figure 8:  $w(L)$  versus  $L$  for two different raster sizes. (x)  $\ell_o = 25$  m. (+) and ( $\triangle$ )  $\ell_o = 250$  m. For  $\ell_o = 25$  m the scaling exponent is  $\chi = 0.75$ , whereas for  $\ell_o = 250$  m  $\chi = 0.57$ .

In Fig. 8  $w(L)$  is depicted versus  $L$  for different raster lengths:  $\chi$  is varying from 0.57 for  $\ell_0 = 250$  m to 0.75 for  $\ell_0 = 25$  m, implying a  $d_f$  from 2.43 to 2.25.

The cross-over phenomena is another important result that we have found in both examples discussed here. We can summarize the findings as follows: The disordered materials (in our case colloidal silica gels) and the Swiss topography have similar structure, namely they seem to be built out of a collection of self-similar objects of the size  $\xi$  (for the gels) or of a collection of self-affine squares of the size  $\xi \times \xi$  (for the Swiss topography) randomly arranged. This implies that the relevant self-affine structure in the Swiss topography has a 5 km scale.

## 5 Acknowledgements

I would like to thank Y.C. Zhang for his continuous help during this work and for interesting and clarifying discussions.

## 6 References

- [1 ] B.B. Mandelbrot (1977): "The Fractal Geometry of Nature", (New York: W.H. Freeman).
- [2 ] T.A. Witten and L.M. Sanders (1981): "Diffusion-Limited Aggregation, a Kinetic Critical Phenomenon", Physical Review Letters, Vol. 47, No. 19, pp. 1400-1403.
- [3 ] M. Kolb, R. Botet and R. Jullien (1983): " Scaling of Kinetically Growing Clusters", Physical Review Letters, Vol. 51, No. 13, pp. 1123-1126.
- [4 ] For dilute solutions see C. Aubert and D.S. Cannell (1986): "Restructuring of Colloidal Silica Gels", Physical Review Letters, Vol. 56, No. 7, pp. 738-741. For concentrated solutions see G. Dietler, C. Aubert, D.S. Cannell and P. Wiltzius (1986): "Gelation of Colloidal Silica", Physical Review Letters, 57, No. 24, pp. 3117-3120.
- [5 ] M. Kardar, G. Parisi and Y.C. Zhang (1986): "Dynamic Scaling of Growing Interfaces", Physical Review Letters, Vol. 56, No. 9, pp. 889-992.

- [6 ] D. Sornette and Y.C. Zhang (1993): "Non-Linear Langevin Model of Geomorphic Erosion Process", *Geophysical Journal International*, Vol. 113, pp. 383.
- [7 ] We are indept to the *Bundesamt fr Landestopographie, Wabern, Switzerland* for making available to us the topographic data of Switzerland with a 250 m raster. The same office offered also a limited set of data with 25 m raster.
- [8 ] G. Dietler and Y.C. Zhang (1992): "Fractal aspects of the Swiss Landscape", *Physica A*, Vol. 191, pp. 213-219.
- [9 ] T.H. Bell (1975): "Statistical features of sea-floor topography", *Deep-Sea Research*, Vol. 22, pp. 883-892.
- [10 ] G.I. Barenblatt, A.V. Zhivago, Yu.P. Neprochov and A.A. Ostrovskiy (1984): "The Fractal Dimension: A Quantitative Characteristic of Ocean-Bottom Relief", *Oceanology*, Vol. 24, No. 6, pp. 695-697.
- [11 ] C.G. Fox and D.E. Hayes (1985): "Quantitative Methods for Analyzing the Roughness of the Seafloor", *Reviews of Geophysics*, Vol. 23, No. 1, pp. 1-48.
- [12 ] D. Gibert and V. Courtillot (1987): "Seasat Altimetry and the South Atlantic Geoid: 1. Spectral Analysis", *Journal of Geophysical Reasearch*, Vol. 92, No. B7, pp. 6235-6248.
- [13 ] J. Huang and D.L. Turcotte (1989): " Fractal Mapping of Digitized Images: Application to the Topography of Arizona and Comparison With Synthetic Images", *Journal of Geophysical Reasearch*, Vol. 94, No. B6, pp. 7491-7495.
- [14 ] W.I. Newman and D.L. Turcotte (1990): "Cascade model for fluvial geomorphology", *Geophysical Journal International*, Vol. 100, pp. 433-439.
- [15 ] G. Dietler, unpublished results. Measurements by atomic force microscope.
- [16 ] A. Czirk, E. Somfai and T. Vicsek (1993): "Experimental Evidence for Self-Affine Roughening in a Micromodel of Geomorphological Evolution", *Physical Review Letters*, Vol. 71, No. 13, pp. 2154-2157.





# List of Expert Meeting Participants

Bernhard Braunecker, Leica AG, Heerbrugg, Switzerland  
Mihai Datcu, DLR, Oberpfaffenhofen, Germany  
Marc De Cort, JRC, European Commission  
Steven de Jong, University of Utrecht, The Netherlands  
Giovanni Dietler, University of Fribourg, Switzerland  
Timothy Ellis, City University, London, UK  
Freddy Fierens, JRC, European Commission  
Stefano Fioravanti, University of Genova, Italy  
Yves Govaerts, JRC, European Commission  
Ioannis Kanellopoulos, JRC, European Commission  
Jacques Lévy-Véhel, INRIA, France  
Shaun Lovejoy, Université Pierre et Marie Curie, Paris, France  
Philippe Martin, JRC, European Commission  
Jacques Mégier, JRC, European Commission  
Jean Meyer-Roux, JRC, European Commission  
Pasquale Nardone, JRC, European Commission  
Laurent Polidori, Aerospatiale, Cannes, France  
Marcel Raffy, GSTS, Strasbourg, France  
Gareth Rees, University of Cambridge, UK  
Paul Rosin, JRC, European Commission  
Gianfausto Salvadori, University of Pavia, Italy  
Daniel Schertzer, Université Pierre et Marie Curie, Paris, France  
Klaus Seidel, ETH, Zurich, Switzerland  
Leonid Vasiliev, Institute of Geography, Moscow, Russia  
Graeme Wilkinson, JRC, European Commission



European Commission

**EUR 16092–Fractals in geoscience and remote sensing**

*G.G. Wilkinson, I. Kanellopoulos, J. Mégier*

Luxembourg: Office for Official Publications of the European Communities

1995–348 pp., 126 fig., 22 tab.–21.0 x 29.7 cm

Image understanding research series

CL-NA-16092-EN-C

This volume contains the edited proceedings of a joint JRC/EARSel expert meeting on the topic of Fractals in Geoscience and Remote Sensing which was held at the Joint Research Centre, Ispra, 14-15 April 1994. The volume contains 13 technical chapters on various aspects of fractal theory and applications in geoscience and remote sensing and includes an introduction by the editors.















